A SUPERCONDUCTING QUANTUM INTERFERENCE DEVICE (SQUID) MAGNETOMETER FOR NANOSATELLITE SPACE WEATHER MISSIONS

by

KEHINDE OGUNYANDA

Thesis submitted in fulfilment of the requirements for the degree

Master of Technology: Electrical Engineering

in the Faculty of Engineering

at the Cape Peninsula University of Technology

Supervisor: Dr. Wilfred Fritz
Co-supervisor: Prof. Robert van Zyl

Bellville
November 2012

DECLARATION

I, Kehinde Ogunyanda, declare that the contents of this dissertation/thesis represent my own unaided work, and that the dissertation/thesis has not previously been submitted for academic examination towards any qualification. Furthermore, it represents my own opinions and not necessarily those of the Cape Peninsula University of Technology.

Signed **Date**

ABSTRACT

In order to effectively determine the occurrences of space weather anomalies in near Earth orbit, a highly sensitive space-grade magnetometer system is needed for measuring changes in the Earth's magnetic field, which is the aftermath of space weather storms. This research is a foundational work, aimed at evaluating a commercial-off-the-shelf (COTS) high temperature DC SQUID (superconducting quantum interference device) magnetometer, and establishing the possibility of using it for space weather applications. A SQUID magnetometer is a magnetic field measuring instrument that produces an electrical signal relative to the sensed external magnetic field intensity.

A DC SQUID was selected, because it is easy to analyse, coupled with the fact that it is the most sensitive and accurate magnetometer type known. SQUIDs can only operate effectively in a cryogenic environment (temperatures below -150 ^{0}C), achievable by using either an active or passive cooling system. The novelty of this research is the fact that the evaluated sensor type has never been reported to have flown on any nanosatellite mission, mainly due to the stringent cooling mechanism required for its operation. Various cryocooling approaches were analysed for the mission, after which a passive cooling system was selected. Modelling and simulation of a passive cooling system, made of four stages of radiators, was done, using the Thermal Desktop software package. These radiators radiate heat into the deep space, and prevent incoming heat from both the Earth and the Sun. In order to mitigate the magnetic field emanating from the satellite structure, the entire cooler assembly that houses the sensor, is made deployable at a distance from the satellite structure, using a boom length of 100 mm. The simulation results show that a cooling capacity of about 18 mW, at a cryogenic temperature of 77 K, is attainable in a 600 km Sun synchronous LEO orbit, with the largest radiator being 100 mm in diameter. Simulations and analyses of the voltage-flux characteristics, voltage-current characteristics, thermal noise effects and readout electronics of a DC SQUID magnetometer were also done, using both PSIM and MATLAB-Simulink packages, so as to predict its practical real-time behaviour.

The experimental work that were done, include the fabrication and testing of the DC SQUID bias and readout electronics, which were later used to test the functionality of the COTS DC SQUID acquired from Star Cryoelectronics. The simulation results and the successful practical tests carried out proved the feasibility of using a SQUID magnetometer for nanosatellite space weather missions. The sensor was as well subjected to a space qualification test (Gamma radiation in this case), in order to observe its durability in space. The outcome of this, however, suggests the need for enveloping the sensor with a radiation-hardened material for it to be durable in space. Further improvements for future work are recommended in the concluding chapter of this thesis.

ACKNOWLEDGEMENTS

I wish to thank:

- My God, the one who has helped me this far in life
- Dr. Fritz, my supervisor, and Prof. van Zyl, my co-supervisor for their untiring guidance given to me throughout the research, despite their busy schedules
- Hon. And Mrs. Ogunyanda, my lovely parents and Mr. Olayemi, my esteemed Uncle, for allowing me to embark on this course of study
- Olamide, Justina, Feyikemi, Feranmi, Anu, Makhetsi, Remi, my lovely sisters, for their prayers towards the success of this project
- Dr. Oladijo, Dr. Olujimi, Mr. Ayeleso, Mr. Ogidan and Mr. Raji, my unforgettable helpers and technical advisers, for linking me up with this great institution and their timely and elderly advice

The financial assistances of the National Research Foundation (NRF) and department of science and technology (DST), through the French South African Institute of Technology, towards this research, are acknowledged. Opinions expressed in this thesis and the conclusions arrived at, are those of the author, and are not necessarily to be attributed to NRF or DST.

DEDICATION

This is dedicated to God Almighty, the author of my life, who has always been the driving force for all my achievements.

TABLE OF CONTENTS

LIST OF FIGURES

LIST OF TABLES

GLOSSARY

Terms, Acronyms and Abbreviations	Definition/Explanation
AC	Alternating Current
ADC	Analogue to Digital Converter
COTS	Commercial-off-the-Shelf
CPUT	Cape Peninsula University of Technology
Cryogenic temperature	Temperature below -150 ^{0}C
CubeSat	Cube satellite
DC	Direct Current
Dewar	A vacuum enclosure for holding liquid cryogen
DST	Department of Science and Technology
EMI	Electromagnetic Interference
EUT	Equipment Under Test
FET	Field Effect Transistor
FLL	Flux Locked Loop
F'SATI	French South African Institute of Technology
GBW	Gain Bandwidth
GEO	Geosynchronous Orbit
GIPD	Gauge Invariant Phase Difference
HMO	Hermanus Magnetic Observatory
HTS	High Temperature SQUID
JJ	Josephson Junction
Kg	Kilogram
LEO	Low Earth Orbit
LNA	Low Noise Amplifier
MATLAB	Matrix Laboratory
MLI	Multi-Layer Insulation
Nanosat	Nanosatellite
Noise	Unwanted random instability in the signal of interest
nT	nano Tesla
Offset	This is the value at which the instrument output deviates from the zero point/reading.
Op-amp	Operational Amplifier
PCB	Printed Circuit Board
PLD	Pulsed-Laser Deposition
RLC	Resistance Inductance Capacitance

Range	Refers to the upper and lower limits of the values which can be recorded by an instrument
RF	Radio Frequency
rms	Root mean square
RSJ	Resistively Shunted Junction
SALT	Southern Africa Large Telescope
SAMA	South Atlantic Magnetic Anomaly
SANSA	South African National Space Agency
SERF	Spin Exchange Relation Free
SIS	Superconductor-Insulator-Superconductor
SQUID	Superconducting Quantum Interference Device
SuperDARN	Super Dual Auroral Radar Network

CHAPTER ONE

INTRODUCTION

1.1 Introduction

With a view to addressing one of the five key challenges in the DST (Department of Science and Technology) ten-year innovation plan, the South African National Space Agency (SANSA) was established in 2009 by the National space Agency Act, with subsequent migration of the Hermanus magnetic observatory (HMO) into the agency in April 2011. More so, the French South African Institute of Technology (F'SATI) was founded at the Cape Peninsula University of Technology by the Department of Science and Technology (DST), to actively participate in building human capital in the field of space science and technology in South Africa. The students enrolled at F'SATI are exposed to practical experience in satellite engineering, using nanosatellite platforms (International Astronautical Congress, 2011).

F'SATI has recently completed a 1U CubeSat (a nanosatellite with standard dimensions of 10 cm X 10 cm X 10 cm, weighing about 1kg). This 1U satellite, named ZACUBE-1, has a high frequency beacon for the characterisation of the Super Dual Auroral Radar Network (SuperDARN) field of view (Visser, 2009). A 3U CubeSat (three stacked 1U CubeSats), named ZACUBE-2, is currently under construction, with a camera as the major payload. A highly sensitive magnetometer is being proposed for future F'SATI 3U projects, for space weather missions.

1.2 Research Background

The place of magnetometers in space weather study cannot be underestimated. As an instance, the discovery of the Van Allen radiation belt (VARB) around the Earth was made possible by the magnetometer onboard the Explorer 1, launched in 1958 (Mitchell, 2007). The first magnetometer in space was used on Sputnik 3 in 1958, for exploring the upper space (Diaz-Michelena, 2009:2274). Magsat, Oersted and some other satellites also used magnetometers for in-depth solar and Earth's magnetic fields studies. The use of magnetometers in space missions has, however, been limited to the flux-gate, search-coil, optically pumped and vector Helium types, due to power, weight, precision, cost and other critical constraints in the space weather and satellite structures (Acuna, 2002: 3717-3736).

For SQUID magnetometers, the inability to provide the suitable and durable cryogenic temperature onboard for their operation, has indeed limited their usability in space. Although superconducting materials have been flown in space, like in the case of the gravity probe B mission, where Niobium was used to encapsulate a gyroscope's rotor, thereby enabling it to sense the gyroscope's direction, but literature has never reported the use of SQUID

magnetometers on any nanosatellite mission (Mester & GP-B Collaboration, 2006:57). Besides these limitations, the advantages of using SQUID magnetometers, in place of other conventional magnetometer types, are due to their very high sensitivity, accuracy and wide dynamic range. SQUID magnetometyers superior sensitivity (< 10 fT $Hz^{-1/2}$), gives room for sensing extremely low magnetic fields, as reported by Faley, Poppe, Urban, Paulson, Starr, and Fagaly (2002:219). They are capable of sensing magnetic fields, even to the range of femto Tesla. The feasibility of using cryogenic sensors, like the SQUIDs, for space applications, has been well established by various missions that employed cryocooling mechanisms for maintaining cryogenic temperatures in space. Section 2.10 discusses further on this. These missions, however, involved larger satellites, unlike the nanosatellite platforms.

1.2.1 Space weather

Space weather can simply be defined as the condition of the Sun and other interplanetary environments like the ionosphere, magnetosphere, and the thermosphere, which has potential influence on any space-borne and ground-based electrical systems (Moldwin, 2008:1). When the diffuse solar radiations emanating from the Sun interact with the interplanetary environment, trapped streams of energetic particles are formed around the VARB. South Atlantic Magnetic Anomaly (SAMA) further results from a portion of the VARB closer to the Earth surface. As depicted in Figure 1.1, the SAMA region is characterised by a very weak magnetic field strength (dark oval portion on the image). The occurrence of the SAMA, coupled with other solar-terrestrial processes like the geomagnetic effects (caused by ionospheric current variation), solar flares, coronal mass ejections, and sunspots, constitute what is known as space weather storms, the effect of which is intense radiation damage and intense ionospheric ionization (Acuna, 2002: 3717-3736; Lanzerotti, 2000: 313-335). Hence, any orbiting satellite in this region is prone to single event upsets (SEUs), surface charging which leads to spacecraft anomalies or total mission failure (Dorman, Belov, Eroshenko, Gromova, Iucci, Levitin, Parisi, Ptitsyna, Pustil'nik, Tyasto, Vernova, Villoresi, Yanke & Zukerman, 2004:2530-2531; NOAA Space Weather Prediction Center, n.d.). It is therefore pertinent to have a magnetometer onboard the satellite for detecting changes in the Earth's magnetic field, so as to know the status of the space weather in the orbit.

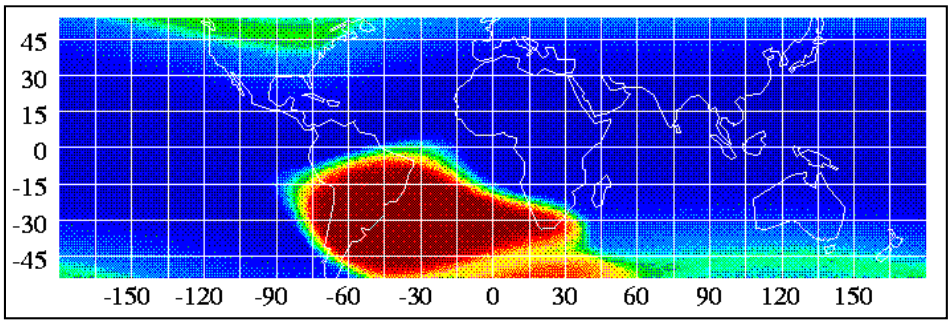

Figure 1.1: Weak magnetic field experienced in the SAMA region (Snowden, 2002)

1.2.1.1 Variation in the Earth's magnetic field

Measurement of the variations in the Earth's magnetic field strength in the orbit is what is mainly used to determine the state of the space weather, especially in the SAMA region, where the Earth's magnetic field is very weak (Heirtzler, 2002:1701). These variations are caused by a number of factors. The geomagnetic effect is one of these factors. It results from variation in the currents present in the ionosphere. These variations happen to be in the range of 10^{-3} to 10^{-1} $nTHz^{-1/2}$ at 0.1 Hz (Clarke & Braginski, 2005:497), depending on the electrical activities at certain latitudes. Geological effects, resulting from the geological sources, both emanating from the Earth's outer crust and local surface, also cause local Earth magnetic variation. These variations are usually intensive at some certain regions, especially in the high-hill areas. The values of the geologic noise are relative to the gradient areas, and can range from 0.05 nT/m to 10 nT/m (Clarke & Braginski, 2005:497). Other causes of space weather storms like the solar flares, coronal Mass ejections, and sunspots, also contribute to the Earth's magnetic field variation.

1.2.2 Magnetic field sensing

Based on their field strengths and measurement range, magnetic field sensors are divided into two categories: gaussmeters and magnetometers. As described by (Macintyre, 1999), Figure 1.2 briefly illustrates these categories, with few examples of each.

A gaussmeter is an instrument that measures the magnitude and/or direction of the magnetic field strength in the high field range, while a magnetometer is an instrument that measures the magnitude and/or direction of the magnetic field strength in the low field range. Magnetometers that measure both the field's magnitude and direction are classified as the vector magnetometers, while those that measure only the field's magnitude are the scalar magnetometers (Macintyre, 1999).

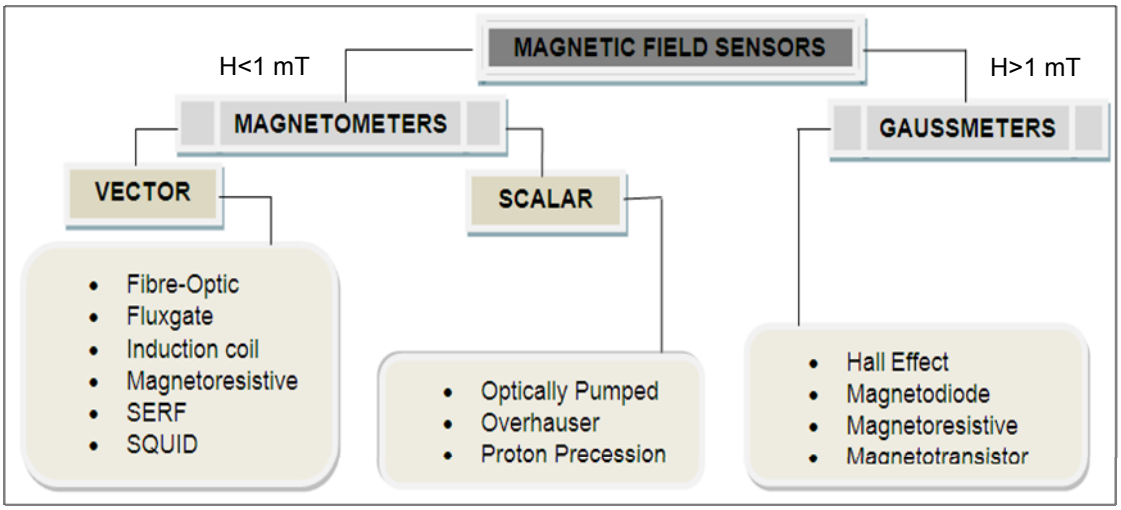

Figure 1.2: Categories of magnetic field sensors

When deployed at a distance farther from the main satellite's body, science-grade vector or scalar magnetometers can be used to map the Earth's magnetic field or used for studying the ionospheric current. More so, orientation magnetometers are used in satellite's attitude determination and control subsystem (ADCS), to determine the satellite's orientation in the orbit. For explicit pointing accuracy, other sensors like star sensors, in conjunction with gyroscopes, are used in place of magnetometers (Diaz-Michelena, 2009:2274).

1.2.3 Criteria for magnetometer and cryocooling system selection

Any magnetometer system to be used in space has to be space-qualified before being integrated with the satellite, to ensure it can withstand the various conditions that it will be exposed to during launch and in-orbit. The expected characteristics of magnetometers for space applications are as listed below (Siziba, 2012:11).

They should:

- have a wide range of measurement (about ± 60, 000 nT)
- be robust and reliable with high performance
- be less power hungry

The selection of the M1000 DC SQUID magnetometer for this research was based on its high sensitivity and accuracy, coupled with the fact that it is not very difficult to analyse as compared to the RF SQUID magnetometer type (Hilton, Dawe, Dubicki, Brain, Lawrence, Whittlesea, Trott, Kim, Atkins, Yates, King, Springford, Powell & Holt, 2001). According to Star Cryoelectronics (2004:5), this DC SQUID has a field sensitivity of about 10 nT per flux quantum, and it can only operate under a typical cryogenic temperature of 77 K.

Due to the required operational temperature of a SQUID magnetometer, it is needed to integrate it with an appropriate cryogenic cooling system to cool it down to the required temperature. This cooling system can be composed of mechanical cooling (by enclosing it in a cryocooler dewar or a cryostat) or composed of passive cooling technology, as it is proposed in this project. Because of the power, weight and space constraints in a nanosat structure, passive cooling technology was considered. The technology is less demanding in terms of weigh and space, and it requires virtually no power for operation. Section 2.10 gives a detailed overview of the passive cooling technology to be employed for this task.

1.3 Objectives of the research

The aims of this research are to:

- analyse the available types of SQUID magnetometers (sensor) suitable for nanosatellite mission
- model and simulate the electrical characteristics of a DC SQUID magnetometer, together with its readout electronics
- model and simulate a passive cooling system for a DC SQUID magnetometer
- fabricate and test the bias and readout electronics for the DC SQUID magnetometer
- test the acquired SQUID magnetometer, using the designed electronics, and use the outcome, together with that of the simulations done, to ascertain its usability for space weather missions
- create a suitable platform for future research on using SQUID magnetometers for nanosatellite space weather missions

1.4 Research statement

This research focussed on the modelling and simulation of a DC SQUID behaviour, its read-out electronics, and a passive cryocooling system, with the fabrication and testing of the electronics, in the real practical sense, so as to verify its usability for nanosat space weather missions.

1.5 Research questions

- What brand of a miniature commercial-off-the-Shelf (COTS) DC SQUID magnetometer can be suitable for nanosatellite missions?
- How can the SQUID magnetometer be simulated in order to predict its behaviour?
- How will the desired operating conditions for the magnetometer be maintained, considering the orbital environmental conditions of the nanosatellite?

- What modifications must be done to the COTS SQUID sensor to make it suitable for the mission?
- How will the whole assembly be integrated into the nanosatellite, considering the weight, size, and power constraints of the satellite?
- How can the whole assembly be shielded from the satellite's stray magnetic field?

1.6 Significance of the research

There is now a great reliance on satellites for information exchange, security, entertainment, and research work by almost every country in the world. Good quality of operation of such satellites is of prime importance. This can be enhanced by using a highly sensitive magnetometer system to effectively monitor and determine the Earth's magnetic field and LEO (low Earth orbit) geomagnetic disturbances resulting from space weather anomalies. Therefore, the success of this research shall primarily help to improve the existing models for predicting space weather conditions, by making use of the data acquired by the sensor. The research will also aid the space engineers in designing space hardened subsystems in the satellites, and boost the level of reliance on such satellites orbiting the Earth, by making use of the information obtained from the space weather conditions in the orbit. This research shall further encourage the adoption of cryogenic technology for space weather missions, and contribute in revolutionising the satellite technology as a whole. More so, with growing interest in nanosatellite (especially CubeSat) platforms by universities for experimental projects, this kind of magnetometer set-up will add to the value of the education and experience offered by such platforms.

1.7 Research delineation

This research is a foundational work on establishing the usability of a COTS SQUID magnetometer for nanosatellite space weather missions. Therefore, it did not concentrate on the design of a new magnetometer and a cryogenic cooler. Commercial off-the-shelve SQUID magnetometer was acquired, tested and irradiated to know its durability in the low earthorbit (LEO). Much attention was paid on simulating the behaviours of both the SQUID magnetometer and the proposed deployable passive cooling systems. The mechanical design of the deployment structure is excluded from the scope of this project. Fabrication and testing of the electronics needed to interpret the sensor's output were also done, together with the radiation test need to establish its durability in the orbital environment.

1.8 Research design and methodology

The following procedures were used to achieve the research outcome:

Literature review: This involved extensive consultation of related resources. Information was gathered from books, published journals, internet search engines and other personnel with broader understanding of magnetometers and cryogenic coolers. As a result of this, the appropriate magnetometer and cryocooler could be selected for the project.

Modelling and simulation: The electrical characteristics of the DC SQUID magnetometer and its readout electronics were simulated, using PSIM and MATALAB- Simulink, in order to theoretically predict their behaviour. A passive cryocooling system was also modelled and simulated using the Thermal Desktop package, so as to safe the cost, time and building the physical system prototype, for predicting its behavior and to confirm its usability for the mission.

Design and fabrication: The required readout electronics for the DC SQUID magnetometer were designed and fabricated, according to the simulation calculations.

Measurements: Functionality tests were carried out on both the fabricated electronics and the acquired SQUID magnetometer. Before testing the sensor, a liquid Nitrogen dewar was used to cool it down. The dewar was employed because in-orbit cooling is difficult to validate on ground. That is why the proposed passive cooling system was simulated. It is to be fabricatedted in the future F'SATI's 3U mission.

Qualification: The COTS SQUID sensor was subjected to a space qualification test, namely the radiation test, in order to know its durability under the LEO environment. Radiation test was carried out in order to verify this durability.

Documentation: Reports on the whole exercise carried out were later recorded and kept for future reference, together with the write-up of this thesis.

1.9 Organisation of the thesis

Chapter one briefly presents an overview of the whole project, which includes the research background, description of space weather, which is the driving force behind this research, and the research objectives. The chapter closes with the organisation of the entire thesis from chapter to chapter. *Chapter two* highlights the literature that was extensively reviewed before and during the development of the research. This has been presented in various sub-headings, to give extensive details on the important information like the magnetometer types,

and the SQUID magnetometer basis, including their operating principle, various types, behaviour and readout electronics, called the flux locked loop (FLL) for linearising their output signals. Details of cryogenic cooling systems for the SQUID sensor operation are presented, with emphasis laid on the passive cooling technology employed in this research work. The chapter closes with how SQUID magnetometers can be adopted into space weather applications. *Chapter three* presents the modelling and simulation of a DC SQUID magnetometer and its readout electronics using the M100 SQUID sensor from Start Cryoelectronics as a baseline. *Chapter four* contains the modelling and simulation of the passive cooling system employed in this research, which consists of four stages of radiators. *Chapter five* reports the experimental work carried out on the fabrication and testing of the bias and readout electronics needed to operate the SQUID magnetometer, together with the radiation test carried out on the sensor. The results of the tests carried out are presented therein. *Chapter six* is the concluding chapter of this research, where conclusions are drawn from the research outcome, with beneficial recommendations for subsequent research work to be carried out on this field of study.

CHAPTER TWO

LITERATURE REVIEW

2.1 Magnetic field basics

A magnetic field is a vector quantity, having both magnitude and direction. The first means of measuring the magnetic field strength was discovered by Oesterd, when he observed the deflection of a compass needle, after placing a current carrying wire near the compass. Faraday's principle of electromagnetic induction eventually gave birth to some of the magnetic field sensors in use today (Macintyre, 1999).

2.2 Magnetometer types

As depicted in Figure 1.2, magnetometers are of two major types, namely vector and scalar magnetometers. Figure 2.1 graphically illustrates the sensitivity range of some of the various magnetometer types that fall under these two categories (Diaz-Michelena, 2009:2273; Siziba, 2012:11). Details about scalar magnetometers are not discussed in this write-up

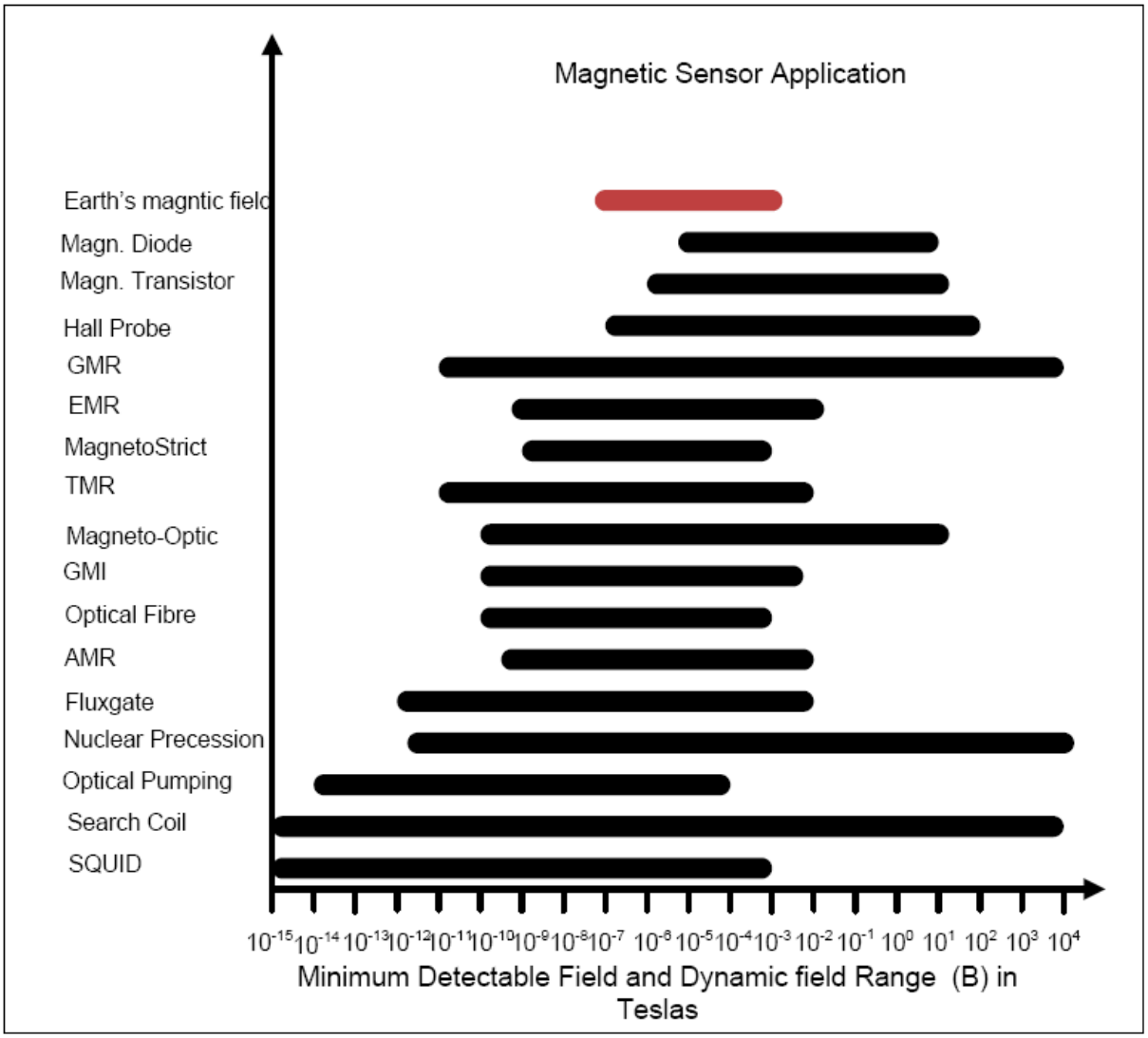

Figure 2.1: Magnetometer types and their measurement range (Diaz-Michelena, 2009:2273)

since this project is centred on SQUID magnetometer, an example of a vector magnetometer. Refer to Macintyre (1999) for details on them. The following sub-sections briefly describe some examples of vector magnetometers.

2.2.1 Search or induction coil magnetometer

This is one of the simplest magnetic field sensing devices. Its principle of operation is based on Faraday's law of magnetic induction. That is, a loop of wire (coil) subjected to a changing magnetic flux, Φ in the enclosed loop area, develops an induced voltage, proportional to the rate of change of the sensed flux (Macintyre, 1999).

As described by Tumanski (2007:32), this kind of magnetometer can be manufactured as two types - air core loop and ferromagnetic core loop. The latter is easier to miniaturise, with improved sensitivity than the former. However, the ferromagnetic core loop type experiences non-linearity, introduced by the core, to the magnetometer's transfer function. Disturbances in the magnetic field to be measured further affect the linearity.

The search coil magnetometer has been widely employed in the study of magnetic field variation, both in land and space environments (Pronenko & Korepanov, 2009:1381).

2.2.2 Fluxgate magnetometer

This also operates based on Faraday's law of magnetic induction. In this case, a current carrying primary coil (excitation coil), produces a varying magnetic field in its core, which in turn induces current in the secondary coil (sense coil). A change in the external magnetic field (to be measured) produces an output voltage in the sense coil. Its characteristics of being rugged, reliable, physically small, with low operating power requirement, and ability to measure the magnetic field vectors over a range of about 0.1 nT to 1 mT from DC to several KHz, have made it to be a very versatile magnetometer, as reported by Macintyre (1999).

The fluxgate magnetometer has always been the most widely used magnetometer, both on Earth and in space (Acuna, 2002: 3717-3736; Primdahl, 1979:241-253). Many of it have been developed and employed for micro-satellites as payloads. An example of such missions is the Astrid-2 satellite (Pedersen, Primdahl, Petersen, Merayo, Peter, & Nielsen, 1999:N124-N129).

2.2.3 Spin exchange relation free (SERF) magnetometer

This magnetometer works by measuring the Larmor spin procession of an optically pumped alkali-metal vapour or a Helium atom in the magnetic field to be measured. It only measures magnetic fields which are less than 0.5 μT. It is highly competitive with the SQUID

magnetometer, in terms of sensitivity. This magnetometer is basically designed to operate in scalar mode, but can be made to operate as a vector magnetometer. Seltzer and Romalis (2004) demonstrated the use of an unshielded SERF magnetometer, operating near a zero magnetic field, as a three-axis vector magnetometer, by means of a feedback system.

The remaining part of this chapter extensively dwells on comprehensive theories and reviews of the SQUID magnetometer, an example of a vector magnetometer, and the cryogenic set-up required for its operation. The chapter concludes with Basis of the Earth's magnetic field measurement.

2.3 The SQUID magnetometer

As the name implies, it is made of a superconducting quantum interface device. It is the most sensitive magnetometer known (Simon, Burns, Colclough, Zaharchuk & Cantor, 2004:50). It is the best sensor to be used for sensing the Earth's magnetic field.

2.3.1 The history of superconductivity

The history of superconductivity dates back to the year 1911, when Kamerlingh Onnes cooled a mercury sample with liquid Helium-4. Helium boils at 4.2 K (HyperPhysics, 2000b). The sample's resistance dropped sharply to a value close to zero. This is a transition from normal metal to the superconducting state, at a temperature lower than the critical (transition) temperature, T_c, as depicted in Figure 2.2. Here, perfect conductivity occurs, but this does not infer that superconductors are perfect conductors, because they also exhibit inductive and capacitive properties, which are acute properties that highly inhibit superconductivity and Josephson effects (discussed in section 2.3.3). Some known superconductors, with their transition temperatures include Thallium-Barium-Calcium-Copper oxide (TBCCO), with a T_c of 125 K, Rhodium (Rh), T_c of 325 K, and Yttrium-Barium-Copper-Oxide (YBCO), T_c of 90 K (Buchal & Welter, 1983:170; Nturambirwe, 2010:3).

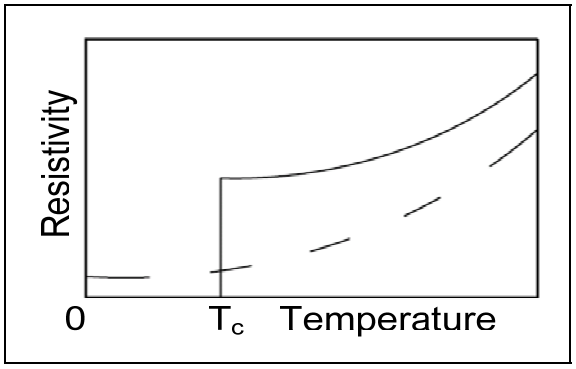

Figure 2.2: Temperature dependence of the resistivity of a normal metal (dashed line), and a superconductor (solid line) (Nturambirwe, 2010:3)

2.3.2 Meissner effect

In the year 1933, Meissner and Oschenfeld discovered that superconductors expel magnetic fields during their transition to superconducting state, a phenomenon known as the Meissner effect (Rabinowitz, Garwin & Frankel, 1973:1). This was later explained by the thought experiments described by Orlando and Delin (1991:66-67), with a view to differentiating between the characteristics of a perfect conductor and a superconductor. He envisioned and compared the characteristics of the conductors at four different states. A perfect conductor only expels any applied magnetic field, after being cooled to a superconducting state, and does not when being cooled in the presence of the field (both during and after cooling). A superconductor expels the field when it is being cooled in the presence of the field. The fundamental unit representing the quantum of magnetic field traversing a superconductor is usually expressed by the flux quantum (known as fluxon), which is given by:

$$\Phi_0 = 2.07 \times 10 - 15 \text{ Wb} \tag{2.1}$$

The Meissner effect exhibited by a superconductor was subsequently proven by London and London in 1935 (Learning Space, 2011). They attributed it to the outcome of the minimized free electromagnetic property of the superconducting current in the superconductor at its critical temperature, T_c. Hence, a superconductor exhibits zero resistivity and perfect diamagnetism towards an externally applied magnetic field (Nturambirwe, 2010:2).

2.3.3 The Josephson effect and SQUID magnetometer operation

The technology behind a SQUID's operation was discovered by Brian Josephson in 1962, as a graduate student at Cambridge University. It was discovered that a superconducting (critical) tunneling current flows between two superconductors separated by a thin layer of insulation, in the absence of any applied voltage (Daniel, 1998:1). This junction of separation is called the Josephson junction (JJ). The value of this critical current through the Josephson junction is affected by the presence of a magnetic field. Depending on the number of Josephson junctions, there are both the radio frequency (RF) SQUID type, composed of a single JJ, and the direct current (DC) SQUID type, composed of two JJs.

Figure 2.3 simply illustrates the working principle of a DC SQUID magnetometer. By applying a DC bias current, I_b, to the SQUID's loop, a voltage is produced across the junctions, which is a periodic function of the sensed magnetic flux through the pick-up loop, with a period of 1 fluxon. The feedback voltage helps to maintain a modulated constant flux magnitude within the SQUID's loop, through the feedback coil and a feedback resistor. This feedback circuitry is termed the flux locked loop (FLL) circuit. The output from the integrator presents a linearised response from the SQUID, relative to the sensed flux. For the RF SQUID type, the

bias is an ac signal. All the enclosed components in the outer dashed box are kept at a cryogenic temperature (achievable by using a cryogenic cooling system), and are magnetically shielded, except the pick-up coil. The rest of the circuitry is left at the ambient temperature. A detailed description of the feedback electronics is presented in section 2.11.

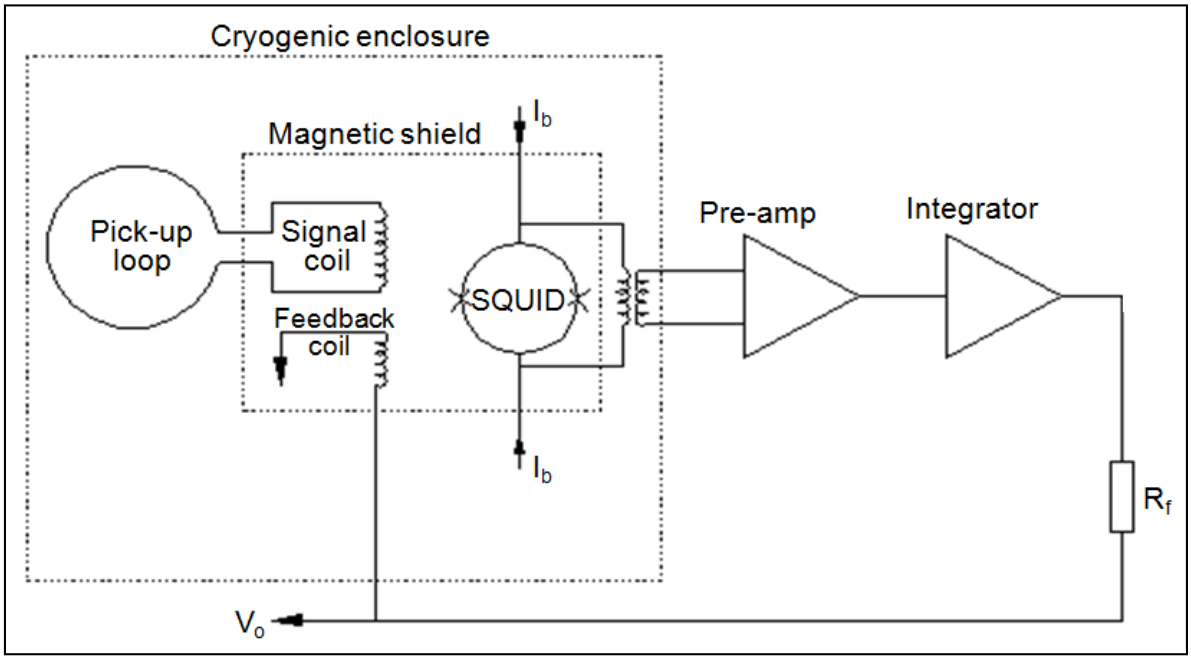

Figure 2.3: DC SQUID magnetometer operation mode

2.4 DC SQUID fabrication procedures

Depending on the choice of materials to be used, the fabrication of a high temperature DC SQUID (HTS or high T_c) starts with the growing of a thin film on a bicrystalline substrate (Nturambirwe, 2010:22-28). For a high temperature SQUID, $YBa_2CU_3O_7$ (YBCO) film is the choice to be used. However, one important constraint in the fabrication is that both the film and the substrate should be physically and chemically compatible. For example, their thermal expansion coefficients must be similar, and the substrate must be resistant to thermal cycle stress, with good stability at very high temperature, since the film is deposited at such a temperature. The substrate can either be composed of MgO, AlO_2, $SrTiO_3$, $LaAlO_3$, $NdGaO_3$ or yttria-stabilised zirconia. MgO is relatively cheap, with an independent thermal dielectric constant of 10 (Burger, 2008:40-42).

The film deposition can either be achieved through the in-situ or ex-situ deposition process. The former brings about smoother film surfaces than the latter. The common techniques employed in these processes are the pulsed-laser deposition (PLD) and magnetron sputtering. In the PLD technique, a high power laser source is used to ablate a portion of the YBCO, with the deposition and growing of the resulting vapour on a heated substrate. In order to enhance smooth formation of the film, the laser energy must be high enough, and it

must not be too high so that YBCO ions do not become energetic, thereby damaging the growing film. In the magnetron sputtering technique, ion plasma is used in place of the PLD's laser source, with the advantage of having a higher deposition rate. Here, a DC magnetron is used to energise and accelerate a portion of the YBCO, to tear out the atoms, which are then deposited on the substrate.

After the YBCO deposition, is the annealing phase in a pure oxygen environment. Here, the substrate is subjected to slow heating and cooling at a proper temperature and pressure, so as to toughen and reduce the brittleness. The deposited YBCO needs to be preserved by a suitable desiccant (drying agent), to prevent chemical reactions that might occur from atmospheric contamination. The effects of these chemical reactions were noticed at the initial stage of Burger's work, when the colour of the deposited YBCO (with embedded Josephson junctions) film started fading out, with the disappearance of the junction's voltage-current characteristics and a complete loss of superconductivity, after a long period of exposure to the atmosphere (Burger, 2008:40-42).

Buttner *et al*., at the University of Stellenbosch, demonstrated a set of locally fabricated Josephson junctions, using magnetron sputtering (Burger, 2008:123-124). Photolithography was subsequently employed after the YBCO deposition, to form the desired DC SQUID pattern. In photolithography, ultraviolet light is used to transfer a desired pattern onto a photoresist (light sensitive) chemical, which is then stuck unto the YBCO sample, thereby forming the desired SQUID pattern (Nturambirwe, 2010:24).

2.4.1 Types and formation of Josephson junctions

The type of Josephson junction employed in a SQUID design greatly influences the SQUID's performance. The following sub-sections describe some commonly investigated types of Josephson junctions for high T_c SQUID sensor fabrication.

2.4.1.1 The natural grain boundary Josephson junction

During the YBCO deposition, there are various weak links that are usually distributed randomly throughout the film. Natural grain boundary junctions are then formed by constricting the film at a specific point (as shown in Figure 2.4), thereby separating one group of weak links from the other. Due to irregularities in the weak links distribution, predicting this kind of junction for design purposes is quite impossible, thereby restricting its use only to the RF SQUID type (Burger, 2008:43).

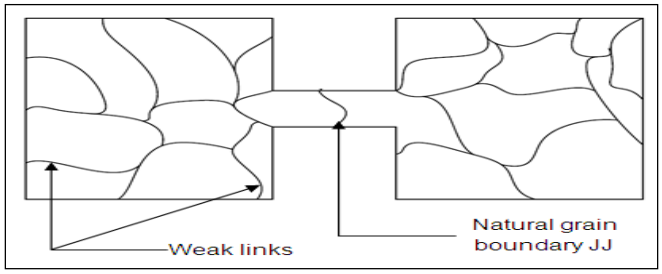

Figure 2.4: The natural grain boundary Josephson junction (Burger, 2008:43)

2.4.1.2 The ramp edge multilayer Josephson junction

The ramp edge multilayer JJ is formed by separating two YBCO film layers with a thin layer of an insulator, together with a normal metal layer composed of substrates (like MgO), to act as a barrier between the two crystalline layers, as shown in Figure 2.5. This kind of junction is employed by both high temperature SQUIDs (HTSs) and low temperature SQUIDs (LTSs).

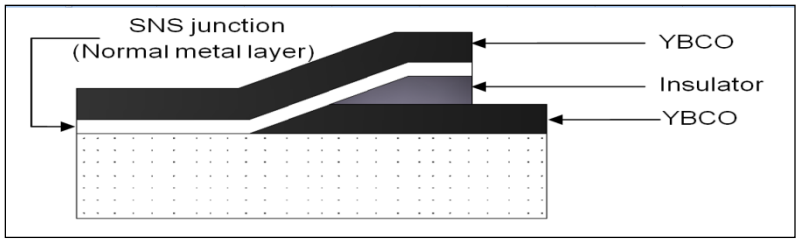

Figure 2.5: The ramp-edge multilayer Josephson junction

In the case of a LTS device, the building block for this junction type is termed the SIS (superconductor-insulator-superconductor) and the SNS (superconductor-normal-superconductor) for a high T_c (HTS) device. These two building blocks are structurally identical, the main difference being the needed external shunt resistors to reduce the hysteresis caused by the occurrence of capacitance between the low temperature multilayer junctions, in the case of the ramp-edge SIS junction (Khare, 2003). In this case, the junctions are regarded as RCSJ (resistively-and capacitively-shunted junctions). This capacitance is extremely smaller in the case of the HTS ramp-edge SNS junction; hence, the junctions are regarded as RSJs (resistively-shunted junctions), with no hysteresis, which makes them ideal for SQUID magnetometer designs. Jia, Yan, Mombourquette and Reagor (1998:3068) have successfully demonstrated a SQUID magnetometer system that uses this ramp-edge SNS junction. In their design, each layer was deposited, precisely patterned, using photolithography and then etched, using argon ions, to form the ramp edge. The ramp area in the design represents the system's active area, where both the normal metal and the insulator layer are the separating mediums between the two YBCO layers. That is how the name "ramp-edge multilayer" came about.

2.4.1.3 The grain boundary Josephson junction

The grain boundary JJ uses the advantage of orientation mismatch in the deposited YBCO superconductor. This is achieved by distorting the orientation of the substrate, before the YBCO deposition. If a uniform substrate is broken into two, and then rejoined in such a way as to create differences in the orientation of the two joined substrates, a bicrystal substrate is created. More so, if a seed layer (thin layer) is deposited on a uniform substrate, in order to create orientation mismatch, a biepitaxial substrate is formed. Depositing YBCO on any of such (bicrystal or biepitaxial) substrates, creates a lattice mismatch angle. Provided the orientation mismatch in the substrates is large enough, a Josephson coupled weak link, otherwise known as the grain boundary JJ, is formed. In order to make the biepitaxial substrate suitable for the YBCO deposition, a buffer layer must be deposited on it before depositing the YBCO. These two kinds of formation are as depicted in Figure 2.6.

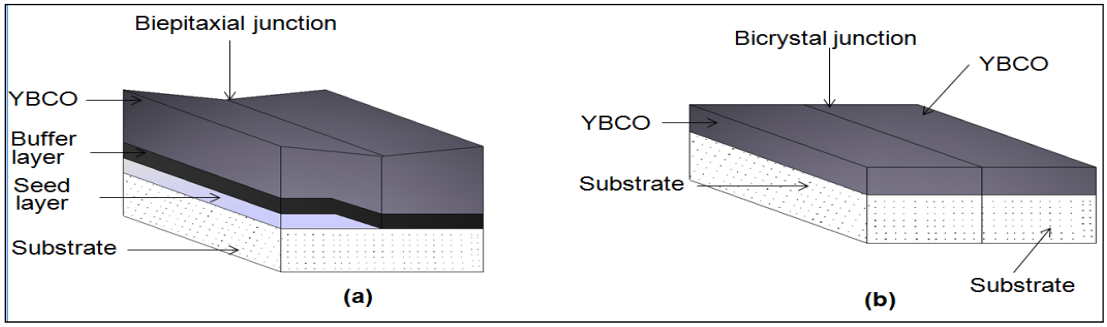

Figure 2.6: The grain boundary Josephson junction on a (a) biepitaxial substrate (b) bicrystal junction

Due to the negligible intrinsic capacitance across the junction, the bicrystal JJ type is a resistively-shunted junction (RSJ) type, and it is very simple to fabricate, unlike the biepitaxial type that requires multiple depositions.

2.4.1.4 The step edge Josephson junction

This kind of Josephson junction is mostly RSJ. There are several means of achieving its design, one of which is cutting a trench on the substrate, before the YBCO deposition. The trench can either be done through milling or using a laser. Weak links are formed at each edge of the trench, which constitute the step edge JJ.

Section 2.5 through section 2.11 presents advanced background knowledge of DC SQUID magnetometers and their readout electronics.

2.5 The SQUID's screening and Stewart-McCumber parameters

Given a SQUID sensor, made of two identical JJs, with critical currents, $I_{c,1}$ and $I_{c,2}$, per junction, self capacitance, C, combined shunt resistances, R_n, and loop area, A_{SQ}, its average critical current is given by:

$$I_{c,av} = (I_{c,1} + I_{c,2}) / 2 \tag{2.2}$$

Its combined shunt resistance is given by:

$$R_n = \frac{R_{n,1} R_{n,2}}{R_{n,1} + R_{n,2}} \tag{2.3}$$

Where,

$R_{n,1}$ and $R_{n,2}$ are the respective junction resistances.

The magnetic flux, Φ_{SQ}, couplingg into the SQUID, by applying a field of magnetic flux density, B to the pick-up loop, is expressed as:

$$\Phi_{SQ} = BA_{SQ} \tag{2.4}$$

Any SQUID's loop, with inductance, L_{SQ}, is prone to hysteresis, when an external magnetic field is brought closer to it. This is because L_{SQ} has some effects on the magnetic flux linking the loop. The mathematical equation describing this hysteresis is given by (Burger, 2008:31):

$$\Phi = 2\,\Phi_J + L_{SQ}\, I_{c,av} \sin(2\,\pi\,\Phi_J / \Phi_0) \tag{2.5}$$

Where,

Φ is the flux from the external magnetic field
Φ_J is the developed flux in the junction
$\Phi_0 = 2.07 \text{ X } 10^{-15}$ Wb is the flux quantum (or fluxon)
$I_{c,av}$ is the average critical junction current of the SQUID

Equation (2.5), plotted with MATLAB, is pictorially represented in Figure 2.7, by considering various SQUID loops. The hysteresis effect is seen to gradually varnish, as L_{SQ} reduces. If the following expression is satisfied, the hysteresis will be completely eliminated:

$$L_{SQ} \ll \Phi_0 / I_{c,av} \tag{2.6}$$

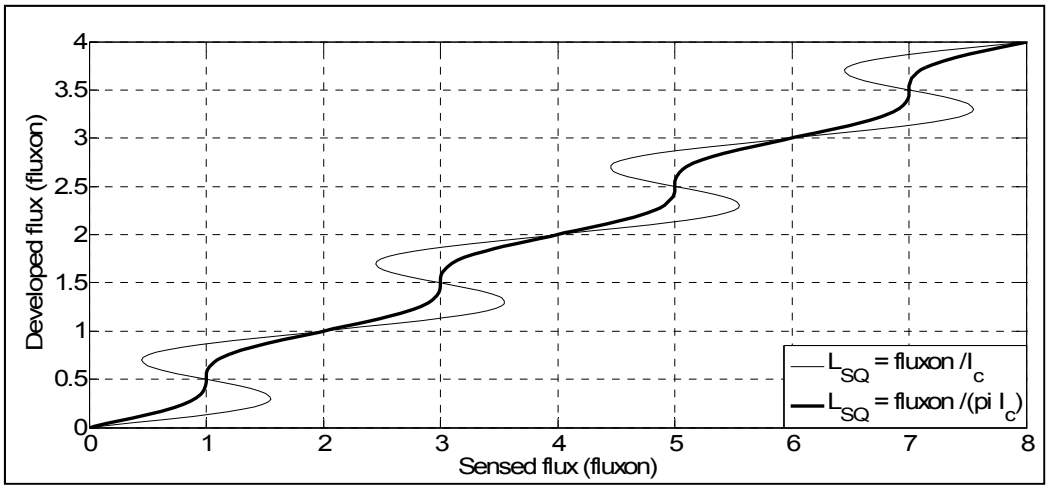

Figure 2.7: The external flux vs. the flux developed across a junction, to demonstrate the hysteresis due to L_{SQ} values

This expression leads us into defining the inductance parameter (or screening parameter), β_L, and the Stewart-McCumber parameter, β_c, which are, respectively, given by equations (2.7) and (2.8).

$$\beta_L = 2L_{SQ}\, I_{c,av} / \Phi_0 \tag{2.7}$$

$$\beta_c = 2\pi\, I_{c,av}\, R_n^2\, C / \Phi_0 \tag{2.8}$$

Ideally, a SQUID system should have a screening parameter of β_L = 1, which satisfies equation (2.6). β_c is also a very useful parameter, which expresses the effect of damping and the possible occurrence of hysteresis in the Josephson junction as well. In order to avoid hysteresis in the JJ's voltage current (V - I) characteristics, this parameter is expected to be less than unity (Clarke & Braginski, 2005:6; Clarke & Braginski, 2004:33). The significance of this shall be discussed in the following sub-section.

2.5.1 RCSJ and RSJ models

As discussed in section 2.4.1.2, RCSJ stands for resistively-and capacitively-shunted junction, while RSJ refers to resistively-shunted junction. If the Stewart-McCumber parameter β_c >> 1, the JJ is said to be highly underdamped, and this represents the RCSJ case. From the RCSJ equivalent circuit, represented in Figure 2.8, a normal shunt resistance, R_n, and a shunt capacitance, C, are used to represent the resistive and capacitive characteristics of the JJ. These two shunt parameters are related with the characteristic voltage, V_c given by (burger, 2008:15):

$$V_c = I_c R_n \tag{2.9}$$

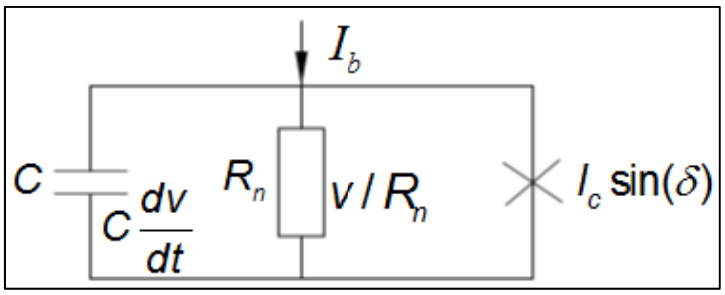

Figure 2.8: The resistively-and capacitively-shunted junction equivalent circuit

The supercurrent across a JJ is described by Josephson's first equation given in equation (2.10) (Clarke & Braginski, 2004:30).

$$I_s = I_c \sin(\delta) \tag{2.10}$$

Where,

δ is the gauge invariant phase difference (GIPD)

Hence, the effective current through the RCSJ is given by:

$$i = I_c \sin(\delta) + \frac{v}{R_n} + C\frac{dv}{dt} \tag{2.11}$$

The GIPD is the 2π periodic Josephson phase difference that develops between the quantum wave functions across each of the two superconductors, when magnetic field is applied. This wave function governs the superconducting current in the JJs. Equation (2.12) is the second Josephson's equation that expresses the voltage, *v* developed across the JJ, if the GIPD is time dependent (Clarke and Braginski, 2004:30).

$$\frac{d\delta}{dt} = \frac{2\pi}{\Phi_0} v \tag{2.12}$$

More information on RCSJ can be obtained from Clarke and Braginski (2004:31-35), while the rest part of this sub-section dwells much on the RSJ model, as it is the basis of the SQUID magnetometer type considered in this research.

A DC SQUID is said to be highly overdamped, if the Stewart-McCumber parameter is extremely small (i.e., β_c). This represents the RSJ case, as shown in Figure 2.9. Most SQUIDs are usually overdamped in the real sense. In this case, the shunt capacitance, C, in the JJ is assumed to be negligible (approximately zero).

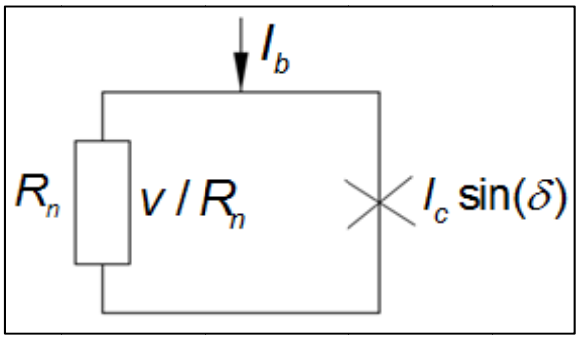

Figure 2.9: The resistively-shunted junction equivalent circuit

The effective current through the RSJ is therefore given by:

$$i = I_{c,av} \sin(\delta) + \frac{v}{R_n} \tag{2.13}$$

Employing equation (2.12), we can as well rewrite equation (2.13) as:

$$i = I_{c,av} \sin(\delta) + \frac{1}{R_n} \frac{\Phi_0}{2\pi} \frac{d\delta}{dt} \tag{2.14}$$

From the RSJ equivalent circuit depicted in Figure 2.9, the time dependent voltage, $u(t)$, normalised by $I_c R_n$ (or V_c), can be represented by (Clarke & Braginski, 2004:33):

$$\begin{aligned} u(\tau) &= (i_b^2 - 1)\left(i_b + \cos\left(\tau\omega_c\sqrt{i_b^2 - 1}\right)\right), \text{for } i_b > i_c \\ &= 0 \text{ otherwise} \end{aligned} \tag{2.15}$$

Where,

i_b is the normalised bias current I_b ($i_b = I_b/I_c$)
$\boldsymbol{\omega_c}$ is the JJ's characteristic frequency ($\boldsymbol{\omega_c} = 2\pi I_c R_n / \Phi_0$)
τ is the normalised time ($\tau = t\,\boldsymbol{\omega_c}$)

Figure 2.10 (plotted with MATLAB) depicts the relationship between the normalised time-dependent voltage, $u(\tau)$ and the normalised time, τ at various normalised bias currents, i_b. The curves show that the amplitudes are all the same, representing the characteristic voltage, V_c, while the oscillation frequencies, together with the offset voltages, (representing

the DC voltages) are dependent on the bias current magnitudes (normalised). These oscillation frequencies, ω and the offset voltages, V_{off} are respectively given by (Clarke & Braginski, 2004:33):

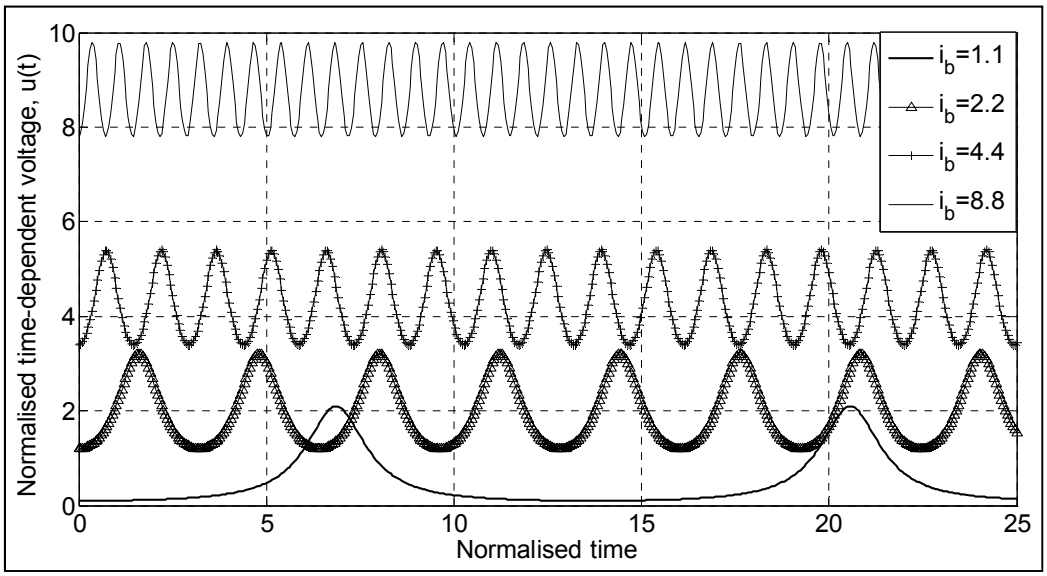

Figure 2.10: Normalised time vs. normalised voltage for resistively-shunted junction

$$\omega = \omega_c \sqrt{i_b^2 - 1} \tag{2.16}$$

$$V_{off} = i_b V_c \tag{2.17}$$

At $i_b < 1$, the i_c arm (the superconducting channel) of Figure 2.9 sustains all the current (i.e., superconducting behaviour). In this case, the junction is said to be resistanceless. As i_b exceeds 1, the excess in the current flows through the junction's resistive channel and produces a rising DC potential across the junction. This potential makes part of the supercurrent in the I_c arm to oscillate at the Josephson frequency, f_J, which is given by:

$$f_J = V_{DC} / \Phi_0 = 483.6\,\text{MHz}\ per\ \mu V_{DC} \tag{2.18}$$

This in turn reduces the maximum DC supercurrent through the junction, thereby forcing more current through the resistive arm. The junction thus acts like a resistive component more and more, at $i_b > 1$. When $i_b >> 1$, the DC voltage across the JJ increases intensely until the whole potential across the junction seems nearly DC.

The time average DC voltage, normalised by $I_c R_n$, can as well be represented by

$$v = \sqrt{i_b^2 - 1}, \text{ for } i_b^2 > 1$$
$$= 0 \text{ otherwise} \tag{2.19}$$

Figure 2.11 (plotted with MATLAB) depicts the relationship between the normalised time average DC voltage, *v* across the JJ junction and the normalised bias current, i_b.

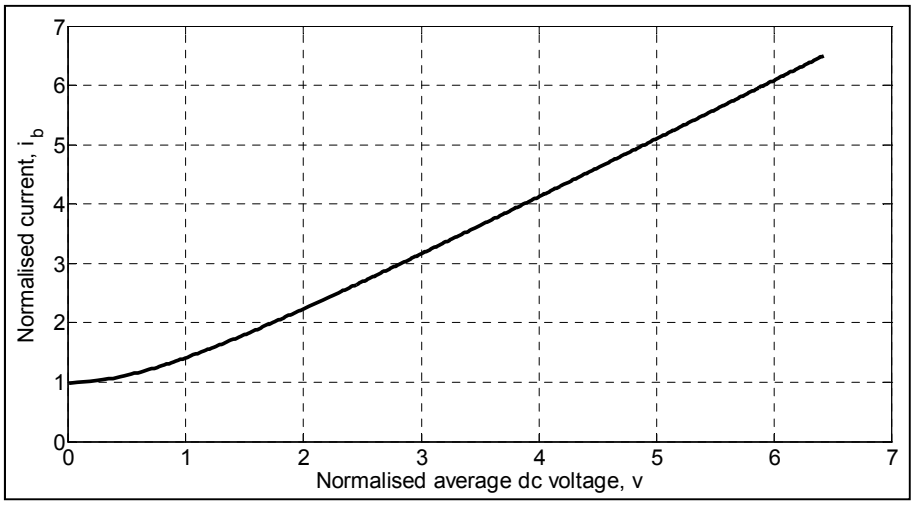

Figure 2.11: Normalised DC voltage vs. normalised bias current for the resistively-shunted junction

From this Figure, no DC voltage exists from current range of 0 to 1, which depicts a hysteretic state of the SQUID's current-voltage characteristics.

2.5.2 The magnetic field pick-up mechanism

As discussed in section 2.3.3 , the pick-up loop is needed to sense the external or applied magnetic flux, and inductively couple it to the superconducting loop (i.e., the SQUID's loop), as depicted in Figure 2.3. The JJ produces a circulating current from the sensed field. This circulating current is then converted into a measurable voltage across the JJ. The SQUID's critical current, I_c is dependent on both the junction temperature and the applied field. Equation (2.20) relates the modulation of I_c, to any applied perpendicular magnetic flux Φ (van Staden, 2007:14; Clarke & Braginski, 2004:3).

$$I_c(\Phi) = I_c(0)\left|\frac{\sin(\pi\,\Phi / \Phi_0)}{\pi\,\Phi / \Phi_0}\right| \tag{2.20}$$

Where,

$I_c(0)$ is the maximum critical current in the absence of any sensed magnetic field

The Fraunhofer curve in Figure 2.12 (drawn from equation (2.20)) shows that the critical current, $I_c(\Phi)$, (normalised to $I_c(0)$) becomes zero at every integer multiple of flux quantum, $n\Phi_0$. This implies that the applied flux is always an integer multiple of the flux quantum, Φ_0, at which the SQUID's critical current is always zero. This expresses the effect of quantisation on the SQUID's loop.

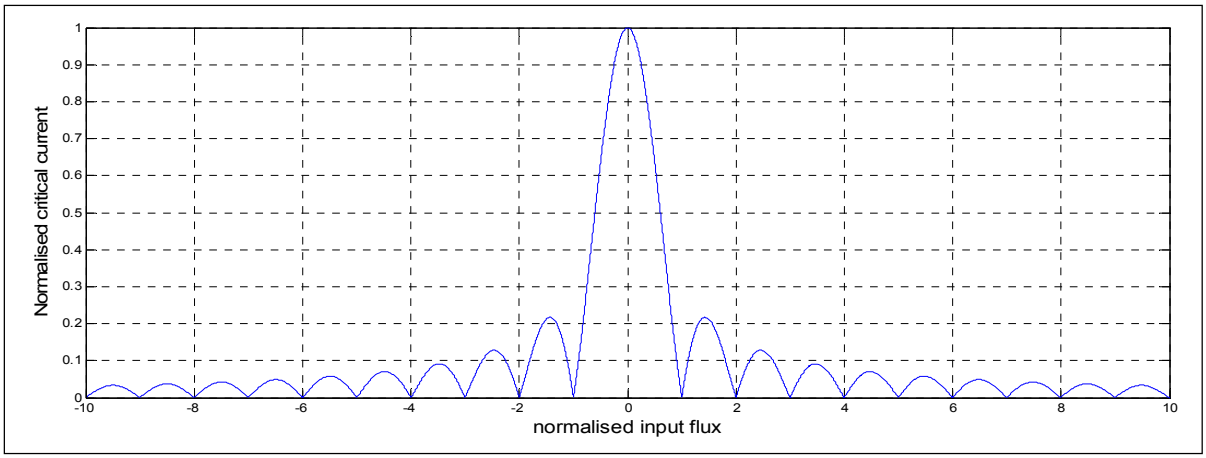

Figure 2.12: Relationship between critical current and magnetic flux

2.5.3 Flux-voltage relations for SQUID magnetometers

The relationship between the SQUID's output and the sensed flux can well be explained using Figure 2.13 (depicted by Macintyre (1999), but modified here for proper comprehension). The two bold curves to the left of the graph are the minimum and maximum critical junction currents ($I_{c,min}$ and $I_{c,max}$), and the dotted line is the applied bias current, I_b. As the sensed flux (in Φ_0) increases, the critical current decreases from $I_{c,max}$ to $I_{c,min}$ when the sensed flux has increased by $\Phi_0 / 2$. With this, the junction voltage has increased from v_{min} to v_{max}. As the flux continues to increase, the critical current increases from $I_{c,min}$ to $I_{c,max}$ when the flux has increased by another $\Phi_0 / 2$, and with this, the junction voltage has decreased from v_{max} to v_{min}. The sequence continues at every $n\Phi_0$, where n is a positive integer. This illustration clearly shows that the SQUID's output voltage is periodical with respect to the sensed flux, and the period is $1\Phi_0$.

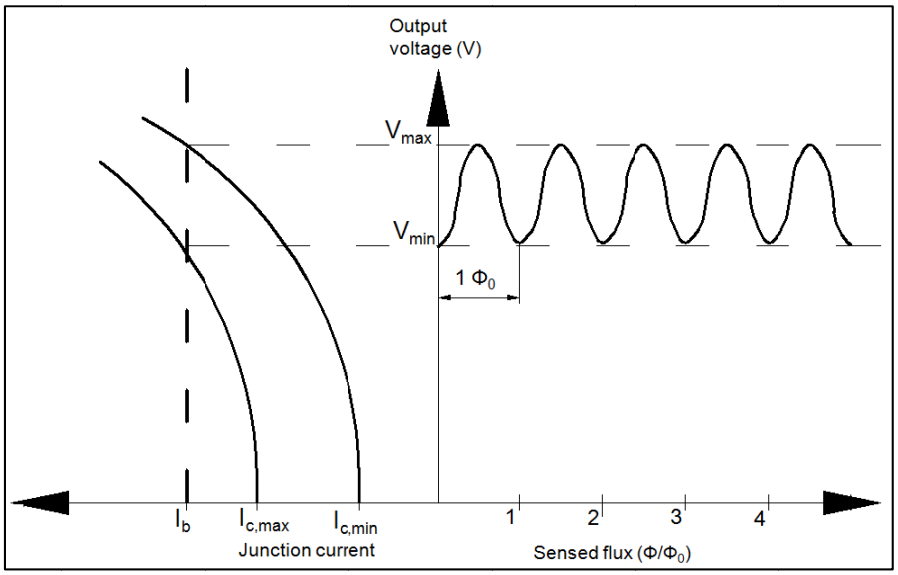

Figure 2.13: Relationship between the SQUID's output voltage and the sensed flux (Macintyre, 1999)

As it can be observed from Figure 2.13, the SQUID's response appears relatively linear at every interval between $n\Phi_0$ and 0.5 $n\Phi_0$, where *n = 0, 1, 2,..,..* Midway between these regions is (2 $n\Phi_0$ + 1) Φ_0 / 4, which describes the SQUID's operating point. Here, the response seems linear.

A highly overdamped DC SQUID magnetometer is formed from the combination of two RSJs (Figure 2.14). The voltage-current characteristic of such DC SQUID can be derived by exploring the characteristics of the RSJ model introduced in section 2.5.1. If equation (2.13) is employed, the effective current through the magnetometer can therefore be written as:

$$\begin{aligned} i &= i_1 + i_2 \\ &= I_{c,1}\sin(\delta_1) + \frac{v}{R_{n,1}} + I_{c,2}\sin(\delta_2) + \frac{v}{R_{n,2}} \end{aligned} \tag{2.21}$$

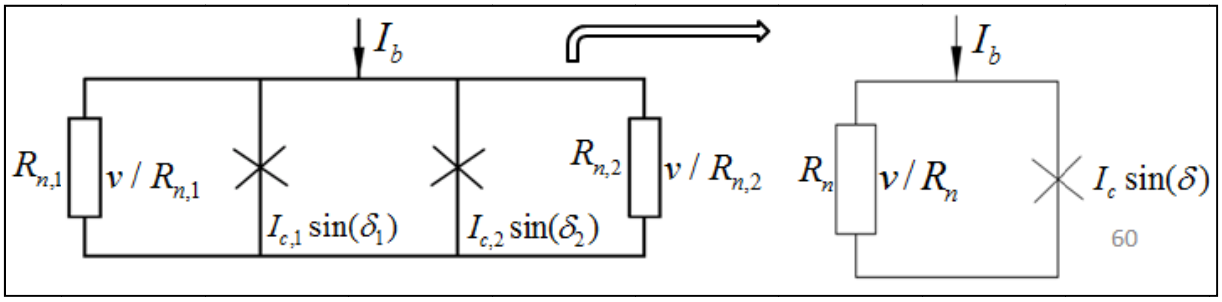

Figure 2.14: The equivalent circuit of a SQUID magnetometer

Where,

i_1 and i_2 are the respective junction currents

By trigonometry, equation (2.21) can be re-written as:

$$i = 2\,I_{c,av}\cos\left(\frac{\delta_1 - \delta_2}{2}\right)\sin\left(\frac{\delta_1 + \delta_2}{2}\right) + v\left(\frac{1}{R_{n,1}} + \frac{1}{R_{n,2}}\right) \tag{2.22}$$

The difference in the GIPDs has been derived to be:

$$\left(\delta_1 - \delta_2\right) = 2\,\pi n + 2\,\pi\,\Phi / \Phi_0 \tag{2.23}$$

Where,

$2\pi n$ is an indication that the phase changes at n multiples of 2π (van Zyl, 2010:61)

This is known as the quantum interference. The combination of both equations (2.22) and (2.23) therefore yields:

$$i = 2I_{c,av}\cos\left(\pi\,\Phi / \Phi_0\right)\sin\left(\delta_2 + \pi\,\Phi / \Phi_0\right) + v\left(1 / R_{n,1+1} / R_{n,2}\right) \tag{2.24}$$

By comparison, both equations (2.13) and (2.24) are synonymous. Similar to equation (2.20), the SQUID magnetometer's critical current can therefore be taken to be:

$$I_{c,SQ} = 2\,I_{c,av}\cos\left(\pi\,\Phi / \Phi_0\right) \tag{2.25}$$

Hence, for a SQUID with minimal hysteresis (satisfying equation (2.6)), its absolute critical current, as a function of the applied flux, is given by:

$$I_{c,SQ} = 2\,I_{c,av}\left|\cos\left(\pi\,\Phi / \Phi_0\right)\right| \tag{2.26}$$

This implies that the maximum current the device can support during superconductivity, decreases as the external flux, Φ increases towards $n\Phi_0 / 2$, where $n = 0, 1, 2,..,..$ The normalised maximum critical current is thus written as:

$$i_{c,SQ} = 2\left|\cos\left(\pi\,\Phi / \Phi_0\right)\right| \tag{2.27}$$

The new GIPD is taken as:

$$\delta = \delta_2 + \pi\,\Phi / \Phi_0 \tag{2.28}$$

By combining equations (2.3) and (2.24) through (2.28), together with the combined junction resistance, R_n given by equation (2.3), the effective current through the SQUID magnetometer can then be re-written as:

$$i = I_{c,av}\,\sin\left(\delta\right) + \frac{1}{R_n}\,\frac{\Phi_0}{2\,\pi}\,\frac{d\delta}{dt} \tag{2.29}$$

Employing equation (2.12), we can as well rewrite equation (2.29) as:

$$i = I_{c,SQ}\sin(\delta) + \frac{1}{R_n}\,\frac{\Phi_0}{2\pi}\,\frac{d\delta}{dt} \tag{2.30}$$

Hence, by considering equation (2.25), we have:

$$i = 2I_{c,av}\left|\cos(\pi\,\Phi / \Phi_0)\right|\sin(\delta) + \frac{1}{R_n}\,\frac{\Phi_0}{2\pi}\,\frac{d\delta}{dt} \tag{2.31}$$

This forms the basic modelling equation for a DC SQUID magnetometer. If equation (2.31) is time-averaged, the voltage across the SQUID's junctions can be expressed as:

$$V = R_n\sqrt{I_b^2 - I_{c,SQ}^2} \tag{2.32}$$

$$= R_n\sqrt{I_b^2 - 4I_{c,av}^2\,\cos^2\left(\pi\,\Phi / \Phi_0\right)} \tag{2.33}$$

Equation (2.33) is the standard time-averaged voltage across the overdamped DC SQUID's junctions, relative to the sensed flux. The frequency of the output voltage is proportional to the differential of the sensed flux (Basso, Perold & Lourens, 1998:126). The SQUID's transfer coefficient, V_Φ is the differential of the average voltage across the SQUID's junctions, with respect to the sensed flux (i.e., $V_\Phi = \partial V / \partial\Phi$).

Figure 2.15 (plotted with MATLAB) shows the graph of the SQUID magnetometer's normalised critical current, with respect to the sensed flux. Figure 2.16 shows the typical voltage current (*V* - *I*) characteristic at various fluxes. This shows that, at the region where the junction current is lower than two times the critical current, $I_{c,av}$, the *V* - *I* characteristic of a SQUID magnetometer is similar to that of a pure resistor, which is linear. This linearity means that, the output voltage behaves in a direct proportion manner to the applied current. The behaviour, however, has a flat response at the region where the junction's current is lower than two times the critical current, $I_{c,av}$. For only one JJ, this flat region covers only 1 $I_{c,av}$. This flat region seems to get narrower, as the sensed field increases from $n\Phi_0$ to $(n + 1)$ Φ_0, where $n = 0, 1, 2,..,$, and the sequence repeats itself, as clearly shown in Figure 2.16 (Clarke & Braginski, 2004:47). This shows that the external magnetic fields have quantum effects on the critical junction current. This phenomenon quite agrees with what Figure 2.13 portrays.

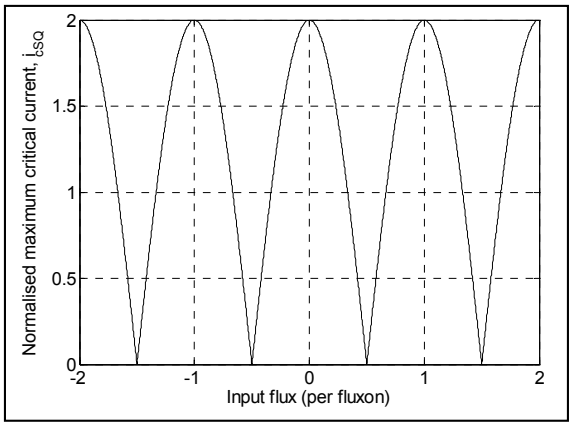

Figure 2.15: Normalised maximum critical current with respect to the sensed flux

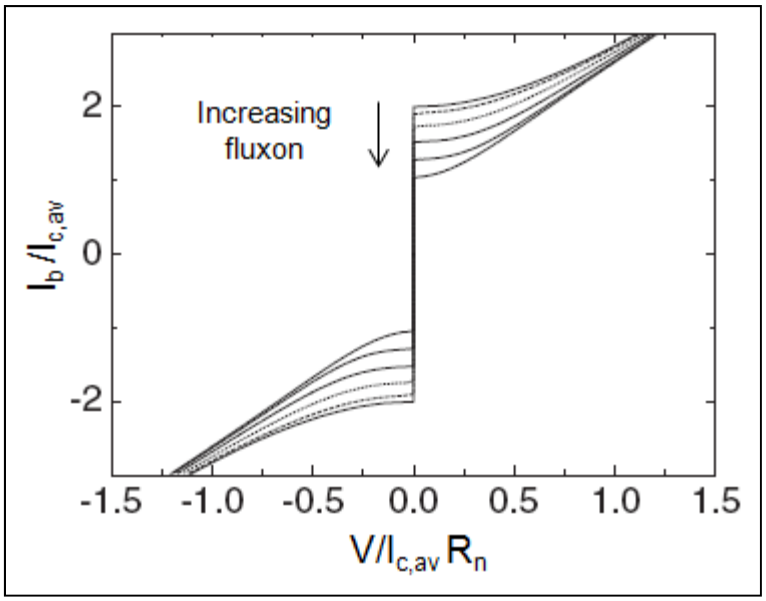

Figure 2.16: The dc SQUID *V* - *I* characteristics in the order of increasing applied flux, from the extreme ends towards the middle (Clarke & Braginski, 2004:47)

If the sensed flux is relatively smaller than Φ_0, the SQUID's transfer coefficient, V_Φ can be obtained from

$$V = 2\pi I_{c,av}\, R_n\, \Phi / \Phi_0$$

Where,

$$\frac{\partial V}{\partial \Phi} = V_\Phi = \frac{2\pi I_{c,av} R_n}{\Phi_0} \tag{2.34}$$

If the SQUID is biased at a current, I_b that keeps the SQUID at the working point W, with V being the voltage across the SQUID, its maximum flux-to-voltage transfer coefficient, V_Φ can be expressed as:

$$V_\Phi = \frac{\partial V}{\partial \Phi} = \frac{R_n}{L_{SQ}} \frac{2\pi I_{c,av} R_n}{\beta_L \Phi_0} \tag{2.35}$$

2.6 SQUID noise sources

The fact that a SQUID is the most sensitive magnetic sensing device does not eradicate the fact that it is also susceptible to noise from various sources. This poses a great challenge on the design of the SQUID system, because attempts to reduce this noise also lead to some trade-offs in other design parameters, especially the loop inductance. As shown in Figure 2.17, noise sources are in two major categories - low frequency, 1/ *f*, noise and white noise.

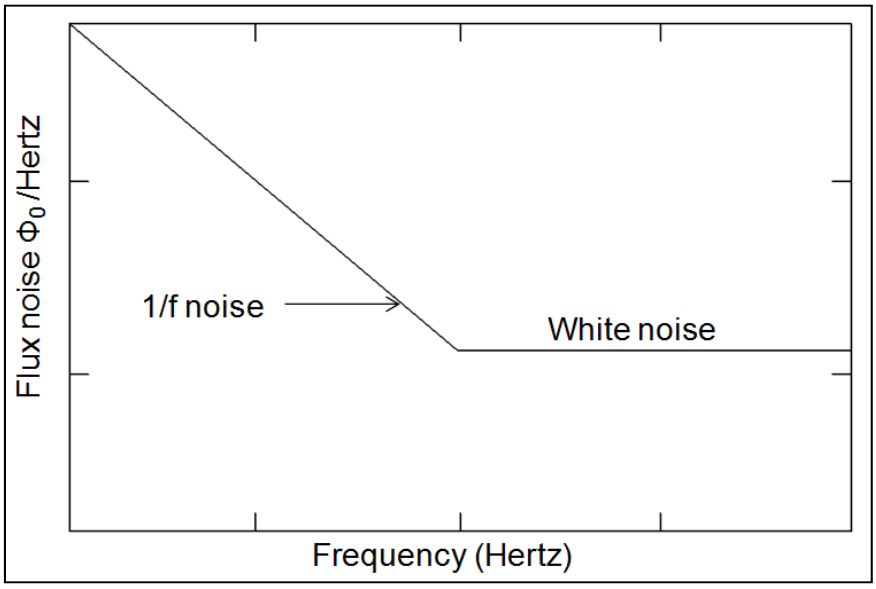

Figure 2.17: Noise power spectral density of a SQUID (Hastings, Mahler, Schneider & Eraker, 1985:554)

The 1/ *f* noise exists as a sloppy response in the very low frequency region (approximately below 1Hz) of the spectrum (Hastings, Mahler, Schneider & Eraker, 1985:554). White noise exists as a constant response from a very low frequency region to a very high frequency region in the spectrum. The following sub-section elaborates on the sources of some of these two categories of noise.

2.6.1 White noise

This is a type of noise that comes as a result of random processes like the flow of charge or thermal vibrations, which is a normal phenomenon for any material at any temperature above absolute zero (0 K). If this noise is generated within the system, it is regarded as intrinsic, but extrinsic, if it is generated from an external source.

Examples of internally generated white noise include the shot (or quantum) noise and thermal noise. Since there will be flow of current between the SQUID's JJ, quantum noise is bound to occur, due to quantum energy fluctuations in the junction's resistance. In the case of the thermal noise, it is the most stubborn of all types of noise that severely affect the SQUID's operation, because the SQUID's loop is always prone to having it after the design. It may result from the junctions' resistance, R_n or thermal fluctuation in the cryogenic cooling system. As a result of this thermal noise, the SQUID must be biased at its working point, *W* with a magnetic flux less than $\Phi_0 / 2$ (it is usually maintained at $\Phi_0 / 4$), otherwise it will not exhibit the quantum effect (Khare, 2003; Burger, 2008:36).

Equation (2.36) is the Johnson Nyquist equation, which describes the thermal noise power in an ideal resistor.

$$S_v(f) = 4k_B TR \tag{2.36}$$

Where,

k_B is the Boltzmann's constant (1.38066 X 10^{-23} J/K),
T is the operating temperature.

The average thermal voltage noise is zero for DC SQUIDs. The rms value of the power spectral density of the voltage noise at frequencies below 1THz is, however, non-zero, and it is given by

$$S_v(f) = 16\, k_B TR_n \text{ in } V^2Hz^{-1}. \tag{2.37}$$

Also, the equivalent flux noise, Φ_n, is expressed as:

$$\Phi_n^2 = L_{SQ} k_B T \tag{2.38}$$

From here, the SQUID's loop inductor is $L_{SQ} = \Phi_n^2/(k_B T)$. This can be used to calculate how much inductive the SQUID's loop should be, in order to avoid the adverse effects of thermal noise. For example, consider a high T_c SQUID operating at $T_c = 77\ K$. By substituting the values of k_B, with $\Phi_n \leq \Phi_0 / 2$ (for quantum effect to occur), $T = 77\ K$, and $\Phi_0 = 2.07 \text{ X } 10^{-15}$ Wb, it can then be inferred that the SQUID's loop inductance is $L_{SQ} \leq 1.0076$ nH.

More so, the thermal flux noise density is expressed as:

$$S_\Phi = S_v(f) / V_\Phi^2 \tag{2.39}$$

2.6.2 Telegraph noise

This kind of noise occurs as a result of manufacturing error in the SQUID, and there is no known solution to such noise. The appearance of this noise indicates the SQUID's end of life (Burger, 2008:48).

2.6.3 Magnetic field noise

This is also regarded as the magnetic field resolution, and it is one of the yardsticks used in comparing different SQUID magnetometers. According to Clarke and Braginski (2005:588), the SQUID's magnetic noise, S_B, is represented by:

$$S_B = S_\Phi / A_{eff}^2 = B_N^2 \tag{2.40}$$

Where,

B_N is the rms magnetic field noise
A_{eff} is the SQUID's effective area
S_Φ is the thermal flux noise density, expressed in equation (2.39).

For a single layer SQUID magnetometer (discussed in section 2.7.1), the effective area of the SQUID can be expressed as:

$$A_{eff} \approx \alpha \left(A_p / L_p \right) L_{SQ} \tag{2.41}$$

Where,

A_p and L_p are respectively the effective area and inductance of the pick-up loop
α is the constant describing the coupling efficiency

α is always unity whenever the current in the pick-up inductor gives a maximum flux in the SQUID's inductor (Khare, 2003).

2.6.4 LIf noise

The LIf noise is a 1/ *f* noise type caused by the critical current, I_c, and fluctuations in the normal junction resistance, R_n fluctuations in a DC SQUID's junction. This critical current fluctuation can either lead to additional voltage across the SQUID's JJ, or flow of circulating current in the SQUID's loop. One of the various means of dealing with the effects of these fluctuations is the use of a bias current feedback (BCF) coil in series with the SQUID's bias circuit, together with an additional positive feedback (section 2.9.1) prior to the pre-amplifier stage. Other means include the use of a current bias reversal and a flux modulation schemes in applications involving low frequencies.

2.7 The SQUID's sensitivity

SQUID's sensitivity is affected by noise, hence, in order to increase the SQUID's sensitivity, the magnetic field noise (equation (2.40)) has to be reduced. This can be achieved by either increasing the SQUID's effective area, or reducing the flux noise. As equation (2.41) shows, increasing the SQUID's loop inductance, L_{SQ}, helps in increasing the effective area, A_{eff}. However, increasing the L_{SQ} also leads to decrease in the flux-to-voltage transfer coefficient, V_Φ (equation (2.35)), which is in turn inversely proportional to the thermal flux noise density, S_Φ (equation (2.39)). This invariably increases the flux noise. Increase in the L_{SQ} additionally makes the selection parameter, β_L, less optimal (equation (2.7)).

With a view to improving the high T_c SQUID's sensitivity, several design possibilities have, however, been discovered to increase the effective area without increasing its loop inductance. These designs include the use of a large area washer DC SQUID or the use of a directly coupled DC SQUID, as fully discussed later in the following sub-sections.

2.7.1 The single layer SQUID magnetometer approach

This kind of SQUID design can either be termed the large area washer HTS SQUID or directly coupled HTS SQUID, depending on the fabrication approach used in attaining the increased effective area. The former design employs the use of a larger film width for focussing the applied field through the SQUID's loop, while the latter uses a secondary larger

superconducting pick-up loop, in parallel with the primary smaller SQUID inductance, to directly inject the sensed field into the SQUID (Burger, 2008:35-38; Jia *et al*., 1998:3068-3070). Equation (2.41) gives the expression for computing the effective area of a directly couple SQUID, and the improved apparent flux is as presented in equation (2.42).

$$\Phi_{eff} = BA_{SQ} + BA_p \left(L_{SQ} / L_p \right) \tag{2.42}$$

Where,

B is the magnetic flux density sensed

Since the secondary superconducting pick-up loop is larger than the SQUID's loop, this implies that the secondary pickup inductor, L_p is also greater than the SQUID's inductor, L_{SQ} which is maintained at its initial value. It is therefore realistic to have an improved sensitivity with these kind of designs (i.e. Large area washer SQUID and directly coupled SQUID).

The first directly coupled SQUID magnetometer was presented by Matsuda, Murayama, Kiryu, Kasai, Kashiwaya, Koyanagi, Endo and Kuriki (1991:3043). It was a LTS (2.2 K SQUID made from a *BiSRCaCuO* film, with a confirmed sensitivity of 1.5 $pTH^{-1/2}$ above 20Hz. A number of reports have been presented on the fabrication of HTS SQUID, with good sensitivities, in later years. An example is the 77K HTS reported by Beyer, Drung, Ludwig, Minotani, and Enpuku (2009:203), with a sensitivity of 32 fT $Hz^{-1/2}$ at 2 Hz. One of the draw-backs of a directly coupled SQUID is its tendency to have an increase in the $1/f$ noise, while cooling it in a static magnetic field.

2.7.2 The flip chip SQUID magnetometer approach

This approach involves the use of a series connected flux transformer (otherwise known as the flux focuser), with the pickup loop, on a separate substrate other than the main SQUID's substrate. The SQUID's loop is then placed on the focuser, whose centre is being mechanically aligned to the SQUID's loop. The flux sensed by this flux transformer (or the focuser) gets concentrated at the centre, and then inductively coupled to the SQUID. With this arrangement, a larger magnetic flux gets to the SQUID, thereby improving its sensitivity, as compared to an ordinary conventional pick-up loop.

While designing this kind of SQUID magnetometer, it is paramount to ensure equality in both the pickup loop inductor, L_p and that of the input coil inductor, L_i, and their sizes and shapes must both match. Flip chip HTS magnetometers have been successfully demonstrated by researchers, with good records of sensitivity, even to the femto Tesla (fT) range. For

instance, Faley, Poppe, Urban, Paulson, Starr, and Fagaly (2001:1383) reported the fabrication of a HTS flip chip magnetometer, with a proven sensitivity of 5 fT Hz $^{-1/2}$ at a low frequency.

2.7.3 The monolithic SQUID magnetometer approach

This kind of approach monolithically couples the flux transformer (discussed in sub-section 2.7.2) and the SQUID's loop onto the same substrate. Various means of going about this design have been reported over the years. Ludwig, Dantsker, Kleiner, Koelle, Clarke, Knappe, Drung, Koch, Alford and Button (2009:1418) have reported the design of an integrated HTS magnetometer (of T_c = *77* K) that exhibited a good sensitivity (37 fT Hz $^{-1/2}$ at 1 Hz and 18 fT Hz $^{-1/2}$ a 1 Hz It was made of 16 SQUID loops connected in parallel, so as to reduce the SQUID's inductance, L_{SQ} without increasing the effective area of the SQUID's inductance. This is a very good approach in reducing the magnetic noise, thereby improving the SQUID's sensitivity.

Another approach was employed by Scharnweber and Schilling (2009), by using a multi-loop pickup coil to match the pick-up loop's inductance and that of the flux transformer, and the fabricated SQUID magnetometer displayed a reduced flux density noise of 100 fT Hz $^{-1/2}$. Drung, Cantor, Peters, Scheer and Koch (1990:406) also employed this monolithic approach, but with a set of 8 parallel pick-up loops to substitute for the need for a flux transformer, in the design of a low noise high speed DC SQUID magnetometer (at 4.2 K). With this, a total loop inductance of 0.5 nH was achieved, with a very high sensitivity of 0.4 nT/ Φ_0.

2.8 The SQUID bias electronics

In order to keep the SQUID at its working point, an approximate bias flux, $\Phi_b = \Phi_0 / 4$ is needed across the SQUID. This can be achieved by applying a bias current I_b to the SQUID's junctions. Different values of bias current produce varying flux-voltage characteristics curves, as displayed in Figure 2.18 (using equation (2.33)). From this Figure, it is required that $I_b > I_{c,av}$ in order to have a full sinusoidal output. This is essential for easy linearisation of the sinusoidal output from the SQUID sensor. According to Burger, I_b is best in the range $3.3\ I_{c,av} < I_b < 3.5\ I_{c,av}$. While providing this bias current, care has to be taken in order not to damage the SQUID. The maximum required bias current to be applied to the SQUID determines how much current is to be supplied from the bias circuit.

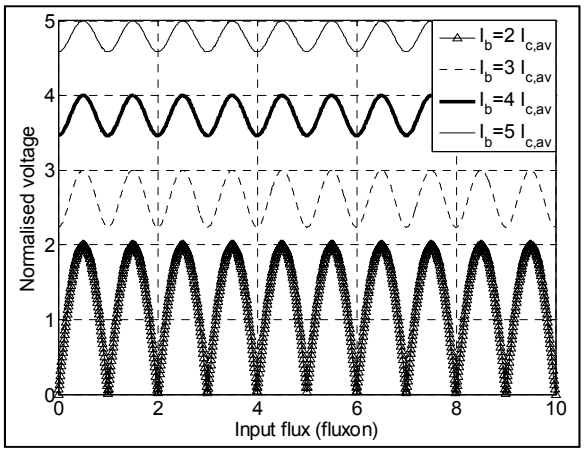

Figure 2.18: Flux-voltage characteristics at various bias currents

2.8.1 Design basics for the SQUID bias circuit

There are various design approaches to bias current circuits. Figure 2.19 presents one very simple approach. This entails a series resistor current source.

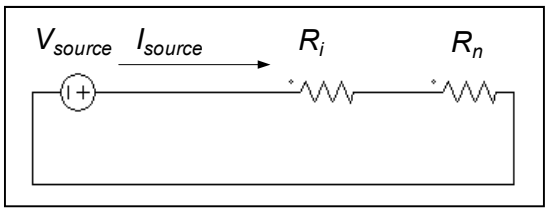

Figure 2.19: A series resistor current source circuit

From the Figure, R_n is the parallel combination of the SQUID's junction resistances, and R_i is the series resistance. For this method to be usable, the QSUID's R_n must be known, otherwise, the expected I_{source} from the current source cannot be pre defined. I_{source} is given by:

$$I_{source} = \frac{V}{R_n + R_i} \tag{2.43}$$

Its main disadvantage is that it has no protection scheme. An accidental voltage, which might be larger than V may lead to a bias current that is larger than the SQUID's. This will eventually damage the SQUID. More so, any variation in the load resistor to this circuit produces varying voltage drops across it, and this invariably makes the I_{source} non-constant.

Another type of bias circuits is the Widlar op-amp current source represented in Figure 2.20. It is a voltage-controlled constant current generator that uses an operational amplifier (op-amp), to either source or sink current, depending on the configuration. This configuration allows for constant voltage difference across the load resistor, thereby producing a constant current output. Unlike the series current source circuit, this type is helpful in that, it can be

used even if the SQUID's normal junction resistance, R_n is unknown. This type of circuit was used by Burger (2008:118) to bias the designed SQUID for a microscope.

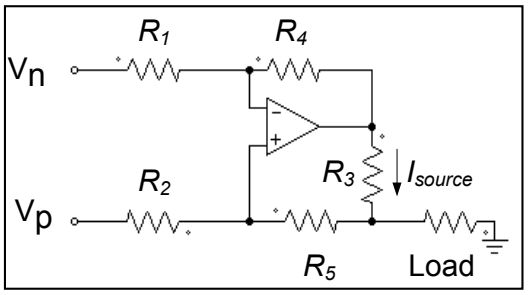

Figure 2.20: Widlar current source /sink circuit for constant biasing current

Depending on the application, either V_p or V_n is to be grounded. To configure this amplifier as a current source (i.e., positive current), the inverting input, V_n should be grounded. Also, the non-inverting input, V_p should be grounded in order to configure it as a current sink (i.e., negative current). As described by the National Semiconductor (2002:10), the resistors R_1 through R_4 can be chosen such that, $R_1 = R_2$ and R5 = $R_4 - R_3$. If the op-amp is considered as an ideal amplifier (i.e. no current goes inside the amplifier), Kirchhoff's current law can be applied to the circuit, and I_{source} is obtained as:

$$I_{source} = \frac{(V_p - V_n)}{R_3}\frac{R_4}{R_1} \tag{2.44}$$

If R_1, R_2 and R_4 can be made equal, then equation (2.44) reduces to:

$$I_{source} = (V_p - V_n) / R_3 \tag{2.45}$$

For example, if a current, $I_{source} = 250$ µA is required, with $V_p = 5$ V and $V_n = 0$ V, we can choose $R_1 = R_2 = R_4 = 22$ kΩ. Then R_3 and R_5 can therefore be calculated thus:

$$R_3 = V_p / I_{source} = 5 / (250 \times 10^{-6}) = 20\,\text{k}\Omega$$

$$R_5 = R_4 - R_3 = 22{,}000 - 20{,}000 = 2\,\text{k}\Omega$$

2.9 The SQUID readout electronics

After biasing the DC SQUID with a constant current, its output voltage is a non-linear periodic function of the sensed steadily increasing magnetic flux (as typically depicted in Figure 2.21 (a)), with, a period of 1 Φ_0 (1 fluxon). By examining Figure 2.21 (a), the SQUID's output voltage seems to follow linearity with the flux amplitude from 0 towards Φ_0 / π, after

which it gets strongly distorted (non-linear). This has been extensively described in section 2.5.3.The linear flux range, Φ_{lin} of the sensed peak-to-peak flux can therefore be approximated as:

$$\Phi_{lin} \leq \Phi_0 / \pi \tag{2.46}$$

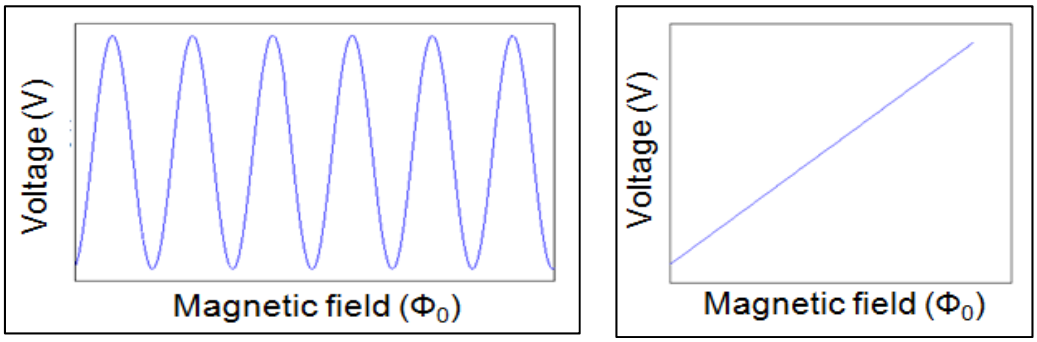

(a) **(b)**

Figure 2.21: DC SQUID output signals (a) periodic and (b) linearised

The non-linear error flux, Φ_{nl} corresponding to this linear flux range can be approximated by the following equation (Clarke & Braginski, 2004:128-129):

$$\Phi_{nl} \approx \pm \delta \Phi_{pp}^3 / \left(48 \Phi_{lin}^2\right) \tag{2.47}$$

Where,

$\delta\Phi_{pp}$ is the flux range.

For instance, given a signal flux range of $\delta\Phi_{pp} = 0.5\ \Phi_0$, equation (2.47) can be used to calculate the corresponding non-linear error flux as $\Phi_{nl} = \pm\ 26\ X\ 10^{-3}\ \Phi_0$. It is, therefore, needed to linearise this function in order to have a wide dynamic range and maximum sensitivity. This can be achieved by using a non cryogenic flux locked loop (FLL) electronics circuit to operate the SQUID in a feedback loop. This FLL operation basically entails driving the SQUID's output through a pre-amplifier, whose output is integrated through an integrator, to produce a linear signal. The linear signal is then used to drive the feedback coil, mutually coupled to the SQUID, through a feedback resistor (Figure 2.3). This output signal driving the feedback coil then generates a counter magnetic flux in opposition to the sensed magnetic flux, thereby cancelling it out. With this, the SQUID is said to be "locked" (i.e. zero magnetic state). The magnitude of the signal used to cancel out the sensed signal represents the magnitude of the sensed magnetic field to be measured. The output voltage of this

electronics (from the integrator) is a linear representation of the sensed flux signal, as depicted in Figure 2.21 (b). This output voltage is maintained until there is a change in the magnitude of the input (sensed) flux, and the SQUID maintains its linearity, until the integrator's supply rail is exceeded.

Before any suitable FLL electronics can be designed for a SQUID magnetometer, parameters like the dynamic range, slew rate, open loop gain, bandwidth and the feedback resistor must be determined. This sub-section briefly describes the expressions for some of these parameters, and the rest are described in the subsequent sections.

Figure 2.22 can be used to compute the feedback expressions for the FLL system (Clarke & Braginski, 2004:132). If $H_{FLL,ol}$ is the FLL's transfer function (TF), $H_{SQ} = H_{SQUID}\, H_{fbCoil}$, the SQUID's TF and $H_{Electronics} = H_{Preamp}\, H_{Int}$, the combined TF for the pre-amplifier and integrator, we can then write:

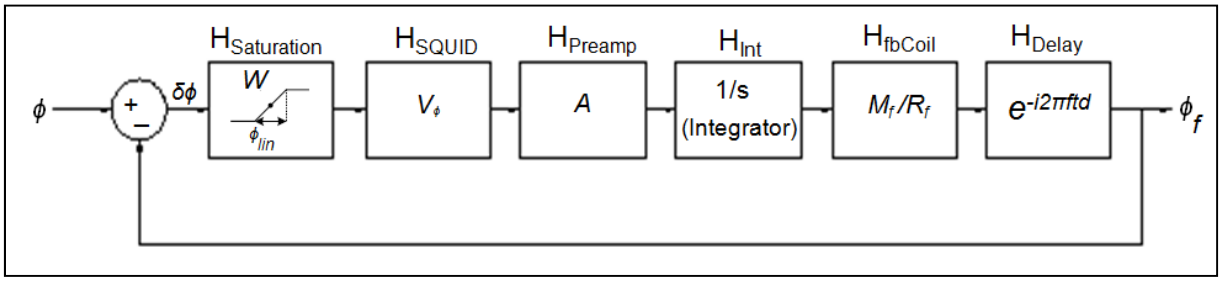

(a)

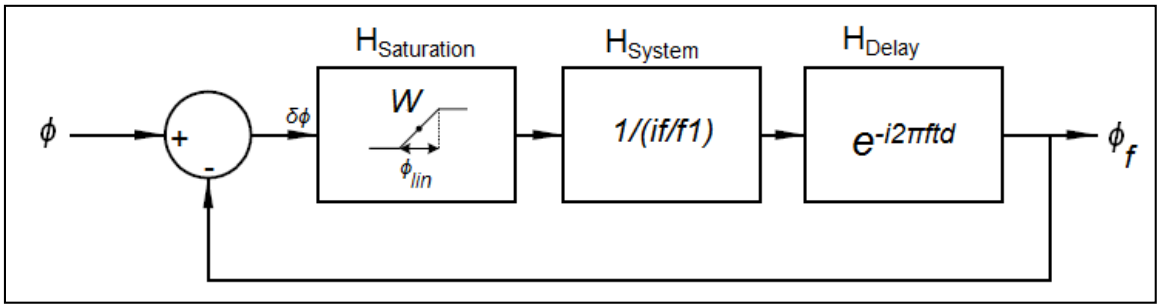

(b)

Figure 2.22: The SQUID Transfer function block diagram for (a) complete transfer function (b) simplified transfer function (Burger, 2008:75)

$$H_{FLL,ol} = H_{Saturation} \,.\, H_{SQUID} \,.\, H_{Preamp} \,.\, H_{Int.} \,.\, H_{fbCoil} \,.\, H_{Delay} \tag{2.48}$$

In a simplified form,

$$H_{FLL,ol} = H_{Saturation} \,.\, H_{SQ} \,.\, H_{Electronics} \,.\, H_{Delay} \tag{2.49}$$

It also follows that,

$$H_{SQ}(i\,2\pi f) = G_{SQ} = V_{\Phi} M_f / R_f \tag{2.50}$$

and

$$H_{Electronics}(i\,2\pi f) = A \,/\, (i\,2\pi f) \tag{2.51}$$

Where,

G_{SQ} the SQUID's open loop gain
V_{Φ} = the flux-to-voltage transfer function
M_f = the feedback coil's mutual inductance
R_f = the feedback resistor
A = the open loop gain
$i = \sqrt{-1}$
f = the frequency of the open loop system.

The open loop FLL has a unity gain at a unity gain frequency, f_1 (the characteristic unity gain frequency of the integrator). This is the frequency at which the integrator's gain is 1. It is given by:

$$f_1 = \frac{1}{2\,\pi R_{\text{int}} C_{\text{int}}} \tag{2.52}$$

Where,

R_{int} and C_{int} are, respectively, the integrator's resistance

The open loop gain can then be written as:

$$A = 2\,\pi f_1 \,/\, G_{SQ} \tag{2.53}$$

With this,

$$G_{SQ} = 2\pi f_1 \,/\, A = H_{SQ} \tag{2.54}$$

Combining the SQUID's and the electronics' TF, we have:

$$H_{System} = H_{SQ}\, H_{Electronics} = G_{SQ}\, H_{Electronics} \tag{2.55}$$

If equations (2.54) and (2.51) are combined, equation (2.55) can then be re-written thus:

$$H_{System} = \frac{f_1}{if} = \frac{1}{if\ /\ f_1} \tag{2.56}$$

From Figure 2.22, the error (tracking) signal, $\delta\Phi$, which is directly supplied to the SQUID is given by the difference between the external flux, Φ and the feedback flux, Φ_f, as follows:

$$\delta\,\Phi = \Phi - \Phi_f$$

When the SQUID is kept at its operating point, *W,* this implies that the applied external flux, Φ, to the SQUID, is kept at approximately Φ_0 / 4 (as discussed in section 2.5.3) and the error signal, which is also the magnetic flux deviation, must be in the range $\delta\Phi \leq \pm\ \Phi_0$ / 4, else, the SQUID's response becomes non-linear (Burger, 2008:36).

More so, since the integrator's output, V_{int}, is linearly related to the applied flux, we then have:

$$V_{Int} = \Phi_f\ R_f\ /\ M_f \tag{2.57}$$

$$\Rightarrow \Phi_f = V_{Int}\ M_f\ /\ R_f \tag{2.58}$$

If $V_{int,max}$ is the integrator's maximum output, the FLL's dynamic range is then given by:

$$\Phi_{dyn} = V_{Int,\max}\ M_f\ /\ R_f \tag{2.59}$$

Any form of delay in a magnetometer set-up is usually attributed to the delay in the transmission lines, because the SQUID and the feedback electronics are regarded to be instantaneous in their responses. The time delay can then be represented by the line delay expression as:

$$H_{Delay}\left(i2\pi f\right) = e^{i2\pi f t_d}$$

Where,

t_d is the time delay

As a function of t_d , the magnitude of the FLL gain, G_{FLL} (for a small input signal) can be written as:

$$\left|G_{FLL,cl}\left(i2\pi f\right)\right| = 1/\sqrt{1+\frac{f}{f_1}\left(\frac{f}{f_1}-2\sin\left(2\pi f t_d\right)\right)} \tag{2.60}$$

As established earlier on, f_1 (the unity gain frequency) is represented in equation (2.52). This can be varied during the design of the integrator circuitry, but the time delay, t_d is determined by the system (length of the transmission lines, especially). The system's magnitude is, however, not affected by this time delay, but it influences the phase, which is a disadvantage (Burger, 2008:77). The system's stability is subject to the combination of these two parameters (i.e., $f_1 t_d$). Figure 2.23 (plotted with MATLAB) shows how the system's response or stability is being affected by the $f_1 t_d$ product. At $f_1 t_d \leq 0.08$, the time delay is negligible, and the system's stability is unaffected. However, at values $f_1 t_d \geq 0.08$, the system becomes unstable, with 0.2 being the worst case.

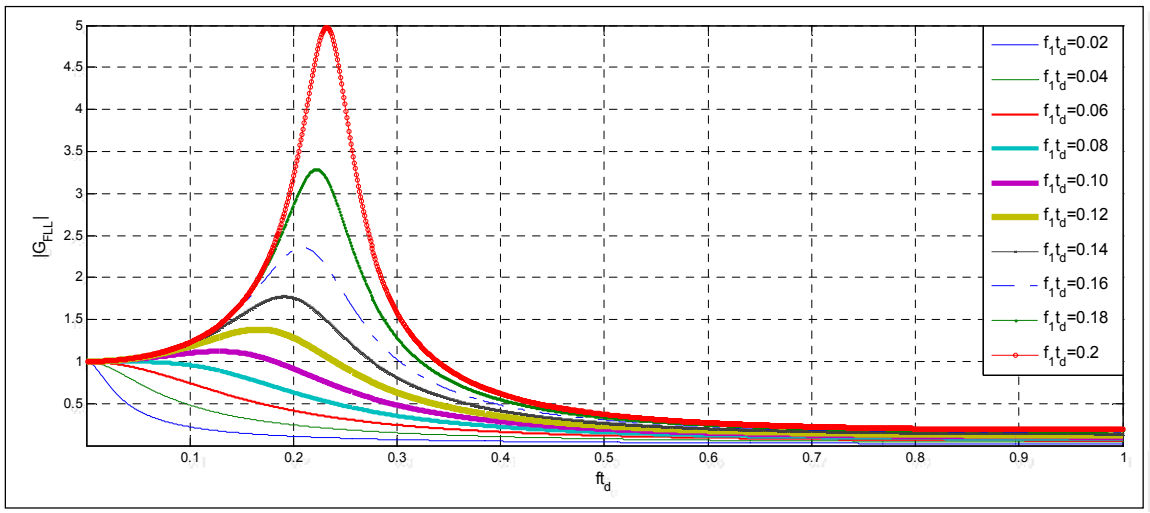

Figure 2.23: Flux locked loop system response versus time delay

A maximum unity gain frequency is possible at $f_{1,max} = 1/(4\pi t_d)$ (or $f_{1,max} = 0.08/t_d$), where the system's behaviour is flat over the frequency, $f\,t_d$ range. This particular response is the 4th line (from the bottom) in Figure 2.23.

Time delay affects the FLL bandwidth (usually abbreviated as f_{3dB}). This is because f_{3dB} is a function of time delay. Its maximum is given by:

$$f_{3dB,maX} = 2.25\, f_1 .$$

At the maximum unity gain, $f_{1,max} = 0.08 / t_d$. The $f_{3dB,max}$ therefore reduces to equation (2.61) (Clarke & Braginski, 2004:133).

$$f_{3dB,maX} = 0.18 / t_d \tag{2.61}$$

Looking at the feedback flux, Φ_f to the coil (Figure 2.22), the FLL slew rate, in terms of magnetic flux, can be represented by equation (2.62) (Clarke & Braginski, 2004:133).

$$\Phi_f \equiv \left| \frac{\delta \Phi_f}{\delta t} \right|_{\max} \tag{2.62}$$

Its maximum, achievable at the unity gain frequency, $f_{1,max}$, is given by:

$$\Phi_{f,\max} = \frac{\Phi_0}{4\, \pi\, t_d} \tag{2.63}$$

For a SQUID to continually be in its locked state, it is required to have a high slew rate, dynamic range and bandwidth. If an increased slew rate is desired, the use of an additional positive feedback (APF) (discussed later in section 2.9.1), can be considered. The use of two-pole integrators, at a corner frequency, $f_2 = f_1 / 4$ can also increase the slew rate, at low frequency applications, as discussed by Clarke and Braginski (2004:135-136).

However, since the SQUID is operated with FLL, if the slew rate is too high, it might be forced to lose its locked state, due to unwanted large transient signals (Clarke & Braginski, 2005:519). The unlocked state occurs when the error signal, $\delta\Phi$ is forced to exceed Φ_0 / 4. Typically, a slew rate between $1\Phi_0$ /μs and 10 Φ_0 /μs is appropriate. More so, to have a read-out electronics with a wider bandwidth, shortening the transmission line between the SQUID and the electronics, together with the right choice of a readout scheme can be helpful.

2.9.1 Design approaches for SQUID readout electronics

The conventional approach for the SQUID readout entails introducing a modulating magnetic field signal into the sensor, and then using the FLL to read changes in the modulating field, which is introduced by the sensed external magnetic field. This is referred to as the

modulated FLL. A typical example of this is as shown in Figure 2.24. It features a preamplifier and a resonating RLC circuit (with the aid of an external oscillator). This kind of design is used in conjunction with a small cryogenic resonant transformer coupled to the SQUID before amplification is done. The transformer, T_{RX} increases the FLL's slew rate, reduces the effect of the noise emanating from the pre-amplifier and matches its high input impedance to the SQUID, by cleverly choosing the transformer's turn ratio. The Resistor, *R* at the transformer's arm helps to protect the transformer's inductor from over-current and short-circuiting. The amplifier is loaded with an RLC modulator, driven by an external oscillator. The modulator helps to maintain very low amplitude at the oscillator's frequency. This approach is, however, limited, both in the flux modulation frequency, and tracking bandwidth. Hence, it is susceptible to stray magnetic field contaminations from sources like, power lines and even minute changes in the Earth's magnetic field. This can cause the FLL to lose its locked state. SQUID systems that use this approach are bulky due to the required large number of components, which in turn make them prone to interference. They are also expensive, and have to be operated in shielded environments. They are highly demanding In terms of bandwidth, when processing the signals. They as well suffer lower slew rates and narrower tracking bandwidth, because they are non-linear.

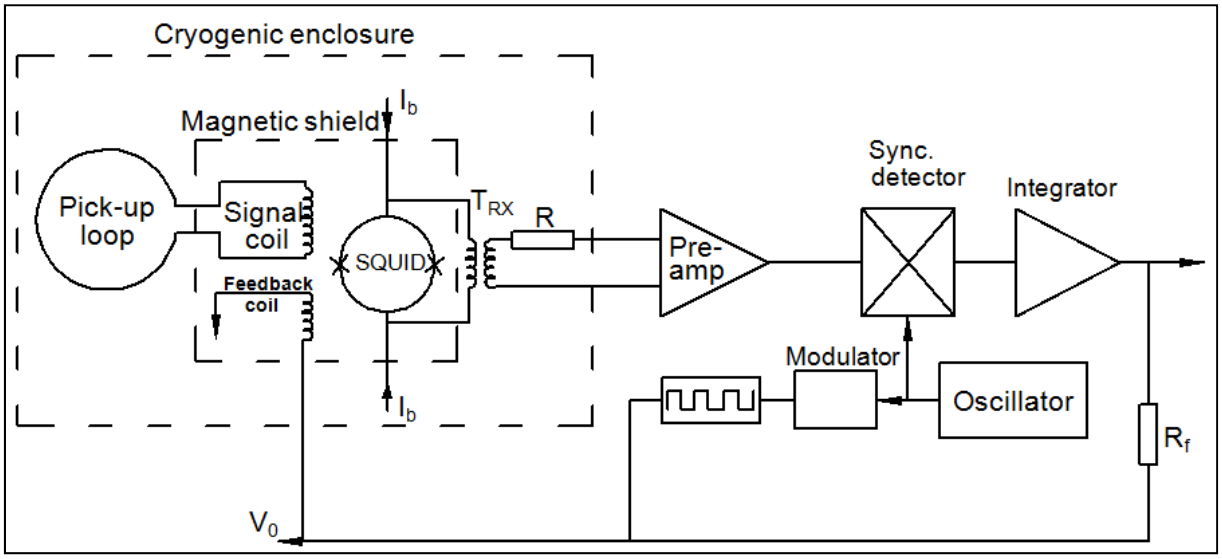

Figure 2.24: A SQUID readout electronics with a step up transformer, a pre-amplifier and a modulator

Flokstra, Ter Brake, Houwman, Veldhuis, Jaszczuk, Caspari and Rogalla (1991:783-784) adapted this method in the design of the readout electronics for the 19-channel DC SQUID magnetometer manufactured for a brain research. The preamplifier was made of Field effect transistors (FETs), with a RLC circuit resonating at 100 kHz. With this method, a very low amplifier voltage noise of 1 nV $Hz^{-1/2}$ was achieved. The measured current noise and the series resistance of the coils also contributed insignificantly to the total noise.

There have been some other attempts to improve on this approach. The work reported by Ganther, Jr. *et al*. (2002a), gave chances for the SQUID to be operated in an unshielded environment, by the introduction of some innovative circuits. Ganther, Jr. *et al*. (2002b) later came about the possibility of using an array of SQUIDs, requiring a few number of connections. The SQUIDs in the array have the opportunity of sharing some common components, thereby making the entire set-up effective, in terms of cost and size.

The second design approach for the SQUID readout is the direct feedback or unmodulated FLL, directly coupled to the SQUID. This method does not require the injection of any modulating magnetic field signal into the sensor. A very good example of this method is the one presented in Figure 2.3 of this write-up. It comprises of only the amplifier and integrator networks. It provides immense advantages over the modulated FLL approach. It is the simplest readout scheme for SQUID magnetometers, requiring fewer and cheaper electronic components. The only non-linear part of the set-up is the SQUID itself, which means there is room for improved slew rate and tracking bandwidth. This approach is good for any nanosatellite mission, since it definitely demands small power and space, as compared to the other type. Ganther and Snap (2006) employed this direct feedback approach, but with the use two stages of integrators, to improve the tracking frequency and slew rate of the system.

For improved voltage sensitivity, high slew rate and effective matching between the pre-amplifier and the SQUID's output, the SQUID system block diagram in Figure 2.25 (a) can be introduced into the unmodulated FLL approach. This is termed the additional positive feedback (APF) method (Clarke & Braginski, 2004:141).

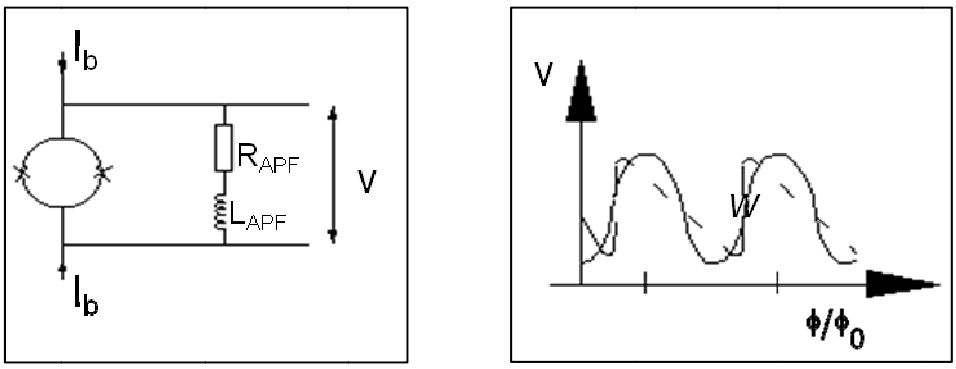

(a) **(b)**

Figure 2.25: SQUID electronics with additional positive feedback (APF): (a) Circuit (b) Voltage-flux characteristics (Burger, 2008:84)

Having biased the SQUID, any increase in the sensed flux produces an increase in the SQUID's output, which in turn produces an increased current flow in the feedback coil, L_{APF} and this eventually induces an additional flux in the SQUID in return. This leads to additional voltage and an eventual steeper voltage-flux ($V - \Phi$) characteristic of the SQUID at the working point (dotted line in Figure 2.25 (b)). The disadvantage of using this design is the fact that the R_{APF} of the APF constitutes a voltage divider for the SQUID's low output impedance and produces additional thermal noise. R_{APF} must therefore be made as small as possible and design the entire APF circuit to have a similar voltage noise as that of the SQUID.

Over the years, improvements work have been made to the SQUID readout electronics at large, even to the extent of having programmable addressable feedback loop models (Star Cryoelectronics, n.d.). This gives room for portable remote control of the SQUID sensor, directly from the user's computer, and provides wide bandwidth operations, together with complex techniques for nulling noise effects. However, the level of sophistication in the readout electronics is highly dependent on the amount of space and power available on the satellite's structure. This is why a simple direct readout electronic is recommended for such missions. The design basics of the various components that make up the unmodulated FLL circuitry are as comprehensively described in the following subsections.

2.9.1.1 The flux locked loop pre-amplifier circuit

As seen from Figure 2.3, the FLL's pre-amplifier's function is to amplify the weak signal from the SQUID by bringing its gain to unity. This implies that the pre-amplifier's gain, A_{Preamp} should be the reciprocal of the SQUID's gain. Hence, from equation (2.54), A_{Preamp} is given by:

$$A_{\Pr eamp} = 1/G_{SQ} = A/\left(2\pi f_1\right) \tag{2.64}$$

The pre-amplifier needs to be designed in such a way as to have a high gain bandwidth, GBW and a high slew rate, SR, which are respectively given by equations (2.65) and (2.66) (Burger, 2008:84).

$$GBW = f_1 / G_{SQ} \tag{2.65}$$

$$SR = f_{\max,SR} \times 2\pi V_{out,peak} \tag{2.66}$$

Where,

$f_{max,SR}$ is the frequency of a signal resulting from slew rate effect
$V_{out,peak}$ is the output signal at its peak

The FLL pre-amplifier is often referred to as low noise amplifier (LNA), since noise is a critical limiting factor in the amplifier circuit. With a view to reducing the noise effect caused by the pre-amplifier, a good design of the amplifier has to be made from the various types available. One of the best of these design types is the 2 op-amp in-amplifier circuit shown in Figure 2.26 (Kitchin & Counts, 2006:2-4). This preamplifier design is a high-impedance instrumentation amplifier, suitable for a DC SQUID biased from a DC current source. A circuit with low input impedance is, however, suitable for a SQUID biased with a voltage source (Drung, 1995:80).

The two op-amps circuit of this circuit (on Figure 2.26) are in voltage feedback (VF) modes. It functions just like a first-order low pass filter for the direct SQUID output (Drung, Bechstein, Franke, Scheiner & Schurig, 2001:880). A similar circuit was used by Burger (2008:121) for the preamplifier stage in the designed SQUID electronics for a SQUID microscope.

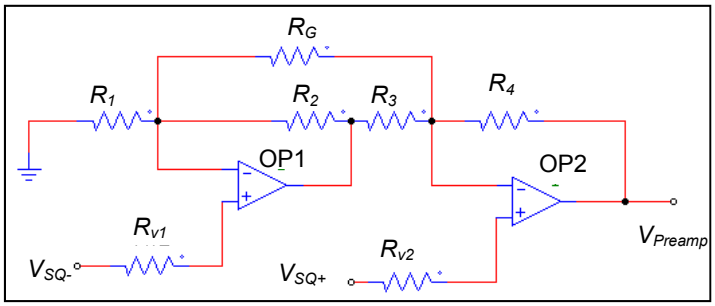

Figure 2.26: A 2 op-amp in-amp preamplifier circuit from 2 op-amps

The transfer function of this amplifier is given by

$$V_{out} = \left(V_{SQ+} - V_{SQ-}\right)\left(1 + \frac{R_4}{R_3} + \frac{2R_4}{R_G}\right).$$

Where,

$R_4 = R_1$ and $R_3 = R_2$

The resistor, R_G, in Figure 2.26 serves the purpose of protecting the circuitry, in case the input voltage exceeds the supply voltage, or the gain exceeds 100. If these two constraints are not exceeded, then R_G is opened. The transfer function then reduces to the following:

$$V_{out} = \left(V_{SQ+} - V_{SQ-}\right)\left(1 + \frac{R_4}{R_3}\right)$$

This implies that the amplifier's gain is

$$\frac{V_{out}}{\left(V_{SQ+} - V_{SQ-}\right)} = \left(1 + \frac{R_4}{R_3}\right).$$

For example, if a gain of 100 is required from the amplifier, R_3 can be chosen as 500 Ω, and R_4 can be calculated thus:

$R_4 = A_{Preamp}$ X $R_3 - R_4$ = 100 X 500 – 500 = 49.5 Ω

With this,

R_1 = 49.5 kΩ and

R_2 = 500 Ω

2.9.1.2 The flux locked loop integrator circuit

The FLL's slew rate and the gain bandwidth, GBW are established by the integrator circuit. The poles and zeros required by the SQUID, to have a stable phase locked feedback, are provided by the integrator as well. Figure 2.27 represents the simplest passive RC integrator circuit, whose transfer function is given by (Al-Alaoui, 1989:1116):

$$H_{\text{int}} = \frac{1}{RC + 1}, \text{ for } RC >> 1 \ .$$

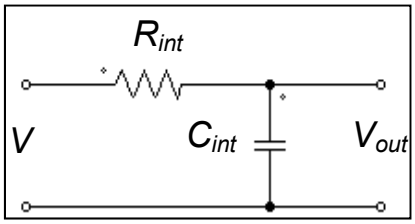

Figure 2.27: An RC integrator circuit

In cases of low frequency applications, this kind of RC integrator, however, needs amplification, since the voltage gain is ≤ 1. This necessitates looking into an integrator circuit composed of an op-amp.

Figure 2.28 depicts a typical single-pole integrator circuit composed of an op-amp, with a unity gain bandwidth, $GBW_{int} = f_1$. This as well acts as a low pass filter to the voltage noise from the preamplifier. At a constant positive input voltage, V the integrator will attempt to produce a changing voltage in the capacitor for maintaining a constant current through the resistor, thereby generating a negative slope voltage, V_{out} at the output. The transfer function for this integrator type is as given in equation (2.67).

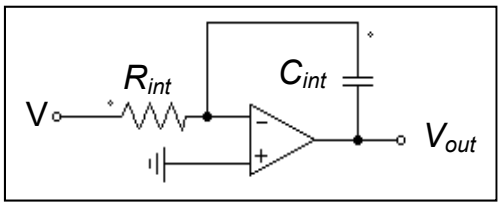

Figure 2.28: An op-amp single-pole inverting integrator

$$G_{Int} = V_{out} = \frac{1}{R_{\text{int}}\, C_{\text{int}}} \tag{2.67}$$

The output voltage is the integral value of the input voltage, V which is given by:

$$V_{out} = -\frac{1}{R_{\text{int}} C_{\text{int}}} \int_{t_1=0}^{t_2} V dt \tag{2.68}$$

For example, if an integrator with a unity gain frequency, f_1 = 1 MHz (i.e., GBW_{int} = 1 MHz) is to be designed, C_{int} can be set as 500 pF, and R_{int} can then be calculated from equation (2.52) as follows:

$$R_{\text{int}} = \frac{1}{2\pi f_1\, C_{\text{int1}}} = \frac{1}{2 \times \pi \times 10^6 \times 500 \times 10^{-12}} = 318\ \Omega$$

Signals from lower frequencies to a certain frequency limit, $f_{max,SR}$, have their frequency performance affected, if the slew rate, SR is not high enough. i.e,

$$f_{\text{max},SR} = \frac{SR}{2\,\pi V_{out,peak}} \tag{2.69}$$

Where,

$V_{Out,peak}$ represents the output signal's peak in Volts

This SR and the open loop integrator's gain can be compensated for by cascading the integrator with a lag compensator (Burger, 2008:82).

2.9.1.3 The flux locked loop feedback circuit

As established earlier in this section, the FLL's dynamic range, Φ_{dyn} is represented by equation (2.59). The FLL's feedback resistor, R_f is therefore represented by:

$$R_f = V_{Int,\max} \frac{M_f}{\Phi_{dyn}} \tag{2.70}$$

Where,

$V_{\mathrm{Int,max}}$ is the maximum output from the integrator circuit, with M_f being the feedback coil's mutual inductance.

If the feedback coil's mutual inductance is known, the feedback resistor can be calculated from equation (2.70). For example, If M_f = 58824 Φ_0 / A, with $V_{Int,max}$ = ± 5 V, and it is desired to design a FLL with a dynamic range of Φ_{dyn} = ± 300 Φ_0, R_f is calculated thus:

$$R_f = 5 \times \frac{58824}{300} = 980\ \Omega$$

2.10 Cryogenic cooling

Before SQUIDs can exhibit Josephson behaviour (i.e., transition to a superconducting state) the sensors must be conditioned to a cryogenic temperature. As stated in section 2.3.1, various SQUID types have different transition temperatures, depending on the kind of materials used in their designs. These temperatures are typically below -150 ^{0}C. This indeed has posed a great deal of challenge to the usability of SQUIDs in some environment such as the low Earth orbit. Cryogenic cooling in space environment can be achieved in three basic ways, which include active cooling, passive cooling, and hybrid cooling. Passive cooling is a cooling mechanism involving the use of radiation mechanism (fully discussed in section 2.10.3). Active cooling uses either cryocoolers for its cooling mechanism (i.e., mechanical cooling, as briefly discussed in section 2.10.2), or a cryogenic fluid, enclosed in dewars. Hybrid cooling employs the use of both active and passive cooling mechanisms to attain cryogenic temperatures, depending on the design requirements.

Lesser cooling power is required for cooling a high T_c SQUIDs (typically between 0.5 W and 2 W for operating temperatures between 60 K and 680 K), as compared to the low T_c

SQUIDs, which consume a lot of cooling power, before attaining superconductivity (Burger, 2008:67). The effectiveness of any cryogenic cooling system is examined, based on its cooling power, reliability, thermal variation, vibration level, noise level, and electromagnetic interference (EMI) level. It is highly desirable to have a robust cryocooling system and keep its vibration level below the SQUID's noise level, in order to make it usable in space.

2.10.1 Thermal variation

If the cryocooling system is not appropriately designed, the SQUID might be subjected to temperature instability, which greatly affects its performance. Fluctuating pressure over the liquid cryogen, and variation in the cold finger temperature (if a cryocooler is used), can lead to thermal variation. Temperature drifts contribute to flux noise and magnetic noise in the SQUID system. It also subjects the SQUID to I_c variation, which in turn contributes to 1/ f noise.

In order to address the challenges posed by temperature drifts, a number of approaches have been attempted. Reversal bias current readout mechanism can be used to address the 1/ f noise challenge, as was employed by Zhang, Wolters, Otto and Krause (2001:181). For high frequency applications, high-pass filter can be used to improve the SQUID's output (Burger, 2008:56). If a liquid cryogen is used, stabilizing its pressure will prevent temperature drift. Lastly, appropriately designing the SQUID and the flux transformer will boost its immunity against temperature drifts.

2.10.2 Cryocooler - an active cooling system

Active or mechanical cooling is a cooling system involving the use of the conventional cryocoolers. Miniature cryocoolers are very small mechanical coolers, capable of maintaining cryogenic temperatures. Various cryocoolers are available today, in different sizes, weights, power consumptions, cooling powers, and cryogenic liquid. Figure 2.29 shows the 3 dimensional view of a typical cryocooler.

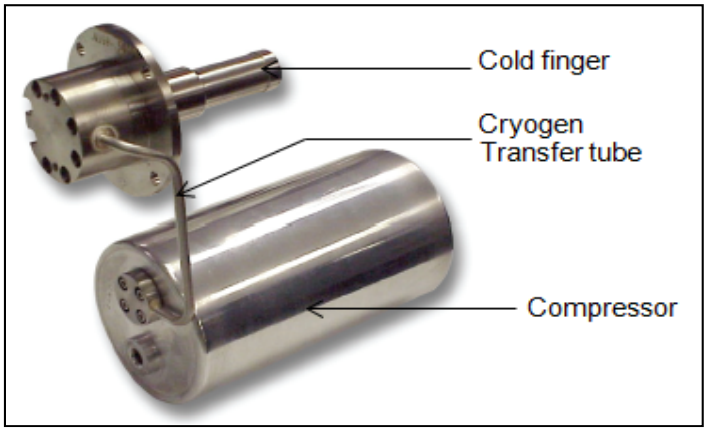

Figure 2.29: 3 dimensional view of a typical cryocooler (Cobham, 2009)

2.10.3 Radiative cooling - a passive cooling system

Radiative cooling is a passive cooling system that involves a long-wave radiation emission of heat from a body to be cooled, due to the thermal motion of charged particles, towards another body, called the heat sink. Although, its operating principle is very simple, but it is very challenging to be implemented and tested (University of Oxford, 2008). It works by directing a radiator, made from a material of very high emissivity, towards the heat sink, thereby radiating heat out into the heat sink. Space missions involving the use of this cooling mechanism use the deep space as the heat sink, while preventing heat contaminations, from the spacecraft body, Sun, and Earth, from reaching the cooled equipment. This kind of heat radiation is achieved in stages, by the use of cleverly designed radiators (as discussed latter in sub-section 2.10.5). The following subsections describe the background theories involved in the radiative cooling system.

2.10.3.1 Black body radiation

Practically, all matters with temperatures above absolute zero exhibit radiation absorption-emission phenomenon, and this is generally termed, radiation. The characteristics of the radiators, which radiate heat in form of electromagnetic waves, dictate the characteristics of the thermal radiation. These characteristics include the surface temperature, reflectivity, emissivity and absorptivity. A material is regarded as a black body, if its body and surface are at thermodynamic equilibrium (i.e., when the net flow of energy is zero). This thermal equilibrium can be well described using Kirchhoff's law of thermal radiation, which states that a material's emissivity and absorptivity become equal at thermal equilibrium. So, a material's emissivity can then be defined by its emission, relative to that of black body. This infers that the emissivity, ε of a black body is 1. The emissivity, ε of a perfect reflector is 0 (SolidWorks, 2008).

2.10.3.2 Thermal analysis

Thermal analysis is needed to observe the distribution of temperature and heat flow across the exposed surfaces of a passive cooling system. When performing this analysis, three means of heat transfer are looked into; which are conduction, convection and radiation. Conduction answers for the heat flow in the material under test, while convection and radiation answer for the heat exchange between the material and the surroundings. Convection requires fluid (liquid or gas) for its transfer, while radiation occurs in form of electromagnetic waves, which requires no medium for propagation (SolidWorks, 2008). Every material above absolute zero temperature radiates heat (as mentioned in section 2.10.3.1). This is the basis of passive cooling in space missions.

The amount of heat transfer due to conduction can be represented by (SolidWorks, 2008):

$$P_{Cond} = K\ A\left(T_{Hot} - T_{Cold}\right) / L \tag{2.71}$$

Where,

K is the conducting material's property called, thermal conductivity
A is the area of the material
L is the material's thickness
T_{Hot} and T_{Cold} are the respective temperatures at the hot and cold sections in the material

The amount of heat transfer due to radiation can be represented by Stefan-Boltzmann as:

$$P_{Rad} = \sigma\ \varepsilon\ A\left(T^4\right) \tag{2.72}$$

Where,

$\boldsymbol{\varepsilon}$ is the emissivity of the body (defined in section 2.10.3.1)
T^4 is the fourth power absolute temperature between the body and the surroundings
σ is Stefan-Boltzmann's constant

Because the pressure is extremely low in space, heat transfer due to convection is absent.

Any object in space is subjected to three kinds of radiation, namely solar flux, Earth infrared (IR) flux, and reflected flux from the Earth's surface, which is otherwise called the albedo effect. See Figure 2.30 for graphical explanation of these three radiation kinds. The object takes the advantage of the deep space, whose radiation temperature is about 3K (Jacques, 2009:16), to sink out its heat, thereby lowering its temperature. At thermal equilibrium, the power radiated to the deep space equals the total incoming heat power to the object, as represented in equation (2.73) Gilmore (2002:557).

$$P_{In} + P_{Ab} = P_E \tag{2.73}$$

And,

$$P_E = A\,\varepsilon\,\sigma\,T^4 \tag{2.74}$$

Where,

P_{In} is the internally generated heat power
P_{AB} is the absorbed heat power, which is the total incoming heat power due to the solar flux, P_s Earth's IR and albedo, P_A

P_E is the heat power radiated out by the object (at an equilibrium temperature, T)

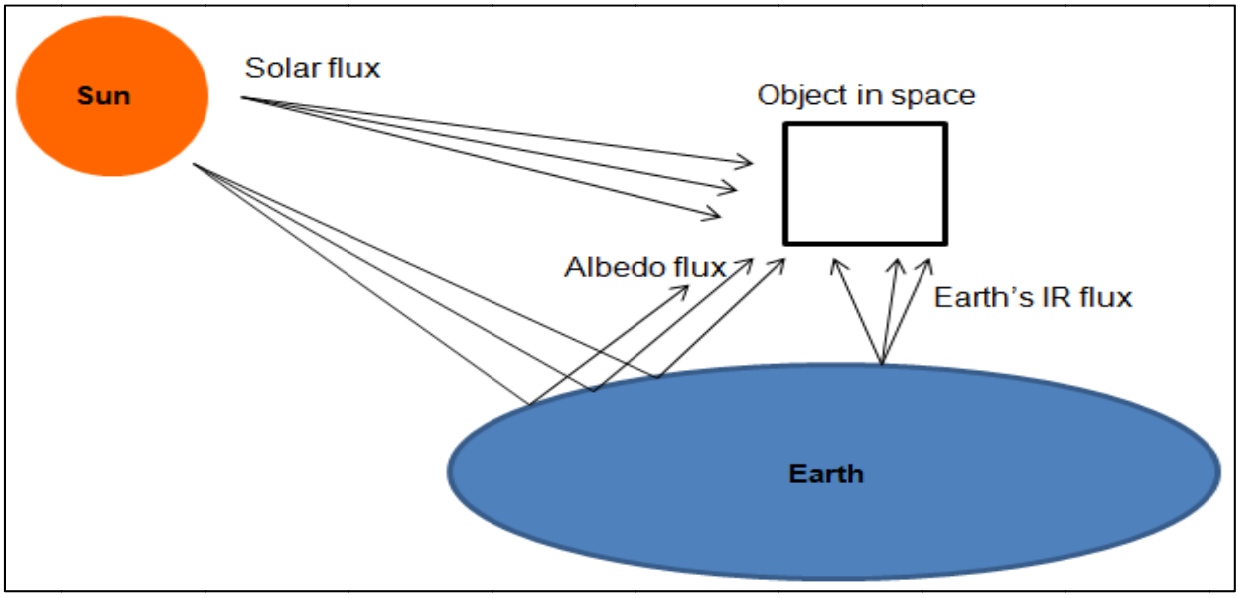

Figure 2.30: The solar flux, Earth infrared flux, and albedo flux

i.e.,

$$P_{Ab} = P_S + P_A + P_E = A\,\alpha\,S_c\,n\sin(\Psi) + A\,\alpha\,q_E \tag{2.75}$$

Where,

S_c is the solar constant, depending on the distance from the Sun, with a mean value of 1367 W/m^2 and a maximum value of 1414 W/m^2

q_A is the albedo flux, depending on the distance from the Earth

q_E is the IR heat flux from the Earth

ψ is the elevation (in degrees) between the normal to the Sun and the object

$A$is the total surface area of the object

n is the fraction of orbit in sunlight

α is the material's absorptivity

If equations (2.74) and (2.75) are employed, the equilibrium equation (equation (2.73)) can therefore be written as:

$$P_{In} = A\,\alpha\,S_c\,n\sin(\Psi) + A\,\alpha\,q_A + A\,\varepsilon\,q_E = A\,\varepsilon\,\alpha\,T^4 \tag{2.76}$$

Equation (2.76)) forms the basis of estimating the size of the radiator to be designed at a desired equilibrium temperature and vice versa (but P_{cond} is assumed negligible here). For

worst case scenario, the total power generated by the satellite's solar panel (which can reach up to 9 W in a 3U nanosatellite (Clark, Strain & Mazarias, n.d.), is assumed to be converted to heat, and this represents the P_{In} in equation (2.76). Due to the orbital parameters like the altitude, inclination angle and beta angle, the Earth's IR heat flux, q_E, and the average albedo flux, q_A differ. See Gilmore (2002:552-561) for further explanations.

Based on some thermal analysis software presently available, two types of thermal analyses can be performed, depending on the duration of interest. These are the steady state thermal analysis and the transient thermal analysis. In the steady state analysis, the thermal state of the system at thermal equilibrium is of interest, regardless of the time taken. In the transient analysis, the thermal state of the system with respect to time is of interest.

2.10.4 Some space missions using passive cooling systems

Various space-based observatories that used passive cooling technology were mainly launched into the deep space orbits (like the L2 Earth-Sun orbit). In these orbits, the environment is thermally stable, with the exception of heat influx from solar flares and albedo. Heat prevention from the Earth is also very much effective as compared to the LEOs. This is because satellites in the LEOs are at close proximity to the Earth, which implies that the Sun and the Earth cannot always be in the same part of the sky. This gives room for variation in the direction of thermal radiation and albedo (Thaller & Guttro. 2010; DiPirro, n.d.). Moreover, satellites at the LEOs are subjected to the heat source from the solar flux.

The first generation Meteosat, launched in 1977, made use of passive cryogenic cooler to aid its goal of providing weather pattern images. Sret 2 mission was later launched to evaluate the performance of a passive cryocooler, due to the challenges experienced with the Meteosat's passive cryocooler, and after 3 years of evaluation, the cooler was still operational (Rolfo, 1978:12-31).

Launched into Saturn in 1997, was the Cassini mission, whose onboard composite infrared spectrometer (CISR), made from the combination of two interferometers, was cooled via a passive cooling mechanism. The satellite was sent to make about 27 scientific explorations of the important elements that Saturn might contain, and it arrived there in 2004.

Passive cooling technology was employed by the Wilkinson Microwave Anisotropy Probe (WMAP) Observatory, launched in 2001. It had some onboard radiometer systems with HEMT (high electron mobility transistors) amplifiers, whose temperatures were to be maintained at approximately $90\,\mathrm{K}$. This was made possible by the aid of passive cooling technology (Bennett, Halpern, Hinshaw, Jarosic, kogut, Limon, Meyer, Page, Spergel, D.N.,

Tucker, G.S., Wallack, E., Wright, E.L., Barnes, C., Greason, M.R., Hill, R.S., Komatsu, Nolta, Odegard, Peiris, Verde & Weiland, 2003:5). Emissions from the Sun, Earth, and Moon were blocked off by WMAP's deployable sunshield, since all the emissions are always on the same part of the deep space due to the strategic location of its orbit, which was at the Earth-Sun second Lagrange point, L2. Passive thermal radiators were also used to radiate heat to the deep space (Wright. 2004).

Launched into a solar orbit (drift-away) in August 2003, was the Pitzer space telescope, also called the cryogenic telescope assembly (CTA), which hybridised a passive cooling system with a Helium cryostat to provide cryogenic cooling for its onboard science instruments (Finley & Schweickart, 2006:1295-1302).

In May 2009, two satellites, the Herschel telescope and the Planck observatory, were launched into orbits around the L2 point by the European space agency (ESA). Herschel carried an onboard 3.5 m diameter Cassegrain telescope, whose cryogenic temperature was maintained by passive cooling technology. The mission was primarily aimed at studying some of the coldest objects in space. It achieved a 55 – 672 μm spectral range of observational opportunity, which is the first of its kind (Pilbratt, 2008:7010 02-7010 03). Planck's observatory 1.5 m telescope carried a high-frequency instrument, (the coldest ever in space), for measurement of the cosmic microwave background (CMB) , which is the left over radiation emitted by hot plasma about 38,000 years of the post-big bang era, and for determining the total amount of atoms in existence. The object's cryogenic temperature was maintained by using several stages of passive cooling. Ever since launched, Planck has been able to accurately measure the CMBC as compared to the previous attempts (European space agency, 2009).

To be launched in 2016, is the NASA's EPIC (experimental probe of inflationary cosmology), being designed to passively cool its telescope's enclosure to 30 K, after which a cryocooler is to further cool it to 18 K, together with the main telescope at 4 K. The passive cooling system is made with a sunshield and four stages of double layered "*V*" grooved radiators, in a decreasing order of angles from the outer shield to the inner shield. These shield the enclosure from the solar radiation, at the same time, cooling it down to the desired cryogenic temperature (Chui, Bock, Holmes & Raab, 2010:633-635). The radiators are used to strategically reflect thermal radiations from the equipment into the heat sink, which is the deep space.

James Webb Space Telescope (JWST), is another observatory to be launched in 2018, into a L2 point orbit. It uses a large, light weight, deployable "*V*" groove radiator for cooling its

optical telescope, with a suite of other instruments, to temperatures lower than 50 K (Cleveland & Parrish, 2005:518).

The Japanese SPICA (Space Infrared Telescope for Cosmology and Astrophysics) mission is a collaborative work of ESA and JAXA (Japan Aerospace Exploration Agency). This satellite carries a 3 m diameter IR telescope, to be cooled down to a cryogenic temperature below 5.5 K, with the aid of a passive cooling system at the first cooling stage and mechanical cooling system at the second stage. It is to be launched in 2018, and operate around the Sun– Earth L2 point, in order to enjoy the thermal stability of the environment. Its passive Cooling System uses the combination of a baffle, a telescope shell, three layers of shield (inner, middle and outer shields), attached to a sunshield for preventing heat contaminations from the surroundings. There is a radiator at the lower part of the satellite, needed to radiate the heat absorbed from the spacecraft bus and sunlight, towards the deep space (Sugita, Sato, Yamawaki, Nakagawa, Murakami, Matsuhara, Murakami, Takada, Takai, Yoshida & Kanao, 2010:566-567).

2.10.5 Design basics for passive cooling system

There is virtually no specific or fixed format for designing passive cooling systems other than being optimal in radiating the heat out of the system to be cooled (in form of emission), and preventing heat contaminations from hotter bodies (in form of absorption). Very good design schemes that can be adopted are those used in the designs of EPIC and SPICA (section 2.10.4).

2.10.5.1 Choice of materials

The choice of materials and the fabrication of each component must be optimised in order to enhance an effective radiative cooling. In the case of SPICA, the trusses that support the telescope array and the shields (made from aluminium plates), are made from materials of low thermal conductivity - precisely, low conductive Alumina fibre reinforced plastics and Carbon fibre reinforced plastics. The baffle is made from high conductive Carbon fibre reinforced plastics for heat dissipation effectiveness. Each of EPIC's radiator's surfaces is coated with materials of varying characteristics, depending on the level of solar absorptivity and infrared emissivity required at each stage. For instance, the outer shield was painted with Teflon, which has a solar absorptivity of 0.14, with IR emissivity of 0.75, in order to reject the heat coming from the Sun. Please refer to Chui *et al*. (2010:634-635) for the characteristics of the coating materials used for each stage.

It is also very pertinent to cleverly select the materials for cable connections between the cooled cryogenic sensors and the readout electronics at the hotter part of the spacecraft, in

order to prevent any parasitic heat conduction from the spacecraft to the cold stage. The wiring materials employed by EPIC were the Manganin wires along the struts and the HTS wires from the optical bench towards the outer shield. In SPICA's case, the connections were also made of Manganin wires.

2.10.5.2 Soldering strategy

The effect of bad soldering on the cryogenic element has to be considered in this kind of mission. The presence of voids in soldered joints constitutes temperature distortion and this can affect heat sinking, as reported by Ciampolini, Ciappa, Malberti, Regli and Fichtner (1999:1115, 1116 & 1118). These voids come into being, either as a result of manufacturing error or repeated thermo-mechanical stresses. Hence, using the right choice of solder (like rosin core solder) and appropriately following the right soldering procedures, are very important, in order to prevent manufacturing errors that may lead to void creation in the junctions.

2.10.5.3 Deployment scheme

Although the materials used for the passive cooling are usually very light in weight, but they are usually very large. A mechanism to get them accommodated in the launch vehicle during the launch process is needed, due to the space constraints in the vehicle. This necessitates adequate deployment mechanism for the passive cooling set-up as soon as the satellite is inserted into orbit. This also helps to prevent the magnetic contamination (emanating from the satellite) from reaching the cooled sensor. The phenomenon of the magnetic field, B at distance, r from a current, I carrying conductor, can be employed in determining the optimal magnetometer position from the satellite bus, which also represents the separation distance of the cooler from the spacecraft. This is pictorially presented in Figure 2.31, using the following equation (Paul, 2004:95):

$$B = \frac{\mu_0 I}{2\pi r} a_\phi \tag{2.77}$$

Where,

$\mu_0 = 4\pi \text{ X } 10^{-7}$ H/m (permeability of free space)

a_ϕ = direction of vector

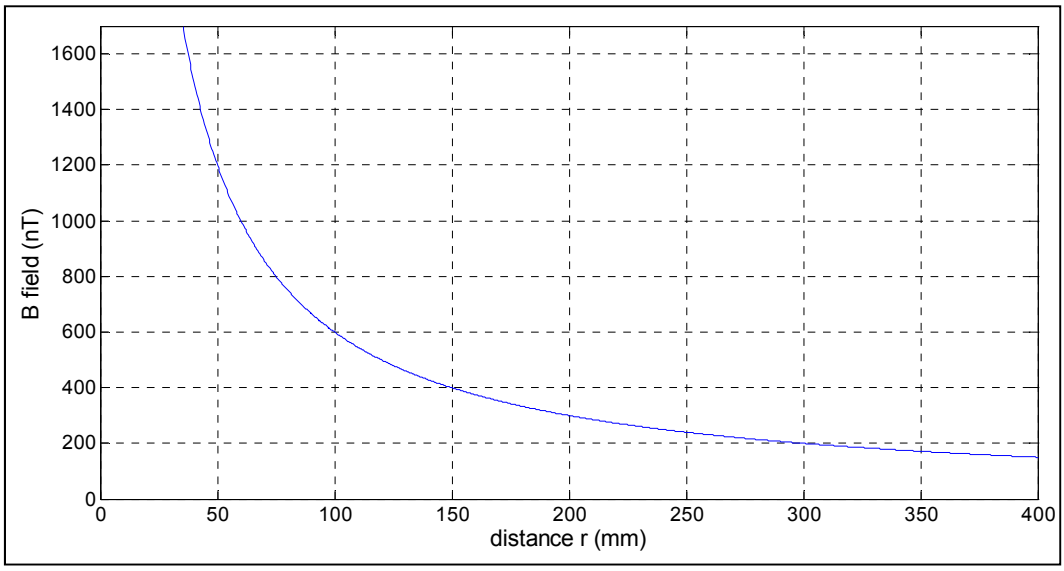

Figure 2.31: Relationship between the magnetic field interference and the magnetometer boom length

Here, the satellite's bus is represented with a current (0.3 A) carrying wire. Choosing a minimum boom length of 100 mm for the magnetometer, a corresponding 600 nT (i.e., 0.006 Gauss) field is inferred. Since the field of interest is the Earth's magnetic field which ranges between 0.3 and 0.6 Gauss (HyperPhysics, 2000a), this 100 mm boom length is therefore appropriate for the sensor. This is because the 0.006 Gauss will contribute little or no effect on the desired measurement.

2.10.6 Radiative cooling versus other cooling mechanisms

As earlier discussed in this section, the cooling system that uses cryostats (enclosed cryogenic fluid inside dewars), is referred to as passive cooling, while the cooling system involving the use of the conventional cryocoolers is regarded as mechanical cooling. Radiative cooling is regarded as passive, because it simply requires no energy for operation. It is simple, durable, reliable and cheaper to fabricate, as compared to the conventional cryocoolers and cryogenic dewars that have been popularly employed for space missions. By using several stages of radiators, the radiative cooling system overcomes the challenges of the high parasitic heat leakage usually experienced by the conventional cryocoolers, when long transfer tubes are involved (Figure 2.29). Since the radiators are made of very light weight materials, and the fact that there is no need for electrical input power, radiative cooling system can be said to have an upper edge over the present day mechanical cooling systems. This is a big concern in nanosatellite applications, because there may not be adequate electrical power to drive the so called mechanical coolers.

Moreover, Mechanical cryocoolers produce noise, vibration and electromagnetic contaminations that can affect the sensitivity of some sensors (like the SQUID) integrated

with them. These effects are due to the cryocooler's spinning cold finger, suspended by the flexure ring (on the compressor), and the mechanical vibration of the motor inside its compressor. See Figure 2.29 for better information on this. More so, some cryocoolers have some metallic components surrounding their cold fingers, and these are in turn subjected to vibrations, which generate eddy currents that constitute contaminations to the SQUID's sensitivity. If cryostats are to be used, liquid cryogens are not always easy to come by, and there is a need for well trained personnel that can safely deal with them. However, there are no such constraints in the case of radiative cooling (Carr, Macfarlane & Donaldson, 2003:245). Radiative cooling is also not faced with the need for cryogenic replenishing caused by evaporation, in the case of cryostats.

2.11 Verification schemes for in-orbit passive cooling

It is only in the orbit that a cryogenic passive cooling can be achieved, but the set-up has to be designed from the Earth (ground). One way of verifying the behaviour of such cooling system on Earth is to fabricate and test its scaled down prototype inside a thermal vacuum chamber (Hongyan, Deping, Weiyang & Zhong, 2005:449). Figure 2.32 pictorially demonstrates this kind of set-up, which includes a vacuum chamber, four stages of radiators, a black cold shield and the equipment to be cooled (i.e., the sensor).

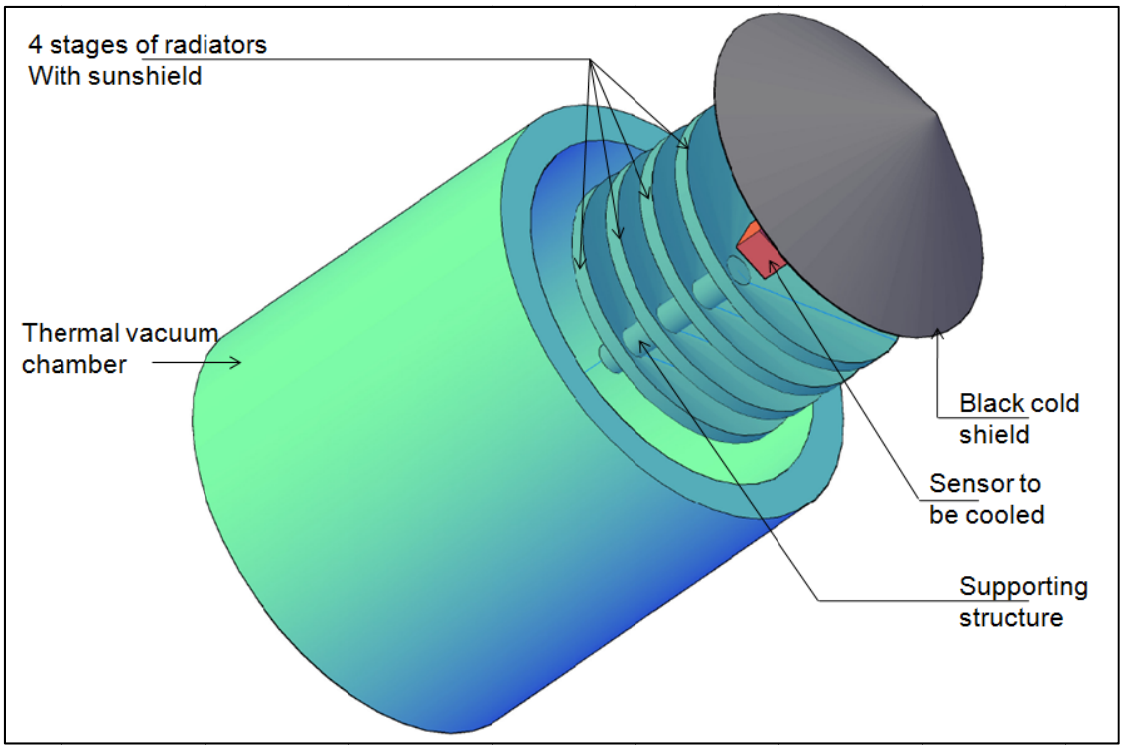

Figure 2.32: Operation of passive cooler in a vacuum chamber

As fully described in section 2.10.5.1, each radiator can be coated with a material of poor solar absorptivity, like Aluminised Kapton, with the first stage having an additional coating of

both poor solar absorptivity and good infrared emissivity, like Silver Teflon, to serve as a sunshield. The cold shield is made of a big black painted honeycomb board, cooled to a very low cryogenic temperature, to represent the cold deep space. After integrating everything together, the entire assembly is then placed in the vacuum chamber. The sensor gets cooled from this cold shield, and the radiators, with the sunshield, expel the heat from the sensor, and prevent any incoming heat from reaching it. In order to null the heat transfer by convection, the pressure inside the vacuum chamber should be maintained at about 5 X 10^{-5} Pa (Hongyan, *et al*., 2005:449). This is because there is no heat transfer through convection in the orbit. Heat contributions from the Sun and spacecraft bus can then be simulated using appropriate heating disks. The passive cooling system for Space Infrared Interferometric Telescope (SPIRIT), was verified based on this approach, but a Helium shroud was used in place of the black cold shield (DiPirro, Tuttle, Ollendorf, Mattern, Leisawitz, Jackson, Francis, Hait, Cleveland, & Muheim, D, 2007:6692 02-6692 03). FASTRAC (formation autonomy spacecraft with thrust, relative navigation, altitude, and crosslink) is another satellite, whose passive cooling system was validated by this method.

Another means of predicting a passive cooling system's behaviour in space is to employ the use of thermal analysis software packages. This may be necessary for reducing the cost, time and stress of building the physical system prototypes, as previously discussed. A number of software packages like the Solidworks, ABAQUS with MATLAB, SamcefField, NX CAD and Thermal Desktop, are capable of this task. Thermal Desktop was employed in this research, because of one of its modules called, RADCAD, which is application specific on radiative heat transfer. Work done with this package is fully described in the chapter four of this thesis.

2.12.1 Orbital analysis for heat rate calculation

In order to compute the solar flux contribution or heat rate due to the satellite's orbital environment, certain parameters, describing the orbit have to be known. The orbital inclination, *i*, the altitude, *h*, and eccentricity, ε are defined by the type of orbit to be used. The orbital beta angle, β which is the angle between the orbital plane and the solar vector is given by the arcsine of the dot product between the orbital vector, $\hat{O}$ and the solar vector, $\hat{S}$.

$$\beta = \sin^{-1}\left(\hat{O}.\hat{S}\right) \tag{2.78}$$

$\hat{O}$ and $\hat{S}$ are defined by the ecliptic solar longitude, Γ and the right ascension of the ascending node, Ω.

$$\hat{S} = \begin{bmatrix} \cos\Gamma \\ \sin\Gamma\cos\varepsilon \\ \cos\Gamma\sin\varepsilon \end{bmatrix} \tag{2.79}$$

$$\hat{O} = \begin{bmatrix} \sin\Omega \\ -\cos\Omega\sin i \\ \cos i \end{bmatrix} \tag{2.80}$$

Ω and Γ are both variables. Ω varies with time, while Γ varies between 0 and 180^0 as the Earth moves about the Sun. A Sun synchronous orbit of $i > 90^0$ has a nearly flat beta angle with respect to time, as demonstrated in (Longo & Rickman, 1995:13-21).

2.13 Shielding strategy and noise control

Since the SQUID magnetometer system is to be onboard the spacecraft, it is subjected to electromagnetic contaminations, in the form of stray RF and low frequency signals, emanating from the surrounding electronics in the spacecraft and various power cables. Low frequency contaminations are in the frequency range of DC to 10 kHz, while RF contamination is in the range of 10 kHz, upward. It is, therefore, pertinent to improvise for proper low and high frequency shielding mechanisms, so as to protect the integrity of the SQUID magnetometer system, or prevent it from losing its locked state.

Shielding basically entails the use of conducting panels to attenuate the penetration of incoming electromagnetic signals into the shielded system. Shielding capability, otherwise known as the absorptivity, A(dB), of the shielding material, is related to its penetration depth, δ(m), and the skin depth, t (m), by (Clarke & Braginski, 2004:273):

$$A = 8.686\, t / \delta \tag{2.81}$$

This implies that, shielding is much more effective, if the shielding material used is of very low penetration depth. The shielding material's reflectivity also helps in attenuating the electromagnetic interference (EMI) to the SQUID.

Using a superconducting shield can help in attaining high attenuation. The whole-body high T_c is an example of this (Clarke & Braginski, 2004:280). The equipment can further be surrounded by mu-metal, for additional attenuation. The SQUID's room temperature FLL electronics too are potential sources of EMI to the SQUID, thus a shielding material like Aluminium, can be used to enclose them, the inside of which may be covered with mu-metal. EMI contaminations that may result from the cable connecting the SQUID to its electronics

can be attenuated by using a twisted pair type of cables, coated with aluminium layer, with dedicated perforated holes for each pair passing through the FLL's enclosure. A very good example of a cable using this mechanism is the popular CAT-5 network cable used for communication in high frequency applications. The twisted pair mechanism primarily helps in cancelling out the coupling magnetic field entering into the cable and in reducing the effects of differential current noise in the cable. The two ends of the twisted cables can further be covered with mu-metal to improve their immunity against EMI.

2.14 Use of SQUID magnetometers for space weather applications

The function of a SQUID magnetometer aboard the satellite is to detect changes in the Earth's magnetic field. The reduction in the Earth's magnetic field, readable from the magnetometer, can then be used as a major indicator of space weather storms in the orbit.

2.14.1 Basics of Earth's magnetic field measurement

Since any space-borne satellite is always in a motion, orbiting the Earth, therefore, any magnetic sensor aboard the satellite experiences changes in its axes due to this motion. A significant aftermath of this is a motion-induced noise in the magnetometer, since it is rotating in the Earth's field. It is therefore desirable to be able to have a measured magnetic field that is motion independent.

To be able to measure the Earth's magnetic field, a form of tensor gradiometer system has to be constructed from a couple of magnetometers (vector or scalar), separated by a baseline. Here, the direction of sensing and the baselines between the magnetometers are fixed in the same reference. Difference between these magnetometers gives the output of the tensor gradiometer. This is extensively discussed in the following sub-section.

2.14.2 Tensor Gradiometer

As previously mentioned, a couple of two vector magnetometers can be combined to form a gradiometer. If the gradiometer is formed from a single sensor (like the SQUID), it is termed an intrinsic gradiometer. This type is usually achieved by coupling two pick-up loops in a flux transformer in parallel or in series. The series-coupled types are preferable for airborne missions, due to the large shielding current that may flow in the parallel-coupled types. The gradiometer is called a configured gradiometer, if it is formed from a set of magnetometers. Perfect linearity experienced in the intrinsic types, for low frequency applications, makes the configured types to be inferior to them. One big problem that may arise in the intrinsic gradiometers is the poor balance in the pick-up loops, if they are wire-wound. This is experienced in the case of LTS magnetometers. It is, however, not so, in the case of HTS

magnetometers, because the loops are formed from photolithography, which makes them highly balanced.

According to Clarke and Braginski (2005:488), there are only five magnetic gradients in free space. For a 5-axis gradiometer, it is possible to represent the independent gradients by a 2-dimensional structure, $G_{i,j}$. An example is given by (2.82) in the form of the magnetic gradient components $\partial B_x/\partial x$, $\partial B_y/\partial y$ and $\partial B_z/\partial z$.

$$G_{i,j} = \begin{pmatrix} \frac{\partial B_x}{\partial x} & \frac{\partial B_y}{\partial y} & \frac{\partial B_z}{\partial z} \\ - & \frac{\partial B_y}{\partial y} & \frac{dB_z}{\partial z} \\ - & - & - \\ & & \end{pmatrix} \tag{2.82}$$

If a magnetometer can measure the on-axis components at $i = j$ (i.e., $G_{i,j}$), then it is referred to as an axial gradiometer, but regarded as a planar gradiometer, if it measures the off-axis components at $i \neq j$. LTS SQUIDs can be configured to measure both, while HTS SQUIDs, which can only easily measure the off-axis components, can be made axial, by mounting them at 45^0 to the mounting frame basis.

2.15 Space radiation

Space borne equipments are subjected to a lot of electromagnetic radiations, which can affect their functionalities and durability. It is therefore necessary to prove that they are space hardened before they can be placed in the orbit. Two types of radiation tests can be carried out on any space-borne component. One of this is the total ionising dose (TID) test, administered in form of rad or Grey (*Gy*), which is for determining the radiation dose tolerance of the equipment under test (EUT). The second type is the single event effect (SEE) test, administered in form of Mev cm2/mg, which is for determining the susceptibility of the EUT to heavy ions radiation. The procedures for carrying out these tests are as depicted in Figure 2.33. Table 2.1 contains some investigated radiation tests carried out on some magnetometers meant for space applications. Some of these specifications are used for about five-year interplanetary missions (Nguyen, Persson & Thornell, 2010). According to Barnad and Steyn (2007), for adequately shielded components, a TID of 10 krad is expected at LEO, for a lifetime of five years. Hence, a TID of 5 krad (or 50 *Gy*) is considered more than suitable for any unshielded COTS in the LEO orbit, for a total life time of about 2 years. With a minimum safety factor of 2, a 100 *Gy* can be considered for design limit.

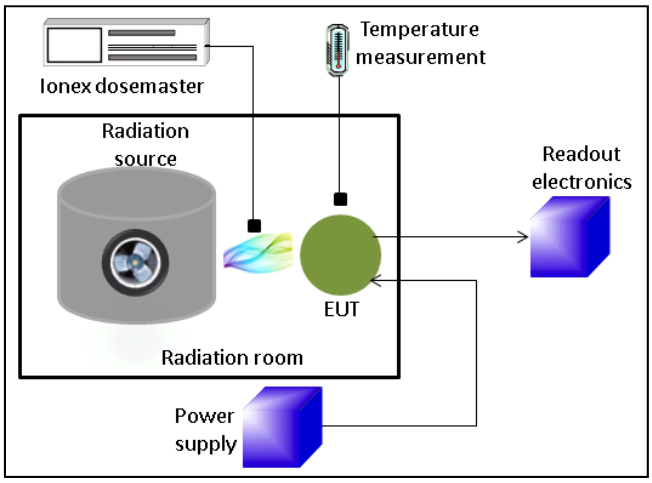

Figure 2.33: Equipment set-up for radiation tests

Table 2.1: Some radiation tests for space-based magnetometers

Sensor	Mission	TID Test	SEE test	TID Test Results	SEE Test Results	References
Tunnelling magnetometer	A nanosat mission not yet specified	100 krad	N/A	No noticeable damage after the test	N/A	Nguyen, Persson & Thornell, 2010
CS5508 A/D converter for a Flux gate magnetometer	International ROSETTA Mission	10 krad	Linear energy transfer (LET) of 42 Mev. Cm2/mg	TID tolerance of 27 krad (low dose), and 20 krad (high dose), strong current consumption, good tendency to recover	High susceptibility to heavy ion radiation	Omerbegoviae, 1999
MFA 102 (Flux gate magnetometer)	N/A	1 cycle of 129.5 krad at 98 rad/min	N/A	Full functionality before and after the test	N/A	Magnes, *et al.*, 2006
MFA 104 (Flux gate magnetometer)	N/A	2 cycles of 261.5 krad at 93 rad/min	N/A	Full functionality before and after the test	N/A	Magnes, *et al.*, 2006
MFA 112 (Flux gate magnetometer)	N/A	2 cycles of 144.2 krad at 56 rad/min	N/A	Full functionality before and after the test	N/A	Magnes, *et al.*, 2006
MFA 109 (Flux gate magnetometer)	N/A	3 cycles of 86.6 krad at 90 rad/min	N/A	Full functionality before and after the test	N/A	Magnes, *et Al.*, 2006
MFA 110 (Flux gate magnetometer)	N/A	N/A	19 cycles of LET range 2.97 - 34 Mev cm2/mg at 4 different ion spices	N/A	Full functionality after the irradiation. No permanent damage	Magnes, *et al.*, 2006
MFA 118 (Flux gate magnetometer)	N/A	N/A	19 cycles of LET range 2.97 - 34 Mev cm2/mg at 4 different ion spices	N/A	Full functionality after the irradiation. No permanent damage	Magnes, *et al.*, 2006
Flux gate magnetometer	N/A	360 krad	N/A	Full functionality before and after the test	N/A	Billingsley Aerospace
Spacemag (Flux gate sensor)	N/A	100 krad	N/A	Full functionality before and after the test	N/A	Bartinton Instruments

2.16 Conclusion

A comprehensive explanation of the basics of the SQUID magnetometer and its operation requirement were presented in this chapter. These basics serve the foundational knowledge needed in both the simulations and experimental work carried out in this research. The theory of superconductivity is needed in order to understand the behaviours of Josephson junctions (JJs), which are the main constituents of a DC SQUID magnetometer. The hysteresis in the $V - I$ characteristic of a basic JJ is dictated by the composition of the junction itself, which can either be RCSJ or RSJ. A high T_c SQUID is mainly RSJ with minimal hysteresis in its $V - I$ characteristic. The presence of external magnetic fields in the SQUID's loop tends to affect the SQUID's $V - I$ characteristic. The mathematical expressions describing this effect were discussed in this chapter. These form the foundational information needed in modelling the SQUID magnetometer. The basics and the significance of the SQUID's bias and read-out electronics were also discussed. Since the bare SQUID's $V - \Phi$ characteristic is sinusoidal, there is need for a read-out electronic that is capable of linearising the SQUID's output. A cryogenic environment is the primary requirement for operating the SQUID magnetometer. The foundational knowledge on how to achieve this, either via mechanical, passive or hybrid method was described, with references to various space missions that have used each of the methods. How the magnetometer can be used for satellite space weather applications were as well discussed. The magnetometer needs to be deployed at a distance from the satellite, in order to prevent the EMI emanating from the satellite bus. How to determine the space radiation tolerance capability of the space borne sensor was as well discussed.

CHAPTER THREE

MODELLING AND SIMULATIONS OF A DC SQUID MAGNETOMETER

3.1 Introduction

It is pertinent to predict the SQUID magnetometer's behaviour via simulations, before subjecting them to real life experiments, because they are quite expensive to acquire, and can be easily damaged during test analysis. To achieve this, PSIM was used to model and simulate a Josephson junction (JJ), using the basic equation that describes the effective current through it. A DC SQUID magnetometer, which is composed of two JJs, was then modelled and simulated using the modelled JJ. Thermal noise simulation was also included, to observe its effects on the magnetometer's output. The modulating property, and the voltage-current (V – I) characteristics of a resistively shunted Josephson junction (RSJ), discussed in section 2.5.1, were observed, together with the V – I characteristic, and the V – Φ characteristic of the DC SQUID magnetometer. The M1000 DC SQUID magnetometer was used as a platform for the simulations done. Appendix A, extracted from the M1000 SQUID datasheet (Star Cryoelectronics, 2011:2), contains all the sensor's specifications used. A directly coupled flux locked loop circuit was later included in the PSIM simulations, in order to amplify and linearise the SQUID's output, which is usually sinusoidal. For efficient simulation speed, physical circuit components like resistors and capacitors could not be used to build some of the sub-systems (especially the integrator) in the PSIM simulations. Hence, the outputs of the simulated DC SQUID and that of the FLL were later validated, using the Simulink toolbox from MATLAB software. This helps to observe the behaviour of some of these physical circuit components. For better axis formatting, all the figures obtained from the simulations were exported to, and plotted with MATLAB. Appendix B contains all the MATLAB codes used for the plotting.

3.2 PSIM simulations

PSIM is a fast and user friendly power electronics and motor control simulation package from Powersim Inc. It consists of three entities - SIMCAD (for circuit schematic editor), PSIM (for simulation), and SIMVIEW (for waveform processing) (Powersim, 2001:1-1). PSIM version 9 was used, due to its fast simulation capability, together with an added advantage of being able to simulate the thermal noise effects on the JJ, by using its random current source block. This feature is not present in the Spice software used by van Zyl (2010).

3.2.1 RSJ model

The RSJ model presented in Figure 2.9 (from section 2.5.1) was used for the JJ simulations contained in this chapter. Equation (2.14) was used to analyse the effective current through this RSJ model. Please refer to section 2.5.1 for the derivation.

3.2.2 The Josephson junction simulation

Equations (2.12) and (2.14) were used in the Josephson junction simulation. The voltage, v across the junction can be compared with the voltage across an inductor, or the current through a capacitor, with the phase, δ being the inductor's current, or the capacitor's voltage.

i.e,

$$v = \frac{\Phi_0}{2\pi}\frac{d\delta}{dt} \Leftrightarrow v_{ind} = L\frac{di_{ind}}{dt} \tag{3.1}$$

Or,

$$v = \frac{\Phi_0}{2\pi}\frac{d\delta}{dt} \Leftrightarrow i_{cap} = C\frac{dv_{cap}}{dt} \tag{3.2}$$

Equation (3.2) was modelled using a voltage-controlled current source, as displayed in Figure 3.1. The voltage across the capacitor is used as the phase, δ, processed through a sine block, multiplied with the critical current, I_c (using a proportional block), and then used to control another voltage-controlled current source. This other current source, whose output represents the voltage across the JJ, is connected in parallel to the JJ's shunt resistor, $\boldsymbol{R_n}$. The voltage sensor is used to convert any signal at its input into voltage. The capacitance value is $C = \Phi_0 /2\pi$. According to the M100 datasheet, a typical critical current, I_c = 20 μA, and a junction shunt resistance, R_n = 6 Ω were used (Star Cryoelectronics, 2011:2). Details of these specifications are contained in Appendix A.

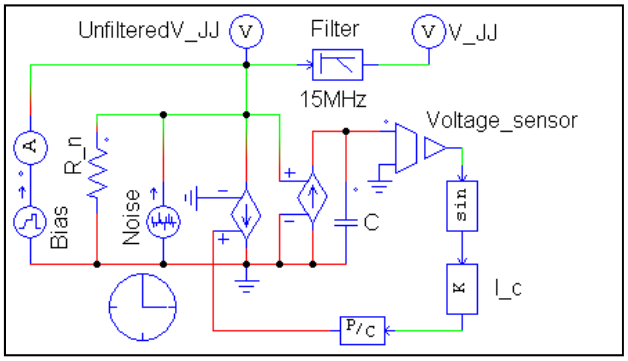

Figure 3.1: The PSIM model of a Josephson junction

Josephson junctions are prone to thermal noise - an intrinsic white noise generated in the JJ, due to the shunt resistance, R_n, as discussed in section 2.6.1. This noise was modelled in parallel with the Josephson junction's shunt resistor, R_n (Figure 3.1), by using a random current source, whose peak-to-peak value is the rms (root mean square) value of the theoretical noise current given by:

$$i_{rms} = \sqrt{4K_B TB / R_n} \tag{3.3}$$

Where,

k_B = 1.38 X 10^{-23} J/K (Boltzmann's constant)

T = the operating temperature (77 K for M1000 SQUID)

B = the noise bandwidth (in Hz)

3.2.3 Results and discussion of the Josephson junction simulation

Figure 3.2 reveals the oscillation of the Josephson junction, by using various constant bias currents, I_b = 1.1 I_c, 2.2 I_c, 4.4 I_c, and 8.8 I_c. The curves show that the amplitudes are all the same, representing the characteristic voltage, V_c of the junction, while the oscillation frequencies, together with the offset voltages, (representing the DC voltages) are dependent on the bias current magnitudes (normalised). This affirms the interpretation of equation (2.15), which describes the oscillating nature of the junction.

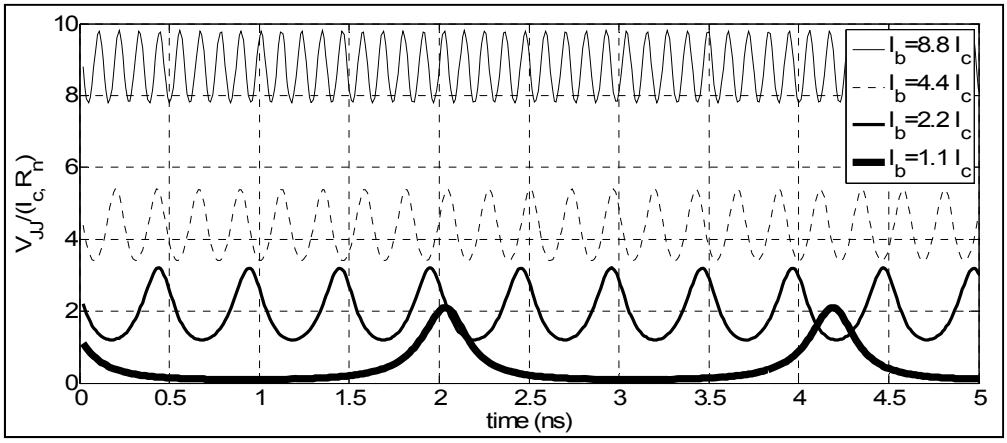

Figure 3.2: The simulated Josephson junction's oscillation at steady bias currents (I_b = 1.1 I_c, 2.2 I_c, 4.4 I_c and 8.8 I_c)

In order to examine the $V - I$ characteristics of the JJ, the bias current, I_b was swept between -3 I_c and 3 I_c. The result of the JJ's $V - I$ characteristic in Figure 3.3 (a) shows the effect of the voltage oscillation, which makes it hard in predicting its behaviour. The junction's output was time-averaged, using a 15 MHz low pass filter (as shown in Figure 3.1), in order to remove the Josephson oscillation. Figure 3.3 (b) shows the output, after processing it through the filter. The flat regions in these Figures represent the junction's critical current (i.e, -I_c and I_c). When the bias current, I_b is less than I_c, there is no voltage across the junction. All the current here are completely absorbed by the JJ, until the bias current exceeds I_c. Thereafter, the junction's time-averaged voltage rises to V_c from 0 V. This affirms the behaviour of a typical JJ, as discussed in sections 2.5.1 and 2.5.3.

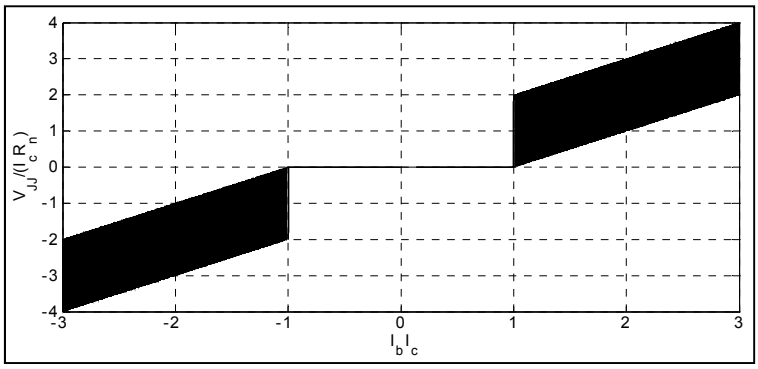

(a)

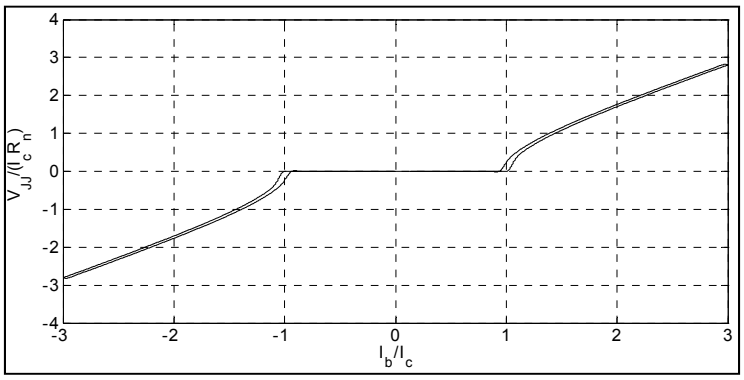

(b)

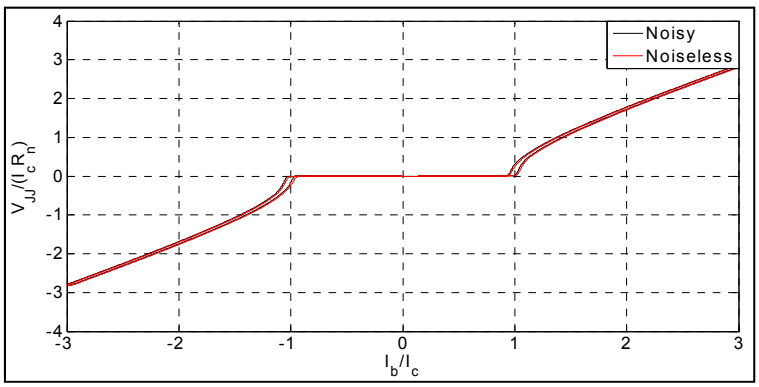

(c)

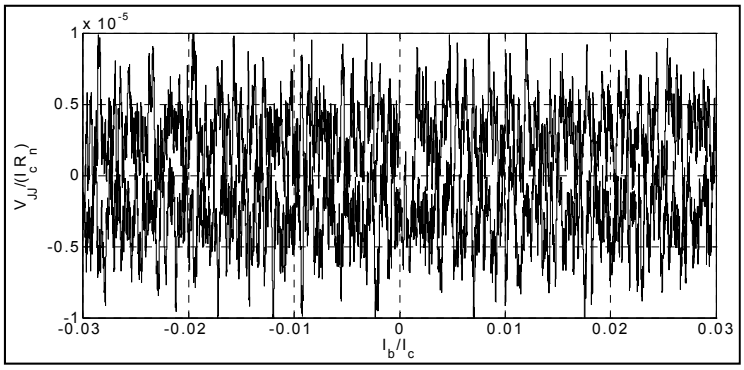

(d)

Figure 3.3: PSIM simulation of the Josephson junction, showing the (a) unfiltered *V - I* characteristic, (b) filtered *V - I* characteristic, (c) superimposed *V - I* characteristic, both with and without noise (d) distorted *V - I* characteristics, when the bias current was swept between – 0.03 I_c and 0.03 I_c

The effect of thermal noise is also presented in Figure 3.3 (c). The $V - I$ characteristics without noise and the one with an added 500 MHz bandwidth noise are both superimposed. The noise effect was insignificant, because the input current sweep is large. The noise effect becomes significant, if the bias current is less than the rms value of the thermal noise, as presented in Figure 3.3 (d). In this simulation, the rms current is I_{rms} = 0.59515 μA, according to equation (3.3). The $V - I$ characteristic, with the bias current swept between -0.03 I_c and 0.03 I_c, became distorted. In fact, no JJ voltage is observable in the output, other than the noise contribution.

3.2.4 The DC SQUID model

Since a DC SQUID magnetometer is formed from the combination of two RSJs, it was modelled by combining two models of the JJ, as Figure 2.14 of section 2.5.3 depicts. A SQUID with negligible inductance, L_{SQ} (as equation (2.6) suggests), is considered for this modelling. Equation (2.31) was used to analyse this model, which is similar to equation (2.14) for the JJ. Please see section 2.5.3 for the derivation.

3.2.5 DC SQUID simulations

Just like the case of the JJ simulation, equation (2.31) is also synonymous to equation (3.2). This was modelled in PSIM, using a voltage-controlled current source. The flux input to the SQUID, and the π (i.e., 3.142) parameter, according to equation (2.31), were modelled using DC voltage blocks, multiplied using a multiplication block, and then processed through a cosine block, before finally coupling it to the capacitor's voltage. See Figure 3.4 for the PSIM model.

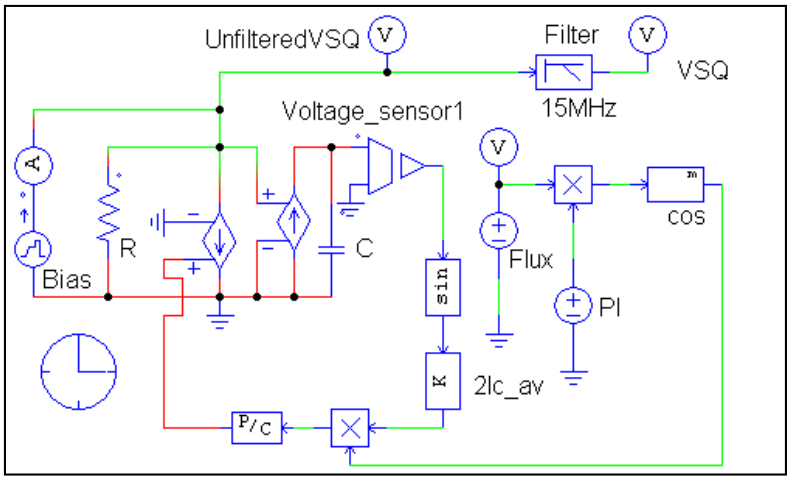

Figure 3.4: The PSIM model of a dc SQUID magnetometer

3.2.6 Results and discussion of the DC SQUID simulation

Considering the fact that the Earth's magnetic field variation is of a small frequency range and amplitude, is of great importance to consider how the SQUID magnetometer responds to a small input flux. Figure 3.5 (a) shows the DC SQUID's response to a swept input of ± 0.5 Φ_0. A sinusoidal response can be observed, with a period of 1 Φ_0. To consider its response to a large flux, a sinusoidal input flux pattern, with $3\,\Phi_0$ amplitude and $5\,\mathrm{kHz}$ frequency, was used as the input flux to the SQUID, and the corresponding output $V - \Phi$ response (without the FLL) is also sinusoidal, as displayed in Figure 3.5 (b). A sinusoidal response was as well obtained, when the input flux was swept between -3 Φ_0 and 3 Φ_0, as seen in Figure 3.5 (c). The outputs from these three Figures establish that the SQUID's behaviour is always sinusoidal, regardless of what magnitude or pattern of change the sensed flux has. It is, however, difficult to know the magnitude of the sensed flux from this output. This therefore calls for the use of a FLL circuit for linearising the SQUID's output. A bias current, I_b of 3.4 $I_{c,av}$ was used to bias the SQUID. This allows the SQUID's response to be fully sinusoidal, thereby making it easy to be linearised.

As it can be observed from Figure 3.5, the SQUID's response appears relatively linear at every interval between $n\Phi_0$ and 0.5 $n\Phi_0$. Midway between these regions, is (2 n + 1) $\Phi_0/4$. This is known as the SQUID's operating point, where the response seems perfectly linear. It is necessary to apply a bias flux of such value to the SQUID, so as to be able to sense small changes, $\delta\Phi$ in the external flux. The slope of a tangent to this point gives the maximum $V - \Phi$ transfer coefficient, which represents the SQUID's sensitivity, V_Φ. In this case, V_Φ = 779.2 mV_c/Φ_0, where $V_c = I_{c,av} R_n$. This sensitivity is needed to compute the SQUID's gain, V_{SQ}.

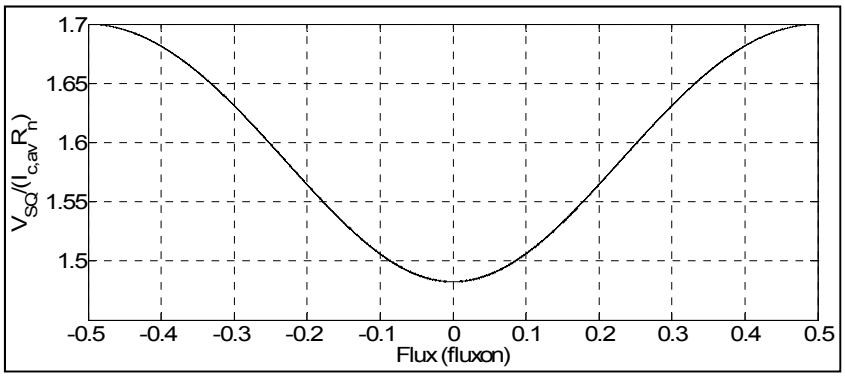

(a)

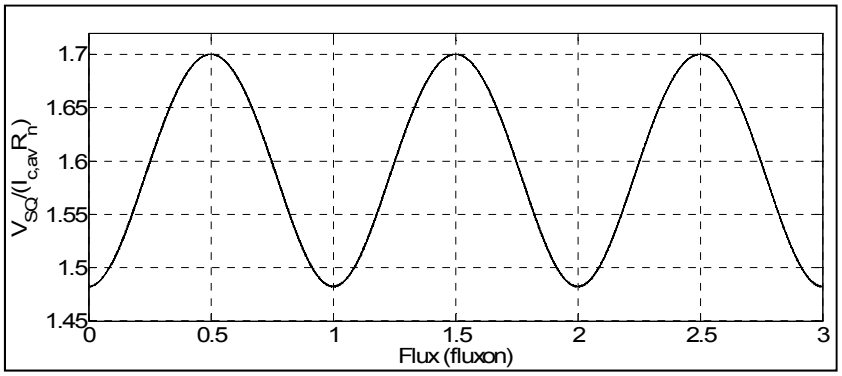

(b)

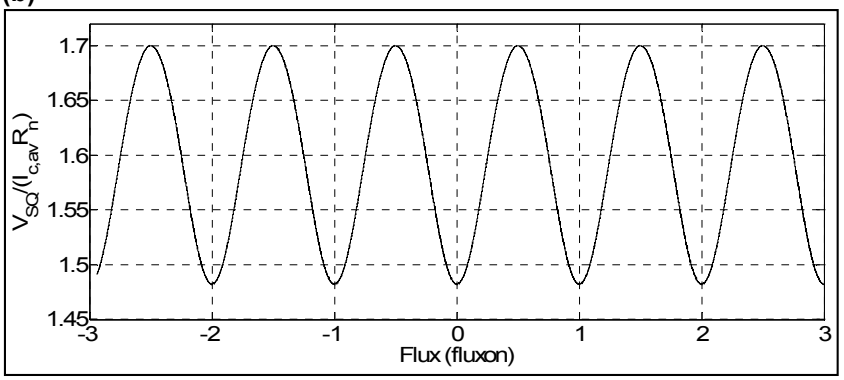

(c)

Figure 3.5: The simulated DC SQUID output voltage-flux response with a (a) swept input of ± 0.5 Φ_0 (b) 3 Φ_0 sinusoidal input at 5 kHz and (c) swept input of ± 3 Φ_0

Figure 3.6 (a) shows the *V* - *I* characteristic of the simulated SQUID, in the absence of any external magnetic flux, when the bias current was swept between – 3.4 $I_{c,av}$ and 3.4 $I_{c,av}$. This result looks like that of the simulated JJ (shown in Figure 3.3), except that the flat region is 2 $I_{c,av}$, instead of 1 $I_{c,av}$. This shows that the SQUID actually contains two JJs. With a $500\ \mathrm{MHz}$ bandwidth noise introduced into the SQUID, its effect is insignificant, as clearly shown in Figure 3.6 (b). This is simply because the current sweep is larger than the rms value of the

thermal noise. It is therefore strongly suggested that the SQUID bias current be reasonably high, so as to suppress the thermal noise effect in the JJs.

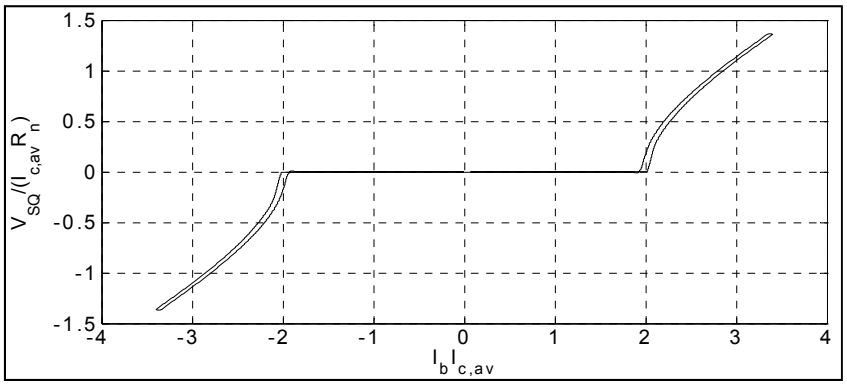

(a)

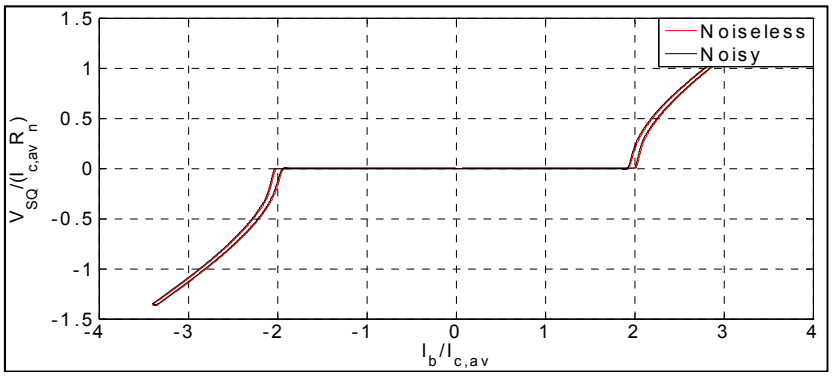

(b)

Figure 3.6: Simulated SQUID's *V - I* characteristics at 0 Φ_0 input flux (a) with no noise introduced (b) with a 500 MHz bandwidth noise superimposed

Magnetic fluxes of 0 Φ_0, 0.25 Φ_0, and 1 Φ_0 were applied to the SQUID, in order to show how the maximum critical current (the flat region) is affected by the sensed field. Figure 3.7 shows the superimposed responses. The flat response is seen to reduce from the maximum value, at 0 Φ_0 (the bold line on Figure 3.7), downwards, as the input flux increases, and increases back to the maximum, at 1 Φ_0 (the bold line on the Figure). This affirms the expected

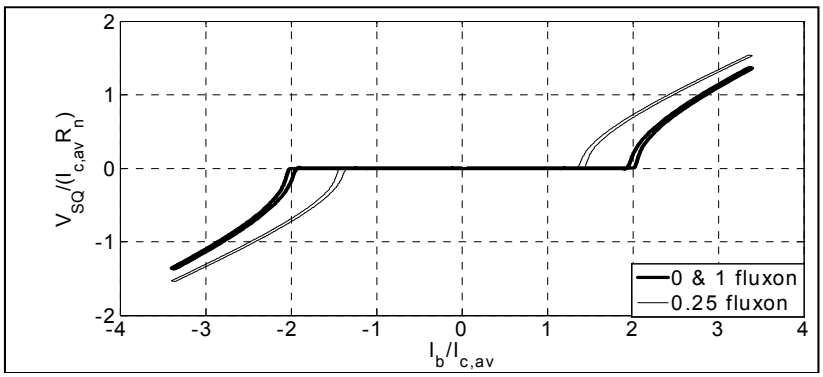

Figure 3.7: Superimposed SQUID's *V - I* characteristics at input fluxes of 0 Φ_0 , 0.25 Φ_0 and 1 Φ_0

behaviour of the SQUID, when it senses external magnetic fields, as previously discussed in section 2.5.3.

Figure 3.8 shows the SQUID's response, when a bias current, I_b of $15\ \mu A$ was used to bias it. No voltage was seen across the SQUID, since the bias current is less than the critical junction current. At this state, the entire current applied to the SQUID only accumulates in the superconducting arms of the JJs. This behaviour also confirms the SQUID's attribute discussed in section 2.5.3.

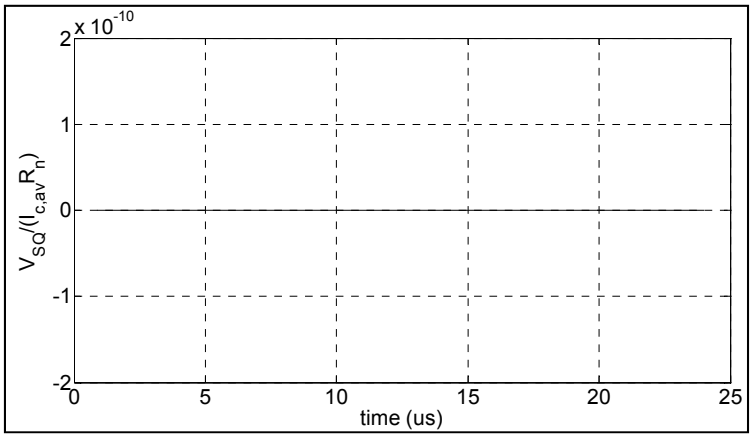

Figure 3.8: The simulated SQUID's voltage response at bias current, I_b =15 µA

3.2.7 The flux locked loop model

One major disadvantage of using the direct output from the SQUID is the difficulty in estimating the sensed flux, because it is periodical with respect to the sensed flux, as discovered in Figure 3.5 (a) through Figure 3.5 (c). Hence there is a need for a flux locked loop (FLL) circuit at the SQUID's output, to linearise its output so as to be able to estimate the value of the sensed signal, and to achieve increased dynamic range. Figure 2.3 is a schematic that describes the mode of operation of a typical FLL electronics, but for simplicity, the basic layout of the FLL is simplified presented in Figure 3.9. This comprises of a preamplifier, integrator and a feedback network, with gain, G_{fb}, to the SQUID. The function of the preamplifier is to bring the SQUID's gain to unity. This means the preamplifier gain, A_{Preamp} is the reciprocal of the SQUID's gain, G_{SQ}. The integrator integrates the signal, and generates an output, which adds fluxes to the SQUID, in order to null the integrator's input. In this case, the SQUID is said to be locked.

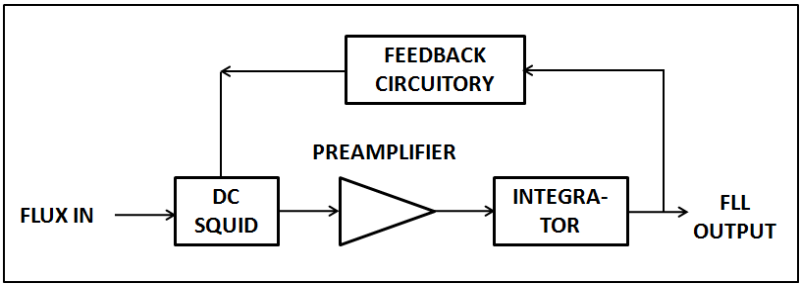

Figure 3.9: The flux locked loop layout

3.2.8 Flux locked loop simulations

The FLL circuit was modelled in PSIM, and coupled to the output of the previously modelled DC SQUID, as shown in the right hand side of Figure 3.10. In order to speed up the simulation time, ideal PSIM blocks were used to represent the preamplifier, integrator and the feedback gain. The physical electronics components needed, for the FLL, will later be examined in the Simulink simulation section.

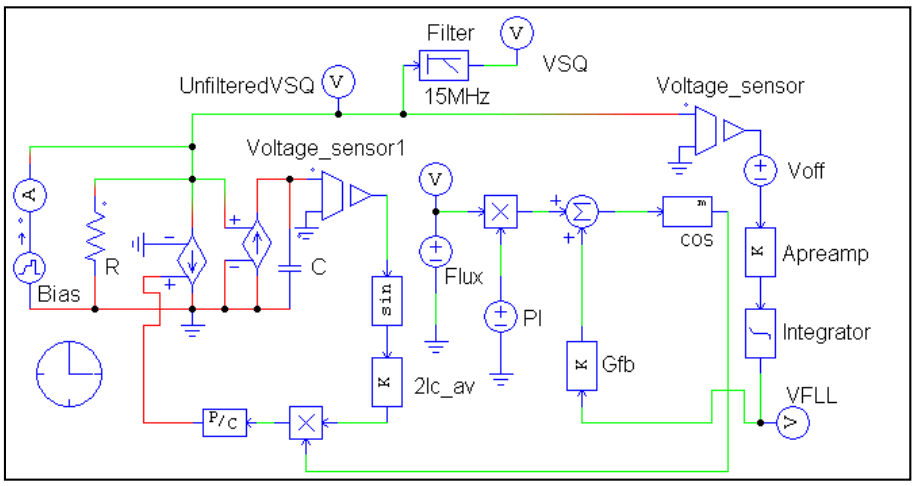

Figure 3.10: The PSIM model of the flux locked loop

A flux range of 750 Φ_0 was considered for the model. This implies a dynamic range, Φ_{dyn} of ± 375 Φ_0. A supply rail of ± 5 V was used in this simulation. This value is supported by most op-amps. The integrator's maximum voltage output can then be fixed as $V_{Int,max}$ = ± 5V. From equation (2.59), the transfer coefficient of the feedback circuitry, otherwise termed the feedback gain, was calculated as:

$$G_f = \frac{M_f}{R_f} = \frac{\Phi_{dyn}}{V_{Int,\max}} = 75\,\Phi_0 / \mathrm{V}$$

Where,

M_f = the feedback coil's mutual inductance

R_f = the feedback resistor

This yields a SQUID gain of 0.0037 obtained from equation (2.50), where V_Φ has already been determined in section 3.2.6, as V_Φ = 413.8 m V_c /Φ. An integrator with a unity gain frequency, f_1 = 36 MHz was considered for this simulation. This yields an integrator with time constant, 268.85 µs. Usually, f_1 is determined from the gain bandwidth product of the integrator's op-amp. This shall be later discussed in the Simulink simulation section (section 3.3.3). The pre-amplifier's gain, A_{Preamp} was calculated to be 270.27, using equation (2.64). As established in section 2.8, a bias current, I_b of 3.4 $I_{c,av}$ was used for this FLL simulation in order to obtain a full sinusoidal direct SQUID output, suitable for linearisation. The DC offset voltage generated by the bias current, I_b has to be compensated for, in the FLL circuit. This value is measurable from the bare SQUID output, and it is represented by the V_{off} block on Figure 3.10. In this simulation, V_{off} = 196.02 µV. The input to the feedback loop may not necessarily come from the low pass filter, since the preamplifier and the integrator act as low pass filters. This is because, in reality, the electronics are limited in terms of cut off frequencies, which makes the signals to be filtered, thereby neglecting the need for any low pass filter.

3.2.9 Results and discussion of the flux locked loop simulation

The modelled FLL was tested, by linearly sweeping the input flux from -1 Φ_0 to 1 Φ_0, as shown in the upper part of Figure 3.11 (a). In order to clearly display the FLL's linearising capability, the direct V - Φ response from the bare SQUID (i.e., before coupling it to the FLL circuit), has been represented in the lower part of Figure 3.11 (a). The resulting linearised FLL's output voltage, with respect to the simulation time, is as displayed in the upper part of Figure 3.11 (b), with a linear slope of -0.83 mV/µs, which represents the slew rate. The lower part of Figure 3.11 (b) shows the FLL's V - Φ response, with a linear slope of -250.8 mV/Φ_0, which is the voltage sensitivity. This linearising capability makes it very easy to know the voltage value that corresponds to any external flux.

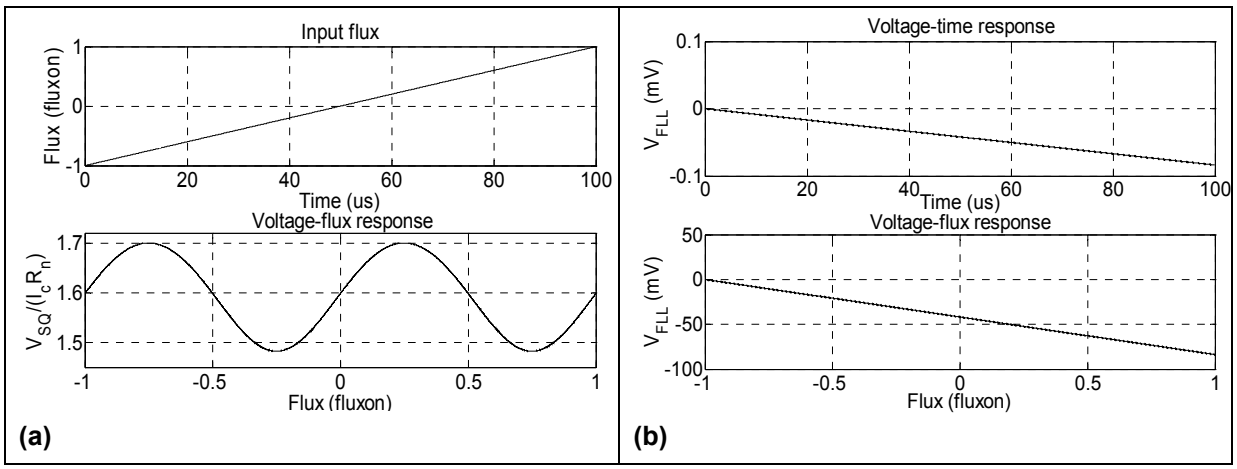

Figure 3.11: The SQUID's voltage response to a swept input flux from – 1 Φ_0 to 1 Φ_0 (a) without the flux locked loop (b) with the flux locked loop

The linearity in the FLL's output is relative to the pattern of change in the input flux. This is demonstrated by using non-linear input fluxes to the SQUID. Figure 3.12 shows the FLL's response to a swept input flux from -1.25 Φ_0 to 0.75 Φ_0 over 50 ns, and then to -1.25 Φ_0 over 50 ns.

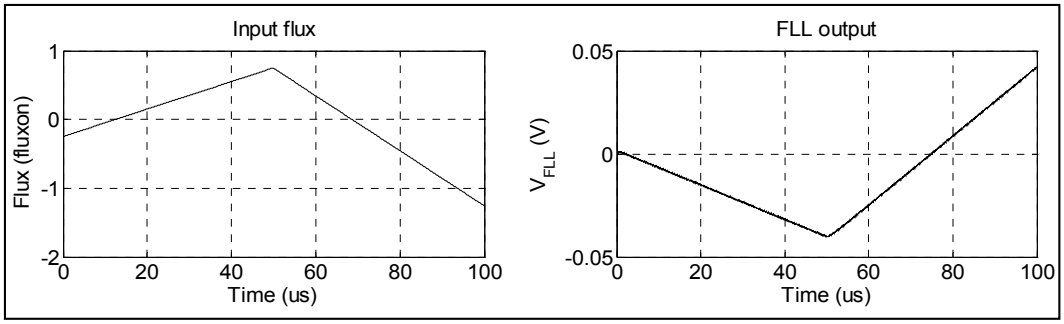

Figure 3.12: The flux locked loop's voltage response to a swept input flux from -1.25 Φ_0 to 0.75 Φ_0, and later to -1.25 Φ_0

By applying a sinusoidal input flux of amplitude, 0.5 Φ_0, at 10 kHz the resulting signal from the FLL is as well a signal with 10 kHz frequency, as displayed in Figure 3.13. This clearly shows that the FLL is indeed a linear *V* - Φ device for the SQUID magnetometer. The use of the FLL helps to maintain the flux in the SQUID at $\Phi_0/4$ (i.e., the working point).

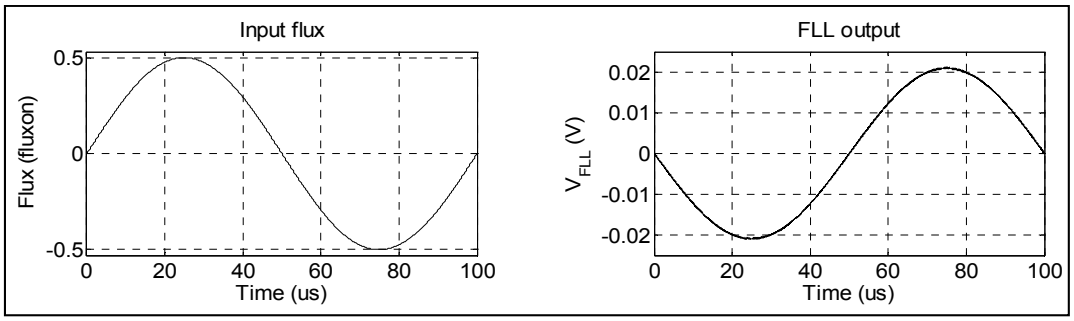

Figure 3.13: The flux locked loop's voltage response to a sinusoidal input flux of amplitude, 0.5 Φ_0 at 10 kHz

3.3 MATLAB-Simulink simulations

Simulink is a companion toolbox in MATLAB for dynamic systems simulations. It is usually called from the MATLAB environment, when the model is to be designed and simulated (Beucher & Weeks, 2006:136). This software was considered in order to observe the behavior of the physical circuit components (like the op-amps, resistors and capacitors) needed in the construction of the readout electronics. These physical components are accessible from the Simscape toolbox in the Simulink library. The Simulink simulations also help to validate the results obtained from the PSIM simulations described in section 3.2.

3.3.1 DC SQUID simulations

Equation (2.33), which describes the SQUID's time-averaged output voltage, relative to the sensed flux, Φ was used to model the SQUID subsystem block. Since the time-averaged voltage equation is used, it is therefore not necessary to average the SQUID's output through a low pass filter, as done in the PSIM simulations. The same parameters used in section 3.2 were also used for this simulation, and the Simulink model, using MATLAB version R2009b, is as shown in Figure 3.14. The internal constituent of the SQUID subsystem block is shown in Appendix D.

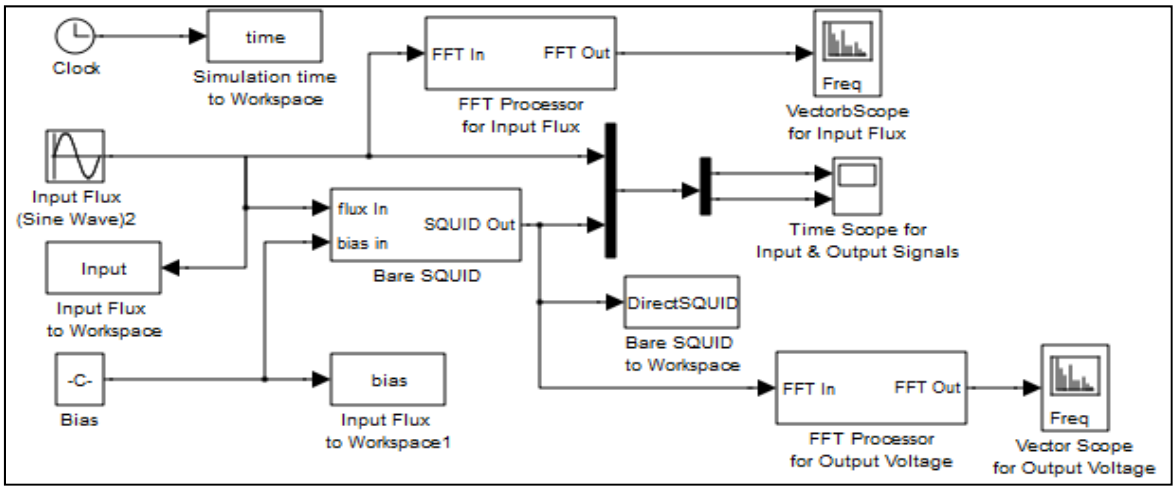

Figure 3.14: The Simulink model of a resistively shunted junction DC SQUID

3.3.2 Results and discussion of the DC SQUID simulation

Figure 3.15 (a) shows the DC SQUID's response to an input flux of 0.5 Φ_0. Figure 3.15 (b) presents the resulting V - Φ characteristic, when a sinusoidal input flux of 3 Φ_0 amplitude, at 5 kHz was used as an input. The output is sinusoidal, with the same maximum peak, just like the output displayed in Figure 3.5. The minimum peaks from Figure 3.5 are affected by the filtering effect of the low pass filter. Both Figure 3.5 and Figure 3.15 have the same minimum peaks, if the cut-off frequency of the filter is made higher, but some level of noise will feature. Figure 3.15 (c) is the resulting sinusoidal response, using a swept input from -3 Φ_0 to 3 Φ_0.

These three outputs validate the PSIM simulations described in section 3.2.6. Irrespective of the pattern of variation the sensed flux takes, the bare SQUID's output is always sinusoidal.

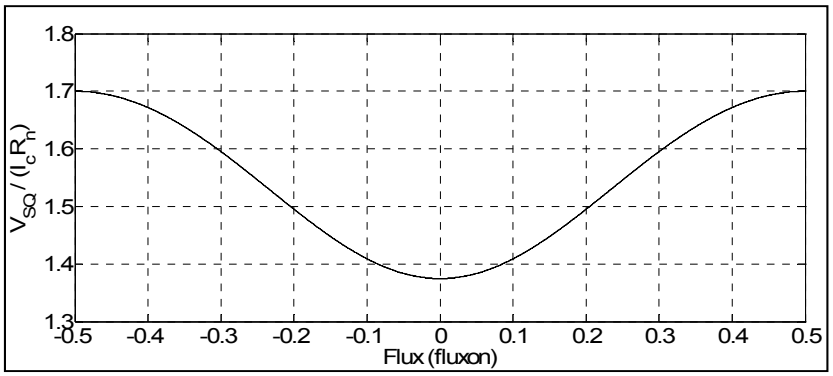

(a)

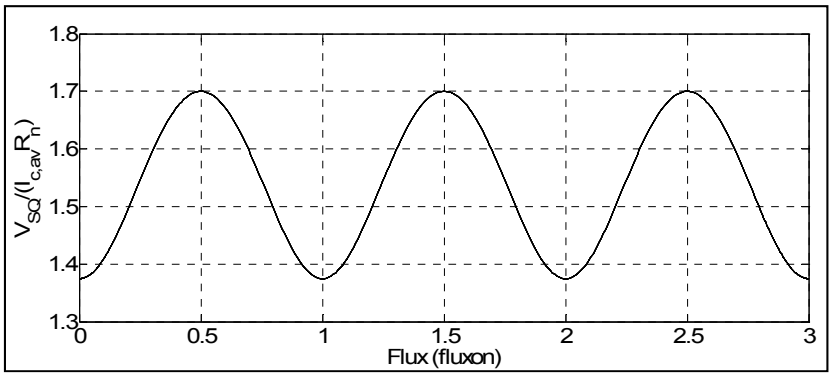

(b)

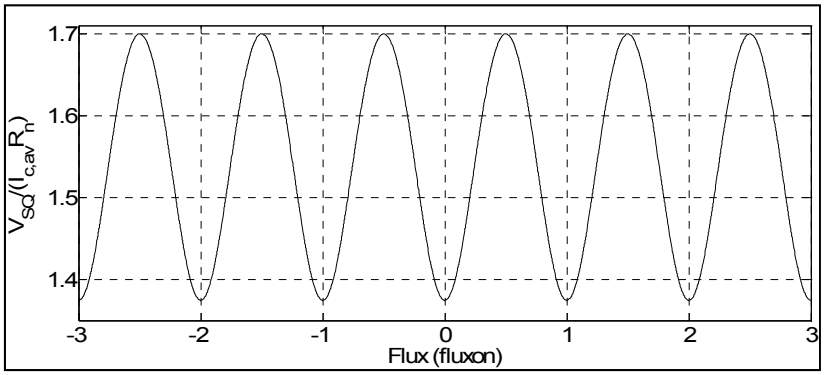

(c)

Figure 3.15: Simulated DC SQUID output voltage-flux response with a (a) swept input of ± 0.5 Φ_0 (b) 3 Φ_0 sinusoidal input at 5 kHzz $5\ \mathrm{kHz}$ and (c) swept input of ± 3 Φ_0

In order to observe its V - Φ_0 characteristics with respect to varying bias current, the bias current, I_b was swept over 2 $I_{c,av}$ through 5 $I_{c,av}$, with a step of 1 $I_{c,av}$. For this, a 3 Φ_0, 5kHz sinusoidal input flux was used throughout. The corresponding outputs are as displayed in Figure 3.16. This clearly points out its dependency on the bias current, I_b. It is obvious that the SQUID's output voltage resolution is limited to 1 Φ_0 (one fluxon).The output became fully sinusoidal at bias currents slightly higher than 2 $I_{c,av}$, and the whole output potential seem

nearly DC, with regression in its sinusoidal nature at very high bias currents. This makes it possible for the FLL to be able to linearise the SQUID's output response. Hence, beyond a bias current of 2 $I_{c,av}$, the SQUID's output voltage can be linearised by using a flux locked loop circuit.

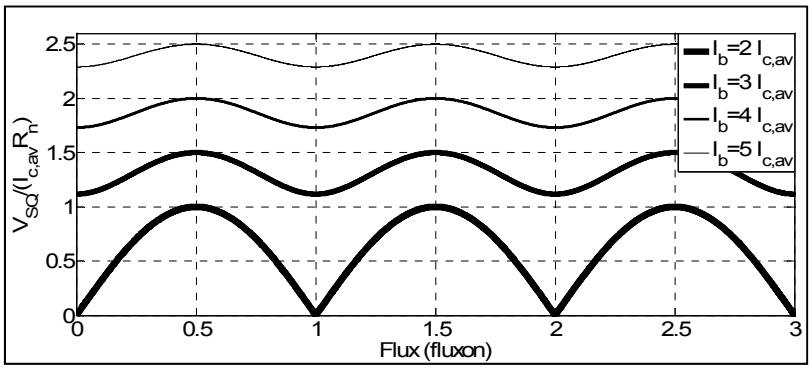

Figure 3.16: The *V* - Φ characteristics with respect to bias the currents, I_b = 2 $I_{c,av}$, 3 $I_{c,av}$, 4 $I_{c,av}$, 5 $I_{c,av}$

To further study the modulating nature of the direct SQUID output voltage, the simulation was done for input sinusoidal fluxes at various amplitudes and frequencies (1 Φ_0 at 5 Hz, 2 Φ_0 at 5 Hz and 2 Φ_0 at 15 Hz precisely). Figure 3.17 (a) through Figure 3.17 (c) presents the respective varying sinusoidal input and modulating output signals (in time and frequency domains). The frequency domain plot is the output from the FFT subsystem block shown in the Simulink model of Figure 3.14. From these Figures, it can be seen that the modulating SQUID output signals (in time domain) are at minimum whenever the sensed fluxes are at their peaks (i.e., both maximum and minimum). For clarity, the left part of Figure 3.17 (a) is as presented in Figure 3.18 in an enlarged form. Here, two of the peaks of the input flux are projected to their corresponding minimum modulations in the output voltage, using the vertical dotted lines. In-between these peaks, where the sensed flux is between -1 and 1, the output voltage modulation is well pronounced. This implies that the variation of the frequency is related to the differential of the sensed flux, as expected of any periodical SQUID output. It is also observable that the bandwidth of the output frequency spectrum is affected by changes in both the amplitude and frequency of the sensed flux. With an input flux of amplitude, 2 Φ_0, at a frequency of 5 Hz, the output, as seen on Figure 3.17 (b), shows an increase in the bandwidth, as compared to that of the 1 Φ_0 amplitude, at 5 Hz input flux, shown on Figure 3.17 (a). When the frequency of the input flux was increased to 15 Hz, maintaining the amplitude at 2 Φ_0, an increase in the output bandwidth was also noticed, as seen on Figure 3.17 (c).

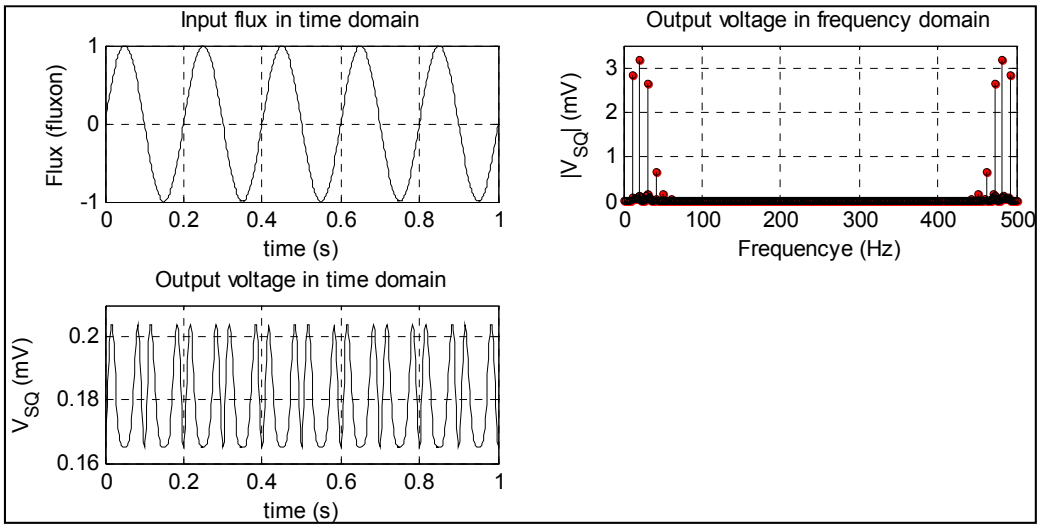

(a)

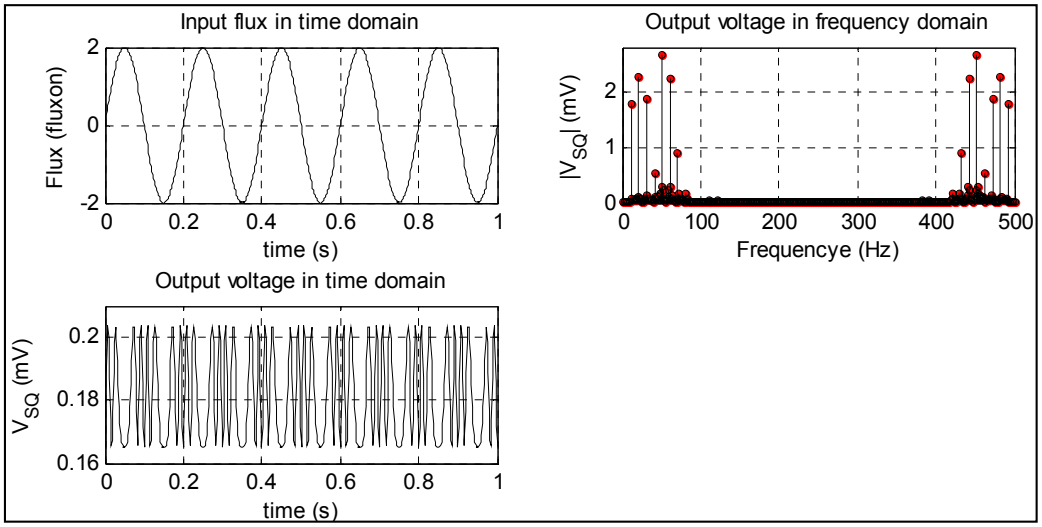

(b)

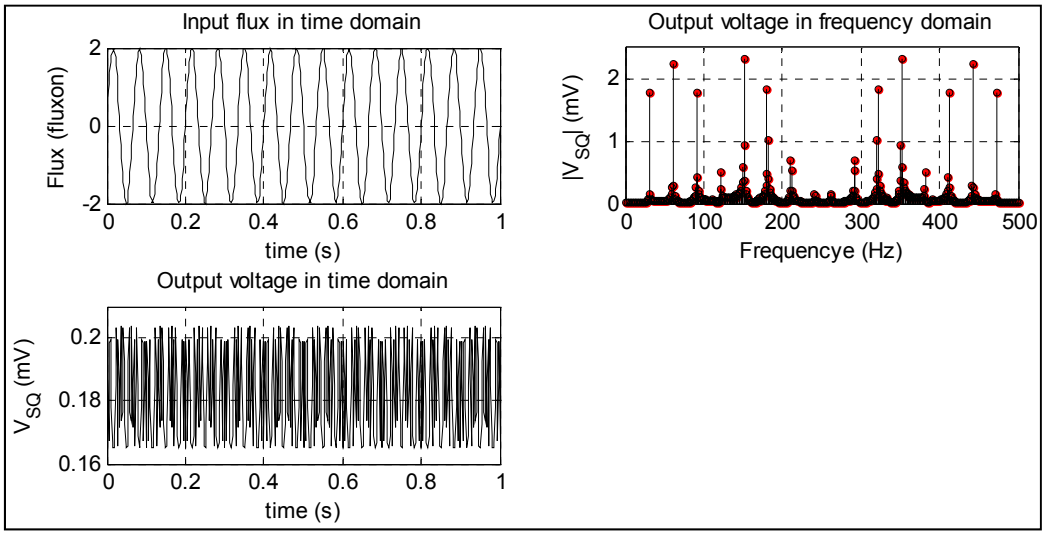

(c)

Figure 3.17: The SQUID's responses, both in time and frequency domains, at sinusoidal input flux of amplitude (a) 1 Φ_0 and 5 Hz (b) 2 Φ_0 and 5 Hz, and (c) 2 Φ_0 and 15 Hz

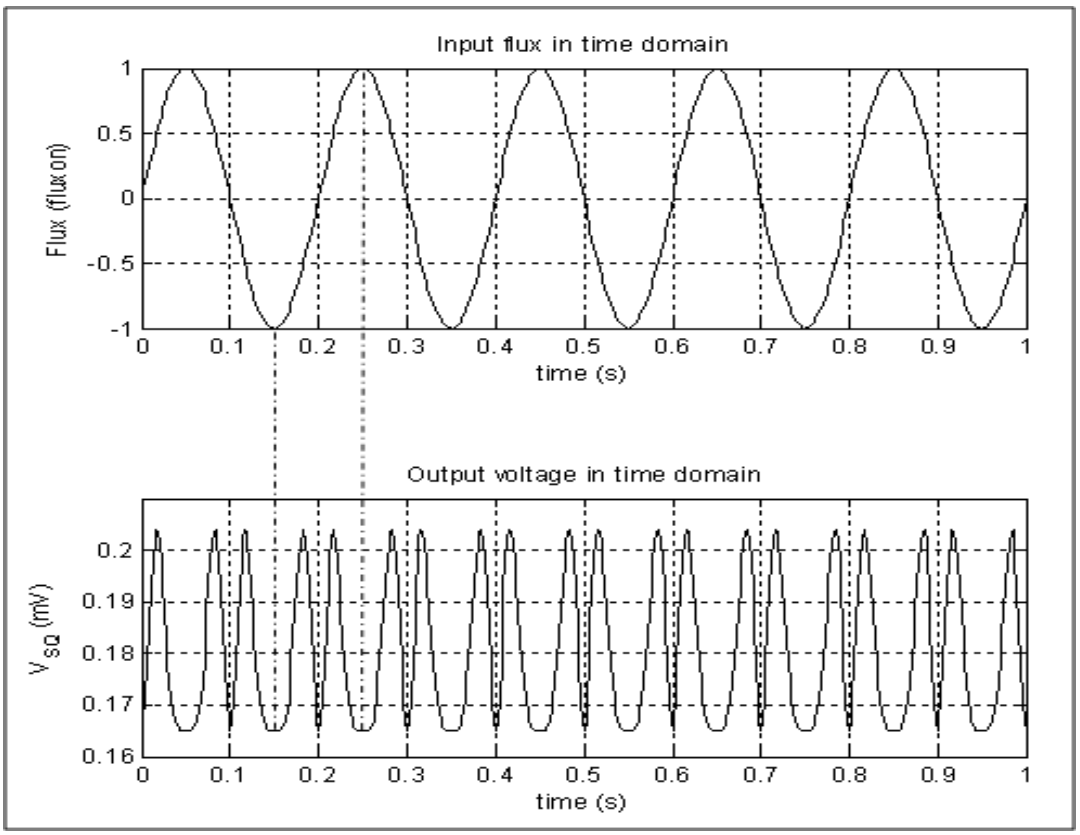

Figure 3.18: The enlarged SQUID's response from Figure 3.17 (a)

Figure 3.19 shows the superimposed responses, when magnetic fluxes of 0 Φ_0, 0.25 Φ_0, and 1 Φ_0 were applied to the SQUID, in order to show how the maximum critical current (the flat region) is affected by the sensed field. The flat response is seen to reduce from the maximum value, at 0 Φ_0 (the bold line on the Figure), downwards, as the input flux increases, and increases back to the maximum, at 1 Φ_0 (the bold line on the Figure). This validates the PSIM simulations results achieved in section 3.2.6, which is the expected behaviour of the SQUID, when it senses external magnetic fields.

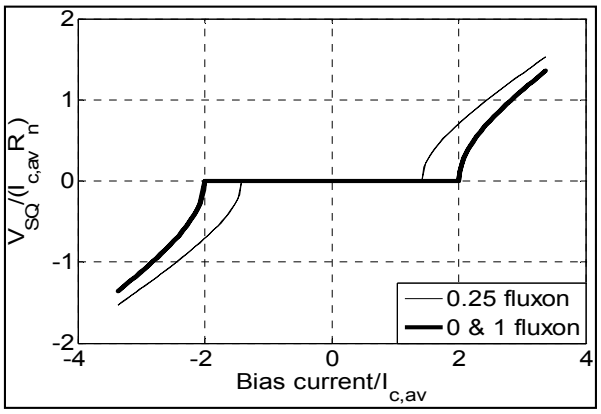

Figure 3.19: Superimposed SQUID's *V - I* characteristics at input fluxes of 0 Φ_0, 0.25 Φ_0 and 1 Φ_0

3.3.3 Flux locked loop simulations

The exact FLL simulated in section 3.2.8, using PSIM, was simulated using the MATLAB-Simulink package. Instead of using computational blocks for the preamplifier, voltage offset, and integrator sub-circuits, as done in the case of the PSIM simulations, physical electronics components are used in this section. The simulation speed is unaffected, when these components are used, due to the fact that MATLAB is fast in computations involving theses components, if the appropriate solver is used. This gives room for being able to know the actual behaviour of the FLL circuit, after frabricating it in reality. These physical components are accessible from the Simscape toolbox in the Simulink library.

The FLL was used to linearise the output of the SQUID simulated in section 3.3.1. The same parameter specifications used for the PSIM simulations were as well used, but detailed calculations for the electronic components have been included here. Given that, M_f = 0.1429 Φ_0 /μA (Star Cryoelectronics, 2011:2), R_f was calculated to be 1.9048 kΩ, using equation (2.70). The integrator's unity gain frequency, was calculated as f_1 = 5.92 MHz, using equation (2.65), with a gain bandwidth product of 1.6 GHz (Texas Instruments, 2008:1). This gives an integrator slew rate, SR of $0.186\ \mathrm{kV/\mu s}$, according to equation (2.66). Having obtained f_1, the integrator's capacitance, C_{int} was chosen to be 82 pF, while R_{int} was calculated to be 327.86 Ω from equation (2.52). In order to have a negative feedback to the SQUID, an inverting integrator was used.

The 2 op-amp in-amp circuit of Figure 2.26 (section 2.9.1.1), was used for the preamplifier, but the first amplifier serves as a voltage subtractor, for the voltage offset compensation. The second op-amp serves as the main SQUID preamplifier. These are fully represented in the top left corner of the FLL Simulink model (from Figure 3.20). By making R_2 = 10 Ω, R_1 was calculated from the following equation:

$$V_{off} = (R_2 / R_1)(^{-}V_{SQ} - V_2) \tag{3.4}$$

With $V2$ = -5 V, and $^{-}V_{SQ}$ = 0 (the SQUID's reference ground), R_1 was calculated to be $255.08\ \mathrm{k\Omega}$. Provided there is no offset, and making R_3 = 100 Ω, R_4 was computed to be 26.93 kΩ, by using equation (3.5).

$$A_{Preamp} = (R_4 + R_3) / R_3 \tag{3.5}$$

It was assumed that the FLL model has ideal electronics with negligible time delay. Hence, time delay was not put into consideration in this simulation.

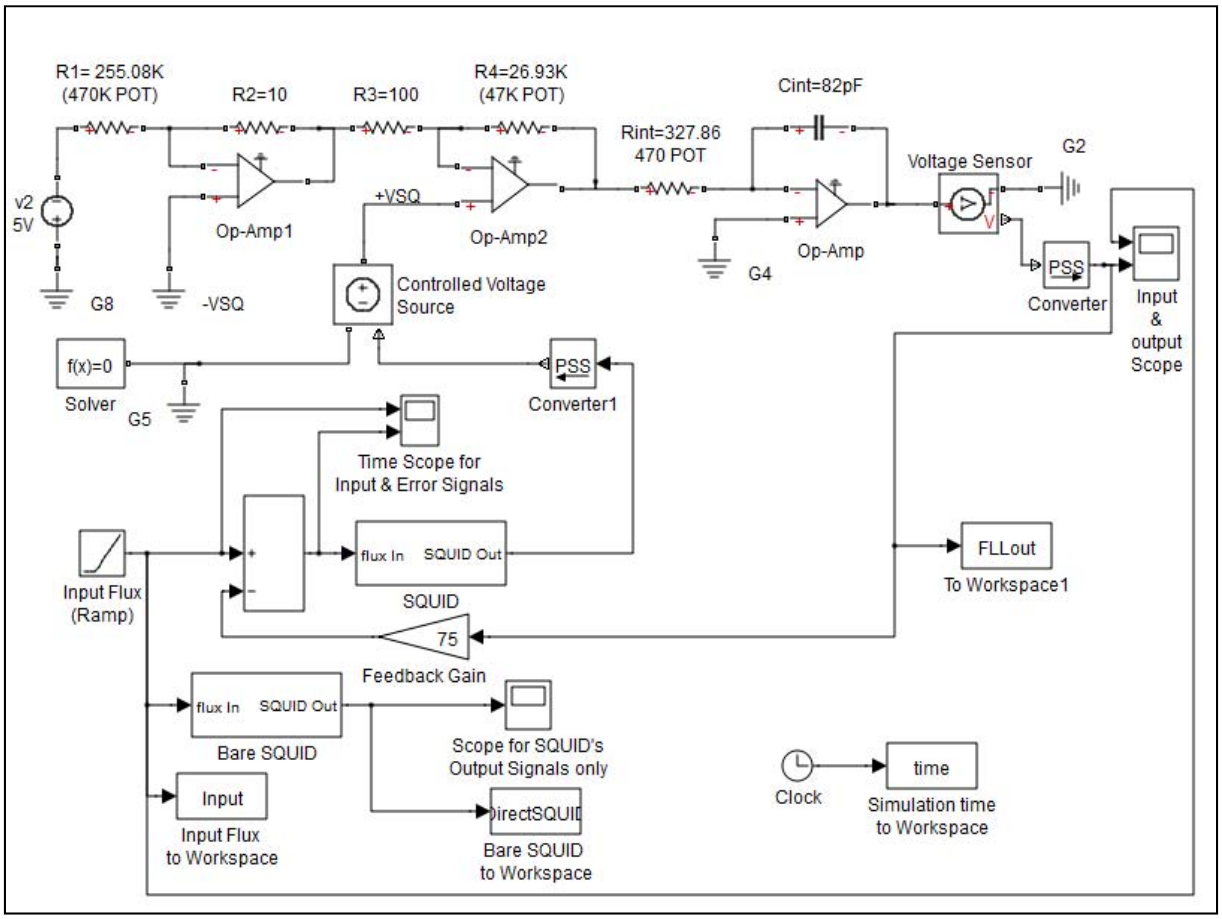

Figure 3.20: The Simulink model of the flux locked loop circuit

3.3.4 Results and discussion of the flux locked loop simulation

Figure 3.21 (a) presents the simulated periodic direct SQUID's output voltage response (before being coupled to the FLL). The linearised FLL's output voltage, both with respect to the simulation time and input flux, are respectively presented in the upper and lower parts of Figure 3.21 (b). Like the case of the PSIM simulation, the input flux was linearly swept from -1 Φ_0 to 1 Φ_0. Linear slopes of -0.83 mV/μs and -249.5 mV/ Φ_0 can be inferred from the results displayed in Figure 3.21 (b), and these respectively represent the slew rate and the voltage sensitivity. It is clear that the results of this Simulink simulation are quite the same as those obtained from the PSIM simulation presented in section 3.2.9.

The sinusoidal SQUID's output (before being coupled to the FLL) shows the difficulty in effectively correlating the sensed (input) flux to the SQUID's output voltage. This is a major disadvantage of using the direct output from the SQUID. Hence, the signal needs to be coupled to a FLL circuit in order to get it linearised for increased dynamic range, thereby making it easy to read out the sensed signal. Because the bias current used was 3.4 $I_{c,av}$ (which is greater than 2 $I_{c,av}$), the direct SQUID output is a full sinusoid (Figure 3.21 (a)). This was also observed in Figure 3.9 of section 3.3.2. Hence, easy linearisation is possible with

the use of the FLL. The output from the simulated FLL (Figure 3.21 (b)) clearly establishes the required linearisation of the SQUID's output signal.

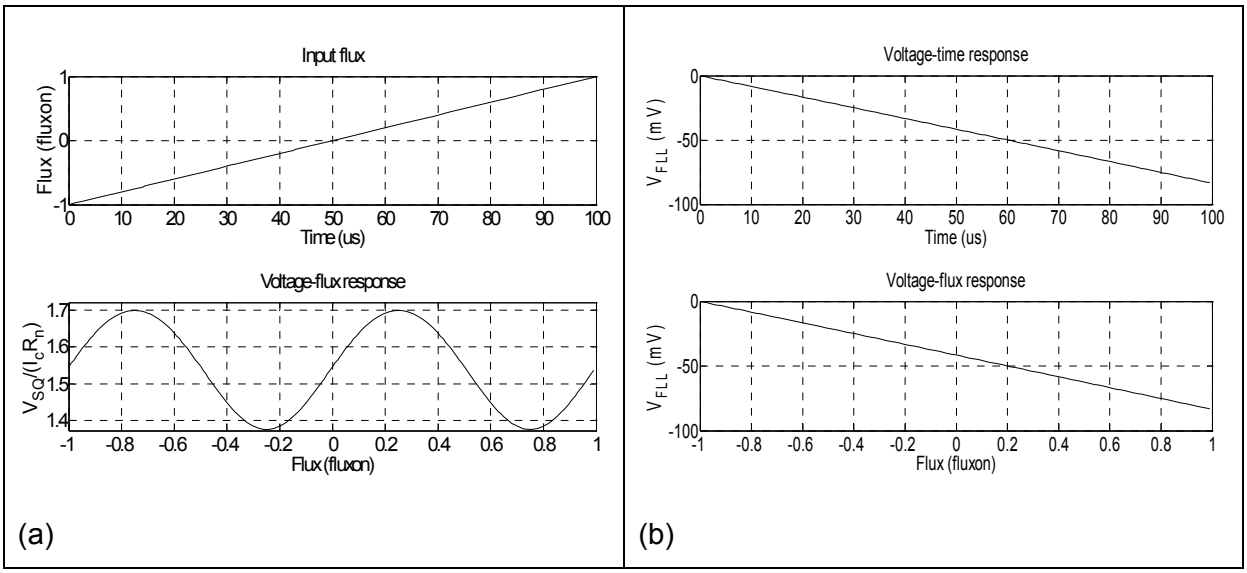

Figure 3.21: The SQUID's voltage response to a swept input flux from -1 Φ_0 to 1 Φ_0 (a) without the flux locked loop (b) with the flux locked loop

3.4 Conclusion

The modeling and simulations done on a Josephson junction and DC SQUID magnetometer's characteristics were described in this chapter. The software employed are both PSIM and MATLAB. The simulation results corroborate the expected behaviours of a typical JJ and DC SQUID magnetometer, with a modulating sinusoidal output voltage, of constant amplitude, V_c and an offset, V_{off} depending on the bias current. The $V - I$ characteristics of the JJ and the SQUID magnetometer are seen to represent the expected behaviours, showing the modulating nature of the junction current as the sensed flux varies. Thermal noise contributions due to the junction's resistance are seen to be insignificant, if large bias signals are involved. This therefore implies that the bias current must be reasonably high, in order to suppress the thermal noise effect in the JJs. The simulations show that the SQUID magnetometer's $V - \Phi$ response is periodical, at a period of $1\Phi_0$. A flux locked loop circuit was thus modelled in order to linearise the SQUID's output, and the resulting response shows that the external flux can be linearly related to the output voltage, with a slope of 464.1 mV/Φ_0.

CHAPTER FOUR

MODELLING AND SIMULATIONS OF A PASSIVE COOLING SYSTEM

4.1 Introduction

To be able to reduce the cost, time and stress of building and rebuilding a passive cooling system, before optimisation can be attained, it needs to be modelled and simulated. Modelling is as well needed, if the system is to be bought, because it might not yet be optimised for the specific need to be met. This section presents the modelling and simulation work done on the passive cooling system needed to cool down the SQUID sensor to a cryogenic temperature of 77 K, using the Thermal Desktop package. The cooling capacity of the cooler was determined when subjected to worst case conditions.

4.2 Thermal Desktop modelling and simulations

Thermal Desktop is a thermal analysis graphical user interface (GUI) software package built in SINDA environment and it uses finite difference method for computing heat equations in a sheet (Thermal Desktop, 2010). The model can be built by combining sheets together and thermal conduction occurs at the sheets' boundaries. The Thermal Desktop modelling work is accomplished in the AutoCAD workspace environment. Its working environment is activated, by clicking the "Thermal" icon on the AutoCAD's tool bar, as indicated on Figure 4.1. The Thermal Desktop tools are located on the either sides of the workspace, as the Figure depicts. One of the Thermal Desktop's modules called, "RADCAD", helps in radiative heat transfer computation, and it uses Monte Carlo technique in computing the coupling between surfaces.

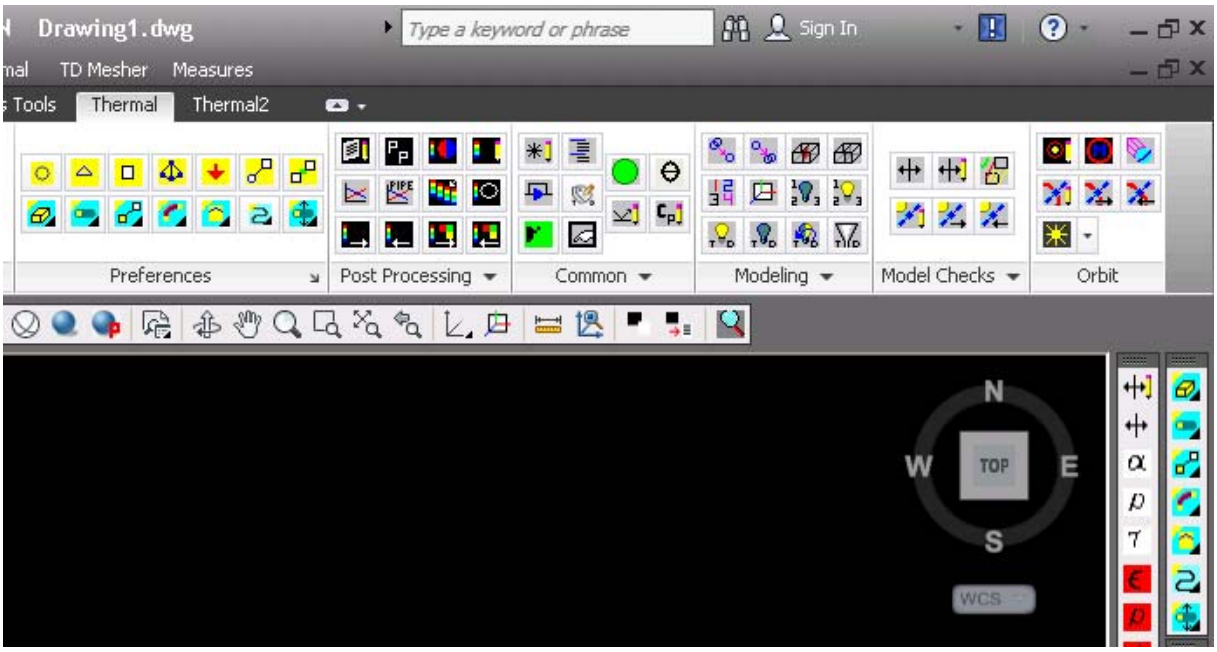

Figure 4.1: The top right portion of the AutoCAD workspace, with the Thermal Desktop mode activated

4.2.1 The passive cooler model

The passive cooling system was modelled using Thermal Desktop 5.5 version, on an Intel core 2 duo machine (with 2.99 GHz, 1.96 GB RAM). It is proposed to deploy the cooler out of the satellite, as soon as it is inserted into the orbit. Figure 4.2 shows the modelled passive cooler (fully deployed out of the satellite), with the dimensions indicated therein. The deployment boom (supporting structure) is put in place, so as help put the sensor at some distance from the satellite structure, thereby mitigating against any magnetic contamination emanating from the satellite. Figure 4.3 shows the cross section before deployment. Figure 4.4 presents the front view of the satellite-cooler integration. Figure 4.5 shows a cross section through the middle of the supporting structure. With this, the cables connecting the SQUID sensor to its electronics are clearly shown. The cooler was made of four stages of double layered conical radiators from a material called Kapton. They are made double layers,

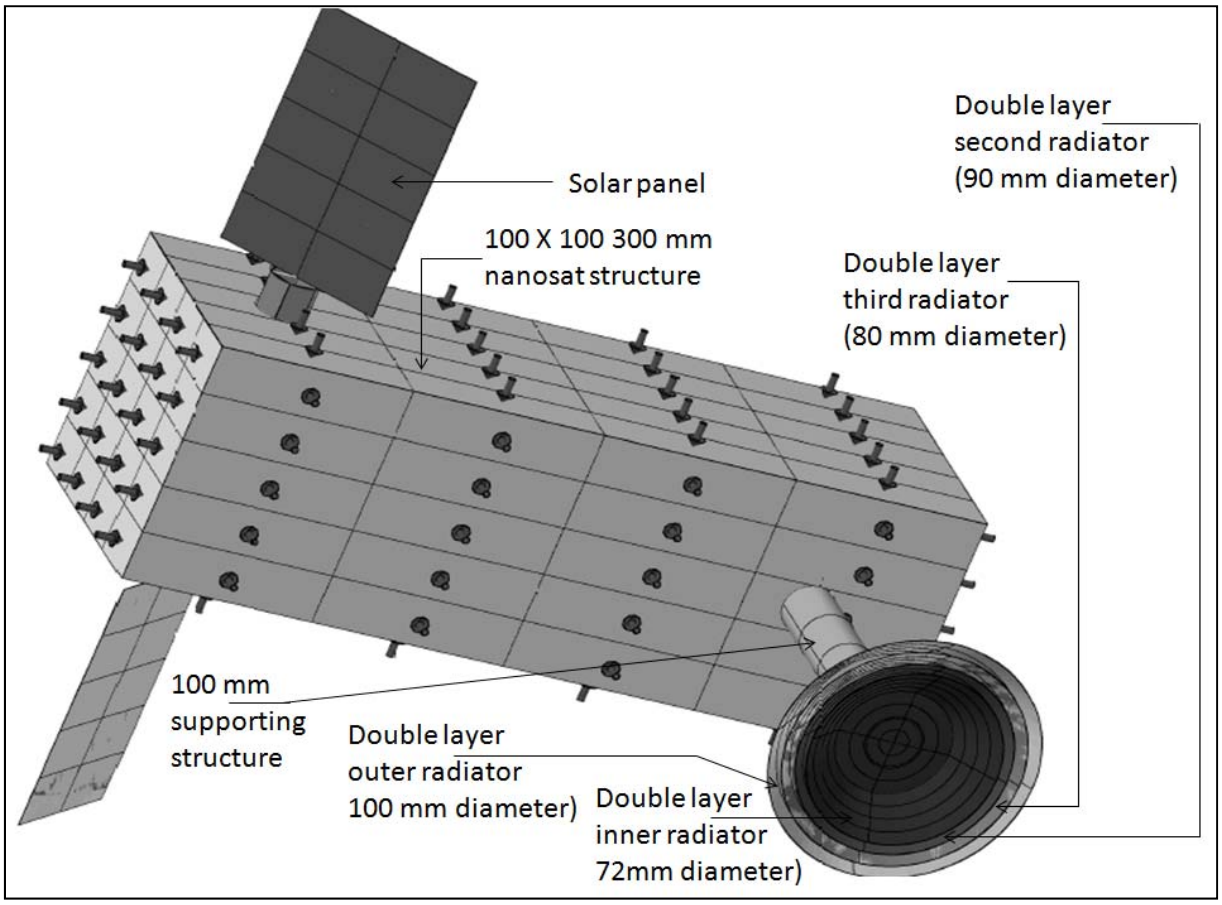

Figure 4.2: The fully deployed passive cooling system structure modelled with Thermal Desktop

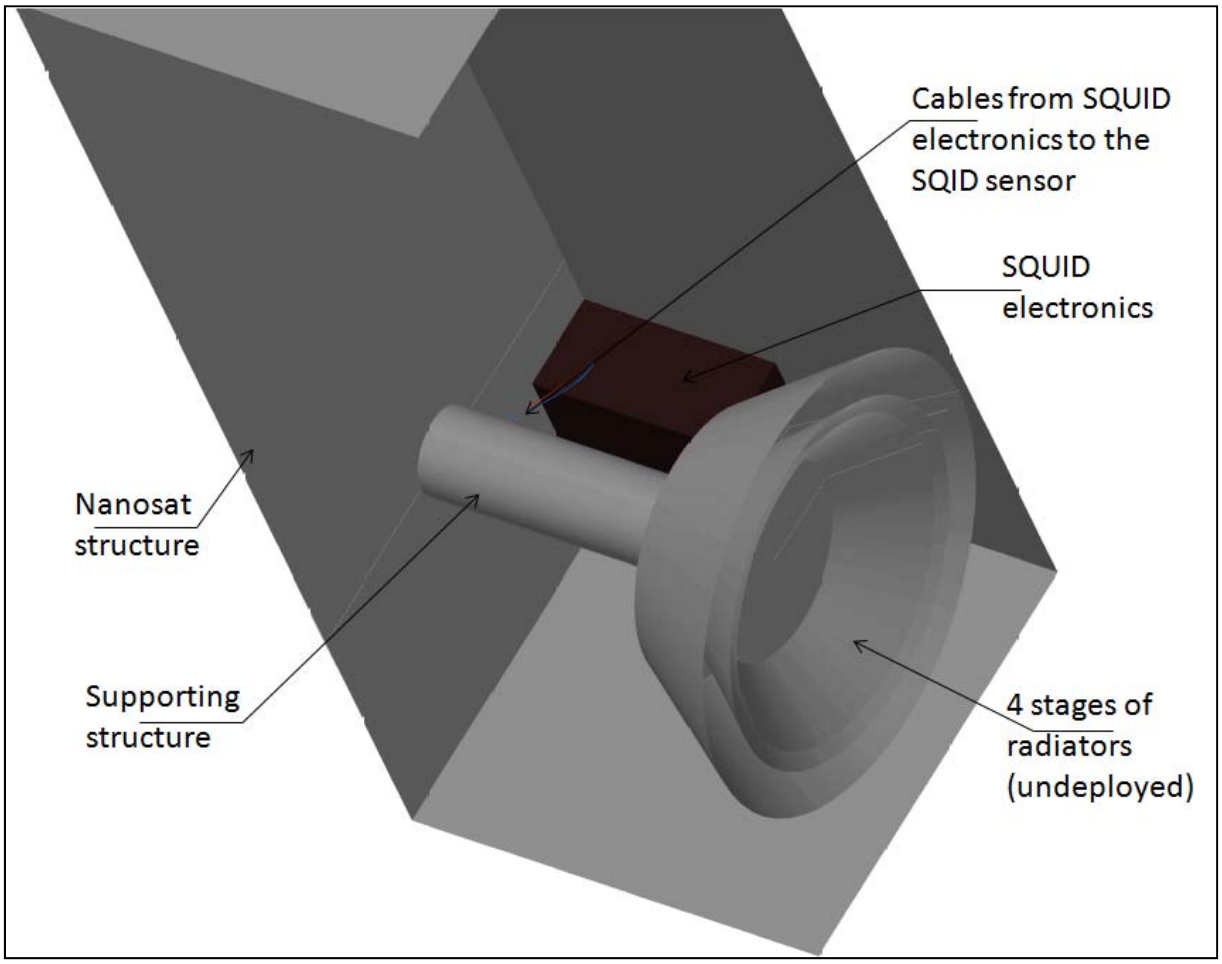

Figure 4.3: The 3 D cross section of the passive cooling system structure modelled with Thermal Desktop before deployment

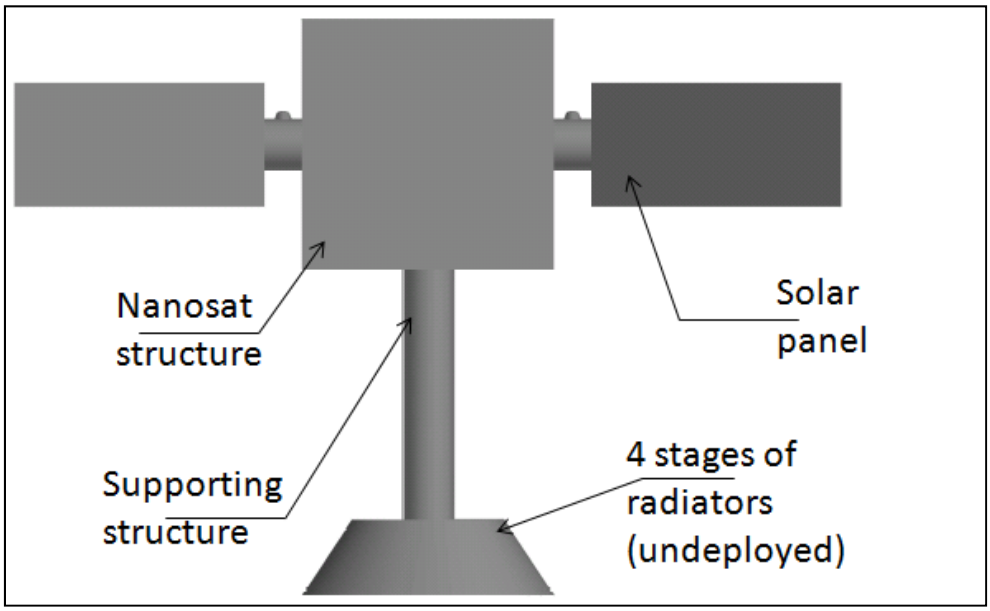

Figure 4.4: The front view of the fully deployed passive cooling system structure modelled with Thermal Desktop

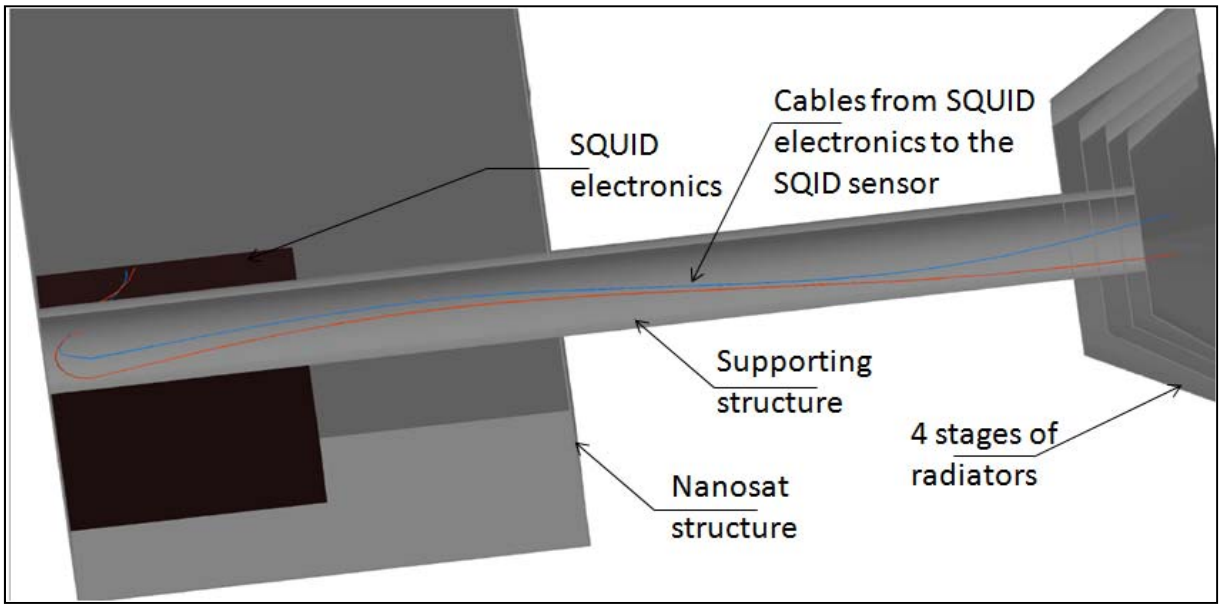

Figure 4.5: The 3D cross section of the passive cooling system structure modelled with Thermal Desktop after deployment

in order to avoid the risk of micro-meteorites from penetrating them, and to give room for temperature difference between each layer. Multi-layer insulation (MLI) was used to separate the layers from each other. A spacing of 5 mm is in-between each of the radiator stages. Table 4.1 and Table 4.2 contain the specifications and properties of the materials used for the model.

Table 4.1: Material specifications for the passive cooler model

	1st radiator	2nd radiator	3rd radiator	4th (Inner) radiator	Support
Outer layer	Material: Kapton Coating: Silvered Teflon Insulation: MLI	Material: Kapton Coating: Silvered Teflon Insulation: MLI	Material: Kapton Coating: Silvered Teflon Insulation: MLI	Material: Kapton Coating: Silvered Teflon Insulation: MLI	Material: Gamma-Alumina Coating: Silvered Teflon Insulation: N/A
Separation	Material: MLI	Material: MLI	Material: MLI	Material: MLI	N/A
Inner layer	Material: Kapton Coating: Black paint Insulation: N/A	Material: Kapton Coating: Black paint Insulation: N/A	Material: Kapton Coating: Black paint Insulation: N/A	Material: Kapton Coating: Black paint Insulation: N/A	N/A
Dimensions	Base radius: 30 mm Top radius: 50 mm Height: 30 mm	Base radius: 27 mm Top radius: 45 mm Height: 25 mm	Base radius: 24 mm Top radius: 40 mm Height: 20 mm	Base radius: 21.6 mm Top radius: 36 mm Height: 15 mm	Base radius: 10 mm Top radius: 10 mm Height: 100 mm

Table 4.2: Material properties for the passive cooler model

Thermophysical properties				
Materials	**Conductivity, K (W/m/K)**	**Density, ρ (Kg/m^3)**	**Specific Heat capacity, C_p (J/Kg/K)**	**Emissivity, ε**
Kapton	0.12	1420	1090	N/A
MLI	$1.2X10^{-6}$	249	0	0.05
Optical Properties				
Coatings	**Absorptivity, α**	**Emissivity, ε**	**α/ε**	
Black paint	0.94	0.9	1.044	
Silvered Teflon	0.08	0.81	0.099	

The passive cooler uses the deep space as the heat sink, by radiating the heat from the inner radiator through the other stages and finally into the cold deep space. The direction of heat radiation is defined by the optical properties of the material coatings. The outer surfaces of the satellite and the radiators are all coated with Silvered Teflon, making use of its poor solar absorptivity and good infrared (IR) emissivity for rejecting the solar flux. The outer sides of the radiators are further coated with MLI. The inside of the radiators are painted black to radiate out any heat from the cooler towards the deep space, due to its good emissive property. The colour map, showing the solar absorptivity profile of the entire model, is displayed in Figure 4.6. Table 4.2 contains all the optical properties of the material coatings used to achieve the radiation effect.

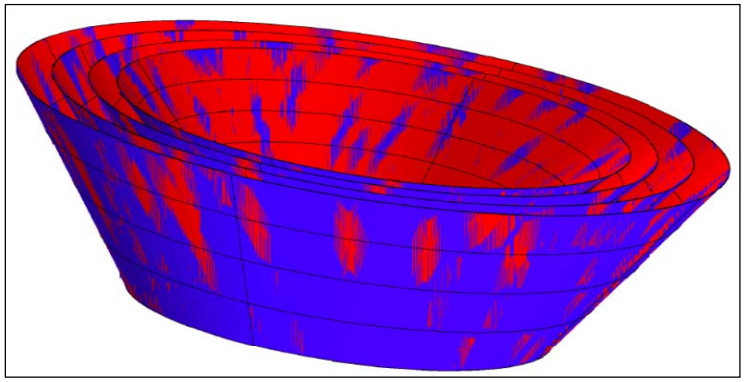

Figure 4.6: The colour map showing the solar absortivity profile of the cooler model

4.2.2 Thermal model input and simulation

The satellite's orbital parameters used are based on the proposed orbit for F'SATI's future mission, which is a circular Sun synchronous LEO orbit, at $600\,\mathrm{km}$ altitude, inclined at an incidence angle of 98^0. Since both Γ and Ω are time dependent (as explained in section 2.12.1), a beta angle, $\beta = 30^0$ was assumed, which is the worst case in calculating the maximum orbital heat rate. This represents a typical basic orbit in the Thermal Desktop

package. These parameters were used to define the satellite's orbit to be used by the software, in computing the orbital heat rates.

A solar flux of 132 W/m^2 was applied on the model. For a worst case scenario, all the power generated by the satellite (typically 9 W for 3U nanosats (section 2.10.3.2)) is considered to be converted to heat. This generated heat, together with the SQUID sensor's heat load were modelled using a feature called, "*heat load on surface*", in the software. The HTS sensor needs a small amount of cooling power (see section 2.10). In order to determine the cooling power (capability) of this model, different heat loads of 5 mW, 18 mW, and 20 mW were applied to the coldest face in the cooler, to represent the sensor's heat load. The satellite's generated heat power is seen as the deep black nuts on the satellite's structure (Figure 4.2). The sensor's heat load is not visible on the Figure, due to the presence of intermediate stages of radiators. An average of 30,000 rays per node, were used on the model, consisting of a total of 1024 nodes. After setting all the needed parameters, the model was simulated, using the "*Run selected case*" button in the case set manager, accessible through the "*Thermal*" tool on the tool bar.

4.2.3 Results and discussion of the simulated passive cooling system

The simulation took an approximate of 5.7s to run. Figure 4.7 (a) shows the simulation result, when there are no heat contributions from the satellite (i.e., the internally generated heat) and the SQUID, which is the heat load. Figure 4.7 (b) shows the result when only the heat contribution from the satellite is considered. In these two cases, cryogenic temperatures, far below 77 K were attained at the cooler's coldest region (where the SQUID must be placed).

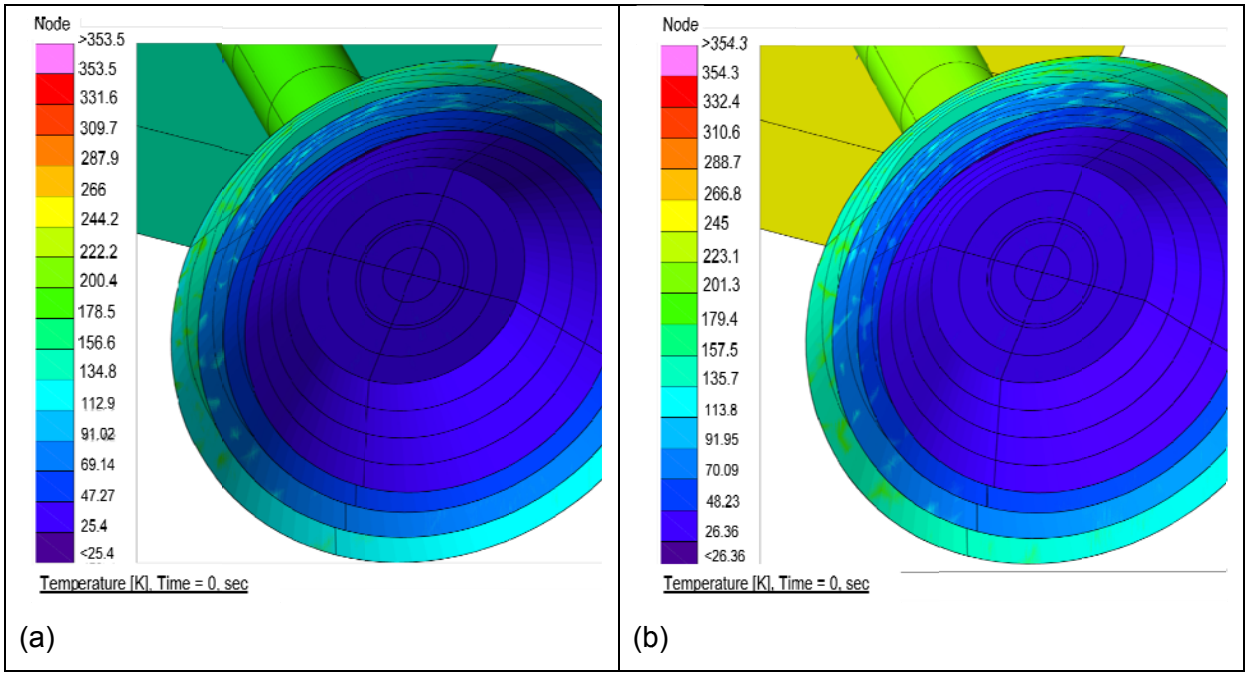

Figure 4.7: Colour map of the passive cooler when: (a) no heat from both the satellite and the SQUID are considered (b) only the satellite's internal generated heat is considered

Figure 4.8 (a), Figure 4.8 (b), and Figure 4.8 (c) are for when both the heat contributions are considered, with respective heat loads of 5 mW, 18 mW, and 20 mW on the cooler. In these three respective cases, the cooler's coldest region, attained temperatures of 43.08 K, 77.85 K and 77.52 K. These figures reveal that the maximum cooling capacity of the model is 18 mW, if a cryogenic temperature of 77 ± 1 K is desired. If the temperature is quite lower than the minimum temperature required for the SQUID's operation, it can be constantly maintained by the help of the heater embedded in the SQUID sensor. This heater is composed of two series resistors mounted on the SQUID.

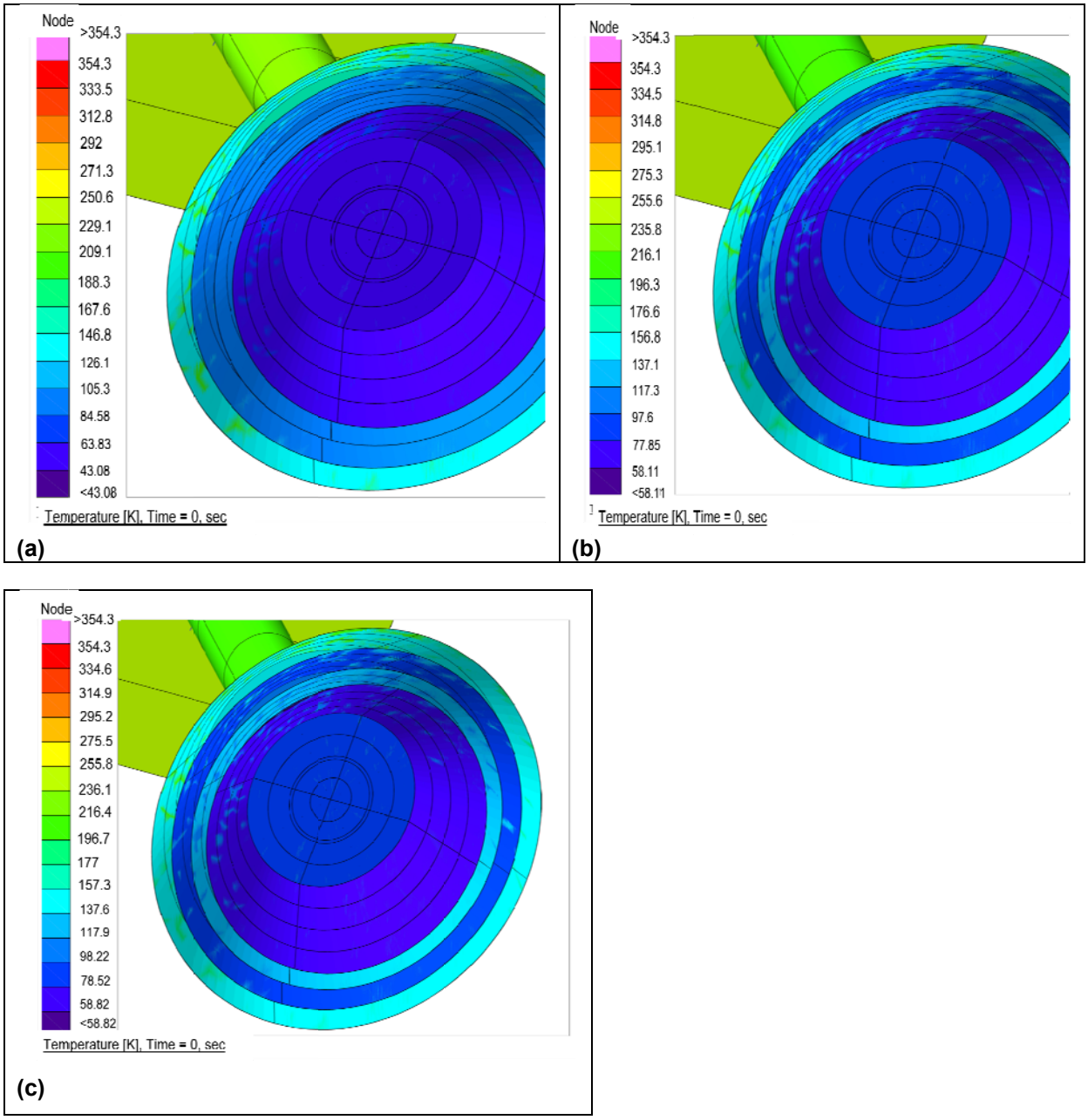

Figure 4.8: Colour map of the passive cooler when the satellite's internal heat is considered with: (a) 5 mW of heat load (b) 18 mW of heat load and (c) 20 mW of heat load

The significance of using double layer radiating materials, in maintaining temperature gradients on the model, can be shown by checking the colour map of the inner and outer parts of the inner radiator (Figure 4.9). This output was taken, when a heat load of 20 mW was considered. The temperature difference from one radiator to the other is as well presented in Figure 4.10.

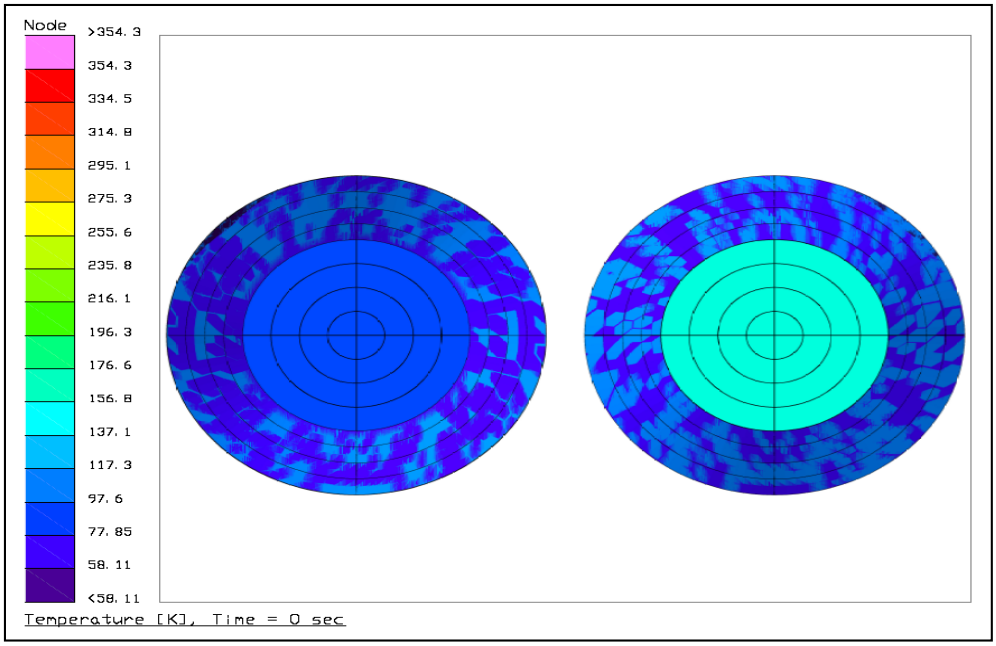

Figure 4.9: The colour map of the inner radiator (inside and outside from right to left)

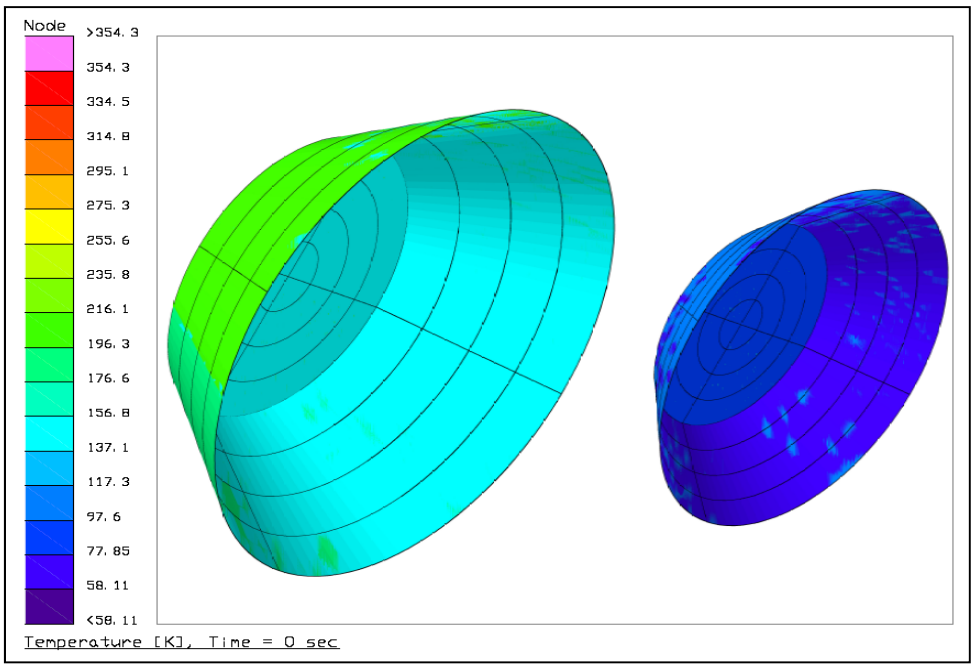

Figure 4.10: The colour map of the first and fourth radiators (from right to left)

4.3 Conclusion

The modeling and simulation of a passive cryogenic cooling system needed for keeping the SQUID at a critical cryogenic temperature (77 K) was described in this section. The software employed is Thermal Desktop. The simulation results show that a cooling capacity of about 18 mW is attainable in the orbit, at a cryogenic temperature of 77.85 K. Since only the SQUID magnetometer sensor is to be used on the nanosat, without building it into any probe, the required cooling power is therefore expected to drop. This infers that the cooling power achieved in the simulation is adequate for cooling the sensor. Hence, the usability of a DC SQUID magnetometer for nanosat space weather missions is therefore corroborated by this simulation result. One critical constraint in this mission is that the satellite's attitude in space has to be 3-axis stabilised, so that the cooler's part backing the Sun remains in its position, otherwise, there will be instability in the equilibrium temperature. This in turn greatly affects the SQUID's performance.

CHAPTER FIVE

EXPERIMENTAL WORK

5.1 Introduction

Having established that the DC SQUID magnetometer can be operated in the satellite orbital environment, the next stage of work is to manufacture the electronics needed to power it and interpret its output. These electronics, which include the bias circuit and the direct readout electronics (i.e., the flux locked loop) were therefore designed and manufactured in this research. Since this work is a foundational research, meant to establish that a SQUID magnetometer is usable for nanosat space weather missions, the designed electronics are only meant to serve as prototypes. Hence, the electronics components (like the resistors and the capacitors) used are not the expensive high precision IC components used in the commercial SQUID electronics. The success of the functionalities of these prototypes will lead to the manufacture of space-qualified electronics, to be adapted into the satellite. The functionality tests done on the fabricated electronics and the SQUID sensor are subsequently reported in the latter part of this chapter, together with the radiation test carried out on the sensor.

5.2 Design and fabrication

The SQUID bias and the readout electronics respectively described in sections 2.8.1 and 2.11 were implemented in this research work. The design and fabrication of these electronics are hereby presented in this section.

5.2.1 The SQUID Bias circuit design and fabrication

Two means of designing the current source for biasing the DC SQUID were discussed in section 2.8.1. As depicted in Figure 2.19, the series resistor current source is considered inappropriate for this task because the SQUID has a theoretical junction resistance, which has to be practically determined. A typical value of 3 Ω was assumed in the simulations carried out. This makes it impossible to know the output current that may be provided by this method. It is also prone to hazard, in the event of any accidental voltage. The Widlar op-amp current source presented in Figure 2.20 was therefore selected for this task, because it addresses the two limitations associated with the first type.

In order not to load the SQUID, it is pertinent to cleverly select the op-amp to be used for the design. It is good for the op-amp to have a high gain bandwidth (GBW), high slew rate, low voltage noise and low current noise. Since the SQUID bias current is in the μA range, it is also very important to use an op-amp of very low input bias current. This lowers the effect of any anomalies on the JJ (with respective minimum, maximum and typical critical current values of 5 μA, 50 μA and 10 μA). Some op-amps properties were evaluated (as presented

in Table 5.1). OPA657, TL072 and TL072 op-amps were considered for this task, since they meet the requirements stated above. Of them all, OPA657 has almost the best characteristics, with a GBW of 1.6 GHz, low bias current of 20 pA, slew rate of 700 V/ µs, voltage noise of 4.8 X 10^{-3} $nVHz^{-1/2}$, offset voltage of 80 µV, and current noise of 4.8 X 1.3 X 10^{-3} $pAHz^{-1/2}$. Appendix E contains some important electrical characteristics of the OPA657 op-amp extracted from the datasheet (Texas Instruments, 2008:3).

Table 5.1: Comparative characteristics of op-amps

	Operational amplifiers					
	OPA657	**OPA656**	**OPA637**	**OPA355**	**TL072**	**OPA134**
Supply voltage (V)	±5V	±5V	±18V	±18V	±2.5V	±36V
-3dB GBW (GHz)	1.6	0.5	0.08	0.45	0.004	0.008
Slew rate (V/µs)	700 (G = 10)	290 (G = 2)	135 (G = -4)	360 (G = 2)	16	±20
Max. Input offset (µV)	1800	1800	250	9000	10000	200
Max. Input bias (pA)	20	20	10	50	200	100
Voltage noise ($nVHZ^{-1/2}$)	4.8	7	5.6	5.8	15	8
Current noise ($pAHZ^{-1/2}$)	$1.3X10^{-3}$	$1.3X10^{-3}$	$12.5X10^{-3}$	$50X10^{-3}$		$3X10^{-3}$

The designed circuit is as presented in Figure 5.1, with a coupled voltage divider network to reduce the output current to the exact bias current needed. A bias current of I_b = 68 µA was designed for, which is in excess of the recommended value of 3.8 $I_{c,av}$ necessary for achieving a full sinusoidal direct SQUID output, suitable for linearisation (section 2.8). The circuit can be tuned to the desired current value, by using the R_{b2} potentiometer on Figure 5.1. A voltage value of V_p = *1.52* V is obtainable from the voltage divider, with R_{b1} = 1.43 kΩ and R_{b2} = 3.27 kΩ (both are obtainable from a 4.7 kΩ Potentiometer). In order to obtain I_b of 65 µA, with V_n being 0 V, and R_1, R_2, and R_4 being 220 kΩ, R_3 was calculated to be 20 kΩ, from equation (2.45). Also, R_5 was calculated as $R_5 = R_4 - R_3$ = 200 kΩ. See section 2.8.1 for comprehensive understanding of the parameters calculations.

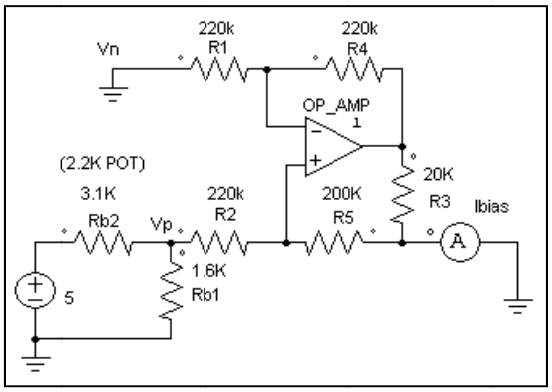

Figure 5.1: The bias circuit schematic

The circuit was initially implemented with OPA657, and latter with OPA134, for the purpose of observing the effect of the GBW in each case. OPA134 has a lesser GBW (8 MHz), but better voltage noise ($200\ \mu V$) (Burr-Brown, 1996:2). Appendix F contains some important electrical characteristics of the OP134 op-amp extracted from the datasheet (Burr-Brown; 1996:2). The PCB layouts (using both OPA657 and OPA134) were designed using KiCad (a PCB modelling software), and the enlarged 3D layouts are as shown in Figure G.1 (a) Figure G.1 (b) (appendix G). The fabricated PCB layouts were populated with the component values calculated above, and the enlarged portions of the final boards are as shown in Figure G.2 (a) and Figure G.2 (b).

5.2.2 The SQUID readout electronics design and fabrication

As established in section 2.9, the function of the readout electronics, otherwise known as the flux locked loop (FLL), is to linearise the SQUID sinusoidal output signal. Due to space constraints in the nanosatellite structure, there cannot be enough room for the present day complex SQUID readout electronics (like those mentioned in section 2.9). The limited power available, also determines how sophisticated the electronics can be. Simple direct readout electronics was therefore designed for, in this project. Please refer to Figure 2.3 and Figure 3.9for schematics that describe the mode of operation of a typical FLL electronics and the way the sub-circuits (i.e., preamplifier, integrator and feedback) are inter-connected. All the FLL sub-circuit components used for this design are the same as those represented in Figure 3.20 of section 3.3.3. For simplicity, the enlarged schematics are presented in the subsections describing the fabrication of each of these sub-circuits.

5.2.2.1 The flux locked loop preamplifier circuit design and fabrication

A preamplifier gain of 270.27 was designed for, using the 2 op-amp in-amp circuit described in section 2.9.1.1. As discussed in section 3.3.3, this gain solely depends on the SQUID's gain, which can be practically determined by the slope of the tangent to its working point. The circuit components were calculated the same way as those used in the simulations were calculated. See Figure 5.2 for the enlarged schematic of this circuit. The potentiometer R1_1 is capable of varying the gain to the desired value. Both OPA657 and OPA134 were also used to design the preamplifier circuit. The offset compensators for the two OPA134 op-amps (op-amp1) and (op-amp2) were implemented using a 100 kΩ potentiometer each. The PCB layouts were designed using KiCad, and their enlarged 3D layouts are as shown in Figure G.2 (a) and Figure G.2 (b) (appendix G). The enlarged portions of the final boards are as shown in Figure G.3 (a) and Figure G.3 (b) respectively.

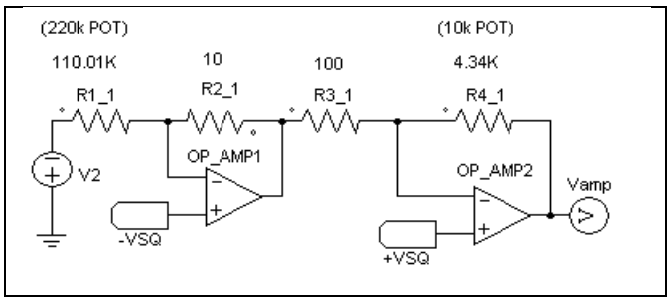

Figure 5.2: The preamplifier circuit schematic

5.2.2.2 The flux locked loop integrator and feedback circuits design and fabrication

As discussed in the FLL simulation of section 3.3.3, the integrator was designed to have a unity gain frequency, f_1 of 5.92 MHz, using the op-amp single-pole inverting integrator circuit described in section 2.9.1.2. Coupled to the output of the integrator, is the FLL feedback resistor, R_f. The circuit components are the same as those calculated in the simulation of section 3.3.3. See Figure 5.3 for the enlarged schematic of these circuits. The "*to_L*$_f$" arm of the schematic is the one that connects to the SQUID feedback inductor. The PCB layouts (using both the OPA657 and OPA134) were designed using KiCad, and their 3D layouts are as shown in Figure G.4 (a) and Figure G.4 (b). The enlarged portions of the final boards are as shown in Figure G.5 (a) and Figure G.5 (b) respectively.

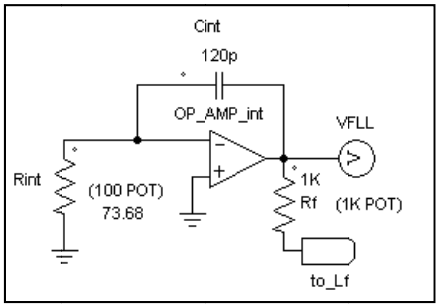

Figure 5.3: The flux locked loop integrator and feedback circuit schematic

5.3 Measurements and results

This section presents the procedures and the outcomes of the functionality tests carried out on the fabricated electronics and the SQUID sensor as well, together with the space qualification test for the sensor. The apparatus used include a power supply unit to power up the electronics, a signal generator for voltage sweep, a cooler of liquid Nitrogen for cryogenic temperature experiment, connection cables for proper connections between all the components, and an Agilent scope to capture the input and output signals. The CSV files obtained from the oscilloscope were exported into and plotted in MATLAB for better axis formatting. Appendix C contains all the MATLAB codes used for the plotting.

5.3.1 Compliance measurements on the bias and preamplifier circuits

In order to verify the functionality of the fabricated circuits, a resistance, the same as that of the equipment under test (EUT), needs to be used as the load. This is termed the compliance test. From the M1000 specification sheet (Star Cryoelectronics, 2011:2), a room temperature resistance of $210\,\Omega$ is across the sensor's bias terminals. As such, a standard resistor value of 220 Ω was used to represent the sensor, but this showed an actual value of 215 Ω, when it was measured. The voltage divider at the input of the bias circuit helps to vary the amount of the input voltage to the circuit, thereby helping to vary the equivalent output current to the desired value. Any voltage developed across the load is the compliance voltage of the current source. These tests were carried out under normal room temperature. Appendix G contains the complete set-up for this experiment.

A 5 V DC was initially used as the input to the current source. The designed OPA657 current source suffered from instability when it was tested. This is probably due to the very high GBW 1.6 GHz of the op-amp, which makes the output vulnerable to oscillations at any slight mismatches between the resistors R_1 and R_2, and the resistors R_4 and (R_3 + R_5), according to Figure 5.1. This might be a bit tolerable at lower GBW, as was observed in the case of the TL072 op-amp (GBW of 4GHz). Figure 5.4 shows both the voltage input to the circuit and the resulting compliance voltage across the load. A compliance voltage of 16.4 mV is expected, which is what is readily displayed on the Figure. The output current of 68 μA is implied from this result, which is what was designed for. Figure 5.5 shows the resulting DC current. This value was obtained by plotting the current equivalent of the input voltage.

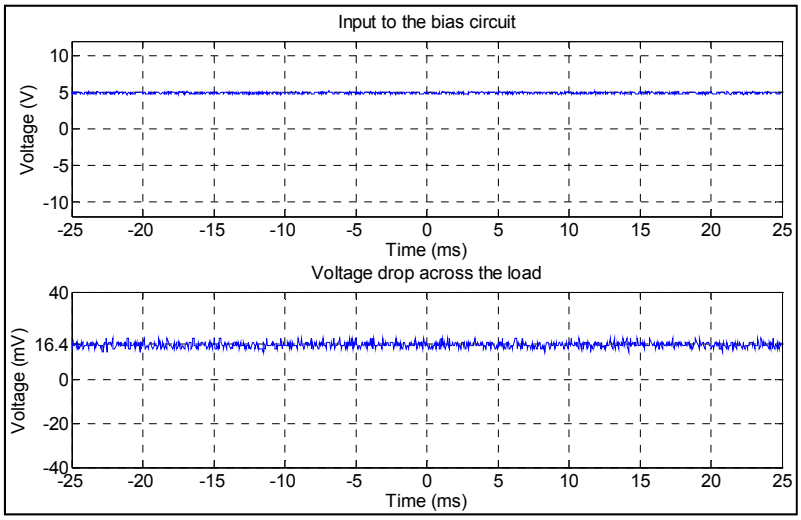

Figure 5.4: The voltage developed across a 216 Ω load, using a 5 V DC input to the bias circuit

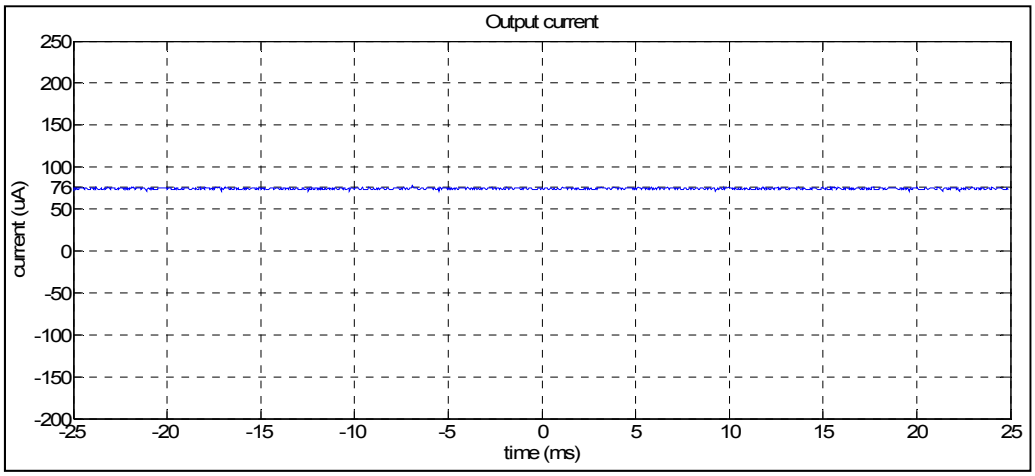

Figure 5.5: The output current from the bias circuit, with 5 V DC input

The noise signature in the output signals is probably due to the contributions from the load's Johnson noise, and the intrinsic noise from the oscilloscope and its probes. The noise is also vividly pronounced, due to the fact that the signal output level is quite low. The preamplifier's functionality was verified by using the output voltage across the 216 Ω load as the input to the preamplifier. This resulted in a DC output voltage of 4.433 V, as displayed in Figure 5.6. With this, a gain of 270.03 can be observed, which is close to the gain of 270.027 designed for. A precise gain value can be achieved by varying the 10 kΩ potentiometer of Figure **5.2**.

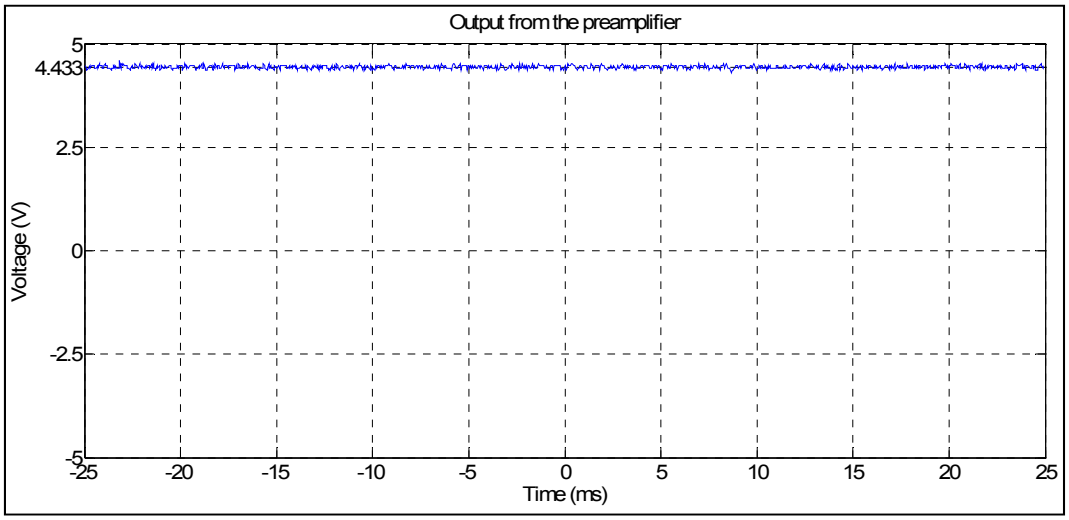

Figure 5.6: The DC output from the preamplifier circuit

In order to examine the behaviour of the load to a current sweep, a voltage sweep of ± 3.5 V**,** at 80 Hz, was used as the input to the bias circuit. Figure 5.7 shows both the voltage input to the circuit and the resulting compliance voltage sweep across the load. A compliance voltage sweep of ± 8.2 mV is expected, which is what is readily displayed on Figure 5.7. The output current of ± 38 μA is implied from this result, which is what was designed for. Figure 5.8 shows the resulting current sweep.

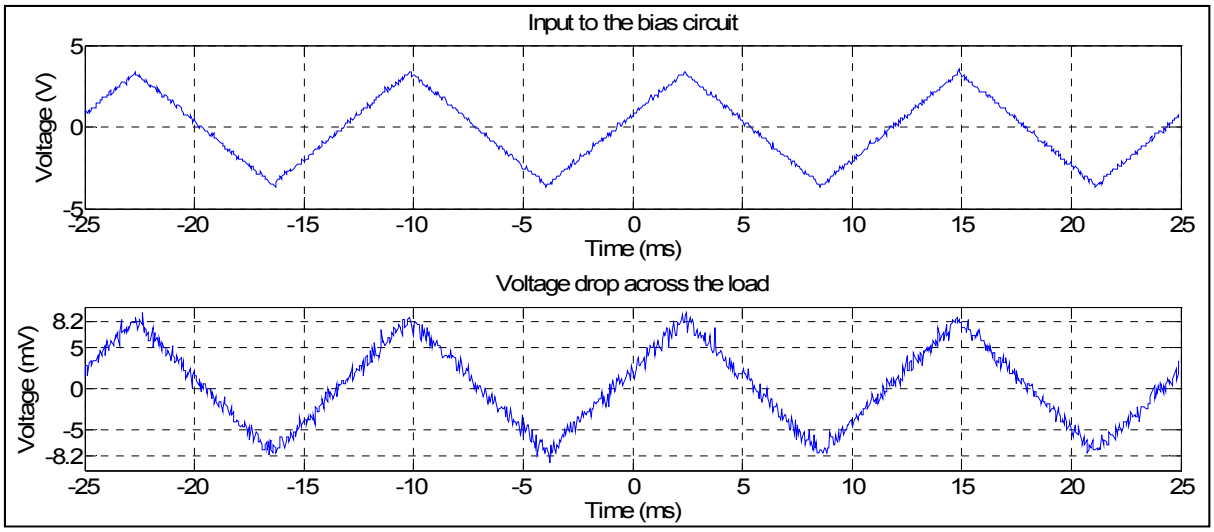

Figure 5.7: The voltage developed across 216 Ω load, using ± 3.5 voltage sweep at 80 Hz as an input to the bias circuit

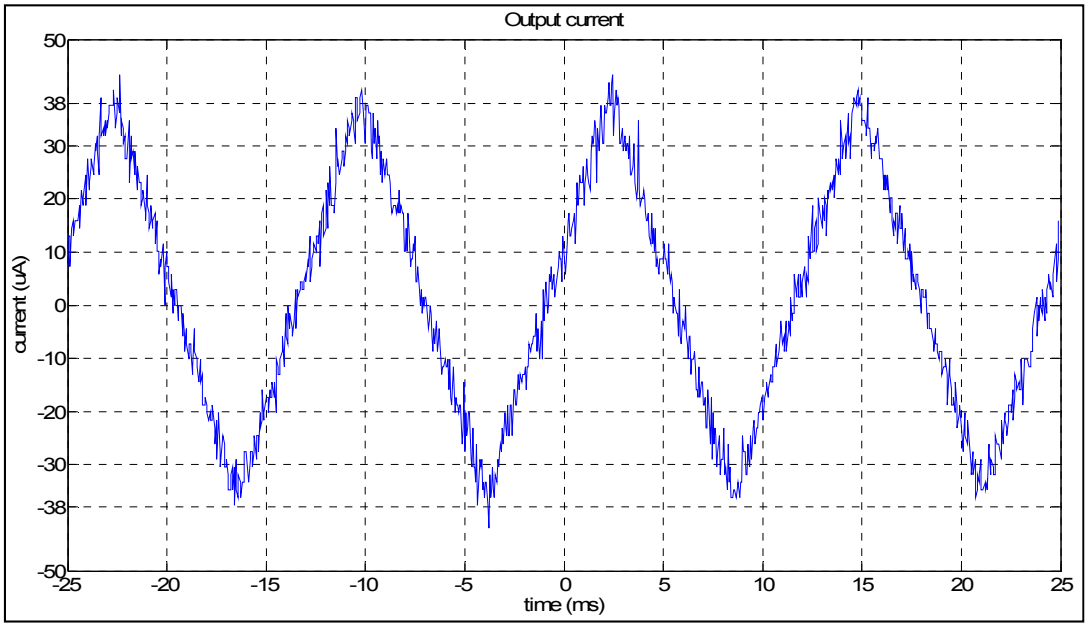

Figure 5.8: The output current from the bias circuit, using ± 5 voltage sweep at 80 Hz

The output voltage across the 216 Ω load was also used as the input to the preamplifier. This resulted into a swept output of ± 2.216 V, as displayed in Figure 5.9. The gain from this measurement agrees with the one displayed in Figure 5.6.

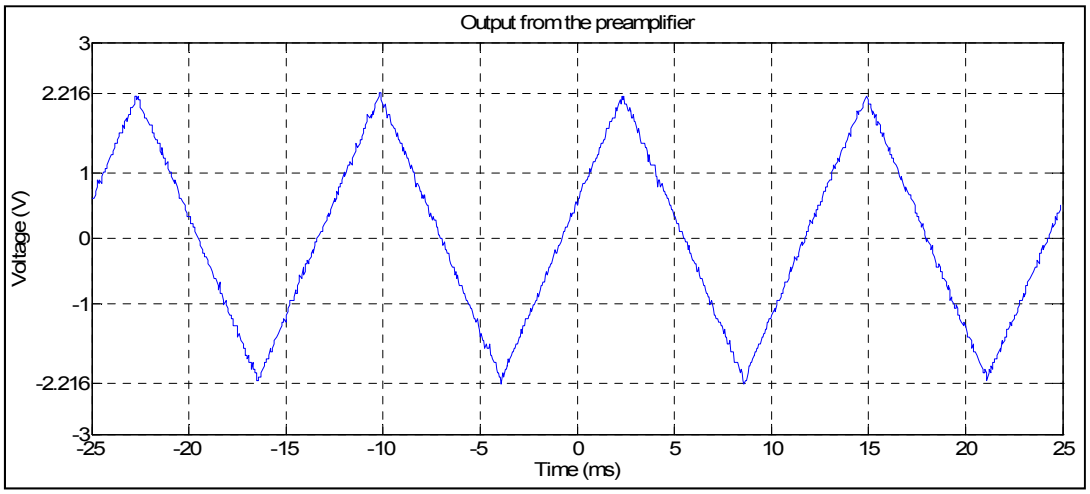

Figure 5.9: The output load voltage sweep from the preamplifier circuit

Figure 5.10 shows the *V* - *I* relation between the preamplifier output and the bias current. A linear relationship can be observed, which is a typical behaviour of any resistive load. Such behaviour is expected of any DC SQUID at room temperature. The resistance of the EUT can be determined by dividing the slope by the preamplifier gain. As displayed on Figure 5.10, we have:

$$R = \frac{Slope}{A_{preamp}} = \frac{2.027 - 0}{270.27\,(34.95 \times 10^{-6} - 0)} \approx 215\,\Omega$$

This resistance value is closely related to the $216\,\Omega$ used in the experiment.

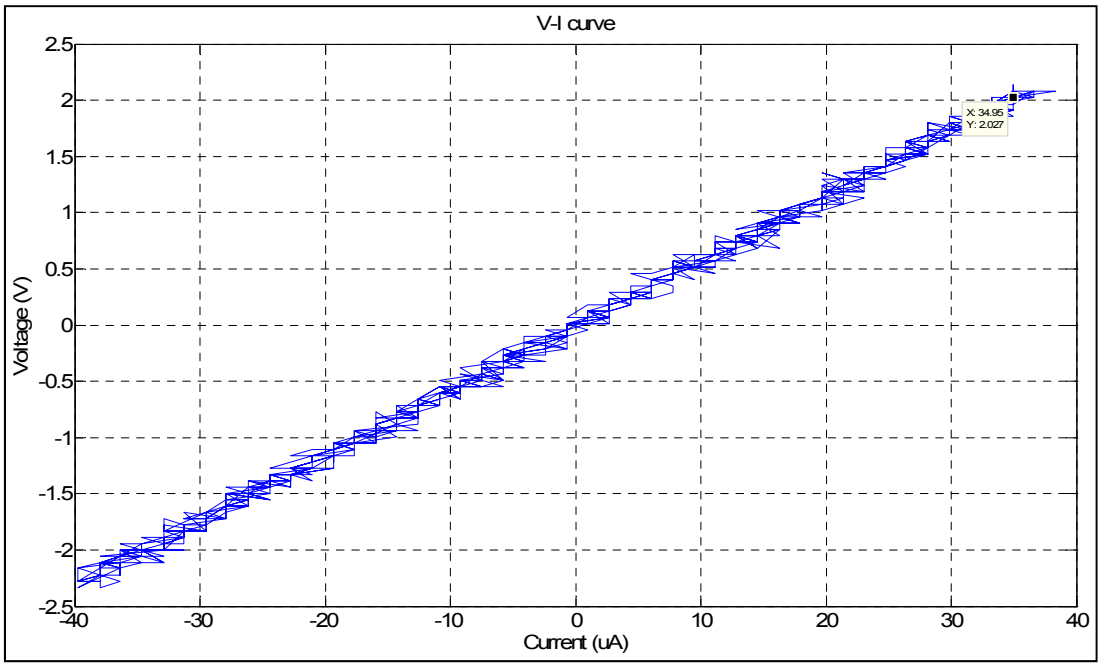

Figure 5.10: The *V* - *I* characteristic of the load

5.3.2 Room temperature measurements on the SQUID sensor

Great precautionary steps must be taken while working with SQUID magnetometers, in order not to damage them, because they are highly sensitive, expensive, and cannot withstand excessive high currents. With a view to determining the sensor's room temperature resistance, a multimeter was used. Usually, when a multimeter is used to take measurements on a device under test (DUT), a minute amount of current is supplied by the multimeter, which in turn passes through the DUT. These current values depending on the selected measurement range in the multimeter. The Ohm range used for this room temperature resistance measurement was determined by using a dummy load of known resistance with a multimeter. Here, the multimeter measured the load resistance, while an oscilloscope was used to measure the voltage developed across the load during the course of the measurement. With this, the current through the load was determined by dividing the measured voltage by the load resistance. The sketch on Figure 5.11 depicts this experimental set-up.

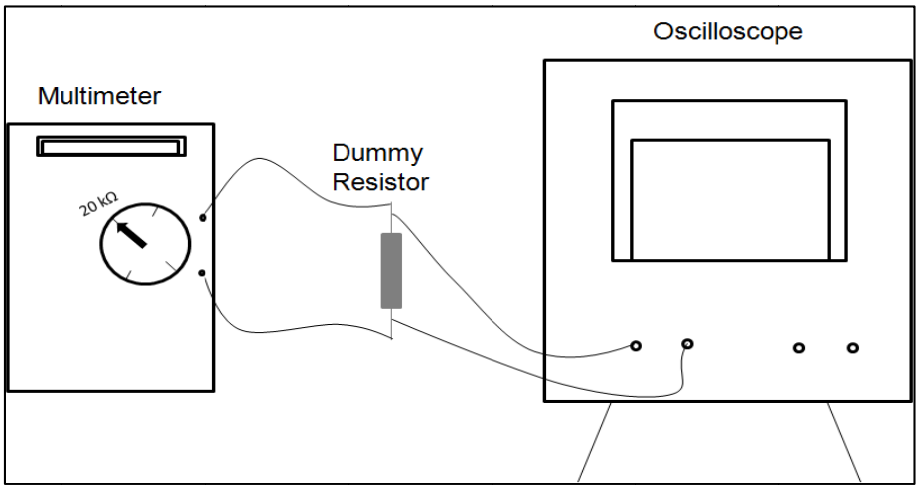

Figure 5.11: The multimeter set-up to determine the room temperature resistance

Figure 5.12 shows the voltage across, and current through a dummy dummy load of 216 Ω, when the multimeter was set to the 20 kΩ range. This shows that a $20\,\mathrm{k\Omega}$ range on the multimeter is safe for measuring the SQUID's resistance, without passing any damaging current through the SQUID. A SQUID resistance of 1.26 kΩ was therefore measured using this range. However, this value greatly conflicts with the expected sensors' room temperature resistance, which should be in few hundred Ohms (typically 210 Ω). This exorbitantly high value poses a challenge on the integrity of the sensor. Since the SQUID sensor is a parallel combination of two JJs, the measured resistance implies that the sensor's junction resistance is $R_n \approx 1.26$ kΩ.

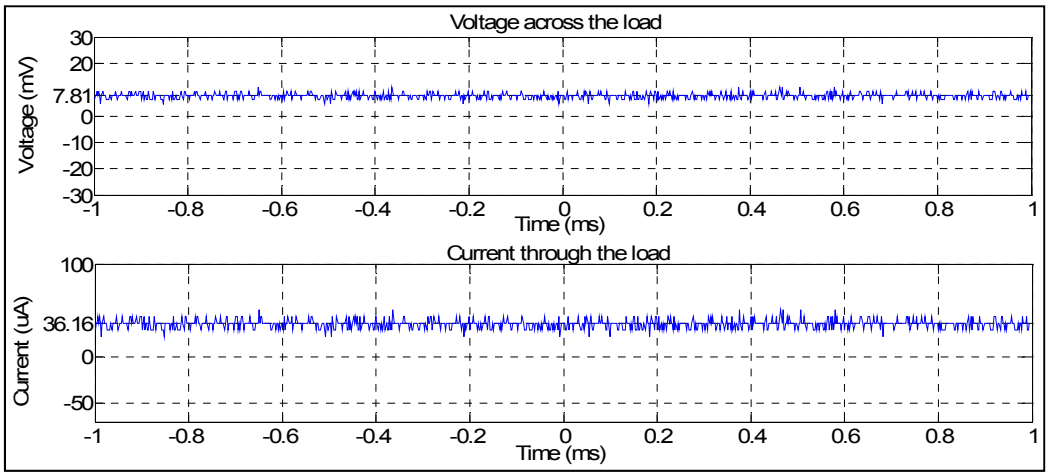

Figure 5.12: The Voltage across, and current through a 216 Ω resistor, using a 20 kΩ multimeter range

In order to ascertain the room temperature resistance value obtained with the multimeter, the fabricated electronics were used to re-determine it, by biasing the SQUID with a 76 μA DC current, and further with a swept current of ± 38 μA. For these two cases, Figure 5.13 (a) and Figure 5.13 (b) respectively show the developed voltages across the SQUID at room temperature. A SQUID junction resistance of $R_n \approx 1.26$ kΩ can be inferred from the two outputs shown in Figure 5.13, which agree with the multimeter measurement.

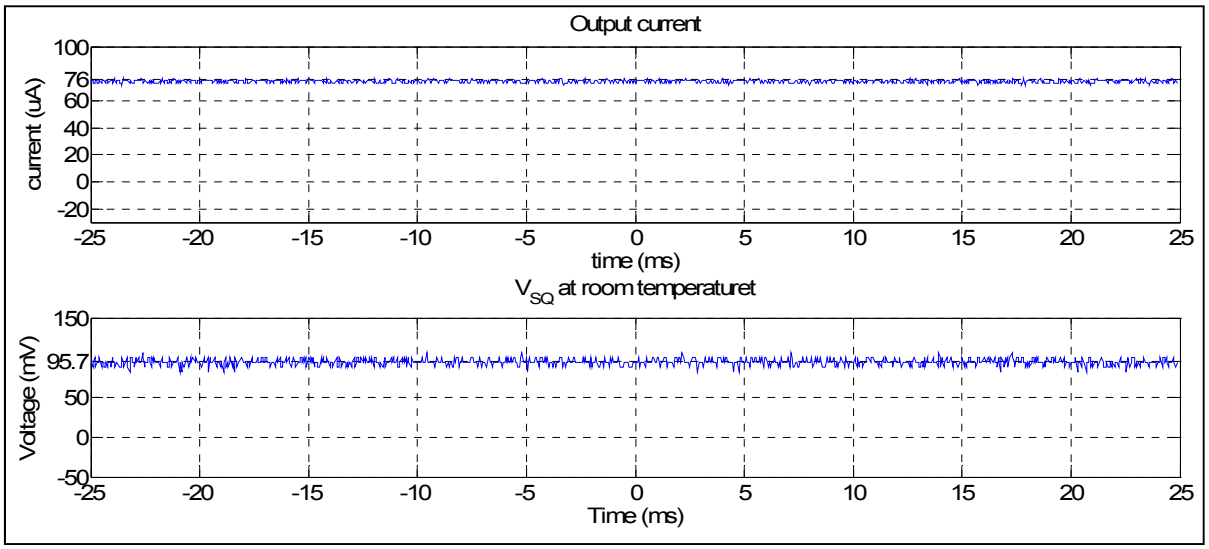

(a)

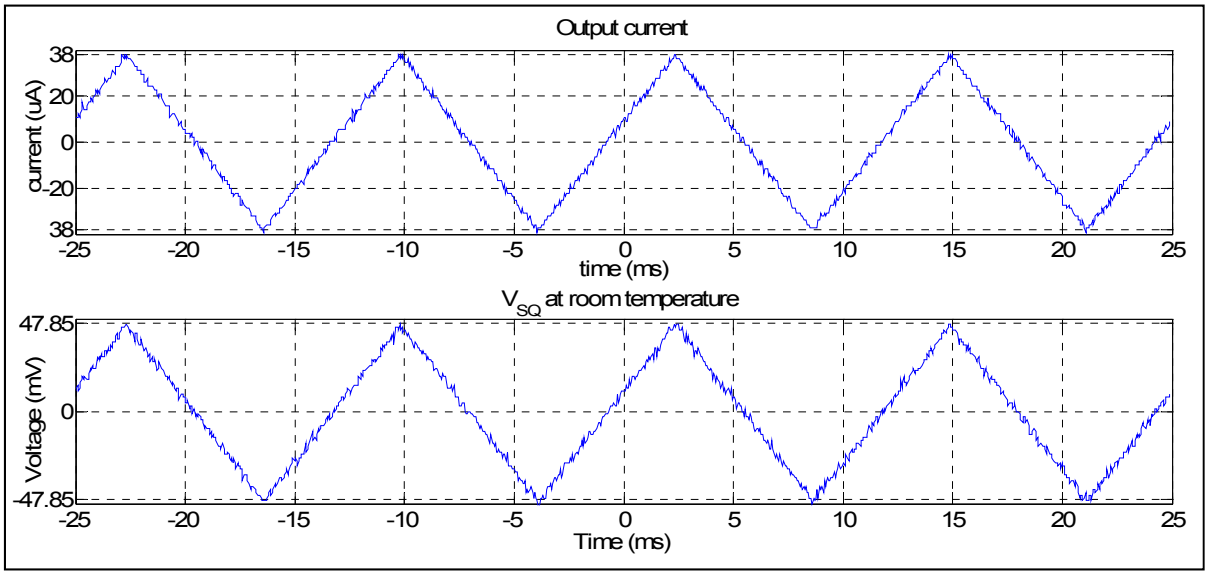

(b)

Figure 5.13: The voltage developed across the SQUID at room temperature, using a (a) DC bias current and (b) swept bias current of ± 38 µA at 80 Hz

The amplification was reduced to 30.0, in order not to drive the op-amp's output to saturation, due to the large SQUID resistance involved, and the corresponding output voltages are respectively presented in Figure 5.14 (a) and Figure 5.14 (b).

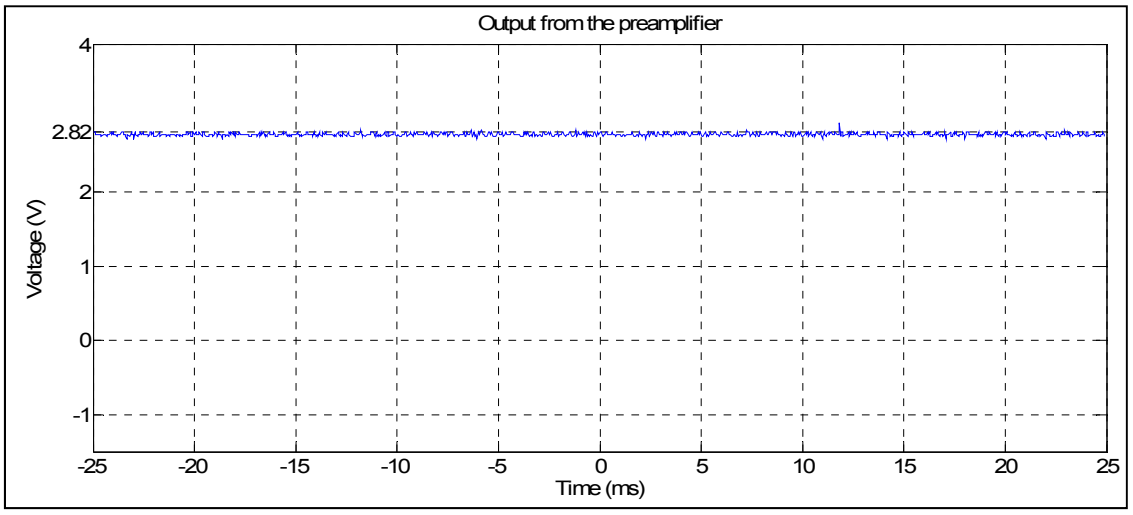

(a)

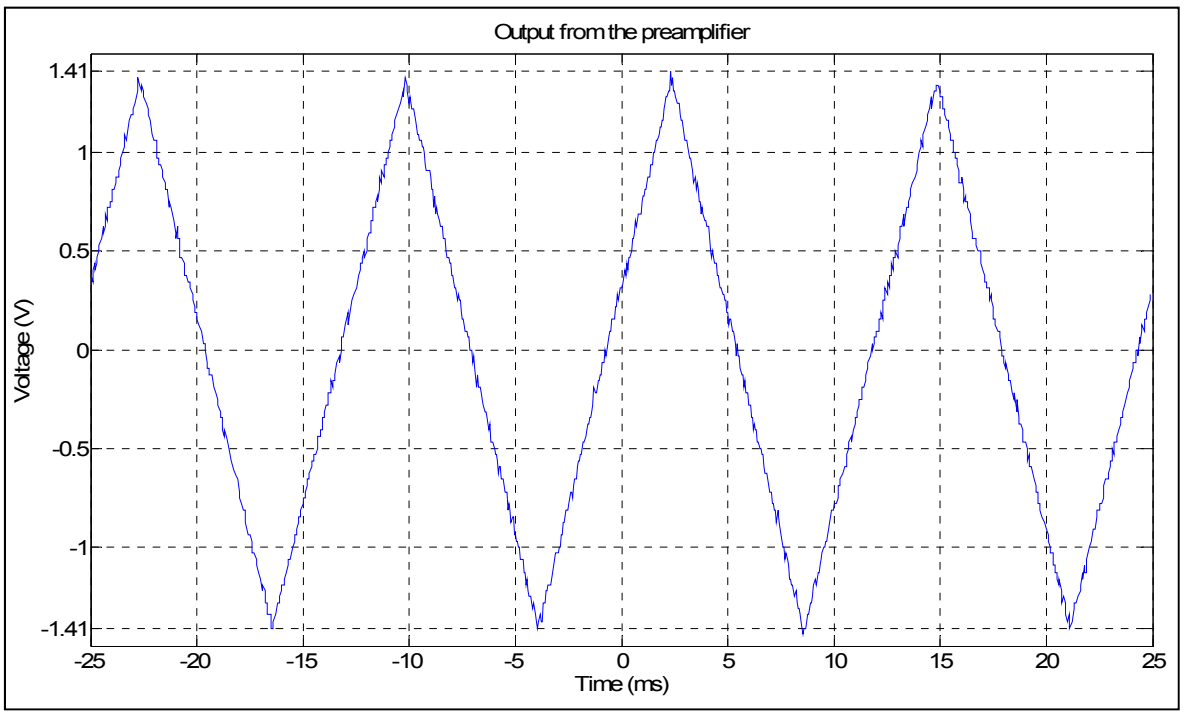

(b)

Figure 5.14: The output voltage from the preamplifier, using a (a) DC bias current and (b) swept bias current of ± 38 μA at 80 Hz

The SQUID's *V - I* curve displayed in Figure 5.15 was obtained by plotting the ± 38 μA bias current from Figure 5.13 (b) against the preamplifier's output from Figure 5.14 (b). A SQUID junction resistance of $R_n \approx 1.27$ kΩ can be inferred from the *V - I* curve, by dividing the slope by 30.0. This also agrees with the multimeter measurement.

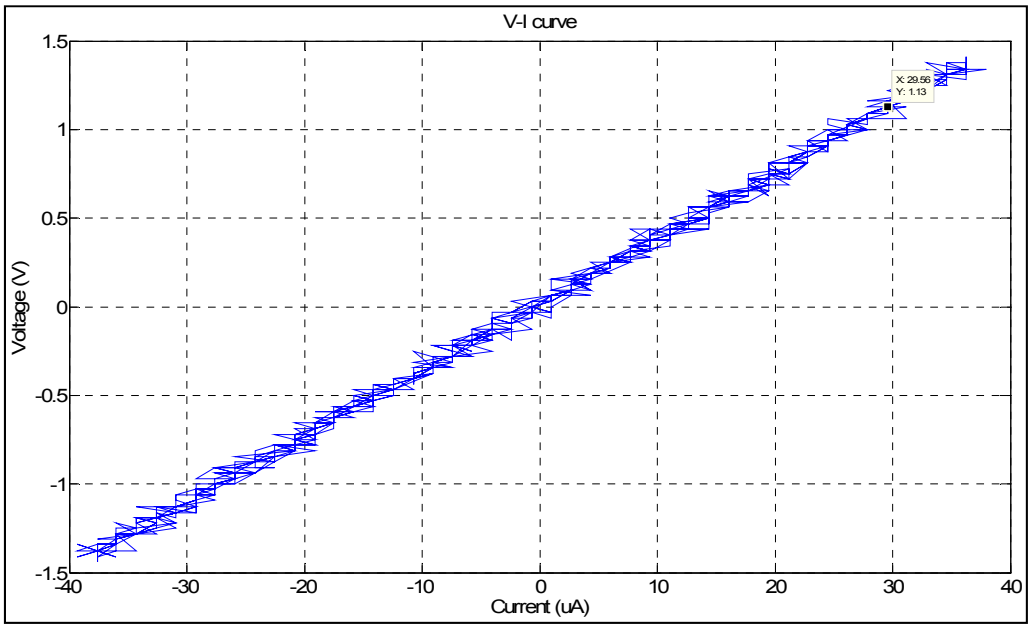

Figure 5.15: The SQUID's *V - I* curve at room temperature

5.3.3 Cryogenic temperature measurements on the SQUID sensor

As stated in section 2.11, it is only in the orbit that a cryogenic passive cooling can be achieved. The proposed passive cooling system for this mission has been modelled and simulated (chapter 4). However, in order to further verify the functionality of the M1000 SQUID acquired, Liquid Nitrogen was used to cool it down to 77 K. The dewar used is a very thick plastic bucket, with a small opening underneath the lid to allow connections to the sensor. Appendix G contains the picture of this dewar and the entire experimental set-up. The sensor was gradually lowered into the Nitrogen contained in the dewar, and allowed to cool for some minutes before taking any measurement. During heating up, the sensor was as well gradually removed from the Nitrogen and allowed to heat up to the room temperature.

After attaining the cryogenic temperature, the SQUID was in turn biased with a $36\,\mu A$ DC current, and further with a swept current of ± 38 μA at 80 Hz. For these two cases, Figure 5.16 (a) and Figure 5.16 (b), respectively, show the amplified voltages across the SQUID at cryogenic temperature. In order to suppress the intrinsic noise from the oscilloscope, an amplification of 747.32 was used. As expected of a DC SQUID magnetometer, its output voltage should be a modulating signal, if its bias current is some multiple of the critical current, $I_{c,av}$. As seen in Figure 5.16 (a), the modulation is not clean. SQUID exhibited this behaviour. More so, the output voltage displayed on Figure 5.16 (b) is not like the pure triangular pattern obtained when the SQUID was observed at room temperature (Figure 5.14 (b)). The resulting *V - I* curve is as displayed in Figure 5.17. This response is somewhat similar to a typical DC SQUID's *V - I* characteristic, as the simulations results presented in chapter 3 depict. However, the flat region, representing the maximum critical current where saturation of the supercurrent occurs, is more or less absent. This

region should cover 2 X the critical current, $I_{c,av}$ typically specified as 10 μA on the specification sheet (see Appendix A). At this region, resistanceless currents are said to flow through the sensor. A number of factors may be responsible for these anomalies. The available environment where the experiments were carried out is not free from magnetic contaminations. Some electronics (like computers, extractor hood, e.t.c.) that can generate magnetic and radio frequency interference (RFI) were present in and around the experiment room. RFI could have also been picked up by the cables used to connect the sensor to the electronics. In order to be able to have a swept current through the sensor, a signal generator (sig-gen) was used for the voltage input to the bias circuit. Since the signal generator uses the 230 V, 50 Hz mains, this is another source of interference on its own. Because SQUID magnetometers are highly sensitive, these unwanted signals were probably picked up by the sensor, thereby causing the JJs to saturate. This phenomenon is termed "*flux trapping*". Another possible cause of this anomaly is the fact that the measured room temperature resistance is rather too high. This might be blamed on a probable damage to any of the JJs, or degradation over time (i.e., aging factor).

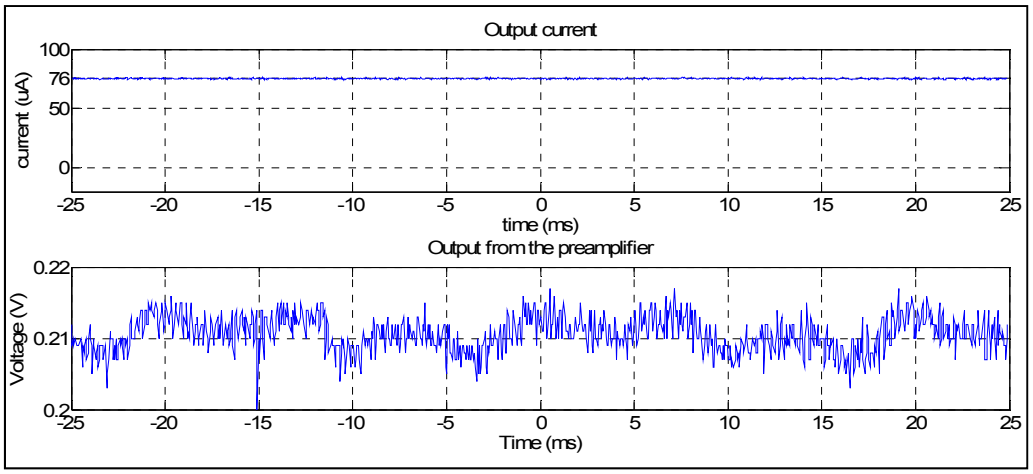

(a)

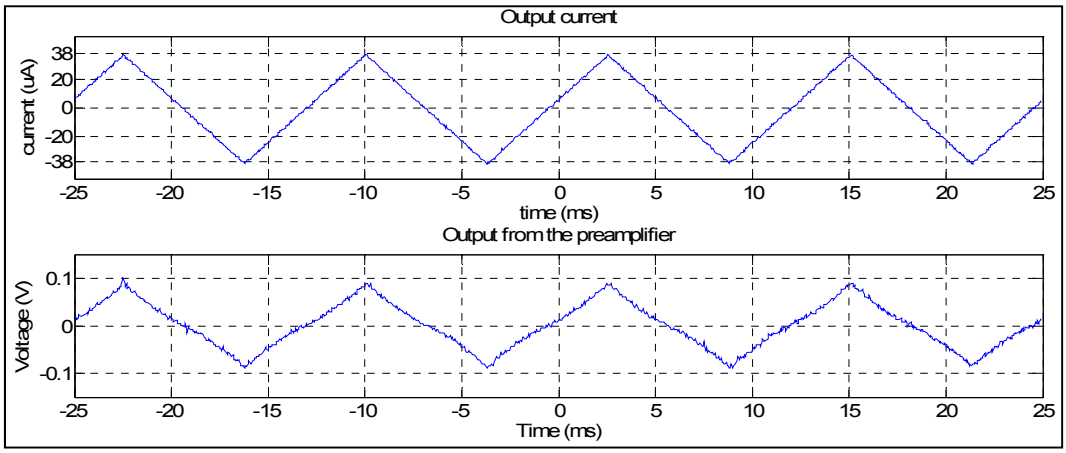

(b)

Figure 5.16: The amplified SQUID voltage at cryogenic temperature, using a (a) DC bias current and (b) swept bias current of ± 38 μA at 80 Hz

A magnet was brought closer to the dewar, so as to observe what happens to the SQUID's response. This was done both with a DC bias current and a swept bias current. The same responses displayed in Figure 5.16 and Figure 5.17 was observed. This is due to the effects mentioned earlier on. The evaluated sensor is the M19 package type of the M1000 magnetometer. This package did not come with any feedback inductor loop. A few turns of copper wire was made and taped to the sensor, so as to serve as the feedback inductor. This feedback coil was then further used for coupling a magnetic field to the sensor, by passing current through it. However, this did not affect the SQUID's response, due to the "*flux trapping*" effect.

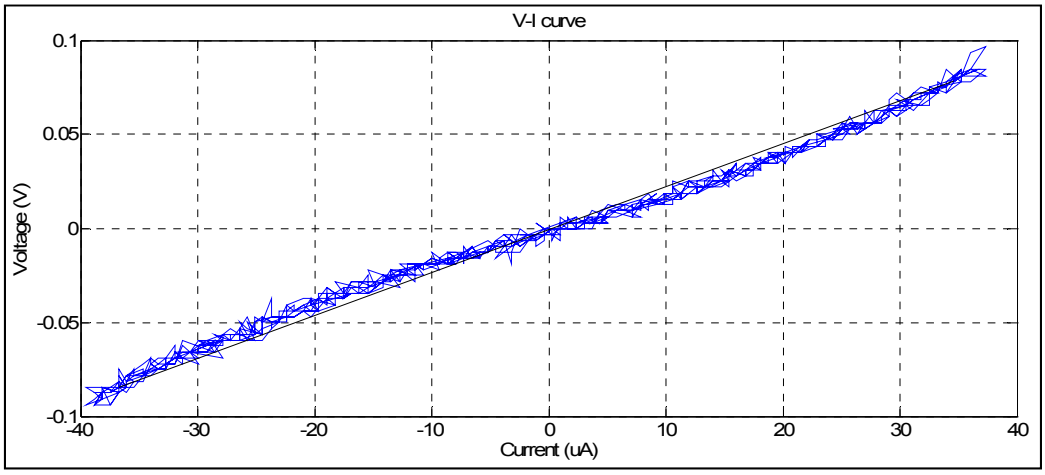

Figure 5.17: The SQUID's *V - I* curve at cryogenic temperature

With a preamplifier gain of 747.32, a junction resistance of R_n = 2X 3.05 Ω can be inferred from Figure 5.20, by determining the slope of a straight line (the black line on F) joining the two flat ends of the *V – I* curve. This value pretty much agrees with the cryogenic junction resistance of 6 Ω presented in the sensor's specification sheet. The Sensor was subjected to various cooling and heating cycles, and the measurements were taken repeatedly. No improvement was observed in the SQUID's responses, both with a DC and swept bias current. The room temperature junction resistance remained at 2 X 1.27 kΩ and the cryogenic resistance at 2 X 3.05 Ω. As such, the amplified SQUID's response did not lock using the electronics, when a triangular magnetic field patter was applied to the SQUID. An integrated version of the preamplifier's output could only be observed from the FLL's output. This is an indication that the applied field and the fed back signal did not couple to the SQUID sensor.

5.3.4 Mr. SQUID experiment

In order to further examine the sensor's attributes, a Mr. SQUID electronics box, acquired from the University of Stellenbosch, South Africa, was used to test the sensor. However, a lot of modifications had to be made, before the sensor could be adapted to the electronics. In place of the plastic dewar, a stainless steel dewar was used. Appendix G shows the front panel of the Mr. SQUID electronics, together the complete experimental set-up. The output labelled "*X*" is the bias current output from the electronics. However, since oscilloscopes can not read out currents, this output is a corresponding voltage across a 10 kΩ resistor. To obtain the actual current output from the scope, the reading must be divided by this resistance value. The output labelled "*Y*" is the output voltage across the SQUID sensor. To obtain the actual voltage, the reading must be divided by the amplifier's gain, which is 10, 000 (Simon, *et al*., 2004:12). In order to observe the sensor's behaviours at a constant bias current, knob "*1*" is turned to the left dirction ($V - I$ mode), while the amplitude knob ("*4*") is completely turned to the left. This amplitude knob can be turned back and forth, in order to have a current sweep through the sensor. Knob "*2*" is used to couple an external field to the sensor, through the feedback coil. In the case of the M1000 sensor used, the feedback coil is not available. This had to be manually made, using a few turns of copper wire. Since an oscilloscope was used as the output plotter, knob "*7*" was maintained at the "osc" position throughout the measurements.

As done with the fabricated electronics, the Mr. SQUID box was as well used to examine the sensor's behaviour at room temperature. Mr. SQUID's default preamplifier gain setting is 10,000. The results displayed in Figure 5.18 and Figure 5.19 show that the SQUID's voltage at room temperature is driving the Mr. SQUID electronics into saturation. This is due to the exorbitant room temperature resistance of the SQUID. The fabricated electronics was able to determine this resistance value, because it was easy to reduce the preamplifier's gain. As stated earlier, the expected room temperature resistance for the SQUID is 210 Ω (or in the few hundred Ohms), according to the M1000 SQUID datasheet (Star Cryoelectronics, 2011:2). This abnormality can either be blamed on junction damage, or degradation over time (i.e., aging factor).

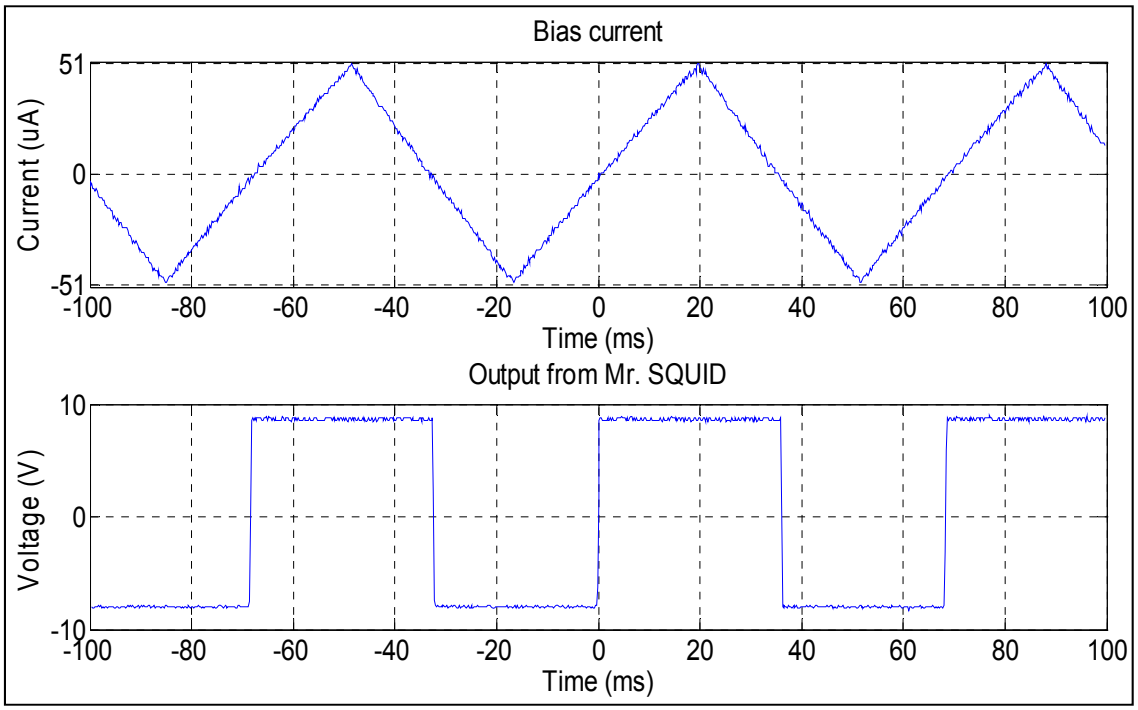

Figure 5.18: Output voltage sweep from the Mr. SQUID electronics with a swept bias current of ± 51 µA

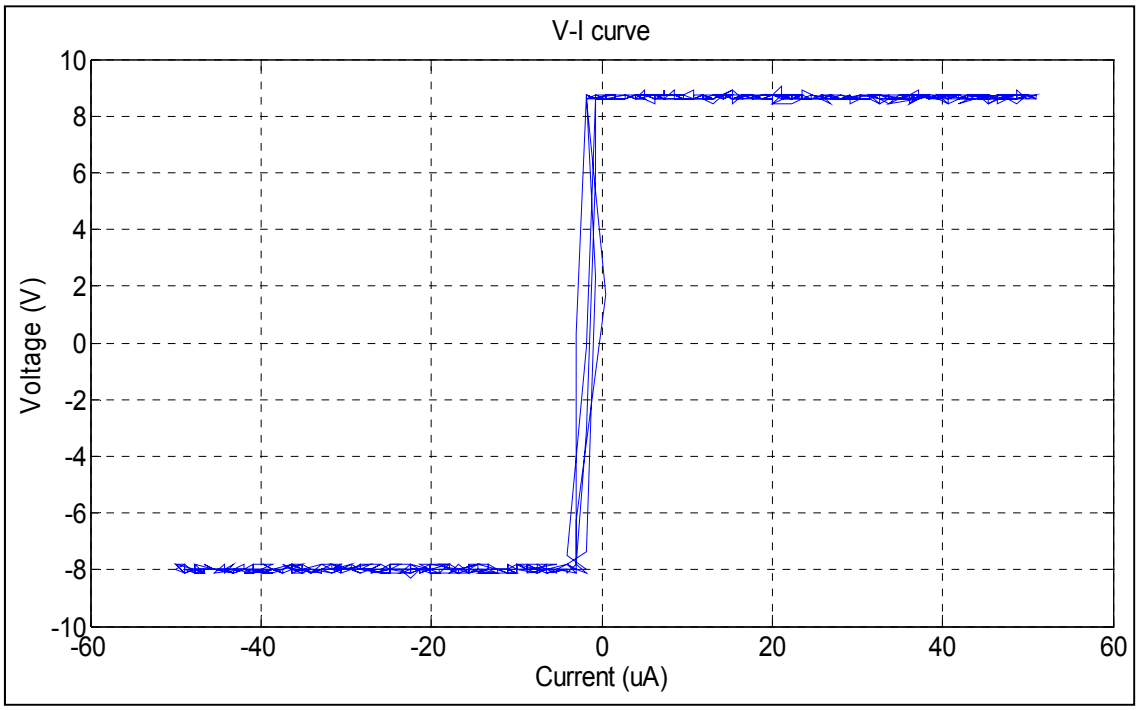

Figure 5.19: The voltage-current characteristic of the SQUID at room temperature

Figure 5.20 down to Figure 5.24 show the SQUID magnetometer's behaviours at various distances of an external magnet to the dewar, when being biased with a constant DC current of 42 µA. Without the application of any external field, the sensor's output voltage was observed to modulate at an offset of about 0.88 V (at a preamplifier gain of 10,000), but with the presence of some noise, due to "*flux trapping*". This is as shown in Figure 5.20. The output voltage is with an amplification of 10,000 from the Mr. SQUID preamplifier. The DC

offset in this response increased, when a strong magnet was placed against the dewar, with a better defined sinusoidal signal, as shown in Figure 5.21. This offset began to reduce as the magnet was withdrawn from the dewar at respective distances of 42 mm, 67 mm and 93 mm. These responses are respectively shown in Figure 5.22, Figure 5.23 and Figure 5.24. Although the signals were not very clear, due to the "*flux trapping*" from some parasitic RF signals in the vicinity, these changes, however, infer that the sensor is capable of sensing magnetic fields.

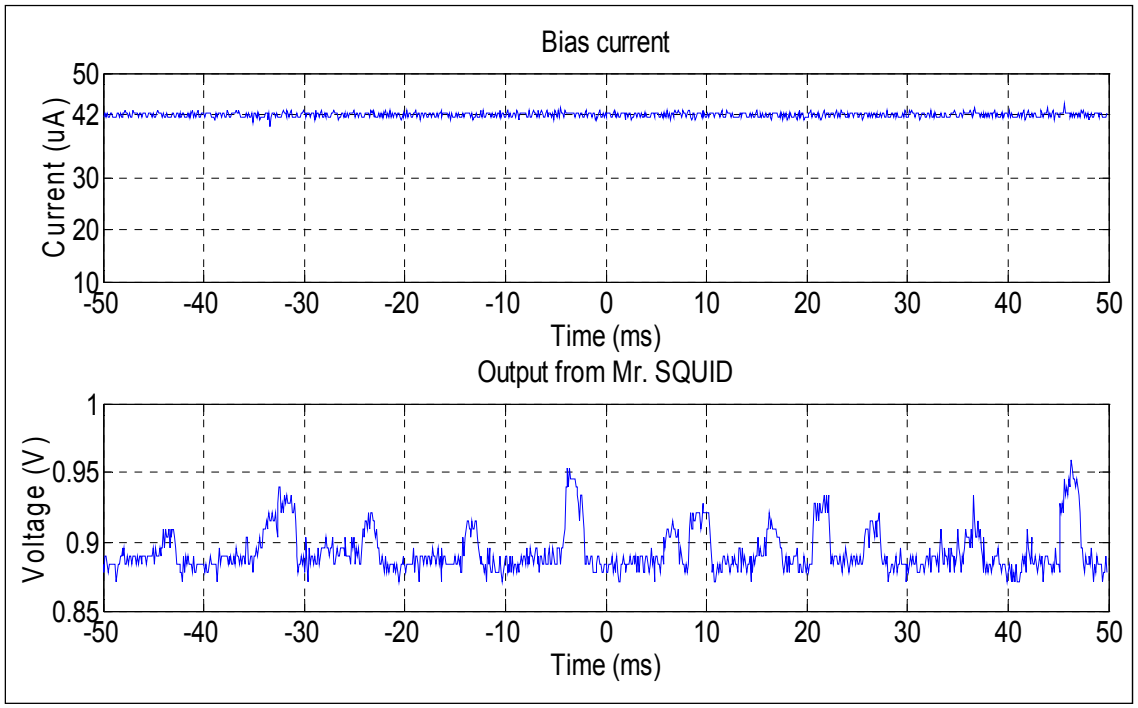

Figure 5.20: The SQUID's responses to a constant bias current of 42 µA, in the absence of eternally applied magnetic field

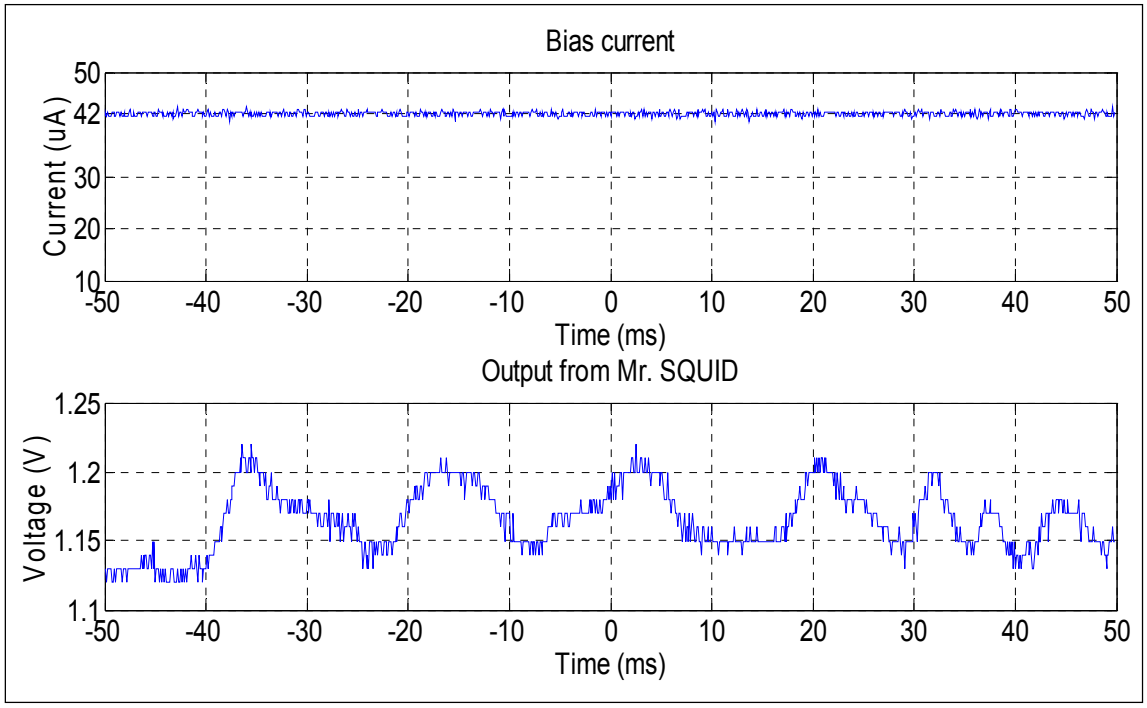

Figure 5.21: The SQUID's responses to a constant bias current of 42 µA, in the presence of eternally applied magnetic field from a magnet directly placed against the dewar

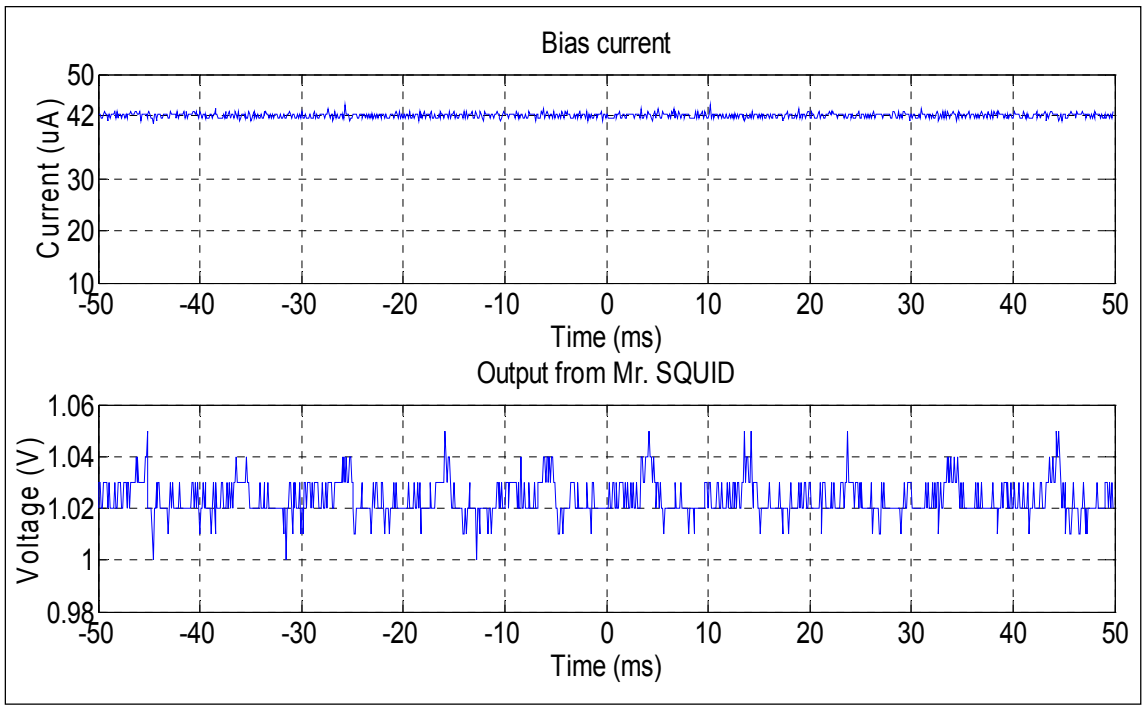

Figure 5.22: The SQUID's responses to a constant bias current of 42 µA, in the presence of eternally applied magnetic field from a magnet placed at 42 mm from the dewar

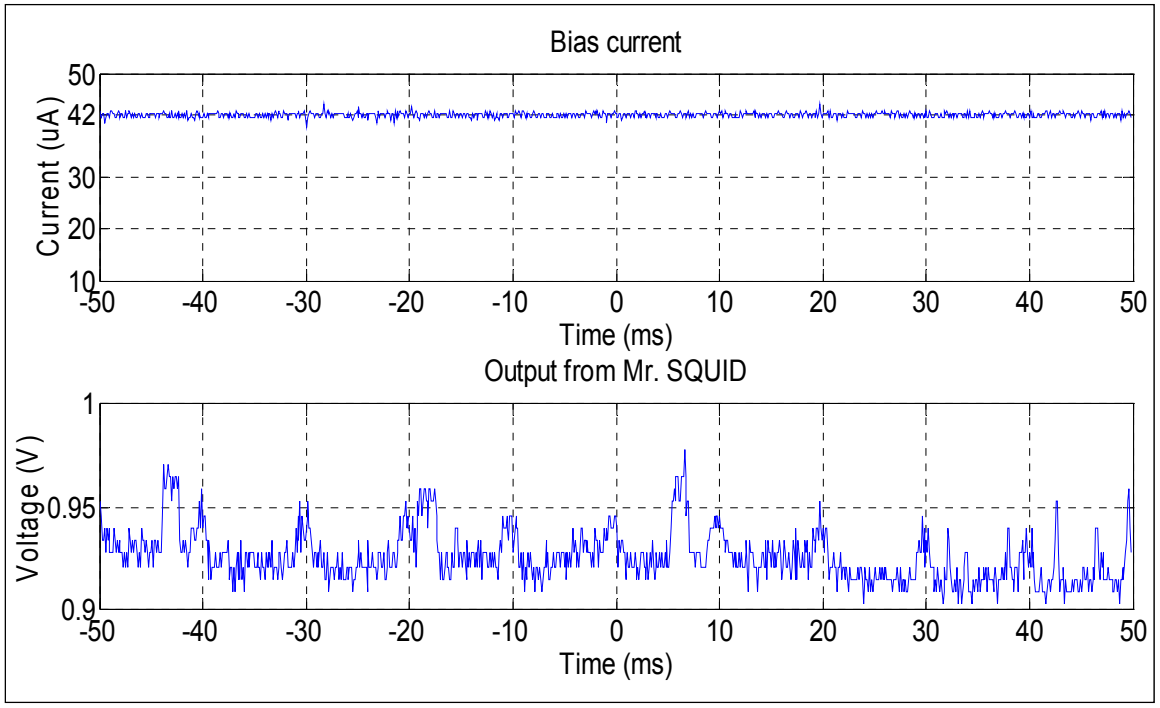

Figure 5.23: The SQUID's responses to a constant bias current of 42 µA, in the presence of eternally applied magnetic field from a magnet placed at 67 mm from the dewar

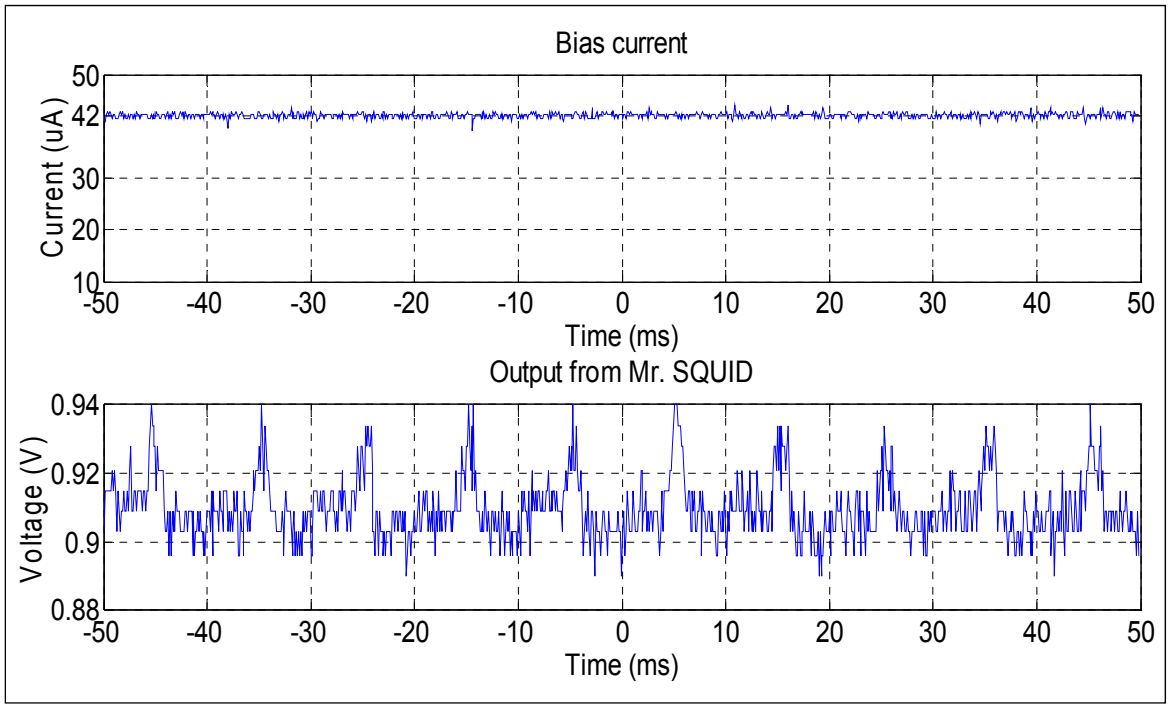

Figure 5.24: The SQUID's responses to a constant bias current of 42 µA, in the presence of eternally applied magnetic field from a magnet placed at 93 mm from the dewar

Figure 5.25 down to Figure 5.29 show the magnetometer's behaviours at various instances of an external magnet to the dewar, when the bias current was swept at ± 51.6 µA. Without the application of any external field, the flat region, representing the maximum critical current is clearly visible, as displayed on Figure 5.25. Here, the current flowing through the sensor is considered resistanceless. This is known as the Josephson effect. With a preamplifier gain of

10,000, a junction resistance of R_n = 2 X 2.5 Ω can be inferred from Figure 5.25. The R_n obtained, when the fabricated electronics was used, is R_n = 2 X 3.05 Ω, which is slightly higher than the one obtained here. This change is as a result of the "*flux trapping*" phenomenon, due to the nature of the dewar and power supply used for the fabricated electronics. This region reduced accordingly, as the magnet was brought closer to the dewar. This very much portrays the characteristics of the DC SQUID simulation results presented in section 3.2.6 and section 3.3.2. The small offset on the voltage axis is due to the offset from the preamplifier inside the Mr. SQUID box. This offset can be nulled by adjusting the op-amp offset compensator potentiometer if the control box can be opened up. This is a confirmation that the sensor is still functional. The seemingly flat region is not completely flat due to either flux "*trapping*", or the equivalent series resistance from the connecting cables between the sensor and the electronics. By comparing the outcomes of the Mr. SQUID experiments with those obtained from the fabricated electronics, better cryogenic responses were obtained from the Mr. SQUID box. This is because the supply to the box is from two 9V transistor batteries, which helps in screening the susceptibility of the output to some interference from the 50 Hz supply mains. Moreover, the dewar used is made of steel, which helps to mitigate the effects of some other magnetic disturbances in the environment.

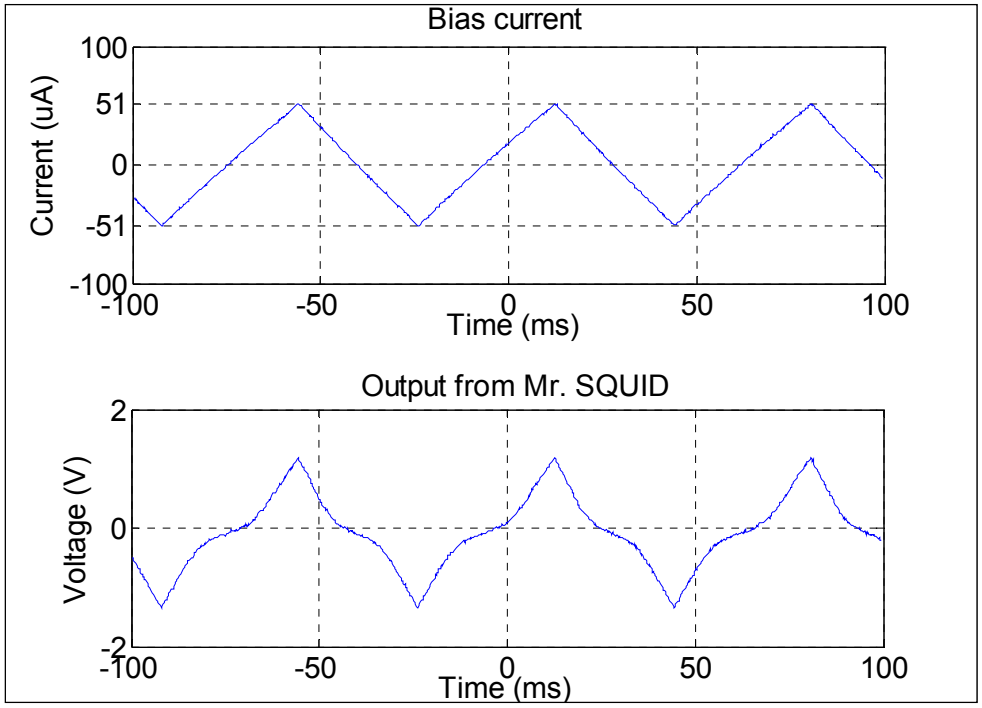

(a)

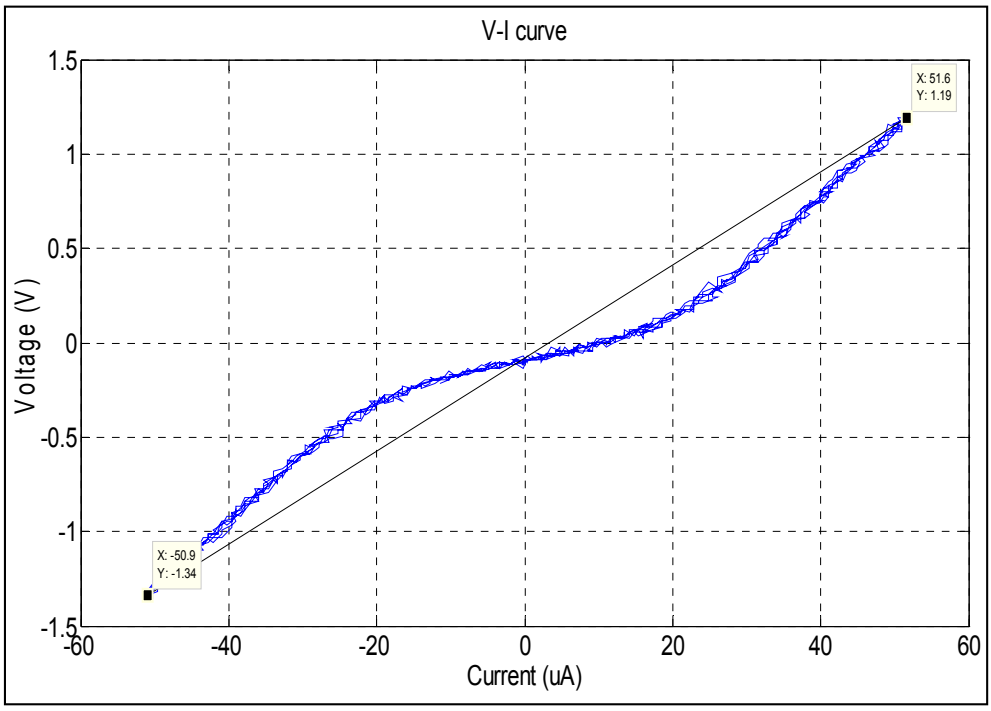

Figure 5.25: (a) The output voltage sweep from the Mr. SQUID electronics with a swept bias current of ± 51 μA in the absence of eternally applied magnetic field (b) The SQUID's *V - I* curve resulting from the swept current

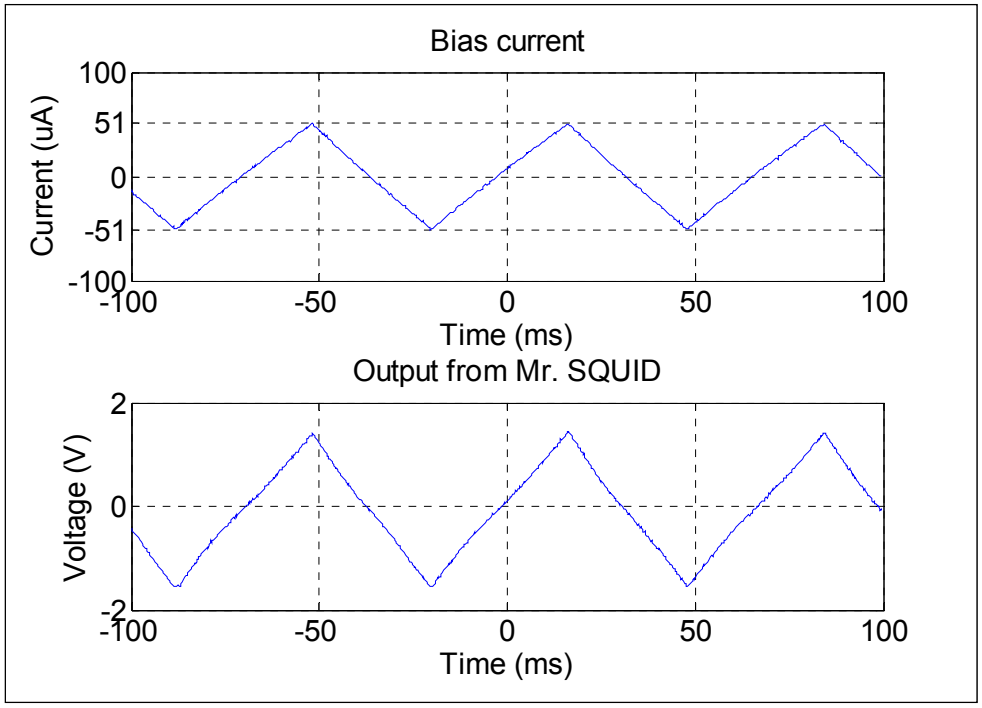

(a)

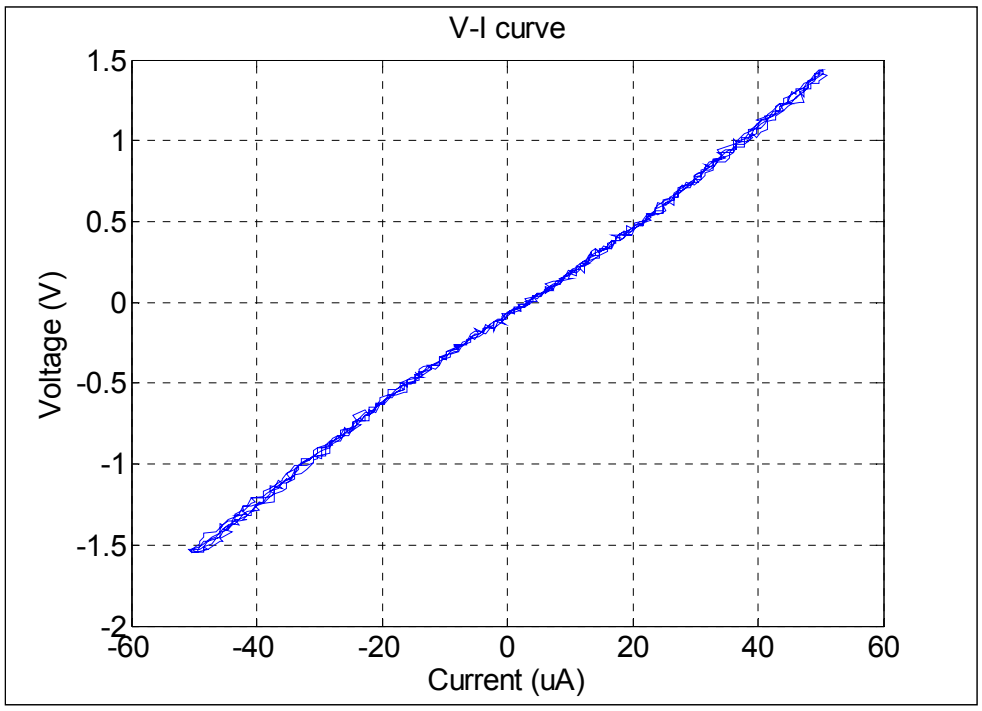

(b)

Figure 5.26: (a) The output voltage sweep from the Mr. SQUID electronics with a swept bias current of ± 51 μA in the presence of an eternally applied magnetic field from a magnet directly placed against the dewar (b) The SQUID's *V - I* curve resulting from the swept current

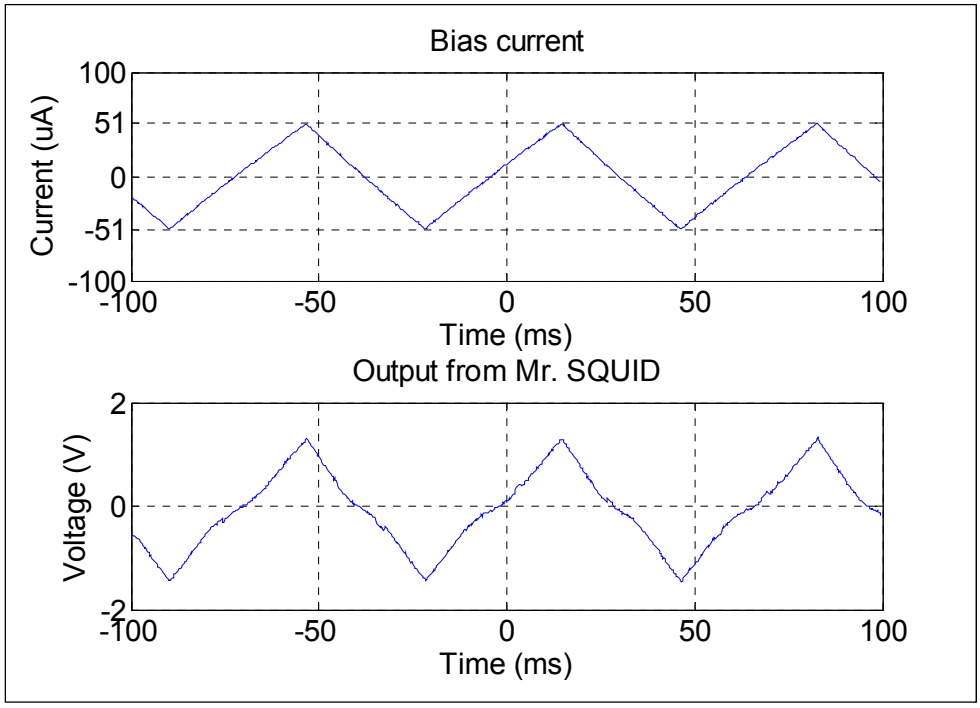

(a)

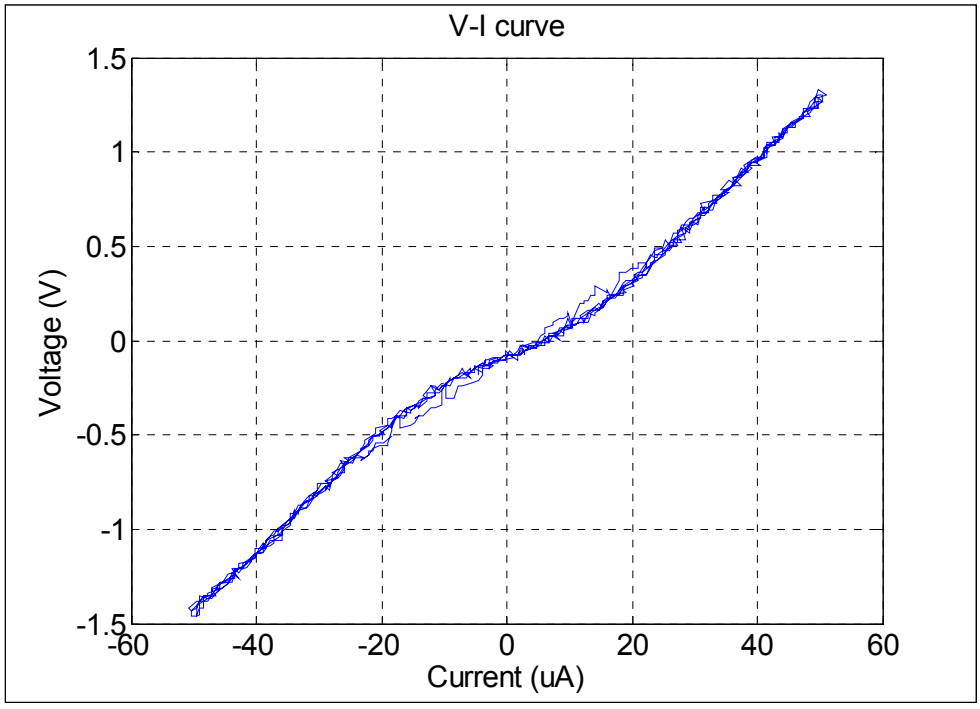

(b)

Figure 5.27: (a) The output voltage sweep from the Mr. SQUID electronics with a swept bias current of ± 51 μA in the presence of eternally applied magnetic field from a magnet placed at 42 mm from the dewar (b) The SQUID's *V* – *I* curve resulting from the swept current

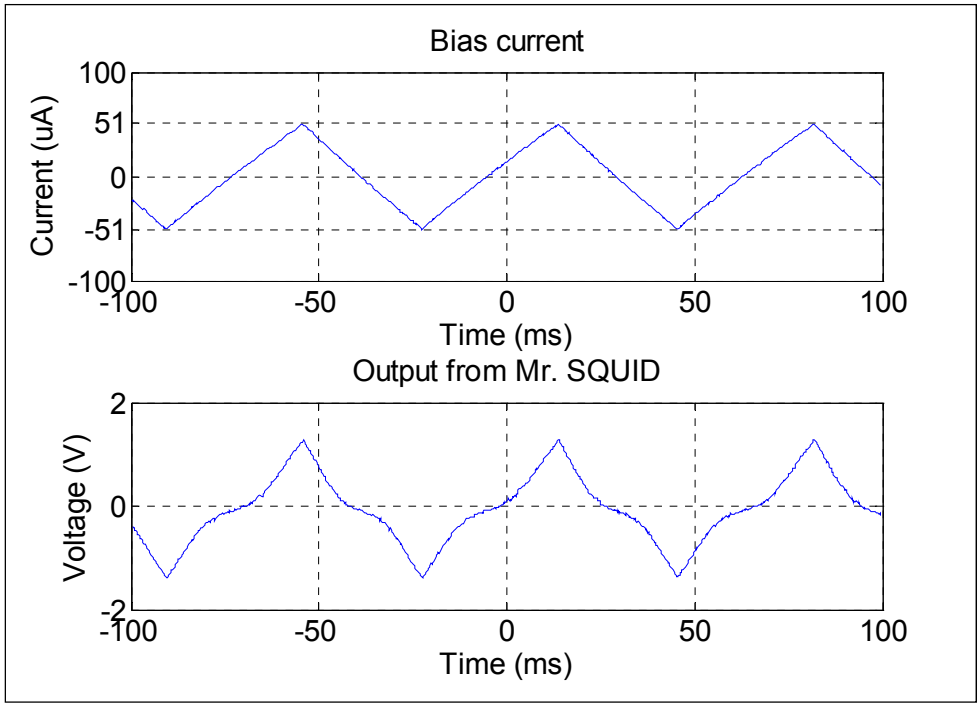

(a)

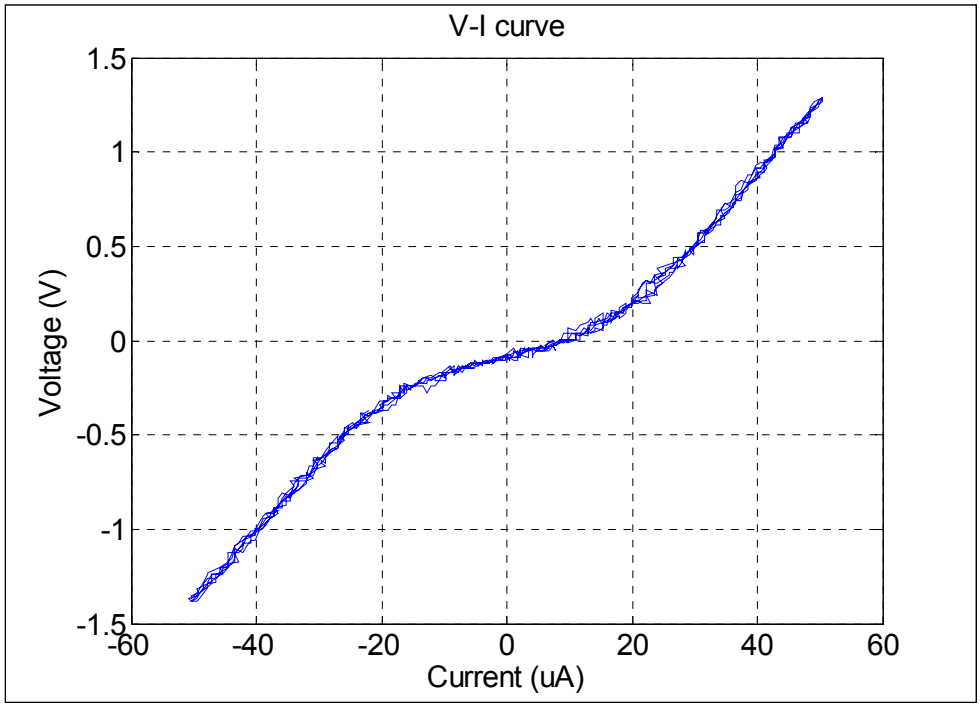

(b)

Figure 5.28: (a) The Output voltage sweep from the Mr. SQUID electronics with a swept bias current of ± 51 μA in the presence of eternally applied magnetic field from a magnet placed at 67 mm from the dewar (b) The SQUID's *V - I* curve resulting from the swept current

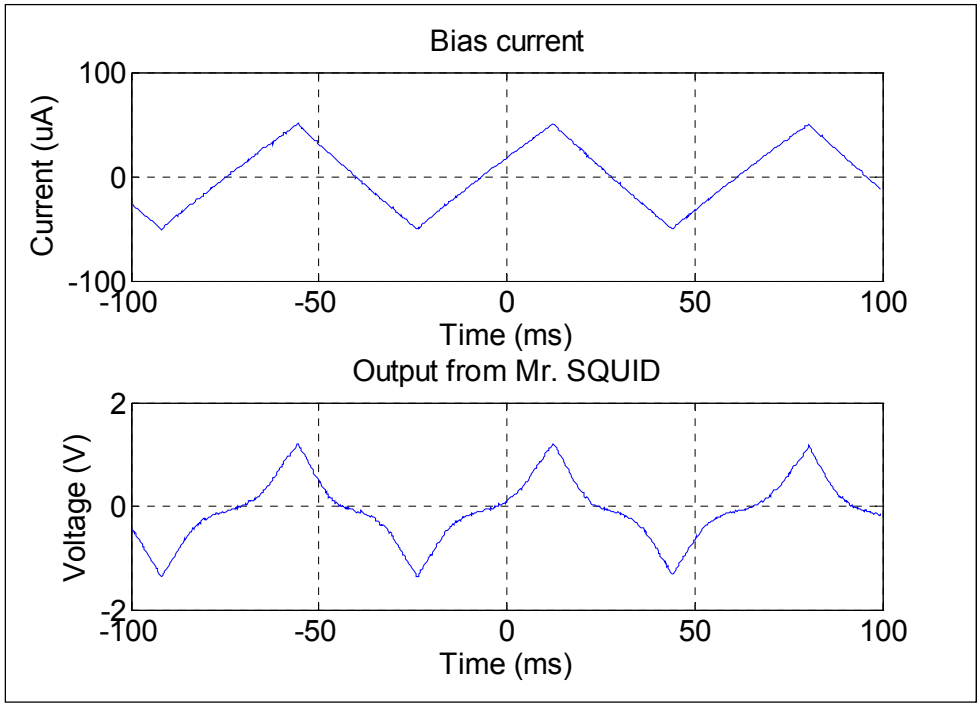

(a)

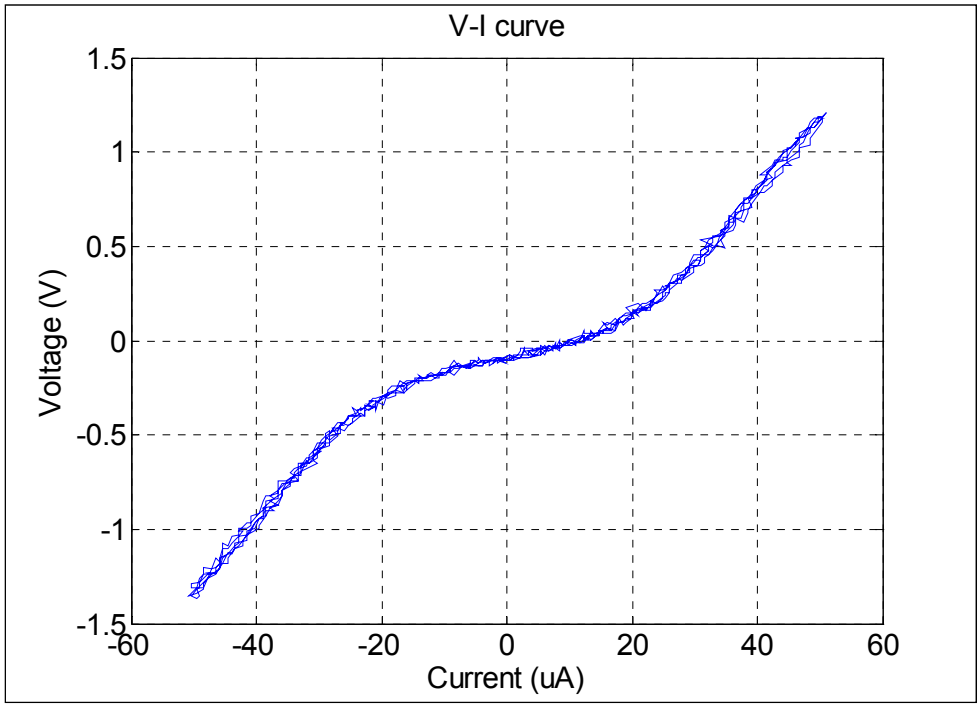

(b)

Figure 5.29: (a) The Output voltage sweep from the Mr. SQUID electronics with a swept bias current of ± 51 μA in the presence of eternally applied magnetic field from a magnet placed at 93 mm from the dewar (b) The SQUID's *V - I* curve resulting from the swept current

5.3.5 Radiation test

Because the evaluated sensor (i.e., M1000 DC SQUID) was acquired off-the-shelf, and it is not space-based, space qualification tests are thus inevitable, before it can be recommended for space applications. Based on the information contained in section 2.15, the DC SQUID sensor was first subjected to a TID of 50 Gy, without considering any safety factor. More dosage was envisaged to be considered if the sensor survived the initial dosage. The dosimetry involved was conducted by Prof. Kobus Slabbert at iThemba LABS, South Africa. The equipment used was an ADCL Medical Theratron 780-C. This is a Cobalt-60 ($^{60}C_0$) Teletherapy machine that generates irradiation of Gamma rays.

The initial calibration of the machine using the following procedures:

- A standard G-value of 15.5/100 eV radiation energy absorbed by ferric ion Fe^{3+} was determined using a Feric dosimeter
- Molar extinction coefficient for HP diode array spectrometer was determined at 304 nm using spectrosol grade Fe^{3+} solution. Optical density readings were made using a quartz glass flow cell
- The dosimeter was checked in $^{60}C_0$ radiation field. A 300 mm X 300 mm X 6 mm build-up was set-up to hold the EUT, and a 300 mm X 300 mm X 50 mm backscatter was placed over it. This is to ensure uniform irradiation on the EUT.
- The output factor was determined for the above, using tissue equivalent ionisation chamber calibrated in standard field of National Metrology Laboratory (CSIR).
- A dosage rate of 0.5041872 Gy/min. The entire duration of the radiation was done five times, over 20 min. intervals, thereby yielding a total irradiation of 50.4 Gy.

Appendix G contains all the set-up for the radiation testing. The radiation set-up is prone to some uncertainties. There may be differences of < 0.5% for repeated readings at each position. Only about 95 % confidence interval of a reading at any position is guaranteed.

The functionality tests were afterwards carried out on the sensor, but the results showed that the sensor has been damaged during the radiation exposure. The sensor's response to a constant DC bias current did not show any oscillation pattern, after cooling it down to 77 K. Figure 5.30 clearly shows this result. A DC output was observed, with the presence of some noise. The sensor can said to be acting like a pure resistance. The reaction was indifferent, even in the presence of an external magnetic field. The saturation of the supercurrent in the *V - I* curve was more or less absent, when a swept bias current was applied to the sensor. Figure 5.31 clearly shows this result. A normal state resistance of $R_n \approx 12.6\ \Omega$ was obtained from the *V - I* curve when a swept current was passed through the sensor, which is an indication of damaged JJs. When external magnetic field was brought close to the dewar, the sensor refused to modulate. Hence, the irradiation dosage can be said to have damaged the

sensor. This shows that unless radiation hardening is ensured, the sensor will not be able to withstand the radiation exposure in the LEO environment, if it is to be used for space weather applications.

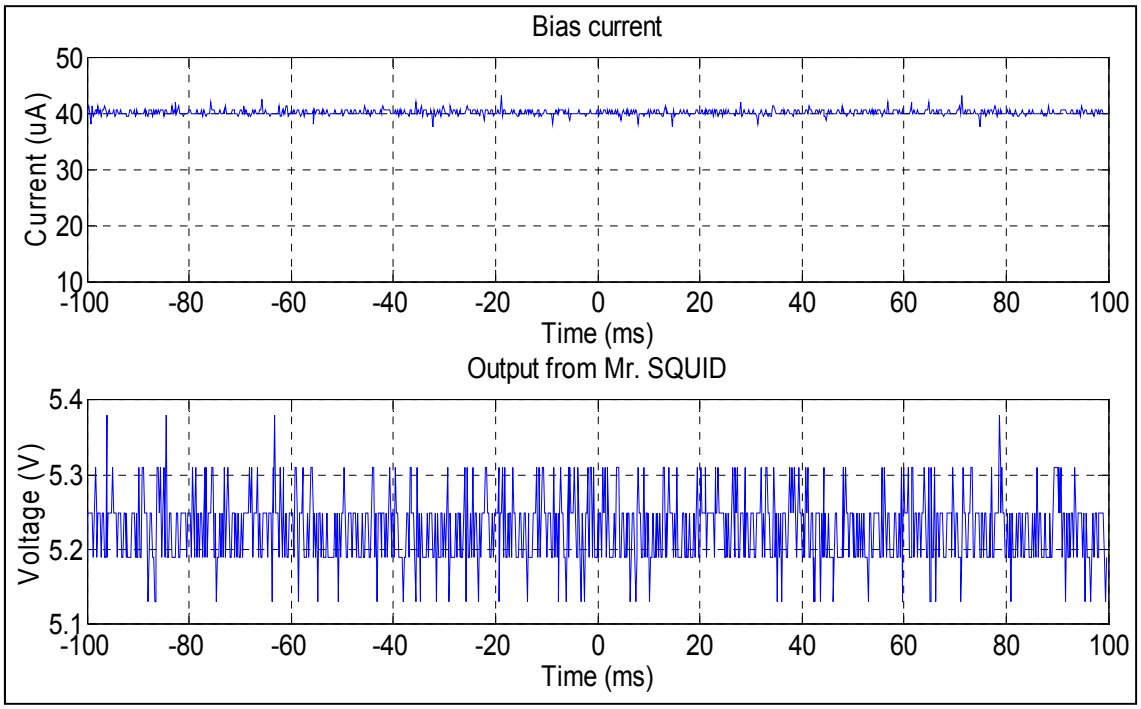

Figure 5.30: The SQUID's responses to a constant bias current of 40 μA, after radiation testing, in the absence of externally applied magnetic field

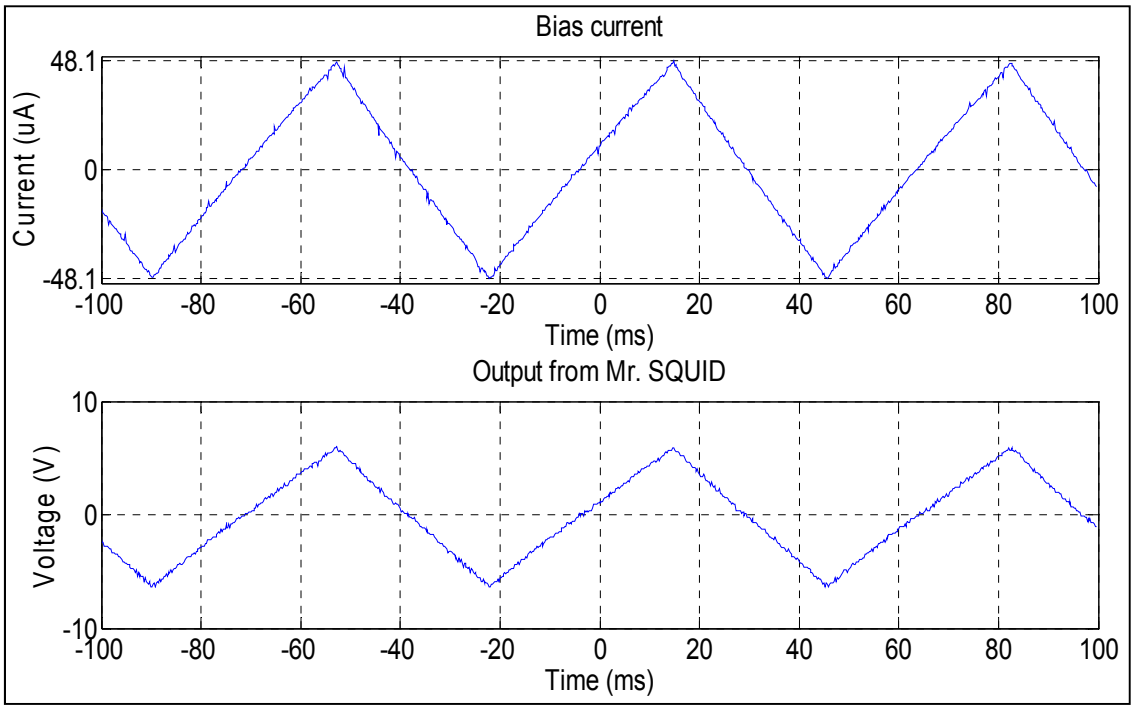

(a)

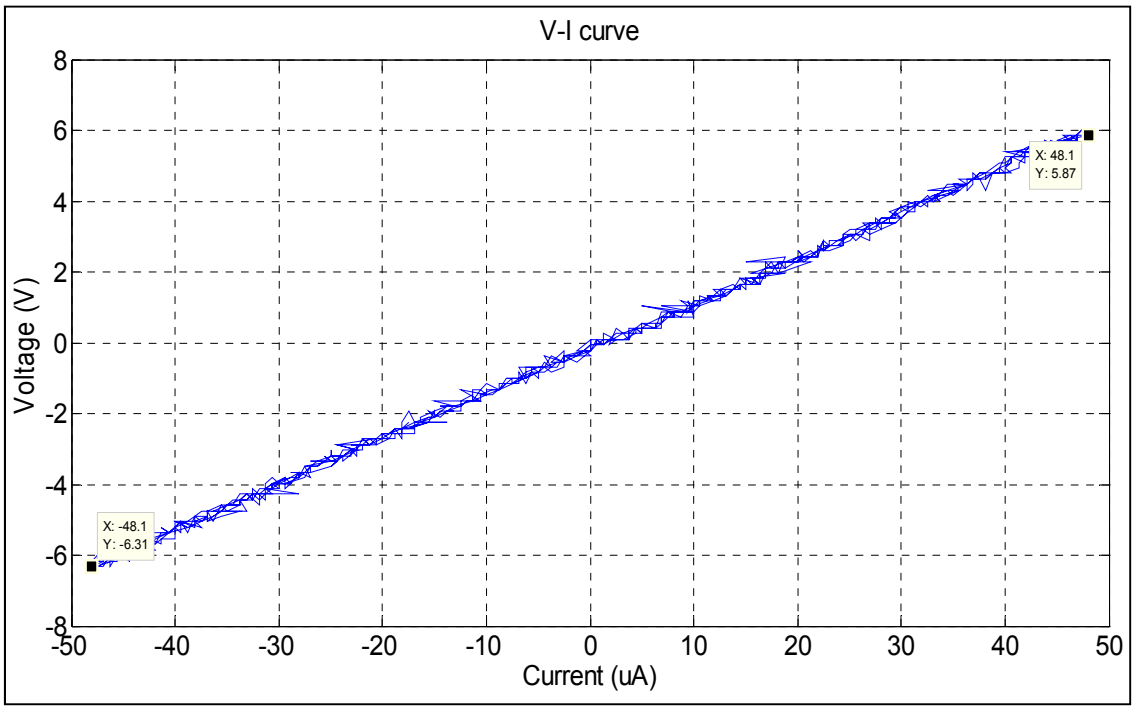

(b)

Figure 5.31: (a) The output voltage sweep from the Mr. SQUID electronics with a swept bias current of ± 48.1 μA, after radiation test, in the absence of an eternally applied magnetic field from a magnet directly placed against the dewar (b) The SQUID's *V - I* curve resulting from the swept current

5.4 Conclusion

This chapter has featured the experimental work carried out in this research. The design, fabrication and testing of the SQUID bias and readout circuits were presented. The compliance test results showed that the fabricated electronics function as expected. A dummy resistor was used to represent the sensor at room temperature, whose *V* - *I* relation turned out to be a linear graph, as expected of any purely resistive load. The room temperature measurement carried out on the SQUID sensor indicated a combined junction resistance of 1.27 kΩ, which quite disagrees with the expected value (210 Ω) specified by the manufacturer. The cryogenic measurement indicated a combined junction resistance of 3.05 Ω, which agrees with the expected cryogenic combined resistance of 3 Ω. The SQUID's *V* - *I* relation obtained resembles that of a typical DC SQUID magnetometer, but the maximum critical junction current, where resistanceless currents flow, seemed not to appear. The anomalies observed in the sensor's characteristics are due to a probable damage to the junctions, degradation over time, or flux "*trapping*", considering the environment where the test was carried out, together with the interference from the 50 Hz supply mains. The designed FLL could not be used for appropriate measurement and eventual calibration of the SQUID magnetometer, due to the absence of the cryogenic feedback coil and other observed anomalies. Attempts were made to make an external feedback coil, but the coil refused to couple magnetic fields to the sensor. More so, the sensor could not survive the space radiation test, which suggests the use of radiation hardening materials like plastic, lead, steel, or lumber wood, to envelope the sensor. This will mitigate the expected radiation effect in the LEO orbit, when the sensor is used for space applications.

CHAPTER SIX

CONCLUSION AND RECOMMENDATIONS

6.1 Introduction

This research is a foundational work, meant to establish the usability of a SQUID magnetometer for nanosatellite space weather missions. Hence, the research is structured, so as to be referenced for future research work. This in turn will help to improve the existing models that predict space weather conditions. This chapter briefly highlights the entire work done, discussing the successful progression from the theoretical background presented in chapters 1 and 2, to the simulations and experimental work presented in chapters 3, 4 and 5.

6.2 Summary

It is so pertinent for space engineers to be able to effectively predict the space weather, because its effects could be severe on the orbiting satellites, so as to be able to design space hardened subsystems in the satellites. Variation in the Earth's magnetic field is a dominant indicator of space weather storm. Hence, a highly sensitive magnetometer is needed for monitoring this variation. SQUID magnetometers are known to be the most sensitive magnetic field measuring instrument. They convert the sensed magnetic fields into sinusoidal outputs, which are in turn linearised by flux locked loop circuits. Their operation requirement is, however, stringent, due to the cooling mechanism needed for cooling them down to their critical (transition) temperatures.

6.2.1 Miniaturisation requirements

Space constraint is a major concern in any nanosatellite mission. As such, the evaluated sensor is a M100 DC SQUID magnetometer with a field calibration of 12 nT/Φ_0 and a foot print of 9 mm x 9 mm, acquired off-the-shelf. This sensor operates at a critical cryogenic temperature of 77 K. These properties, together with the proposed cooling system helped in addressing the question of what brand of a sensitive and miniaturised SQUID magnetometer system will be suitable for nanosatellite missions.

6.2.2 Modelling and simulation of the SQUID magnetometer

Simulating the sensor is necessary in order to know what to expect, when the sensor is subjected to real life experiments. The theoretical background presented in chapter 2 was applied in the simulations and experimental work carried out. A very good platform for observing the SQUID magnetometer's behaviour, in simulation sense, was presented in chapter 3, including the required readout electronics needed to linearise its output. Both PSIM and MATLAB-Simulink were the software used for the simulation work. This therefore helped in addressing the question of how to simulate the SQUID magnetometer's behaviour.

The simulation results, presented in chapter 3, conform to what are obtainable in the consulted literature.

6.2.3 Modelling and simulation of the proposed passive cooling system

The SQUID magnetometers' usage in space (especially on nanosatellites) is limited, due to the difficulty in providing suitable and durable cryogenic temperature (77 ± 1 K in this case) for their operations. Since nanosatellites have the constraints of both power and volume, a passive cooling system was proposed. Simulation of this cooling system was performed, using Thermal Desktop software, as reported in chapter 4. The largest dimension of the modelled cooler structure is 100 mm. The entire size of the cooler provides a good chance of getting it accommodated in the nanosatellite structure. The cooling power achieved in the simulation further proves the possibility of having such a cooling system on a nanosatellite for conditioning the sensor to the desired cryogenic temperature of 77 ± 1 K. This therefore satisfied the question of how to maintain the desired operating conditions for the magnetometer.

6.2.4 Stray magnetic shielding mechanism

The satellite structure itself can serve as a source of magnetic field, due to the operation of some RF components therein. Since the mission is meant for sensing only the Earth's magnetic field, a mechanism was proposed in order to prevent this magnetic contamination from reaching the sensor. This was put into consideration in the modelling and simulation of the proposed cooling system. The entire set-up (i.e., the cooler-sensor assembly) is made deployable at a distance from the satellite structure, using a boom length of 100 mm, so as to mitigate the magnetic field emanating from the satellite. This thus addressed the issue of how to shield the whole assembly from the satellite's stray magnetic field.

6.2.5 Integration of the cooler-sensor assembly into the satellite

Due to the space constraints in the launch vehicle, the cooler-sensor assembly cannot be lunched in a deployed state. A mechanism to get them accommodated in the launch vehicle during the launch process was therefore proposed. The entire assembly are to be confined in the satellite structure until orbit insertion is completed, before finally deploying it. The modelling work done on this was reported in chapter 3. Since the cooler's dimensions are not bigger than the satellite structure itself, and the entire cooler-sensor assembly is to be deployed after launch, the question of how to integrate the assembly into the satellite is thus addressed. All the needed physical mechanical details to accomplish this shall be considered in the future research work.

6.2.6 Modification requirements

The acquired sensor could not be directly adapted into the satellite, due to some constraints like the limited space and power supply. These were considered in the manufacturing of the electronics needed to power the sensor and interpret (linearise) its output. As such, the electronics were designed to be very simple, avoiding any possible form of sophistication. They were designed to run on a 5 V DC supply. The evaluated sensor was not built into a probe, as it is the practice of most of the conventional SQUID magnetometer set-up. Its input and output terminals were directly adapted to the electronics, using connection cables. This approach, together with the fabricated electronics, help in conserving the power consumption and space in the nanostellite structure. Hence, the question of what modifications to be made in order to make the sensor suitable for the mission was addressed. The electronics functioned as expected, when tested. The room temperature experiment carried out on the M100 SQUID magnetometer, acquired off-the-shelf, posed a challenge on its integrity due to the abnormal junction resistance obtained. The SQUID's behaviours observed at cryogenic temperature, through the aid of the designed electronics, somewhat resemble what is obtainable in the literature. The measured cryogenic resistance was satisfactory. The *V - I* response obtained was relatively linear, due to "*flux trapping*", interference from the 50 Hz supply mains, Josephson junction degradation and the nature of the plastic dewar used. As a result of this, a Mr. SQUID electronics box, equipped with much shielding facilities, was further used to evaluate the sensor's behaviours, which gave better results, but with the presence of a little bit of "*flux trapping*". Before the electronics box could be used, the sensor's terminals had to be further adapted to the output and input ports on the box. Of course the use of a steel dewar in place of the plastic type contributed to the better results obtained with the Mr. SQUID electronics. The sensor's output could not be linearised, due to the absence of the cryogenic feedback coil and the presence of the observed anomalies in the sensor's behaviours.

6.2.7 Qualification test

It is obvious that the sensor will be subjected to a lot of electromagnetic radiations, which can affect its functionalities and durability, when launched into space. It was therefore necessary to subject it to space radiation test before it can be placed in the orbit. The review in chapter 2 shows that a total ionising dose (TID) of 5 krad (i.e., 50 Gy) is to be expected by the unshielded COTS device in the LEO orbit, for a total life time of about 2 years. A total TID of 100 Gy was therefore decided, considering a safety factor of 2 for the radiation test. This was to be achieved in two stages, using 50 Gy per stage. However, the sensor could not survive the first stage of the radiation test. This means there is a need for radiation hardening materials to envelope the sensor, if it must be used for space application. This will mitigate

the expected radiation effect in the LEO orbit, when the sensor is used for space applications.

6.3 Future work

For the fact that most of the results of this research are positive, it is therefore reasonable to consider future improvements on the work. The use of standard high-precision IC components, that are space hardened, are suggested to be used in designing the SQUID readout electronics, instead of the sub-standard components used for the prototype in this research. A brand new DC SQUID sensor, whose integrity is still fully intact, is as well suggested to be acquired. This new sensor should be radiation-hardened in order to prevent any radiation-related damage in the orbit. Shielded cryocables should be used for making connections between the sensor and its electronics, in order to prevent the "*flux trapping*" phenomenon experienced in the testing of the prototype electronics. Proper RF shielding should be put in place, in order to prevent any RFI (radio frequency interference) that can contribute to the "*flux trapping*" phenomenon. DC transistor batteries should be used as the supply to the electronics, so as to reduce the interference from the 50 Hz mains, which can interfere with the sensor's output. For data logging and processing, the use of an analogue to digital converter (ADC) is suggested for digitising the FLL's output. Materials like plastic, lead, steel, and lumber wood should be evaluated and used for hardening the sensor against the radiation damage experienced in this research.

6.3 Publications in press

Ogunyanda, K., Fritz, W. And van Zyl, R.R. PSIM simulations of a DC SQUID magnetometer. Journal of Engineering Design and Technology. (Date submitted: 28 November, 2012).

BIBLIOGRAPHY

Acuna, M.H. 2002. Space-based magnetometers. *Review of Scientific Instruments*, 73(11): 3717-3736.

Al-Alaoui, M.A. 1989. A novel approach to designing a noninverting integrator with built-in low frequency stability, high frequency compensation, and high Q. *IEEE Transactions on Instrumentation and Measurement,* 38(6): 1116-1121.

Analog Devices. n.d. Micropower, Single and dual supply rail-to-rail instrumentation amplifier.

Barnard, A., & W.H. Steyn. 2007. Low cost TID testing of COTS components. *IEEE Radiation and Its Effects on Components and Systems (RADECS) Conference*, 1-4.

Basso, V.G., Perold, W.J. & Lourens, J.G. 1998. A Dual SQUID Linearization Concept Using a Phase Modulation Scheme. *IEEE Transactions on Applied Superconductivity ASC,* 8(3): 125-131.

Bennett, C.L., Halpern, M., Hinshaw, G., Jarosic, N., kogut, A., Limon, M., Meyer, S.S., Page, L., Spergel, D.N., Tucker, G.S., Wallack, E., Wright, E.L., Barnes, C., Greason, M.R., Hill, R.S., Komatsu, E., Nolta, M.R., Odegard, N., Peiris, H.V., Verde, L. & Weiland, J.L. 2003. First year Wilkinson microwave anisotropy probe (WMAP) observations: preliminary maps and basic results. Astrophysical Journal, 3: 1-43.

Beucher, O. & Weeks, M. 2006. *Introduction to MATLAb & simulink: a project approach*. New Delhi: Hingham, Massachusetts.

Beyer, J. Drung, D. Ludwig, F. Minotani, T. & Enpuku, K. 2009. Low-noise $YBa_2Cu_3O_{7-x}$ single layer DC superconducting quantum interference device (SQUID) magnetometer based on bicrystal junctions with 30° misorientation angle. *Applied Physics Letters*. 72(2): 203-205.

Billingsley Aerospace. 2005. Space Qualified Attitude Control Magnetometers. http://www.magnetometer.com/dsgnqual.php. [29 October 2012].

Buchal, C.H. & Welter, J.M. 1983. Rhodium sets new standards: superconductivity near absolute zero. *Platinum Metals Rev.,* 27**,** (4): 170-174.

Burger, W.A. 2008. The design and analysis of a DC SQUID for a SQUID microscope. Unpublished thesis, Stellenbosch University, South Africa.

Burr-Brown. 1996. White Paper on high performance operational amplifiers. Dallas.

Carr, C., Macfarlane, J.C. & Donaldson, G.B. 2003. A Fully Portable, Cryocooler-Based HTS SQUID NDE Instrument. *IEEE Transactions on Applied Superconductivity ASC,* 13: 245-249.

Chui T., Bock J., Holmes W. & Raab J. 2010. Thermal design and analysis of a multi-stage 30 K radiative cooling system for EPIC. *Cryogenics Cryogenics,* 50(9): 633-637.

Ciampolini, L., Ciappa, M., Malberti, P., Regli, P. & Fichtner, W. 1999. Modelling thermal effects of large contiguous voids in solder joints. *Microelectronics Journal,* 30(11): 1115-1123.

Clark, C., Strain, A. & Mazarias, A.L. n.d. A high performance, very low cost power system for microspacecraft. www.clyde-space.com/documents/1497. [12 April 2012].

Clarke, J. & Braginski, A.I. 2004. *The SQUID handbook: vol. I, fundamentals and technology of SQUIDs and SQUID systems.* Sl Weinheim: Wiley-VCH.

Clarke, J. & Braginski, A.I. 2005. *The SQUID handbook: vol. II, Applications of SQUIDs and SQUID systems.* Sl Weinheim: Wiley-VCH.

Cleveland, P.E. & Parrish, K.A. 2005. Thermal System Verification and Model Validation for NASA's Cryogenic Passively Cooled James Webb Space Telescope (JWST). *S.A.E. transactions*, 114:518-528.

Cobham. 2009. LC1061 linear cryocooler (light weight 1 What). http://www.cobham.com/media/64933/ADV10575.pdf. [5 August 2011].

Daniel, B.Y. 1998. Electronic characteristics of SQUIDs. Unpublished BSc thesis, Massachusetts Institute of Technology.

Diaz-Michelena, M. 2009. Small Magnetic Sensors for Space Applications. *Sensors*, 9:2271-2288.

DiPirro, M. n.d. Cryogenic technology for CM-pol: passive cooling and stored cryogen systems. NASA/Goddard Space Flight Centre. http://cmbpol.uchicago.edu/workshops/technology2008/depot/dipirro-passivecooling_revb.pdf. [30 November 2011].

DiPirro, M., Tuttle, J., Ollendorf, S., Mattern, A., Leisawitz, D., Jackson, M., Francis, J., Hait, T., Cleveland, P. & Muheim, D. 2007. High-fidelity cryothermal test of a subscale large space telescope. *Proceedings- SPIE the International Society for Optical Engineering,* 6692: 6692 02-6692 03.

Dorman, L.I., Belov, A.V., Eroshenko, E.A., Gromova, L.I., Iucci, N., Levitin, A.E., Parisi, M., Ptitsyna, N.G., Pustil'nik, L.A., Tyasto, M.I., Vernova, E.S., Villoresi, G., Yanke, V.G. & Zukerman, I.G. 2004. Different space weather effects in anomalies of the high and low orbital satellites. *Advances in Space Research*, 36: 2530–2536.

Drung, D. 1995. Advanced SQUID read-out electronics. *Proceedings of the NATO Advanced Study Institute on SQUID Sensors: Fundamentals, Fabrication and Applications*, 329: 63-116.

Drung, D., Cantor, R., Peters, M., Scheer, H.J. & Koch, H. 1990. Low-noise high speed DC superconducting quantum interference device magnetometer with simplified feedback electronics. *Applied Physics Letters*, 406-408.

European space agency. 2009. ESA news: ESA to launch two large observatories to look deep into space and time. http://www.esa.int/esaCP/SEMEOSZXDUF_index_0.html. [30 November 2011].

Faley, M.I., Poppe, U., Urban, K., Paulson, D.N., Starr, T.N. & Fagaly, R.L. 2001. Low noise HTS DC-SQUID flip-chip magnetometers and gradiometers. *IEEE Transactions on Applied Superconductivity*, 11(1): 1383-1386.

Faley, M.I., Poppe, U., Urban, K., Paulson, D.N., Starr, T.N. & Fagaly, R.L. 2002. Sensitive HTS DC

Finley, P.T. & Schweickart, R.B. 2006. Mid-mission Update of Spitzer Space Telescope Cryogenic Performance. *AIP Conf. Proc.,* 823 (1): 1295-1302.

Flokstra, J., Ter Brake, H.J.M., Houwman, E.P., Veldhuis, D., Jaszczuk, W., Caspari, M., Rogalla, H., Marti´nez, A. & Rillo, C. 1991. A 19-channel d.c. SQUID magnetometer system for brain research. *Sensors and Actuators A: Physical Sensors and Actuators A: Physical,*

27(1-3): 781-785.

Ganther, Jr., K.R. & Snap, L.D. 2002(a). Readout electronics for dc SQUID magnetic measurements. *United States Patent*. US6420868B1.

Ganther, Jr., K.R. & Snap, L.D. 2002(b). Frequency multiplexed flux locked loop architecture providing an array of dc SQUIDs having both shared and unshared components. *United States Patent*. US6356078B1.

Ganther, Jr., K.R. & Snap, L.D. 2006. System having unmodulated flux locked loop for measuring Magnetometic fields. *United States Patent*. US7091718B1.

Gilmore, D. 2002. *Spacecraft Thermal Control Handbook: vol. I, fundamentals and technology*. Virginia: American Institute of Aeronautics and Astronautics.

Hastings, R., Mahler, R., Schneider, R. & Eraker, J. 1985. Cryogenic magnetic gradiometers for space applications. *IEEE Trans.Geosci.Remote Sensing IEEE Transactions on Geoscience and Remote Sensing,* GE-23(4): 552-561.

Heirtzler, J.R. 2002. The future of the South Atlantic anomaly and implications for radiation damage in space. *Journal Of Atmospheric and Solar Terrestrial Physics,* 64(16): 1701-1708.

Hilton, S.G., Dawe, R.N.S., Dubicki, J.E., Brain, M., Lawrence, B., Whittlesea, S.J., Trott, M.D, Kim, J.S., Atkins, T.J., Yates, S.J.C., King, C.W., Springford, M., Powell, B.J. & Holt, D.R. 2001. Superconducting Quantum Interference Devices (SQUIDs) and their applications. http://rich.phekda.org/squid/index.html. [10 October 2011].

Hongyan, X., Deping, D., Weiyang, W. & Zhong, L. 2005. The working performance of radiant cooler in thermal vacuum test. *Proceedings of the Twentieth International Cryogenic Engineering Conference (ICEC20),* Shanghai, n.d. Shanghai Institute if Technological Physics: 449-452.

HyperPhysics. 2000a. Magnetic field of the Earth. http://hyperphysics.phy-astr.gsu.edu/hbase/magnetic/magearth.html. [29 October 2012].

HyperPhysics. 2000b. Liquid Helium. http://hyperphysics.phy-astr.gsu.edu/hbase/lhel.html. [29 October 2012].

International Astronautical Congress. 2011. *French South African Institute of Technology.* http://iac2011.com/space-south-africa/fsati. [23 August 2011].

Jacques, L. 2009. Thermal design of the oufti-1 nanosatellite. Unpublished thesis, University of Liège, Belgium.

Jia, Q.X., Yan, F., Mombourquette, C. & Reagor, D. 1998. Directly coupled direct current superconducting quantum interference device magnetometers based on ramp-edge Ag:YBa2Cu_3O_{7-x}/Pr$Ba_2Cu_3O_{7-x}$/Ag:$YBa_2Cu_3O_{7-x}$ junctions. *Applied Physics Letters,* 72(23): 3068-3070.

Khare, N. 2003. *Handbook of high-temperature superconductor electronics. s.l.*: Marcel Darker.

Kitchin, C. & Counts, L. 2006. *A designer's guide to instrumentation amplifiers*. New York, NY: Analog Devices 2000.

Lanzerotti, L.J. 2000. Space weather effects on communications. In Daglis I.A. Space storms and space weather hazards. *Proceedings of the NATO Advanced Study Institute on Space*

Storms and Space Weather Hazards, Hersonissos, Crete, 19-29 June, 2000. Dordretcht: Kluwer Academic Publishers: 313-335.

Learning Space. 2011. Superconductivity. http://openlearn.open.ac.uk. [1 September 2011].

Longo, C.R.O. & Rickman, S.L. 1995. *Method for the calculation of spacecraft umbra and penumbra shadow terminator points*. Houston: Lyndon B. Johnson Space Center.

Ludwig, F., Dantsker, E., Kleiner, R., Koelle, D., Clarke, J., Knappe, S., Drung, D., Koch, H., Alford, N.M. & Button, T.W. 2009. Integrated high-Tc multiloop magnetometer. *Applied Physics Letters*. 66(11): 1418 – 1420.

Macintyre, S.A. 1999. Magnetic field measurement. In Webster, J.G. The measurement, instrumentation, and sensors handbook. Boca Raton, Fla.: CRC Press published in cooperation with IEEE Press: 36-18.

Magnes, W., H. Hauer, Valavanoglou, A., M. Oberst, Neubauer H., Baumjohann, W. & Falkner, P. 2006. White Paper on magnetometer front-end ASIC (MFA). AMICSA. Space Research Institute, Austrian Academy of Sciences, Fraunhofer Institute for Integrated Circuits , Germany, Institute of Geophysics and Planetary Physics , UCLA, USA and European Space Research and Technology Centre, ESA.

Matsuda, M., Murayama, Y., Kiryu, S., Kasai, N., Kashiwaya, S., Koyanagi, M., Endo, T. & Kuriki, S. 1991. Directly-coupled DC-SQUID magnetometers made of Bi-Sr-Ca-Cu oxide films. *IEEE Transactions on Magnetics (Institute of Electrical and Electronics Engineers),* 27(2): 3043-3046.

Mester, J., & GP-B Collaboration. 2006. Testing Einstein in space: The gravity probe B relativity mission. Seminaire Poincare, IX, 55-61.

Mitchell, D.P. 2007. Sputnik-3. http://www.mentallandscape.com/S_Sputnik3.htm. [27 August 2011].

Moldwin, M. 2008. *An introduction to Space Weather*. Cambridge University Press, New York.

National Semiconductor. 2002. Application note 31 op amp circuit collection. http://www.ti.com/lit/an/snla140a/snla140a.pdf. [15 May 201].

Nguyen, H., Persson, A., & Thornell, G. 2010. Material- and fabrication-governed performance of a tunnelling magnetometer. *Adv.Nat.Sci: Nanosci.Nanotechnol.Advances in Natural Sciences: Nanoscience and Nanotechnology, 1*(4), 045006.

NOAA Space Weather Prediction Center. n.d. Satellites and Space Weather. http://www.swpc.noaa.gov/info/Satellites.html. [15 August 2011].

Nturambirwe, J.F.I. 2010. Superconducting quantum interference device (squid) magnetometers: principles, fabrication and applications. Unpublished thesis, Stellenbosch University, South Africa.

Omerbegoviae, A. 1999. White paper on radiation evaluation of the CS5508 (20-bit ADC crystal Sem). Space Research Institute SRI in Graz in co-operation with the European Space Agency ESA and TU Graz.

Orlando, T.P. & Delin, K.A. 1991. *Foundation of applied superconductivity.* Reading, Mass.: Addison-Wesley.

Paul, C.R. 2004. *Electromagnetics for Engineers: with Applications to Digital Systems Electromagnetic Interference*. Hoboken: John Wiley and Sons.

Pedersen, E.B., Primdahl, F., Petersen, J.R., Merayo, J.M.G., Peter, b. & Nielsen, O.V. 1999. Digital fluxgate magnetometer for the Astrid-2 satellite. *Meas. Sci. Technol.*, 10:N124-N129.

Pilbratt, G.L. 2008. White Paper on Herschel mission overview and key programmes. Noordwijk: European Space Agency, Research and Scientific Support Dept.

Powersim. 2001. PSIM user manual. http://tec.upc.es/ep/psim-manual.pdf. [26 April 2012].

Primdahl, F. 1979. *The fluxgate magnetometer.* s.l.: Kobenhavn.

Pronenko, V. & Korepanov, V. 2009. Induction coil magnetometers-a review. *Geophysical Research abstract,* 11:1381.

Rabinowitz, M., Garwin, E.L. & Frankel, D.J. 1973. An investigation of the very incomplete Meissner effect. *Lett.Nuovo Cimento Lettere Al Nuovo Cimento Series 2,* 7(1): 1

Rolfo, A. 1978. A cryogenic passive radiative cooler three years in space flight results. *ICEC 7; Proceedings of the Seventh International Cryogenic Engineering Conference,* A79 (31001): 12-31.

Scharnweber, R. & Schilling, M. 2009. Integrated YBa2Cu3O7 magnetometer with flux transformer and multiloop pick-up coil. *Applied Physics Letters*. 69(9): 1303 – 1305.

Seltzer, S.J. & Romalis, M.V. 2004. Unshielded three-axis vector operation of a spin-exchange-relaxation-free atomic magnetometer. *Applied Physics Letters,* 85(20): 4804-4806.

Simon, R.W, Burns, M.J., Colclough, M.S., Zaharchuk, G. & Cantor, R. 2004. Mr. SQUID user's guide. Santa Fe: STAR Cryoelectronics, LLC.

Siziba, E. 2012. Evaluation of a fluxgate magnetometer for a CubeSat. Unpublished thesis, Cape Peninsula University of Technology, South Africa.

Snowden, S.L. 2002. South Atlantic Anomaly. http://heasarc.gsfc.nasa.gov/docs/rosat/gallery/misc_saad.html. [27 October 2011].

SolidWorks. 2008. Thermal analysis. http://www.solidworks.com. [11 February 2012].

Spacemag. n.d. Space mag Inovation in magnetic measuring instruments. http://www.bartington.com/Literaturepdf/Datasheets/Spacemag%20DS2714.pdf. [29 October 2012].

Star Cryoelectronics. 20011. White Paper on HTS magnetometer M1000. Santa Fe.

Star Cryoelectronics. 2004. White paper on SQUID sensors. Santa Fe.

Star Cryoelectronics. n.d. pcSQUID user's manual. http://www.starcryo.com/pcSQm21.pdf. [22 August 2012].

STMicroelectronics. 2001. White Paper on general purpose single operational amplifier. Italy.

Sugita, H., Sato Y., Yamawaki T., Nakagawa T., Murakami H., Matsuhara H., Murakami M., Takada M., Takai S., Yoshida S. & Kanao K. 2010. Cryogenic system design of the next generation infrared space telescope SPICA. *Cryogenics Cryogenics,* 50(9): 566-571.

Texas Instruments. 2008. White Paper on 1.6GHz, low-noise, FET-input operational amplifier. Dallas.

Thaller, M. & Guttro, R. 2010. NASA mission news: 'L2' will be the James Webb Space Telescope's Home in Space. http://www.nasa.gov/topics/universe/features/webb-l2.html. [30 November 2011].

Thermal Desktop. 2010. Introduction to Thermal Desktop. http://www.crtech.com/introTD.html. [12 August 2012].

Tumanski, S. 2007. Induction coil sensors-a review. *Measurement science & technology,* 18(3): R31-R46.
University of Oxford. 2008. Passive cooling. http://www.atm.ox.ac.uk/main/Capabilities/passive_coolers.html. [7 December 2011].

van Staden, W.F. 2007. The fabrication of PBCO buffered step-edge Josephson junctions. Unpublished thesis, Stellenbosch University, South Africa.

van Zyl, D.S. 2010. SQUID detected low- field NMR for the evaluation of internal fruit quality. Unpublished thesis, Stellenbosch University, South Africa.

Visser, D F. 2009. White Paper on CPUT CubeSat – Mission requirements and technical specifications. Cape Town: Cape Peninsula University of Technology.

Wright, E.L. WMAP design and first-year results. 2004. http://www.accessscience.com. [30 November 2011].

Zhang, Y., Wolters, N., Otto, R. & Krause, H.J. 2002. Non-constant bias current for DC SQUID operation. *PHYSICA C,* 368(1-4): 181-184.

APPENDICES

Appendix A: Star Cryoelectronics M1000 SQUID magnetometer specifications

2 SPECIFICATIONS

Table 2.1 Specifications, M1000 dual-SQUID magnetometer chip.

Parameter	Value			
Pickup loop size	8.7 mm × 7.45 mm OD, 3.8 mm ×2.7 mm ID			
Feedback coil inductance L_f	Embedded in package, see Figure 3.2			
Operating temperature	75 to 79 K (77 K typical)			
	Min.	Typ.	Max.	Unit
SQUID critical current $2I_C$	10	20	100	μA
SQUID resistance $R/2$	-	3	-	Ω
Feedback mutual inductance[1] $1/M_f$	-	7	-	$\mu A/\Phi_0$
Voltage swing ΔV	-	30	-	μV
Field calibration	-	12	-	nT/Φ_0
Field noise $S_B^{1/2}(f)$, f > 10 Hz	50	-	100	$fT/Hz^{1/2}$
Temp. coefficient at 77K	-	1	-	nT/K
Heater power (~110 Ohm at 77 K)	-	-	1.1	W
Heat time to normalize	-	-	15	Sec
Storage temperature (dry)	0	20	40	°C

[1]M1000 packaged in LEMO package assembly

3 ROOM-TEMPERATURE RESISTANCES

(See Safe Handling Procedures before making any resistance measurements on the SQUID)

Table 3.1 M1000 packaged in LEMO package assembly (see Figure 3.1)

Contacts	Pins[1] (+/-)	Resistance [Ω]
Bias	8,9	210
Voltage	2,3	5
Heater	1,4	105
Modulation	7,10	6
Feedback[2]	6,5	6

[1]See mechanical specifications, magnetometer sensor assembly
[2]Modulation and Feedback are summed inside sensor assembly

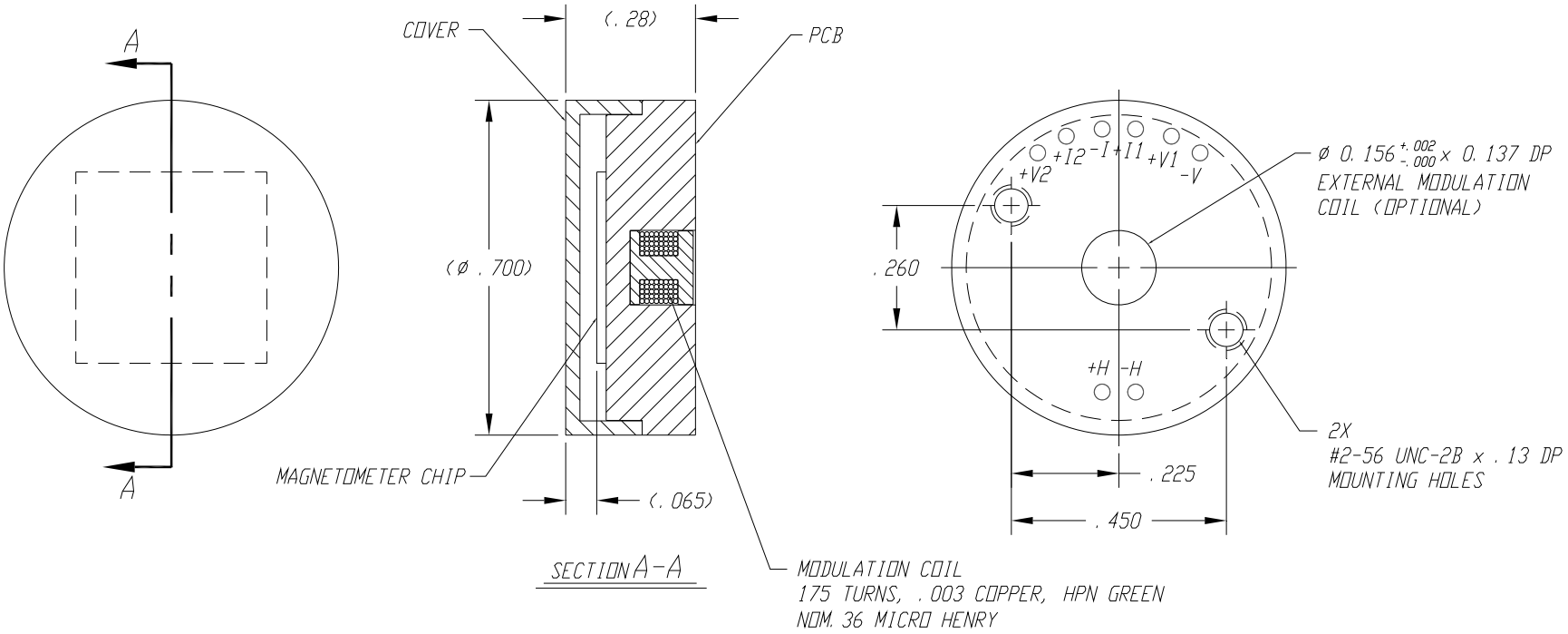

NOTES: UNLESS OTHERWISE SPECIFIED.

1 MATL: COVER G-10
PCB FR-4

2 ALL CONTACT VIAS ARE WITHIN ø 0.639

Figure 3.2 Mechanical specifications, M1000 magnetometer button package.

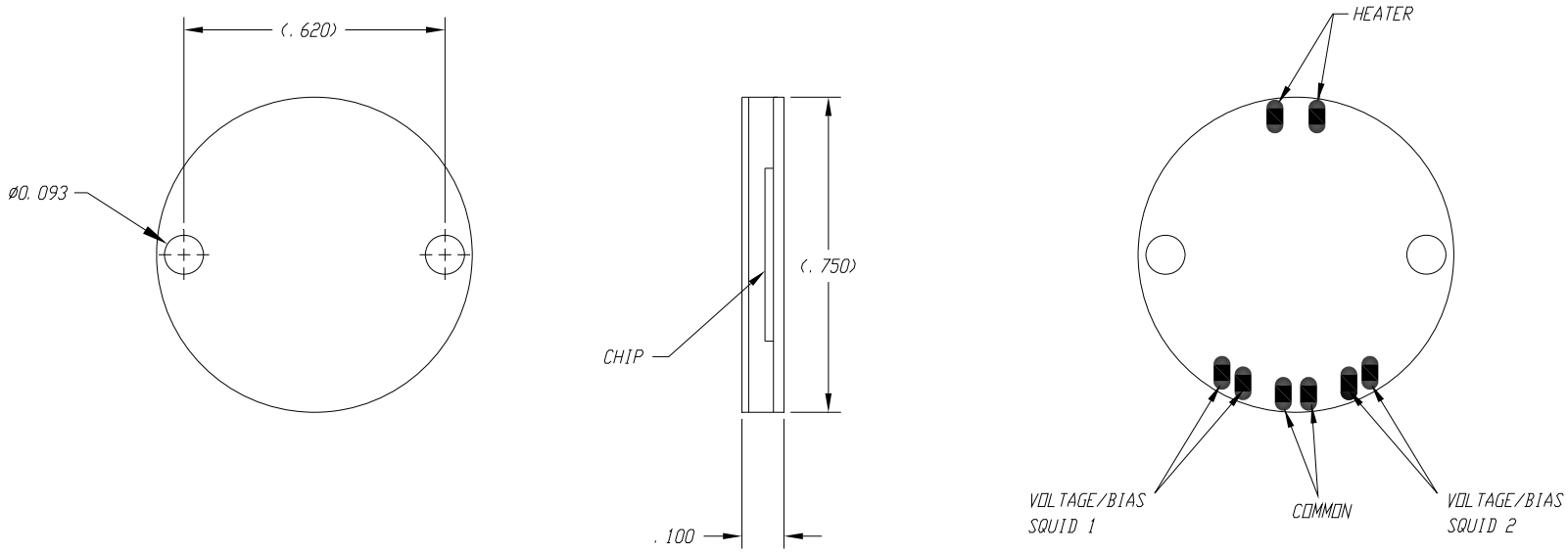

Figure 3.3 Mechanical specifications, M19 package.

Appendix B: MATLAB code for plotting the data of all the simulations

Data plotting for the simulated JJ's oscillation at steady bias currents

```
%This code plots the voltage across the Josephson junction against the
simulation time
clc;clear all;close all
Uiimport %this prompts to selct the file to be imported
Ic=20e-6;Rn=6;%the critical junction current and the normal junction
resistance
plot(Time*1e9,JJ8_8/(Ic*Rn),'black');hold on %this plots the VJJ at 8.8 Ic
plot(Time*1e9,JJ4_4/(Ic*Rn),'black');hold on %this plots the VJJ at 4.4 Ic
plot(Time*1e9,JJ2_2/(Ic*Rn),'black');hold on %this plots the VJJ at 2.2 Ic
plot(Time*1e9,JJ1_1/(Ic*Rn),'black');hold off %this plots the VJJ at 1.1 Ic
%axis([0 5 0 10]); % for axis trimming
Grid
xlabel('time (ns)')
ylabel('V_J_J/(I_c_,R_n)')
```

Data plotting for the simulated $V-I$ characteristics

```
clc;clear all;close all
Uiimport %this prompts to selct the file to be imported
Ic=20e-6;Rn=6; %the critical junction current and the normal junction
plot(Bias/Ic,VSQ0/(Ic*Rn),'black');grid
ylabel('V_J_J/(I_cR_n)')
xlabel('Bias current/I_c')
```

Data plotting for the simulated $V-\Phi$ characteristics

```
clc;clear all;close all
Uiimport %this prompts to selct the file to be imported
Ic=20e-6;Rn=6; %the critical junction current and the normal junction
plot(Flux,VSQ/(Ic*Rn),'black')
%substitute Time for Flux in case of the V-time response
ylabel('V_S_Q/(I_c_,_a_vR_n)');
xlabel('Flux (fluxon)');grid
%axis ([-3 3 1.55 1.7]); % for axis trimming
```

Appendix C: MATLAB code for plotting the data all the measurements

Data plotting for the input to the bias circuit and the voltage across the SQUID/load

```
clc;clear all;close all
Uiimport %this prompts to selct the file to be imported
subplot(2,1,1) %for the input to the bias circuit
plot(second*1e3,Volt1);grid
title('Input to the bias circuit')
xlabel('Time (ms)');
ylabel('Voltage (V)')
%axis([-25 25 -5 8]); % for axis trimming

subplot(2,1,2) %for the voltage across the SQUID/load
plot(second*1e3,(Volt*1.0*1e3));grid
title('V_S_Q at room temperature')
```

Data plotting for the bias current

```
clc;clear all;close all
Uiimport %this prompts to selct the file to be imported
plot(second*1e3,Volt1*0.2195/20e3*1e6); Current equivalent of the input
voltage
grid
title('Output current')
ylabel('current (uA)');
```

```
Xlabel('time (ms)')
%axis([-25 25 -150 150]); % for axis trimming
```

Data plotting for the bias current and the voltage across the SQUID

```
clc;clear all;close all
Uiimport %this prompts to selct the file to be imported
subplot (211) %for the bias current
plot(second*1e3,Volt1*0.2195/20e3*1e6);grid
title('Output current')
ylabel('current (uA)');
Xlabel('time (ms)')
%axis([-25 25 -150 150]) %for axis trimming

subplot(212) %for the voltage across the SQUID/load
plot(second*1e3,(Volt*1.0*1e3));grid
title('V_S_Q at room temperaturet')
xlabel('Time (ms)');
ylabel('Voltage (mV)')
%axis([-25 25 -50 50])%for axis trimming
```

Data plotting for the $V-I$ characteristics

```
clc;clear all;close all
Uiimport %this prompts to selct the file to be imported
plot(Volt1*0.2195/20e3*1e6,Volt);grid %plots the current equivalent of the
input voltage against the voltage across the SQUID/load
title('V-I curve')
xlabel('Current (uA)');
ylabel('Voltage (V)');
%axis([-25 25 -5 5]) % for axis trimming
```

Data plotting for the multimeter ohm range

```
clc;clear all;close all
Uiimport %this prompts to selct the file to be imported
subplot(2,1,1) %for the input voltage
plot(second*1e3,Volt1*1e3);grid
title('Voltage drop across the load')
xlabel('Time (ms)');
ylabel('Voltage (mV)')
%axis([-25 25 -6 6]); % for axis trimming

subplot(2,1,2) %for the output bias current
plot(second*1e3,(Volt)/216*1e6); % Current equivalent of the voltage drop
across the load
grid
title('Current through the load')
xlabel('Time (ms)');
ylabel('Current (uA)')
%axis ([-25 25 -20 20]); % for axis trimming
```

Appendix D: The Simulink subsystem block for a DC SQUID magnetometer

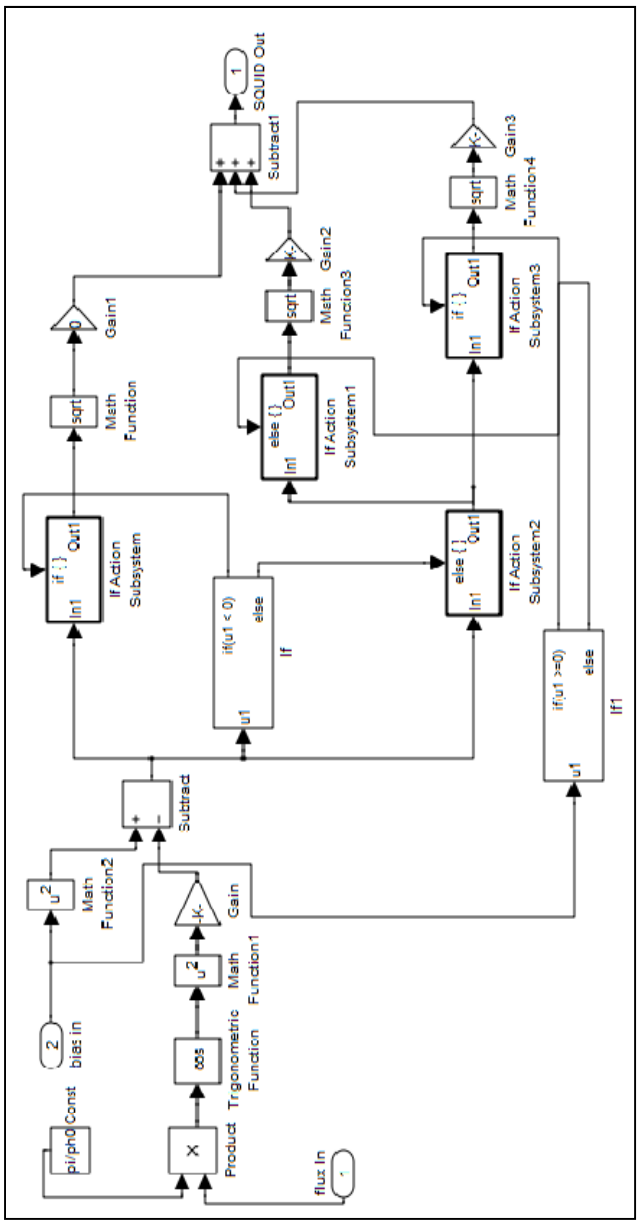

Figure D.1: The Simulink subsystem block for a DC SQUID magnetometer

Appendix E: Electrical characteristics of OPA657

ELECTRICAL CHARACTERISTICS: V_S = ±5V

R_F = 453Ω, R_L = 100Ω, and G = +10, unless otherwise noted. Figure 1 for AC performance.

PARAMETER	CONDITIONS	OPA657U, N (Standard-Grade)						TEST LEVEL(3)
		TYP	MIN/MAX OVER TEMPERATURE					
		+25°C	+25°C(1)	0°C to 70°C(2)	–40°C to +85°C(2)	UNITS	MIN/ MAX	
AC PERFORMANCE (Figure 1)								
Small-Signal Bandwidth	G = +7, V_O = 200mV$_{PP}$	350				MHz	Typ	C
	G = +10, V_O = 200mV$_{PP}$	275				MHz	Typ	C
	G = +20, V_O = 200mV$_{PP}$	90				MHz	Typ	C
Gain-Bandwidth Product	G > +40	1600				MHz	Typ	C
Bandwidth for 0.1dB flatness	G = +10, 2V$_{PP}$	30				MHz	Typ	C
Peaking at a Gain of +7		7				dB	Typ	C
Large-Signal Bandwidth	G = +10, 2V$_{PP}$	180				MHz	Typ	C
Slew Rate	G = +10, 1V Step	700				V/µs	Typ	C
Rise-and-Fall Time	0.2V Step	1				ns	Typ	C
Settling Time to 0.02%	G = +10, V_O = 2V Step	20				ns	Typ	C
Harmonic Distortion	G = +10, f = 5MHz, V_O = 2V$_{PP}$							C
2nd-Harmonic	R_L = 200Ω	–70				dBc	Typ	C
	R_L > 500Ω	–74				dBc	Typ	C
3rd-Harmonic	R_L = 200Ω	–99				dBc	Typ	C
	R_L > 500Ω	–106				dBc	Typ	C
Input Voltage Noise	f > 100kHz	4.8				nV/√Hz	Typ	C
Input Current Noise	f > 100kHz	1.3				fA/√Hz	Typ	C
DC PERFORMANCE(4)								
Open-Loop Voltage Gain (A_{OL})	V_{CM} = 0V, R_L = 100Ω	70	**65**	64	63	dB	Min	A
Input Offset Voltage	V_{CM} = 0V	±0.25	**±1.8**	±2.2	±2.6	mV	Max	A
Average Offset Voltage Drift	V_{CM} = 0V	±2	**±12**	±12	±12	µV/°C	Max	A
Input Bias Current	V_{CM} = 0V	±2	**±20**	±1800	±5000	pA	Max	A
Input Offset Current	V_{CM} = 0V	±1	**±10**	±900	±2500	pA	Max	A
INPUT								
Most Positive Input Voltage(5)		+2.5	**+2.0**	+1.9	+1.8	V	Min	A
Most Negative Input Voltage(5)		–4.0	**–3.5**	–3.4	–3.3	V	Min	A
Common-Mode Rejection Ratio (CMRR)	V_{CM} = ±0.5V	89	**83**	81	79	dB	Min	A
Input Impedance								
Differential		10^{12} || 0.7				Ω || pF	Typ	C
Common-Mode		10^{12} || 4.5				Ω || pF	Typ	C
OUTPUT								
Voltage Output Swing	No Load	±3.9	±3.7			V	Typ	B
	R_L = 100Ω	±3.5	**±3.3**	±3.2	±3.1	V	Min	A
Current Output, Sourcing		+70	**50**	48	46	mA	Min	A
Current Output, Sinking		–70	**–50**	–48	–46	mA	Min	A
Closed-Loop Output Impedance	G = +10, f = 0.1MHz	0.02				Ω	Typ	C
POWER SUPPLY								
Specified Operating Voltage		±5				V	Typ	A
Maximum Operating Voltage Range			**±6**	±6	±6	V	Max	A
Maximum Quiescent Current		14	**16**	16.2	16.3	mA	Max	A
Minimum Quiescent Current		14	**11.7**	11.4	11.1	mA	Min	A
Power-Supply Rejection Ratio (+PSRR)	+V_S = 4.50V to 5.50V	80	**76**	74	72	dB	Min	A
(–PSRR)	–V_S = 4.50V to –5.50V	68	**62**	60	58	dB	Min	A
TEMPERATURE RANGE								
Specified Operating Range: U,N Package		–40 to 85				°C	Typ	
Thermal Resistance, θ_{JA}	Junction-to-Ambient							
U: SO-8		125				°C/W	Typ	
N: SOT23-5		150				°C/W	Typ	

NOTES: (1) Junction temperature = ambient for 25°C specifications.

(2) Junction temperature = ambient at low temperature limit; junction temperature = ambient +20°C at high temperature limit for over temperature specifications.

(3) Test Levels: (A) 100% tested at 25°C. Over temperature limits by characterization and simulation. (B) Limits set by characterization and simulation. (C) Typical value only for information.

(4) Current is considered positive out-of-node. V_{CM} is the input common-mode voltage.

(5) Tested < 3dB below minimum specified CMRR at ±CMIR limits.

Appendix F: Electrical characteristics of OPA134

At T_A = +25°C, V_S = ±15V, unless otherwise noted.

PARAMETER	CONDITION	OPA134PA, UA OPA2134PA, UA OPA4134PA, UA MIN	TYP	MAX	UNITS
AUDIO PERFORMANCE					
Total Harmonic Distortion + Noise	G = 1, f = 1kHz, V_O = 3Vrms				
	R_L = 2kΩ		0.00008		%
	R_L = 600Ω		0.00015		%
Intermodulation Distortion	G = 1, f = 1kHz, V_O = 1Vp-p		–98		dB
Headroom(1)	THD < 0.01%, R_L = 2kΩ, V_S = ±18V		23.6		dBu
FREQUENCY RESPONSE					
Gain-Bandwidth Product			8		MHz
Slew Rate(2)		±15	±20		V/µs
Full Power Bandwidth			1.3		MHz
Settling Time 0.1%	G = 1, 10V Step, C_L = 100pF		0.7		µs
0.01%	G = 1, 10V Step, C_L = 100pF		1		µs
Overload Recovery Time	(V_{IN}) • (Gain) = V_S		0.5		µs
NOISE					
Input Voltage Noise					
Noise Voltage, f = 20Hz to 20kHz			1.2		µVrms
Noise Density, f = 1kHz			8		nV/√Hz
Current Noise Density, f = 1kHz			3		fA/√Hz
OFFSET VOLTAGE					
Input Offset Voltage			±0.5	±2	mV
	T_A = –40°C to +85°C		±1	±3(3)	mV
vs Temperature	T_A = –40°C to +85°C		±2		µV/°C
vs Power Supply (PSRR)	V_S = ±2.5V to ±18V	90	106		dB
Channel Separation (Dual, Quad)	dc, R_L = 2kΩ		135		dB
	f = 20kHz, R_L = 2kΩ		130		dB
INPUT BIAS CURRENT					
Input Bias Current(4)	V_{CM} =0V		+5	±100	pA
vs Temperature(3)			See Typical Curve	±5	nA
Input Offset Current(4)	V_{CM} =0V		±2	±50	pA
INPUT VOLTAGE RANGE					
Common-Mode Voltage Range		(V–)+2.5	±13	(V+)–2.5	V
Common-Mode Rejection	V_{CM} = –12.5V to +12.5V	86	100		dB
	T_A = –40°C to +85°C		90		dB
INPUT IMPEDANCE					
Differential			10^{13} || 2		Ω || pF
Common-Mode	V_{CM} = –12.5V to +12.5V		10^{13} || 5		Ω || pF
OPEN-LOOP GAIN					
Open-Loop Voltage Gain	R_L = 10kΩ, V_O = –14.5V to +13.8V	104	120		dB
	R_L = 2kΩ, V_O = –13.8V to +13.5V	104	120		dB
	R_L = 600Ω, V_O = –12.8V to +12.5V	104	120		dB
OUTPUT					
Voltage Output	R_L = 10kΩ	(V–)+0.5		(V+)–1.2	V
	R_L = 2kΩ	(V–)+1.2		(V+)–1.5	V
	R_L = 600Ω	(V–)+2.2		(V+)–2.5	V
Output Current			±35		mA
Output Impedance, Closed-Loop(5)	f = 10kHz		0.01		Ω
Open-Loop	f = 10kHz		10		Ω
Short-Circuit Current			±40		mA
Capacitive Load Drive (Stable Operation)			See Typical Curve		
POWER SUPPLY					
Specified Operating Voltage			±15		V
Operating Voltage Range		±2.5		±18	V
Quiescent Current (per amplifier)	I_O = 0		4	5	mA
TEMPERATURE RANGE					
Specified Range		–40		+85	°C
Operating Range		–55		+125	°C
Storage		–55		+125	°C
Thermal Resistance, θ_{JA}					
8-Pin DIP			100		°C/W
SO-8 Surface-Mount			150		°C/W
14-Pin DIP			80		°C/W
SO-14 Surface-Mount			110		°C/W

NOTES: (1) dBu = 20*log (Vrms/0.7746) where Vrms is the maximum output voltage for which THD+Noise is less than 0.01%. See THD+Noise text. (2) Guaranteed by design. (3) Guaranteed by wafer-level test to 95% confidence level. (4) High-speed test at T_J = 25°C. (5) See "Closed-Loop Output Impedance vs Frequency" typical curve.

Appendix G: Fabrication and experimental set-up

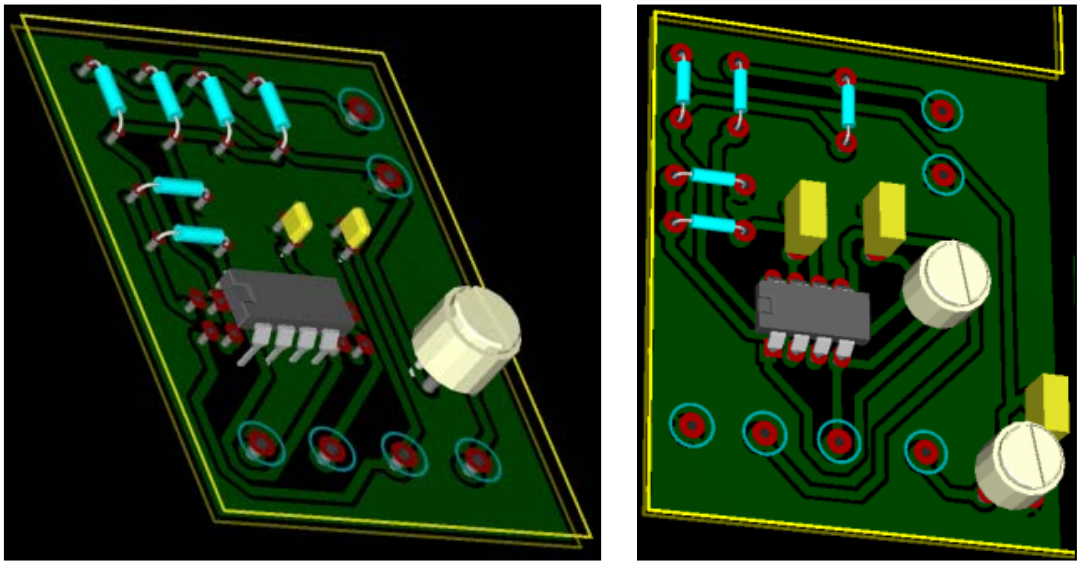

(a) (b)

Figure G.1: The PCB model for the bias circuit with the (a) OPA657 and (b) OPA134 op-amp

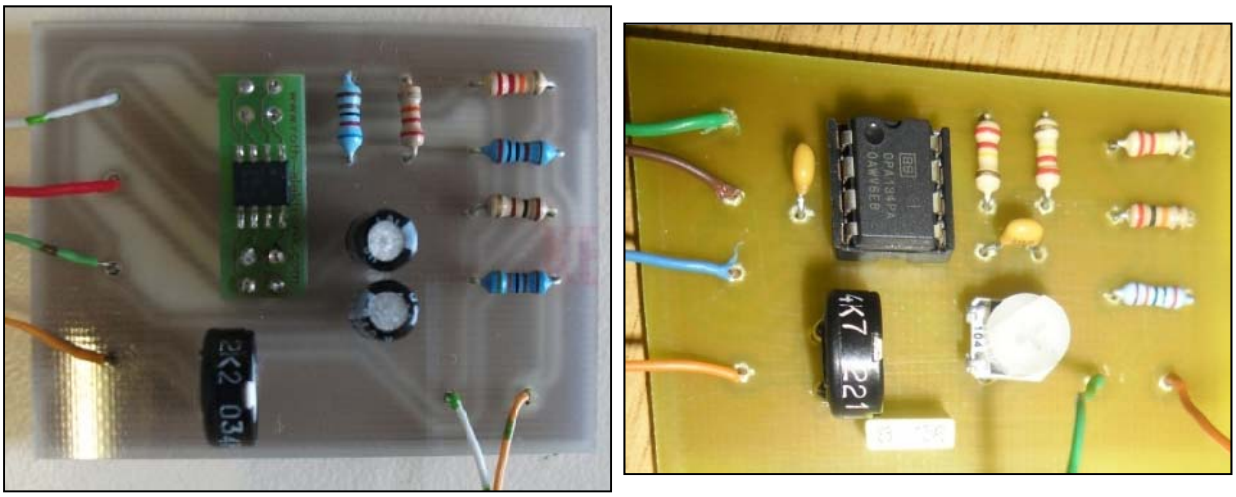

(a) (b)

Figure G.2: The fabricated bias circuit with the (a) OPA657 and (b) OPA134 op-amp

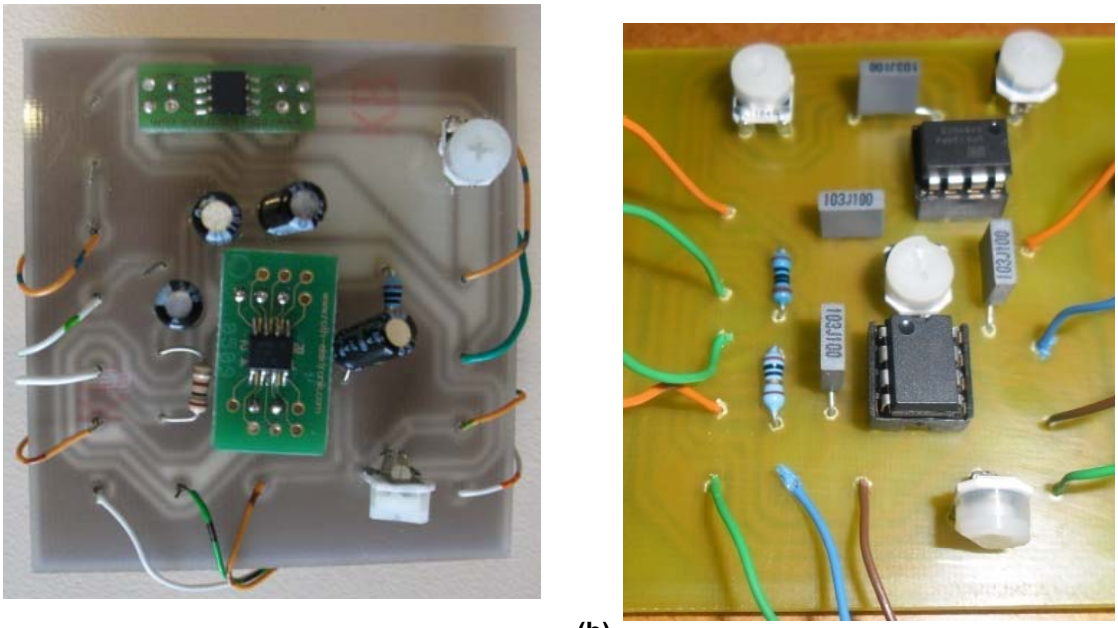

(a) (b)

Figure G.3: The fabricated preamplifier circuit with the (a) OPA657 op-amp and (b) TL702 and AD627 op-amps

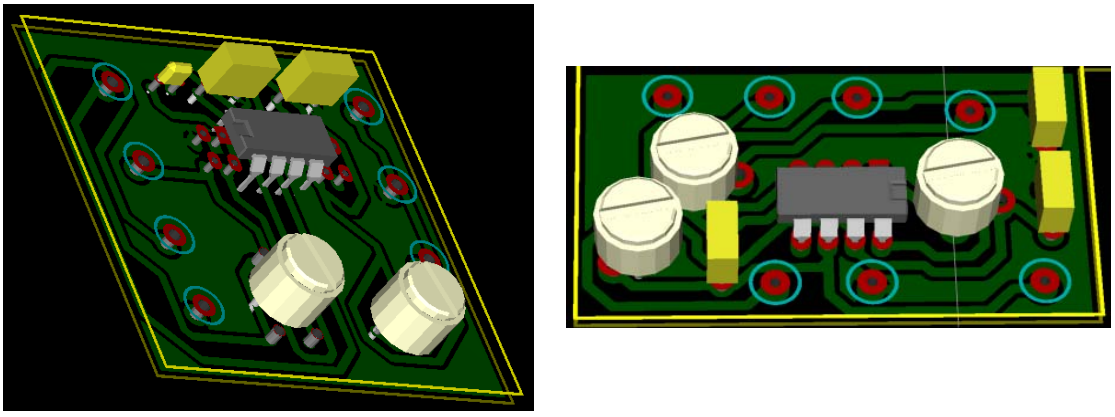

(a) (b)

Figure G.4: The PCB model of the integrator and feedback circuits with the (a) OPA657 op-amp and (b) OPA134 op-amp

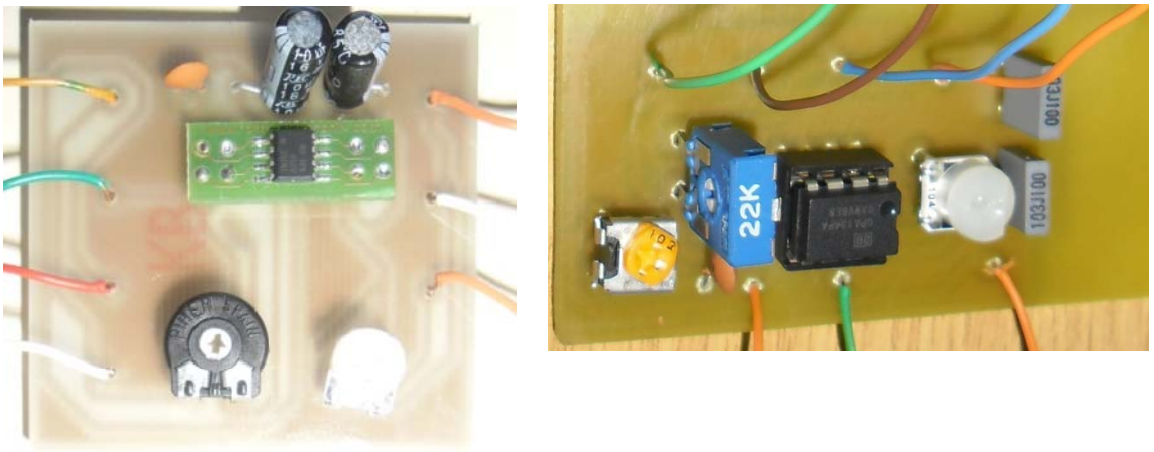

(a) (b)

Figure G.5: The fabricated integrator and the feedback circuits with (a) OPA657 op-amp and (b) TL702 op-amp

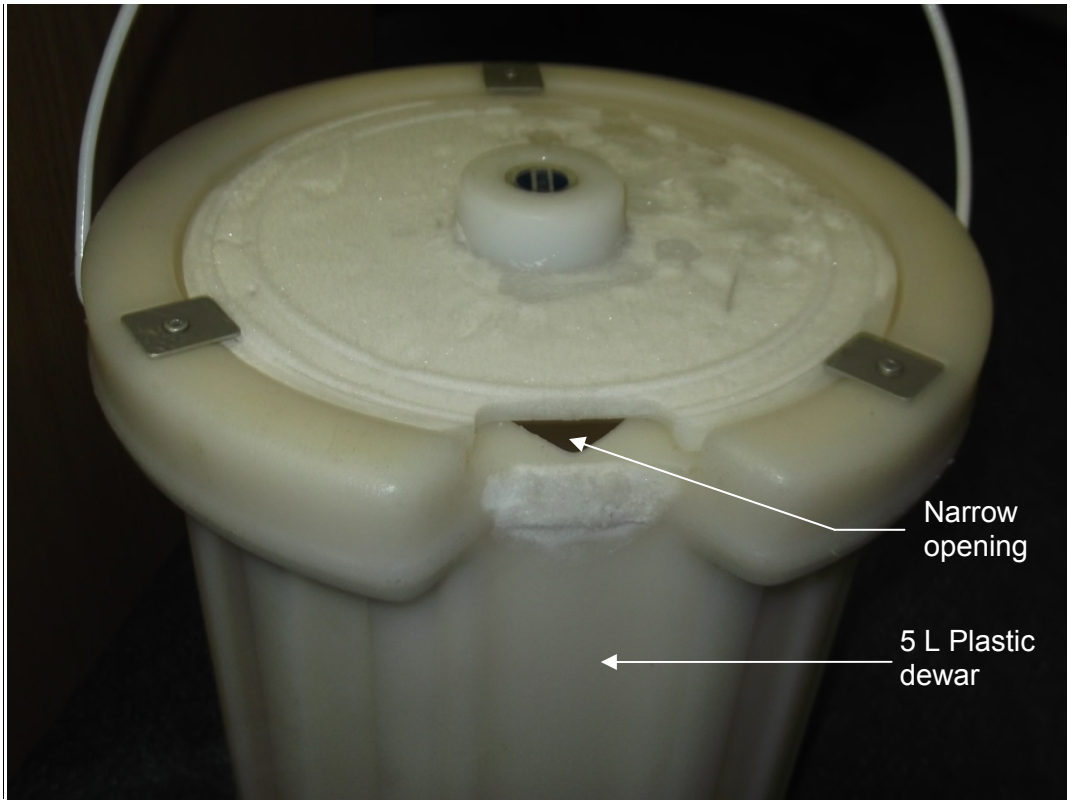

Figure G.6: The plastic dewar

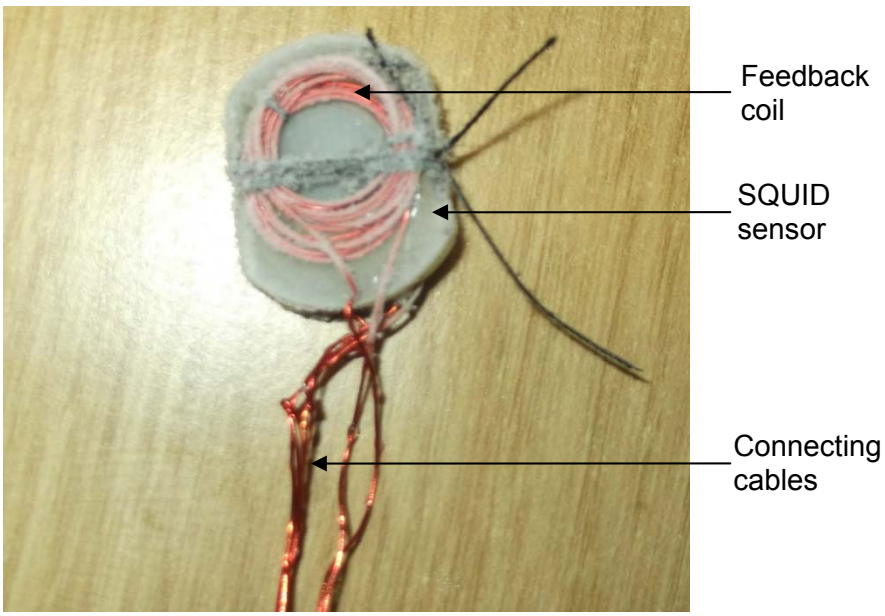

Figure G.7: The SQUID sensor during the heating process

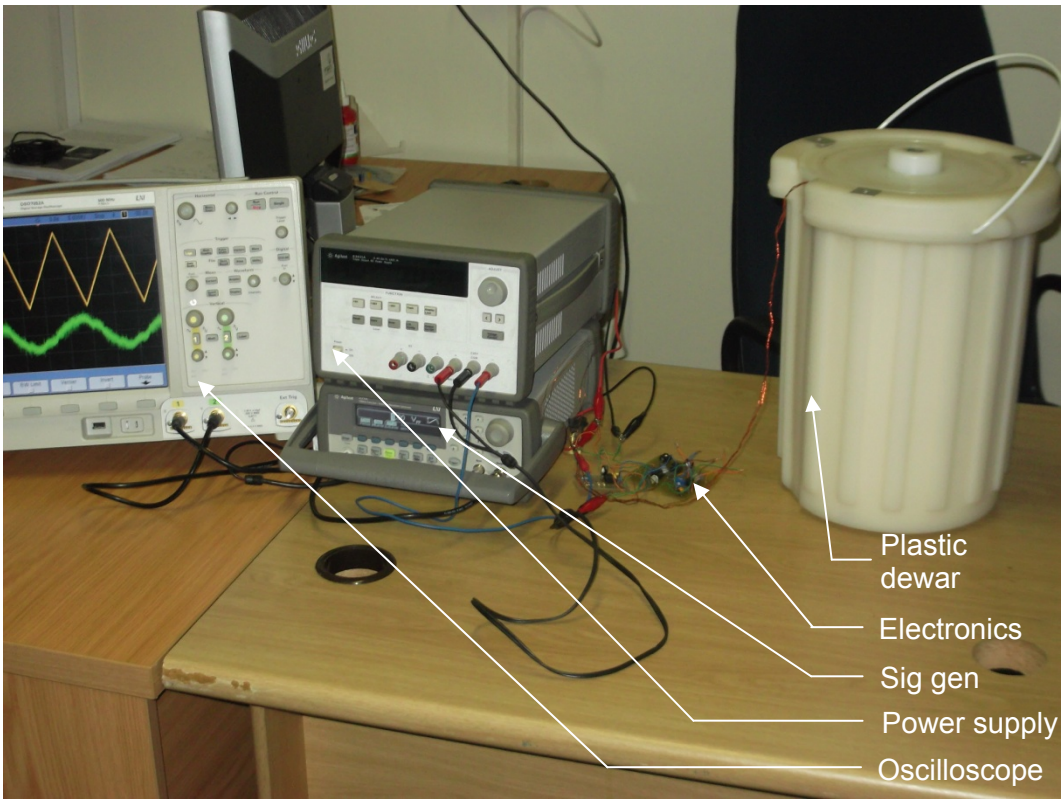

Figure G.8: The experimental set-up for the fabricated electronics

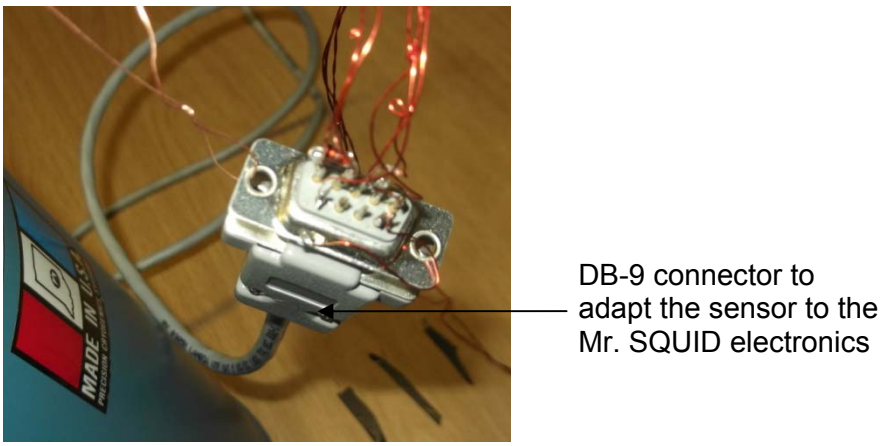

Figure G.9: Connections for adapting the sensor to the Mr. SQUID electronics set-up

Figure G.10: The Mr. SQUID front panel

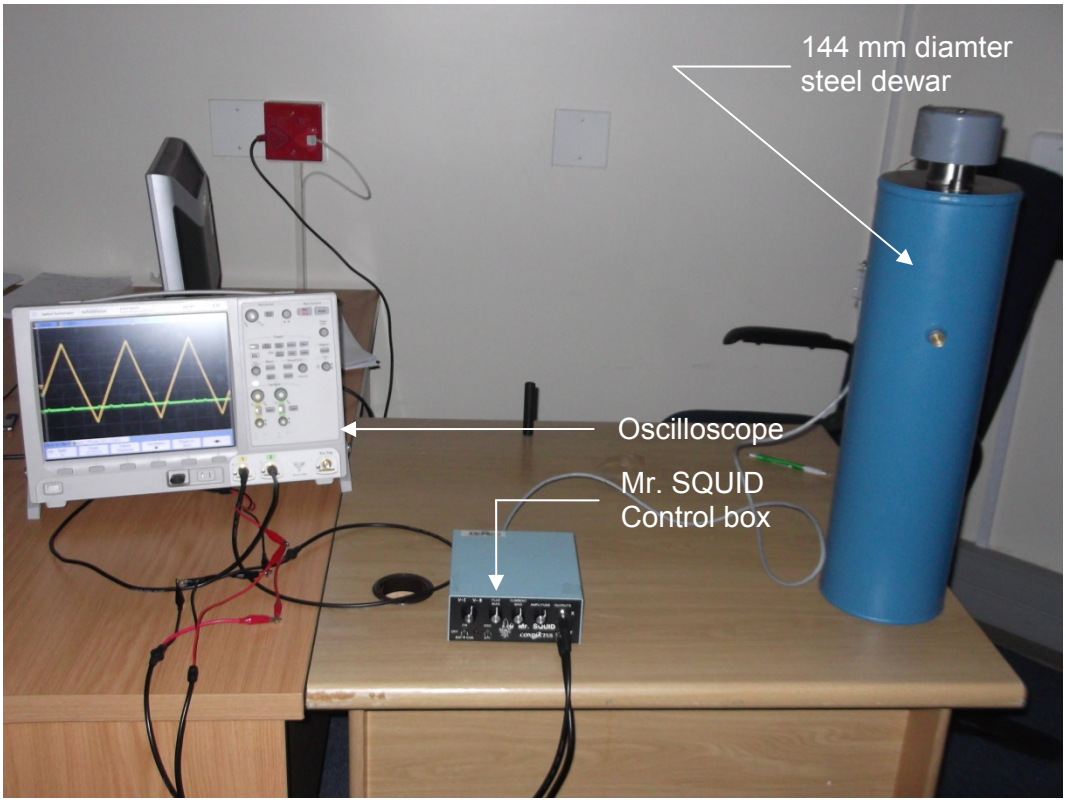

Figure G.11: The Mr. SQUID set-up

Figure G.12: The ADCL Medical Theratron 780-C with the SQUID sensor on the build-up

Figure G.13: A closer look at the ADCL Medical Theratron 780-C

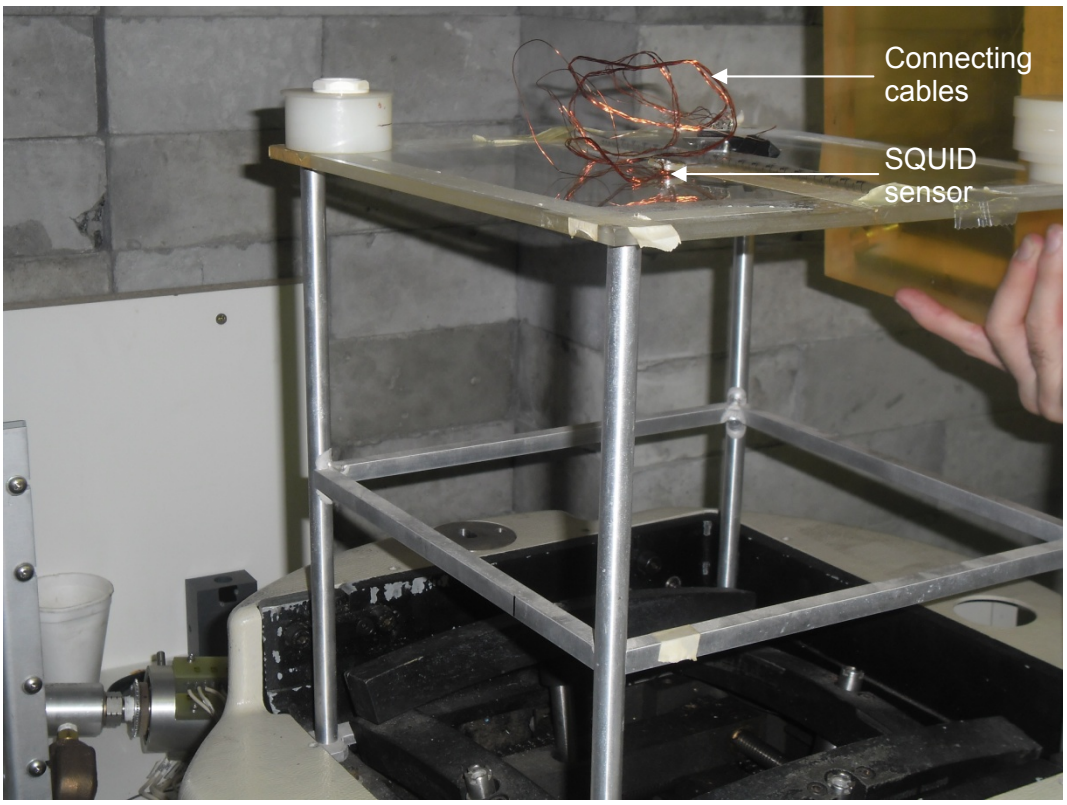

Figure G.14: ADCL Medical Theratron 780-C without backscatter

Figure G.15: The ADCL Medical Theratron 780-C control panel